CRANFIELD UNIVERSITY

Petros Gkotsis

Development of mechanical reliability testing techniques with application to thin films and piezo MEMS components.

School of Applied Sciences
Nanotechnology Group

PhD Thesis

CRANFIELD UNIVERSITY
School of Applied Sciences, Department of Materials
Nanotechnology Group

PhD Thesis

Academic Year 2009–2010

Petros Gkotsis

Development of mechanical reliability testing techniques with application to thin films and piezo MEMS components.

Paul B Kirby

Supervisor

April 2010

This thesis is submitted in partial fulfilment
of the requiremetns for the degree
of Doctor of Philosophy

© Cranfield University 2010. All rights reserved. No part of this publication may be reproduced without the written permission of the copyright holder.

To my dear wife Ioanna and my parents for their love and support

Abstract

This work focuses on the development of a method for probing the mechanical response of thin film materials based on miniature tensile testing. A number of mechanisms that may compromise the performance and potentially limit the operational lifetime of MEMS devices which incorporate functional ferroelectric ceramics were also identified and investigated. Reliability of piezo MEMS components was studied at a wafer and at a device level through the development of appropriate techniques based on miniature tensile testing, time- resolved micro RAMAN spectroscopy and laser Doppler vibrometry. Micro tensile testing was further used for the extraction of the elastic properties of various thin film materials.

A miniature tensile stage was developed in common with DEBEN UK for the mechanical characterization of functional thin film materials like PZT and ZnO ceramics, which are commonly used in MEMS fabrication. The stage is offered with a piezo electric motor which can be fitted with interchangeable heads. These can be combined with different types of mounting jaws, enabling both conventional tensile testing and compression testing to be performed. Strains and displacements were measured in- situ using an optical, non destructive method based on CCD imaging. The elastic constants of polymer (LCP), LCP-Au bilayers and electroplated Ni were defined in good agreement with the literature. However yield of successfully released ceramic samples was rather poor so a collaboration with IMTEK at Germany was established. Using their facilities batch processing of a large number of wafers was possible. The Young's modulus of pzt

was found equal to $57 \pm 8\ GPa$ and the fracture strength of the composite samples (oxide/Pt/pzt) $323 \pm 22\ MPa$ with a Weibull modulus 3.6 ± 0.7.

Stresses in the thin films typically used in piezo MEMS fabrication were studied. The wafer curvature technique was employed and a high tensile stress ($\approx 900 - 1100\ MPa$) in the Pt layer, typically used as a template layer for the proper $\mathrm{Pb(Zr}_x, \mathrm{Ti}_{1-x})\mathrm{O}_3$ (PZT) pervoskite nucleation, was confirmed. A technique for the elimination of this stress is presented involving the use of adhesive wafer bonding and bulk micromachining procedures to remove the Pt layer following the PZT deposition. Devices based on this scheme were fabricated where the Si structural layer was replaced by Ni and Al.

It was found that the application and curing of the adhesive could cause the ferroelectric response of the PZT film to deteriorate depending on a number of parameters, namely the composition of the PZT layer, the top electrode used and the type of the underlying barrier layer (SiN_x or SiO_2). The effect of different top electrode configurations was investigated and Pt was found to work better with both 30/70 and 52/48 sols spun on oxide coated Si wafes. A post anneal of the ferroelectric stack at an elevated temperature would recover the ferroelectric response in most cases.

A dynamic stress analysis method for reliability studies of MEMS, based on time-resolved micro-Raman spectroscopy, was developed. This new technique is illustrated for a PZT actuated silicon cantilever resonator. Time resolved stress maps were measured when the cantilever was driven at the first ($6.094\ kHz$) and second ($37.89\ kHz$) resonant frequencies, which were defined using Laser Doppler Vibrometry. Stress amplitudes and the phase delay relative to the driving voltage were investigated. The maximum stress in the first resonant mode was observed in the beam anchor as expected and was found equal to $\approx 120\ MPa$ while in the second resonant mode the maximum stress of $\approx 180\ MPa$ occured in the middle of the beam length.

Acknowledgements

I would like to express my gratitude to Dr P.B. Kirby for offering me the opportunity to pursue this graduate study at Cranfield University under his supervision. I would also like to thank Mr R.V. Wright for his input, support and insightful discussions on almost every scientific aspect related to this research.

The main funding source for the completion of this project has been from Qinetiq through the MEADE project. Their contribution and support is therefore gratefully acknowledged. I would also like to epxress my sincere thanks to DEBEN UK for the collaboration in the development of the miniature tensile stage.

During the last year of my thesis a collaboration with Prof Oliver Paul's group at IMTEK in Freiburg was established and a number of samples were measured using their lab facilities in July 2009. I would thus like to take the opportunity and thank IMTEK once again and in particular Dr Joao Gaspar for his contribution. He has been very generous in sharing with me his expertise on miniature tensile testing and never hesitated to offer his support on the completion of these measurements no matter how busy he was.

I had also the chance to work closely with the group of Prof Martin Kumball in Bristol University and especially with Dr James W. Pomeroy in testing the micro RAMAN time resolved dynamic stress measurement method they have developed, on piezo actuated MEMS components. It has been a great pleasure to work with them.

I would also like to express my thanks to Farizah Saharil from KTH in Sweden for all the samples she prepared for me for the development of the stress

elimination scheme.

I do feel grateful to many people from the Nanotechnology group in Cranfield University, especially my dear friends and co- patriots Carlos Frangiadakis, who has also been a great flat- mate and George Skoufias. Of course a lot of people from the group have been very supportive and helpful like Dr Meilign Zhu, Dr Glenn Leighton, Dr Debabrata Bhattacharyya, Matthew Taunt, Andrew Stallard and Dr Chris Shaw. I thank you all and wish you family happiness and success in your careers.

Had there not been for Prof Eugenia Mytilinaiou and her references and my close friends Michalis Papapetrou and Giorgos Kolias who encouraged me in the first place to leave Greece, I would probably have never taken this step myself. I would like to express my gratitude to them once again.

Finally I would like to thank my parents for their support and encouragement, my brother especially for his guidance in MATLAB programming and of course my beloved and caring wife Ioanna.

Contents

Abstract VII

Acknowledgements IX

List of Figures XV

List of Tables XXVII

Terms and Symbols XXXI

1 Literature Review 1

1.1 Introduction 1

1.2 Mechanical Characterization of Thin Film Materials 5

1.3 Tensile Testing of Thin Film Materials 7

1.4 Thin Film Stresses 11

1.4.1 Wafer Curvature Technique 15

1.4.2 RAMAN Spectroscopy 16

1.5 Ferroelectricity- Piezoelectricity- PZT 18

1.6 Fatigue 22

1.7 Research Objectives 27

2 Experimental Setup 29

2.1 Tensile Test 29

2.1.1 Tensile Stage Design 29

2.1.2 Strain- Displacement measurement 32
2.1.3 Fabrication Process 40
2.1.4 Mask Design- Sample Layout 44
2.2 Stress Elimination Scheme by the Removal of Pt Template Layer 58
2.2.1 Fabrication of stress free microcantilever 60
2.3 Piezo MEMS Reliability Testing 62
2.3.1 Mask Design 62
2.3.2 Fabrication Process 63
2.3.3 Composite Piezoelectric Beam Model 67
2.3.4 Device Modelling 70
2.3.5 Laser Doppler Vibrometer 76
2.3.6 Electric- Ferroelectric Characterization 78
2.3.7 Stress Measurements 82

3 Tensile Testing **85**
3.1 First Mask Set 85
3.1.1 PZT Testing 85
3.1.2 Electro Plated Ni Testing 89
3.1.3 LCP- LCP Au Composite Testing 92
3.2 Second Mask Set 95
3.2.1 PZT Testing 95
3.2.2 Si Frame Stiffness 102
3.3 IMTEK Samples 106
3.3.1 Data Processing 111
3.4 Equivalent Spring Constant of Composite Samples 118
3.5 Elastic Properties and Fracture Strength of PZT Ceramic 125

4 Residual Stress Elimination Scheme **133**
4.1 Sample Preparation 133

4.2 Layer Stress Measurements 136
4.3 Stress Elimination Scheme by the Removal of Pt Template Layer 141
4.4 Device Fabrication 144
4.4.1 Residual Stress Induced Deflection of a Cantilever Beam . 144
4.4.2 Fabrication Process 146
4.5 Ferroelectric- Electric characterization 147
4.6 Polarization Collapse 150

5 Dynamic Measurements 163
5.1 Device fabrication 163
5.1.1 Microcantilevers 163
5.1.2 PZT bimorphs 165
5.2 Electric- Ferroelectric Characterization 168
5.3 Laser Doppler Vibrometry 170
5.4 Accelerated Fatigue Testing 174
5.5 RAMAN Results 176
5.6 Device Modelling 178

6 Discussion- Conclusions- Recommendations for Future Work 185
6.1 Discussion 185
6.2 Conclusions 188
6.3 Recommendations for Future Work 192

References 195

Appendices 217
A-1 MATLAB model of the static tip deflection of a multimorph beam due to thin film residual stress. Linear and nonlinear case 219
A-2 Modification of MATLAB model for verification of ANSYS 2-D analysis 221

A-3 ANSYS Finite Element Model of a multimorph piezoelectricaly actuated beam 221
A-4 2-D analysis of a piezo actuated multi layered Si beam. 227
B-1 ANSYS finite element model of a small Si frame for tensile testing of ceramics. 231
B-2 ANSYS finite element model of a single layer dog bone shaped structure with anchor part 235
B-3 ANSYS finite element model of a three layer dog bone shaped structure with anchor part 239
C-1 PZT properties from Ferroperm Catalogue 243

List of Figures

1.1 Engineering Stress- Strain curve. The inclination of the linear part is the Young's modulus, σ_Y is the yield stress, UTS the ultimate tensile stress and σ_F the fracture strength. 8

1.2 Average stress×mean thickness versus mean thickness during film growth on oxidized Si wafers. The features of initial compressive stress, then tensile stress, and then again compressive stress with a plateau are typical for a wide range of materials. After Freund and Suresh [34]. 12

1.3 Average stress versus mean thickness after film growth on oxidized Si wafers. Type I materials withstand very high intrinsic stresses which, depending on the deposition conditions, can be as high as 1 GPa tensile or compressive. As the substrate temperature rises, stress in Type I materials follows the Type II curve. After Thompson and Carel [134]. 13

1.4 Perovskite structure of $PbTiO_3$ crystal in (a) the paraelectric cubic and (b) the ferroelectric tetragonal phase. 20

1.5 Polarization P as a function of the applied electric field E for a typical ferroelectric ceramic. The polarization at zero field P_R is called the remanent polarization and the field E_C necessary to zero the polarization is the coercive field. 21

1.6 Tension- tesion cycle stress for tensile mode fatigue testing. 23

1.7 Stress S vs number of cycles N to failure (S-N) curves for different types of materials. Curves (a) and (b) are commonly encountered when ductile materials are tested. Ceramics do not have a significant cycling fatigue effect (curve c). 24

2.1 Maximum applied normal stress as a function of the cross sectional area of the tested sample for different load cells 31

2.2 Prototype tensile stage kit, equipped with horizontal gripping jaws for conventional tensile testing. 32

2.3 Prototype tensile stage kit, equipped with vertical gripping jaws and point tip for bending and crack initiation experiments. In the inset the pushing tip is shown in contact with a metal sample. . . 33

2.4 Equivalent spring constant of the load cell, the tested sample and the piezo element. The force from the extension/ contraction of the piezo is applied on the load cell and the sample. 34

2.5 The tensile stage kit mounted in the SEM chamber using the specially designed fixture. 39

2.6 Fabrication process. First metallization step (b), deposition of the ceramic (c) and second metallization step (d). 40

2.7 First photolithography. Device patterning (a), etching of Cr/Au (b) and PZT layers (c). Etching of bottom electrode and oxide films from the front (d). 42

2.8 Front to back alignment (a) and DRIE Si etch (b). Final release of the structures by RIE etching of the oxide, Ti/Pt layers (c). . . . 43

2.9 Schematics of a dog bone shaped sample geometry attached on a rectangular Si frame. Two pairs of mounting holes are defined on both the tested film and the supporting frame. The Si supporting beams are cut after securing the frame on the tensile stage. 45

2.10 Computer Aided Design of the first mask set with the large dog bone shaped structures. There are three silicon frames with three parallel dog bone samples each. 46
2.11 Photograph of sample fabricated using the first mask set. The Si supporting beams are cut after mounting the sample on the tensile stage. 47
2.12 Schematics of a test structure. There are four dog bone shaped samples bridging the gap between the fixed and the moving part of the Si frame. The two parts of the frame are connected through parralel Si suspension beams, the fixed part is mounted on the load cell using the mounting holes and a compression load is applied on the moving part using the special pushing tip. 49
2.13 Schematic of the second mask design. There are 38 small dog bone samples in total which are attached on 7 different stages. Five of the stages come with 4 samples attached, there is one stage has 6 samples and one stage comes with 6 samples and 6 counter samples. In the inset the moving platform with the 4 samples and the 6 supporting beams is shown. 50
2.14 Silicon frame with 6 samples and 6 counter samples for the evaluation of the residual stress. This platform requires 8 supporting beams instead of the 6 used in the simpler stages with the 4 samples. 51
2.15 Calculated sample stiffness in the x,y and z direction relative to the stiffness of a $< 110 >$ oriented Si beam is plotted in α, assuming a beam thickness equal to 525 μm and variable lengths, widths. Sum of ratios of sample stiffness over beam stiffness in the x, y and z direction is plotted in β as a function of the beam width and length. 52
2.16 Deformation of a 425 μm thick small Si frame under the action of gravity. 53

2.17 Deformation of a 525 μm thick large Si frame under the action of gravity. 54

2.18 Tip displacement of a 525 μm and a 425 μm thick Si suspension beam as a function of the applied force. In both cases the response of the beams is well within the linear limits. 55

2.19 Surface traction exerted from the sample pad on the Si frame. . . 56

2.20 Schematics of IMTEK test structure courtesy of Dr Joao Gaspar. 57

2.21 Stress elimination scheme based on adhesive wafer bonding. . . . 59

2.22 Design rules for fabrication of cantilever type device based on the stress elimination scheme. In (b) the new structural layer (Ni, SiN_x) is deposited on top of the back etched ferroelectric stack (a). The films are etched using the appropriate masking material (c) and the devices are finally released by etching the adhesive layer in high power isotropic O plasma (d) 61

2.23 PZT stack deposition on SOI wafer (a) and (b). Top electrode deposition (c) and PZT, bottom electrode patterning and etching (d). Device layer etch (e) and final release (f). 65

2.24 Fabrication process of the PZT bimoprhs. A second PZT stack is deposited by means of sol gel deposition on top of the initial stack (b). AZ-5214E negative resist is combined with the mask sets and electroplated Ni is used as the masking material for the dry etching (c). After the DRIE release (d) the SiO_2 is RIE etched. The bottom Pt electrode can be etched as well. 66

2.25 Tip deflection of a 1400 μm long piezo actuated cantilever Si beam as a function of the applied field calculated by different models. Thickness of the Si structural layer is $10\mu m$ 72

2.26 Static tip deflection of a multilayered piezo activated cantilever derived from ANSYS 2D non linear finite element analysis. The applied voltage is 5 $Volts$. 73
2.27 Static tip deflection of a multilayered piezo activated cantilever derived from . The applied voltage is 5 $Volts$. 74
2.28 First modal shape of a BBS1-4 type device respectively calculated using ANSYS 3D linear finite element analysis. The applied voltage is 2 $Volts$. 76
2.29 First modal shape of a BBS5-8 type device respectively calculated using ANSYS 3D linear finite element analysis. The applied voltage is 2 $Volts$. 77
2.30 Maximum deflection profile of a BBS1-4 bridge type bimoprh at the first resonant frequency. In red the stress intensity profile in the lower PZT structural layer. Note the different y-axis. 78
2.31 PSV Polytec Laser Doppler Vibrometer set up. 79
2.32 Weyne Kerr precision component analyser model 6425 with probe station and optical microscope. 80
2.33 Radiant RT66A set up for ferroelectric characterization. 81
2.34 Veeco DEKTAT surface profilometer. 82
2.35 The Al made jig used for keeping the wafers leveled during curvature measurements. The pin hole and the groove used for referencing are labelled. The ball bearings where the 100 mm wafers are placed are also illustrated 83
2.36 Schematic of the microcantilever and the objective lens set up used for the dynamic stress measurements. 84

3.1 SEM micrograph of a released composite Pt/PZT sample fabricated using the first mask set in the SEM chamber. 88

3.2 SEM micrograph of the tested sample. In the inset the cracked beam is shown under higher magnification. 89
3.3 SEM micrograph of a dog bone Si structure. Silicon was used after the initial unsuccessful experiments with the ceramics in order to test the method with thicker samples. 90
3.4 SEM micrograph of a Ni plated sample. Burnt resist residue still present. 91
3.5 Load vs displacement data (α) and Stress vs strain data (β) for the electro plated Ni samples. The strain data in (β) was extracted using digital image correlation techniques. From the inclination of the linear fitted line the young's modulus is evaluated. 92
3.6 SEM micrograph of the top surface of the LCP dog bone shaped structure (α) and the LCP-Au composite (β) samples. 93
3.7 Load vs displacement (top) and Stress vs DIC extracted strain data (bottom) for the LCP samples. From the inclination of the linear fitted line the young's modulus is evaluated. 94
3.8 Load vs displacement (top) and Stress vs DIC extracted strain data (bottom) for the Au covered LCP samples. From the inclination of the linear fitted line the young's modulus is evaluated. 95
3.9 Released small dog bone shaped PZT structures on silicon frame. There is still a thin layer of hardened resist covering the devices. . 96
3.10 Optical micrograph of one of the PZT dog bone shaped samples that was successfully released using high O_2 DRIE plasma etching. In the inset a micrograph at smaller magnification is illustrated. . 97
3.11 Experimental Load vs Displacement curve for the two tested PZT samples. The initial non linear part of the curve is due to the time needed for the pushing tip to come into firm contact with the moving frame. At sample fracture an abrupt fall is observed. . . . 98

3.12 Detail of the load vs displacement curve in the region of the first sample fracture. Graphical evaluation of the sample Young's modulus from the change in the curve inclination. 99

3.13 Graphical calculation of the fracture strength of the first sample from the load vs displacement curve. 100

3.14 Detail of the load vs displacement curve in the region of the second sample fracture. Graphical evaluation of the Young's modulus of PZT from the change in the curve inclination. 101

3.15 Graphical calculation of the fracture strength of the second sample from the load vs displacement curve. 102

3.16 SEM micrograph of the fractured samples of PZT after testing. Both samples cracked at points close to the pad attached on the stationary frame. Part of the anchors is released and this results in non uniform loading of the suspended part. 103

3.17 SEM micrograph of the cracked region in one of the tested samples. In the inset a cross section of the cracked area under higher magnification is presented. The crack appears transgranular. . . . 104

3.18 Marker displacement as a function of marker position. Green dots show the marker displacement in pixels in the y axis, parallel to the direction of the applied load. 105

3.19 Force vs displacement measured on the back left suspension beam of the moving Si frame. The red line corresponds to the linear fit of the experimental data. 106

3.20 Force vs displacement measured on the back right suspension beam of the moving Si frame. The red line corresponds to the linear fit of the experimental data. 107

3.21 SEM micrograph of one of the Si suspension beams. The beam thickness is not constant thoughout the beam length as a result of the DRIE etch process. The edges also appear rounded. 108
3.22 SEM micrograph of a dog bone shaped structure that has been wet etched. In the inset the pronounced undercut of the side walls is illustrated. 110
3.23 SEM micrograph of a dog bone shaped structure that has been dry etched using Ni hard masking. In the inset the almost perfectly vertical side walls are shown. 111
3.24 Optical micrograph of a released dog bone shaped structure fabricated using mask set from IMTEK. 112
3.25 Force vs displacement curve for a PZT 30/70 sample measured at IMTEK. 113
3.26 SEM micrograph of a released dog bone shaped structure fabricated using IMTEK mask set. The released part of the anchor pad due to Si overetching is visible. 114
3.27 Calibrated force values vs experimental time. Load cell drift is also estimated by the inclination of the red line which corresponds to the linearly fitted horizontal parts of the load cell curve. 115
3.28 Calibrated force values vs displacement during sample loading (blue line) and unloading (red line). 116
3.29 Calibrated force values vs displacement during sample loading (blue line) and unloading (red line) magnified for the graphical evaluation of the sample Young's modulus and fracture strength. 118
3.30 Graphical evaluation of the sample Young's modulus and fracture strength. Red lines correspond to the linear fit of the experimental values. 119

3.31 SEM micrograph of the cross section of a tested sample. In the inset the PZT layer over the Pt/ oxide underlayer is shown under higher magnification. 120

3.32 Layer structure of the tested devices and the simple mechanical equivelant of the three parallel connected sprigs. 121

3.33 ANSYS model of the composite dog bone structure in the case of the thinner oxide and ceramic films used. On the first column the displacement in the x, y and z direction under an applied force of 0.02 N is depicted. Next to each displacement the mean stress in the corresponding direction is presented. 123

3.34 γ constant as a function of the assumed PZT Young's modulus for different cases of composite structures and different lengths of the suspended anchor part. 124

3.35 Histogram of PZT Young's modulus data obtained from testing IMTEK and Cranfield samples. A normal distribution function.fits the experimental data. 126

3.36 Cumulative fracture probability of a composite $\mathrm{Si\,O_2/Pt}/PZT$ structure as a function of the measured tensile strength for two different types of samples. 127

3.37 Fracture probability of a composite $\mathrm{Si\,O_2/Pt}/PZT$ structure as a function of the measured tensile strength for two different types of samples. 128

3.38 Deflection profiles of different membranes as a function of the applied pressure. Blue lines correspond to the full ferroelectric stack while the red and the green ones were obtained from the reference wafers. 129

4.1 Wafer deflection measured using a DEKTAK surface profiler after layer by layer film deposition. The data is plotted as a function of the scanned length. 134

4.2 Exposed back of α the Pt and β the PZT film after completion of the back etching process. 141

4.3 Cross sectional view of the back etched ferroelectric stack (α). Columnar grain structure of the ceramic (β). 143

4.4 Sem micrograph of the area of the ceramic where the EDX analysis was performed. The points of interest are shown. In (β) the results of the analysis from point 1 are plotted. 144

4.5 Linear and non linear model of the tip deflection due to residual stress to be expected for a typical Si beam with a Autop electrode and for a beam fabricated based on the stress elimination method where the Pt layer has been replaced by a Au film and a low stress SiN_x film is introduced to serve as the structural layer. 145

4.6 SEM micrographs of the released beams fabricated based on the stress elimination scheme. Sputter deposited Al is used as the structural layer. 146

4.7 Polarization vs field (P-E) hysteresis loops of a ferroelectric stack which has been wafer transfered using (α) MRI-9000 and (β) BCB as the bonding layer. The wafer on which the stack was initially deposited on has been etched from the back. Loops before and after poling of the stack are illustrated. 148

4.8 Dielectric constant (α) and dielectric loss (β) of a PZT 30/70 film with a sputter deposited Cr/Au top electrode, after stress elimination. 149

4.9 Polarization vs field (P-E) hysteresis loops (α) and dielectric permittivity- loss as a function of frequency (β) obtained before and after heat treatment of a PZT 30/70 film deposited on a standard wafer when Cr/Au is used as the top electrode. Annealing time is 1 hr at 350 ^oC. 150

4.10 The sputter deposited Cr/Au dots serving as top electrodes of the ferroelectric stack (α) show apparent signs of damage after heat treatment (β). 153

4.11 Polarization vs field (P-E) hysteresis loops (left column) and dielectric permittivity ϵ and loss $\tan\delta$ (right column) of a ferroelectric capacitor formed by a PZT 30/70 film with a sputter deposited Ti/Pt (top) and Pt (bottom) top electrode, before and after heat treatment. 154

4.12 Polarization vs field (P-E) hysterisis loops of a PZT 52/48 film with a (111) orientation. The film is deposited on a standard wafer and the Cr/Au top electrodes are deposited prior to the heat treatment (red) and after the heat treatment (blue line). Clearly damage occured in the electrode area. 155

4.13 Polarization vs field (P-E) hysteresis loops before and after heat treatment of a (100) oriented PZT 52/48 film deposited on a standard wafer when Pt is used as the top electrode. 156

4.14 Polarization vs field hysterisis loops of PZT 52/48 films deposited on a standard wafer with a (111) orientaion using sputter deposited Pt as the top electrode. All four samples were annealed at 350^oC for 1 hr. The top right and both the bottom loops were obtained from samples that have been heat treated before for 1 min at temperatures between 400 ^0C and 500 ^oC. 157

4.15 Hysteresis loop of a (111) oriented PZT 52/48 film which has undergone the stress elimination process with sputter deposited Pt serving as the top electrode (red curve). The hysteresis loop of the same film before processing is also plotted for comparison (blue curve). In (β) the dielectric permittivity- loss of the film before and after processing are plotted as a function of frequency. 159

5.1 Optical micrographs of (α) the BCB wire- bonded Si cantilevers that were used for RAMAN spectroscopy and (β) the same cantilevers under higher magnification. The wire bonded pads that provide access to the top and bottom electrode are also illustrated. 165

5.2 SEM micrograph of a PZT bimorph (α) and the released beam under higher magnification (β). The left anchor has been over etched. 167

5.3 Polarization versus field (P-E) ferroelectric hysteresis loop of the device PZT film before and after poling. 169

5.4 Dielectric permittivity- loss as a function of frequency before and after PZT poling. Note double y- axis. 170

5.5 Polarization versus field ferroelectric hysteresis loop of the bimorph top and bottom PZT film. 171

5.6 Dielectric permittivity and dielectric loss of the bimorph top and bottom PZT film. 172

5.7 First resonant mode of the cantilever beam used for RAMAN stress measurements. The resonant frequency is 6.094 KHz 174

5.8 Second resonant mode of the cantilever beam used for RAMAN stress measurements. The resonant frequency is 37.890 KHz . . . 175

5.9 SEM micrograph of the broken anchor of a PZT bimorph (α). Detail of the crack initiation area (β). 177

5.10 SEM micrograph of the bottom of the PZT bimorph after failure (α). The cracked area under higher magnification (β). 178
5.11 SEM micrograph of the cracked area (α). Detail of the crack (β). 179
5.12 Dynamic stress map of the micro cantilever vibrating at the 1st resonant frequency 180
5.13 Dynamic stress of the micro cantilever vibrating at the 2nd resonant frequency 181
5.14 Dynamic stress at the base of the micro cantilever vibrating at the 1st (α) and 2nd (β) resonant frequency as a function of time. . . . 182
5.15 Calculated versus measured stress profiles for the 1st and 2nd resonant frequency using PZ24 parameters (α) and PZ34 parameters (β). 184

List of Tables

2.1 Miniature tensile stage specifications 30

2.2 Sample dimensions. 44

2.3 Geometry of F1-3 cantilevers and BBS1-8 bridge type PZT bimorphs. 63

2.4 Material properties of the non piezo electric layers used in device modeling. For the piezo electric film the properties of PZ23 ceramic from Ferroperm catalogue were used. 71

2.5 The first four resonant frequencies of the piezoactuated cantilever devices and of the bridge type bimorphs used for dynamic measurements, as they were calculated using ANSYS FEA for the frequency range $1 \dots 200$ kHz. The properties of the PZT film were taken from FERROPERM catalogue (material PZ24). 75

3.1 Samples fabricated for on wafer testing at IMTEK. 109

3.2 Specifications of the tested samples. The dimensions (L_{sam}, w_{sam}) of the tested structure as well as the mean length and the mean width (L_{anc}, w_{anc}) of the two suspended anchor parts were optically measured. In the last three columns the composite Young's modulus, the fracture strentgh and the residual stress which were graphically determined are presented. 117

3.3 Young's modulus/ plane strain modulus E/ E_{ps}, fracture strength/ strain $\tilde{\sigma_F}$ ϵ_F, weibull modulus m and residual stress/ strain σ_R/ ϵ_R evaluated using micro tensile and bulge testing. 132

4.1 Layer stress calculated after the deposition of each film on a Si wafer when scans are performed perpendicular to the primary flat (s1) and parallel to that (s2). In the last column the relative difference as a percentage of s1 is calculated. 135

4.2 Layer stress calculated after etching of the films comrising the ferroelectric stacks using dry etching (S1) and wet etching (S2) techniques. The layer stress during stack fabrication are also presented in columns 1 (for sample S1) and 3 (sample S2). The PZT ceramic had a composition of Zr/Ti = 30/70 137

4.3 Layer stress calculated after etching the films comrising a ferroelectric stack, when standard oxidized Si wafers are used as substrates (column 2 for PZT 52/48 and 3 for PZT 30/70) and when low stress PECVD SiN_x coated wafers are used for PZT 30/70 deposition (column 4). 139

4.4 Layer stress calculated after deposition of each film comrising a ferroelectric stack (column 2), after etching of each film following the completion of the stack (column 3) and finally after etching of the films following the release of the stack from the Si subtrate using wafer bonding (column 4). 142

4.5 Calculated mean dielectric permittivity of the ferroelectric capacitors with a Cr/Au top electrode before and after heat treatment for 1 hr at 350 ^oC as a function of frequency. The relative change does not depend on the frequency. 151

5.1 Resonant frequencies of the piezoactuated cantilevers F1-3 used for dynamic stress evaluation measured using LDV. 173

5.2 Resonant frequencies and tip deflections measured by LDV. Quality factors were also evaluated from the FWHM of the spectral response. 173

5.3 Resonant frequencies of the PZT bimorph devices measured using LDV. 176
5.4 Resonant frequencies of type F1 piezoactuated cantilever used for dynamic stress measurements, calculated using ANSYS FEA for different types of PZT film. The properties of the different types of film were taken from FERROPERM catalogue. 183

Glossary

Symbol	Description
A	Cross Sectional Area, 30
$C\left(u,v\right)$	Correlation Factor, 37
E	Young's Modulus, 8
$E/\left(1-\nu^2\right)$	Plane Strain Modulus, 6
E_C	Coercive Field, 20
$K_{I,II,II}$	Stress Intensity Factor mode I, II, III, 25
L	Length, 32
P_R	Remanent Polarization, 20
P_{SAT}	Saturation Polarization, 20
R	Radius of Curvature, 15
S_e	Endurance Limit, 23
T_0	Ambient Temperature, 15
T_C	Curie Temperature, 18
T_{cryst}	Crystallization Temperature, 15
T_{ij}	Stress Tensor, 36
α_f	Thermal Expansion Coefficient, 15
ϵ_0	Residual Strain, 6
ϵ_d	Dielectric Permitivity, 73
κ	Curvature, 63
ν	Poisson's Ratio, 8
ρ	density, 7
σ	Tensile Stress, 30

σ_F	Fracture Strength, 8
σ_Y	Yield Stress, 8
σ_f	Residual Stress, 15
σ_{th}	Thermal Stress, 15
$\tan \delta$	Dielectric Loss, 73
$\vec{F}$	Force Vector, 34
$\vec{P}_S$	Spontaneous Polarization Vector, 18
d_{ij}^E	Piezoelectric Matrix under Constant Field, 34
h	Height, 30
i, j, k	Indices 1,2,3, 36
k	Equivelant Spring Constant, 32
s_{ij}^E	Stiffness Matrix Constant Field, 34
t_f	Film Thickness, 15
t_s	Substrate Thickness, 15
u, v, w	Displacement in x, y, z Direction, 36
$u_{i,j}$	Partial Derivative, 36
u_{ij}	Strain Tensor, 36
w	Width, 30
x, y, z	Cartesian Coordinates, 36
AFM	Atomic Force Microscopy, 10
BCB	Benzocyclobutene-based Polymers, 144
CCD	Charge Coupled Device, 38
CVD	Chemical Vapor Deposition, 11

DC	Direct Current, 29
DIC	Digital Image Correlation, 10
DRIE	Deep Reactive Ion Etching, 42
EDX	Energy Dispersive X-ray, 138
f.c.c.	face centered cubic, 14
IC	Integrated Circuit, 2
LCP	Liquid Crystal Polymer, 81
LDV	Laser Doppler Vibrometry, 70
LEFM	Linear Elastic Fracture Mechanics, 24
MEMS	Micro Electro Mechanical systems, 1
poly-Si	Polycrystalline Silicon, 4
PVD	Physical Vapor Deposition, 11
PZT	Lead Zirconate Titanate, 4
rf	Radio Frequency, 1
RIE	Reactive Ion Etching, 41
RTA	Rapid Thermal Anneal, 132
SCS	Single Crystal Silicon, 4
SEM	Scanning Electron MIcroscopy, 29

TEM	Transmission Electron Microscopy, 10
XRD	X-ray diffraction, 10

Chapter 1

Literature Review

1.1 Introduction

Micro Electro Mechanical Systems MEMS are miniature systems capable of performing real time, complex interactions with their environment. Their operation is based on converting energy from one form to the other by making use of different physical and chemical phenomena. They usually combine in an integrated system mechanical, electrical, optical and even fluidic interconnected components. They were first envisaged by R.P. Feynman in one of his famous lectures on physics [31] during the 60s.

Research and development interest on MEMS technology has rapidly increased in the past twenty years. Today there is a broad range of scientific and industrial MEMS applications, encompassing sensors and actuators [91], micro mirrors and micro pumps [15], rf components [132] and biological systems. The range of possible applications is still expanding.

Many examples of these MEMS devices have been commercialized such as accelerometers [151, 141], which are nowadays used in almost every car, micro pumps [73], pressure sensors in "smart" tyres, piezo actuated ink- jet heads used for print-

ing and the Digital Micro Mirror Devices (DMD) used for projection applications [29, 123, 116].

These applications demand accurate and reliable operation of devices, often under harsh environmental conditions [71]. A MEMS device may operate under excessive temperatures and moisture, often at resonant frequency during its entire lifetime, or in contrast may perform a critical operation just a few times during its service. MEMS devices in certain cases will probably be exposed to high radiation and/or impact shocks, as in the case of space applications and should still keep operating within specifications. It is clear that in order for MEMS technology to become commercially successful the factors that influence the reliable operation and may reduce lifetime of a device have to be understood and so the failure mechanisms in the micro scale need to be studied [140].

MEMS fabrication is mainly based on methods like surface and bulk micro machining which were initially developed and used by the integrated circuits (IC's) industry. It is this characteristic that makes on chip integration and batch fabrication of MEMS components easy [80]. Of course reliability of ICs has been extensively studied and the physical mechanisms associated with failure of ICs are well understood. Since MEMS fabrication is based on methods initially developed by the IC's industry, it was recognized early that residual stresses in thin films, deposited during surface micro machining would play an important role in MEMS devices as well. Uncontrolled residual stresses that normally arise during processing of thin films, can cause buckling and even de lamination of the films from the substrate [33, 34]. Functionality of MEMS devices fabricated using surface micro machining could be seriously compromised by excessive stresses in the films used in their fabrication as they can cause out of plane bending of the freestanding parts, as well as stress stiffening and shift of the resonant frequencies of the structure [113].

On the other hand the situation in MEMS can be quite different from the IC in that in many cases there are moving, impacting parts where operational strains arise during dynamic excitation. The impact that these dynamic stresses have on the operational lifetime of a MEMS component is obviously not accounted for by the accelerating testing of the electrical properties which is typically performed in the IC industry. In addition new functional materials like ceramics and shape memory alloys have been incorporated in MEMS devices and issues are arising about the potential influence that their chemical processing might have on Si toughness [114]. And the situation becomes even more complicated by the introduction of novel techniques like selective [24] and wafer transfer bonding [98] for producing more complex MEMS geometries.

In addition it was observed that the mechanical properties of the materials in the micro scale vary substantially, depending on a number of different parameters like size, deposition method and processing conditions [35]. A direct consequence of device miniaturization is that the ratio of the surface area over the volume of micro structures increases, resulting in the surface effects becoming more important and sometimes dominant at these scales. Thin film materials are typically deposited on much thicker substrates with a thickness which is much smaller than the in plane dimensions [16]. Most of these deposition methods result in films with a columnar grain structure which are transversely isotropic in the film plane, usually with large residual strains built into them and with a mean grain size considerably different than those encountered in bulk samples [134]. In certain cases the effect of the substrate clamping can be rather pronounced altering the film mechanical response.

Since these properties are closely associated with the performance and the durability of a MEMS device it is obvious that assuming their bulk values for modeling purposes may lead to erroneous results which deviate considerably from the

response of the fabricated device. Furthermore, accurate evaluation of the mechanical parameters may only be performed on samples prepared based on the fabrication process of interest.

Many researchers have therefore stressed the need to develop MEMS specific reliability testing methodologies in parallel with techniques for the mechanical characterization of thin films at a more fundamental level. Testing is currently performed at a specimen- wafer level (wafer curvature, tensile testing, bulge testing, axisymmetric plate bending, M test, nano indentation, beam bending etc) and at a device level where prototype structures are fabricated and tested usually under dynamic conditions [35]. The former methods are better suited for the extraction of the elastic and static fracture properties where the latter may be used for accelerating fatigue testing[90].

Single Crystal Silicon (SCS) and polycrystalline Silicon (poly-Si) are the main mechanical elements in most MEMS devices to date and so a lot of studies have been conducted on them.

Both elastic properties as well as fatigue mechanisms of single crystal Si (SCS) [6, 7, 32, 53, 121] and polycrystalline Si (poly-Si) [119, 120, 88, 89, 90] have been and are still being investigated as these are the most commonly used structural materials in MEMS fabrication and the slow crack growth mechanism in them is not yet quite well understood. In addition several attempts to measure the elastic properties of various thin film materials used in MEMS fabrication like Au and Ni have been made [47, 46] using different approaches.

Summarizing the current situation there is a need to measure accurately the mechanical properties of various thin film materials used in MEMS fabrication, like $Pb\left(Zr_xTi_{1-x}\right)O_3$ (PZT) ferroelectric ceramics, since knowledge of accurate values is a prerequisite for accurate modeling and successful low cost design of any

micro-structure. In addition, influence of PZT processing on Si toughness has to be investigated and the exact mechanism of slow crack growth in SCS structures under cycling loading needs to be clarified. Fatigue in SCS structures under cyclic tensile or torsional loading can be further studied using statistical models fitted with experimentally obtained data. Fatigue trials on different structural layers like Ni and SiN_x are also of great interest.

1.2 Mechanical Characterization of Thin Film Materials

Many different methods have been developed for probing the mechanical response of thin film materials like the beam bending test, the bulge test, the instrumented nano indentation test, the axisymmetric plate bending test, RAMAN spectroscopy, the M-test, the use of passive strain sensors, the wafer curvature technique, dynamic (resonant) tests and the tensile test [130].

Each method shows certain advantages concerning sample preparation, sample handling and the type of material properties that can be extracted from the experimental data. In particular beam bending may be used for the extraction of Young's modulus and the calculation of bending strength of a material using simple beam type structures which are easy to fabricate and measure. However one should be extremely careful with the interpretation of the results as the appearance of strain gradients due to the bending motion [95] or the movement of the loading point in the case of cantilever bending [76] may affect the data.

M-test is a variant of the beam bending test where an attractive electrostatic force is applied on the tested beam until it is no longer supported by the restoring force due to the beam stiffness [105]. The method can be used for the extraction of

the Young's modulus and the residual stress of a free standing beam however this technique imposes very stringent conditions on the tested structures which are rarely met [131].

In bulge test the static deflection of a membrane film under a varying differential pressure is measured. The deflection profile of a membrane under a pressure P is determined by the plane strain modulus $E/\left(1-\nu^2\right)$ and the prestrain ϵ_0 that may have risen in the film during deposition or due to thermal treatment. Apart from the plane strain modulus, the fracture strength and the residual stress in the films, the fracture energy of the film- substrate interface can be evaluated using the bulge test [133]. The film diaphragms used for testing are easy to fabricate by simply depositing the film of interest usually on one side of a Si substrate wafer [149]. The other side of the wafer is then patterned and the Si is etched using bulk micro machining techniques until the membranes are released. Due to its flexibility and robustness bulge testing is a very popular option [149, 37, 8, 101] for thin film mechanical characterization its main drawback being the difficulty in the extraction of the properties in case stress concentration points are formed at the membrane edge during Si etching.

The instrumented nanoindentation test is another traditional thin film mechanical characterization method which is easily realised using a mechanical probe (Berkovich or Vickers indenter) to penetrate a specimen surface. The penetration depth is monitored as a function of the applied load and the modulus as well as the strength of the tested material are extracted. However for large penetration depths in thin film testing the curvature of the indenter tip as well as the substrate stiffness need to be taken into account [133]. Furthermore the Poisson's ratio of the specimen needs to be assumed when the nanoindentation is used for the evaluation of the Young's modulus [133, 34, 84].

Axisymmetric plate bending test is mainly used for fracture strength characterizations. The samples are easy to fabricate and the test results are less prone to errors due to the probe geometry or the boundary conditions of the tested structure.

The wafer curvature test and the spectroscopic based techniques like RAMAN spectroscopy were initially used for measuring the residual stress in thin film materials however they can be used for the extraction of the Young's modulus as well [131]. Stress gradients in thin films can be determined by using either the spectroscopic and diffraction based methods or by integrating on the wafer passive strain sensors which can be used for residual stress measurements as well [131]. These methods will be further discussed in the context of the thin film stresses section.

Finally in dynamic tests the first resonant frequency of a beam is measured which in the case of a free standing cantilever type beam is a function of the density ρ and the Young's modulus of the material. For bridge type beams the first resonant frequency also depends on the residual stress built in the beam [113]. Frequency measurements should be carried out under vacuum conditions as air damping can cause the resonant frequency of the micro fabricated beam to shift.

1.3 Tensile Testing of Thin Film Materials

Tensile testing of bulk materials is a well established characterization method that has been in use for quite a long time. Early on it was understood that simple geometries allow easy and accurate extraction of the required parameters. Beam type samples with a rectangular cross section can be used as the tensile load should be uniformly applied with no points of excessive loading due to stress

concentration, as this would cause the sample to fail pre maturely invalidating the result of the test. Analysis of dog bone shaped structures shows that they are ideally suited for this type of testing.

In tensile testing a uniaxial load is continuously applied on a carefully prepared sample and the corresponding displacement is recorded. The load vs displacement curve can be converted to a stress vs strain curve, if the sample's geometry and the test stage's stiffness are taken into account, giving the engineering stress-strain curve. From the engineering stress strain curve different elastic properties of the tested material can be derived in a rather straightforward manner.

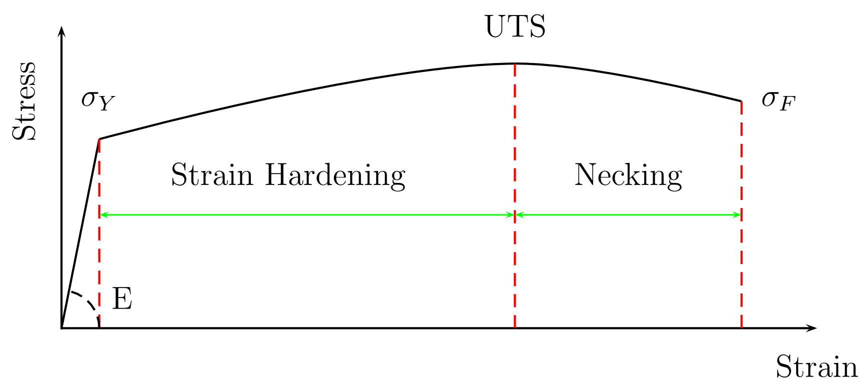

Figure 1.1: Engineering Stress- Strain curve. The inclination of the linear part is the Young's modulus, σ_Y is the yield stress, UTS the ultimate tensile stress and σ_F the fracture strength.

In figure 1.1 a typical engineering stress-strain curve of a ductile material is presented. There is a great variety in the shape of the obtained curves since for example brittle materials do not usually experience yielding and they fracture once the elastic limit is passed. In summary a tensile test can provide information on the values of the mechanical properties of a material as well as on the way

a structure deforms and fractures. The material properties that can be directly measured are Young's modulus $E = d\sigma/d\epsilon$ from the inclination of the linear part of the curve, Poisson's ratio $\nu = -\epsilon_{trans}/\epsilon_{logn}$ as the ratio of the transverse over the longitudinal strain, yield stress σ_Y and fracture strength σ_F . Application of tensile loads on pre cracked samples can also be used to determine the fracture toughness of the tested material for the specific crack geometry.

Based on the knowledge gained from testing bulk materials, miniature tensile testing is often also performed on dog bone shaped samples. Handling samples in thin film form though, demands extra care and initial experiments revealed problems associated with keeping the sample axis properly aligned to the applied load.

Two different approaches have been taken to achieve good alignment: on chip testing, where a micro actuator is fabricated simultaneously with the tested geometry, has been successfully implemented [115] but is also known to suffer from inherent limitations on the maximum load that can be applied and the use of an external actuator [81, 82, 46] although in that case sample handling and gripping can be rather difficult so special techniques like electrostatic [139], mechanical [44] or adhesive gripping [19] have been developed.

An alternative concept is to deposit the tested film on top of a Si substrate and etch a rectangular window from the back side of the wafer thus fabricating specially designed silicon frames where the samples are attached on. This in principle facilitates handling, mounting and gripping the sample on the external actuator by either mechanical means or adhesive gluing [81, 94, 69, 46]. After mounting on the tester, two out of the four mutually parallel Si beams which define the supporting frame are cut so the sample is released for testing.

More complex designs where a compressive [59] or torsional [6] load is applied on a

specially prepared moving frame where one end of the tested sample is attached, have also been presented. The motion of this frame results in the application of tension on the sample. These designs minimize the risk of accidental sample fracture that may occur when the supporting frame sides are cut. An additional advantage in this case is that proper alignment of the sample axis with the applied load is ensured during sample fabrication. A design based on this concept was recently used in order to perform the tensile testing at a wafer level [39] for the first time by eliminating the need to release the supporting frame from the substrate.

An additional challenge is to measure with adequate accuracy the forces applied on the tested sample as well as the corresponding displacements. Accurate force measurements are a major issue in integrated on chip actuators which can prove rather difficult to calibrate [115]. Loading mechanisms employing external piezoelectric, translational [81, 59, 39] or magnetic actuators [51] on the other hand are most commonly used. Especially piezoelectric transducers are linear in response and combined with low capacity load cells offer high force resolution and excellent precision at relatively low cost.

Due to the small dimensions of the miniature tension samples conventional strain gauges cannot be employed. As a result many different direct strain measurement methods have been proposed and tested. These include Digital Image Correlation [51] techniques, Scanning Electron Microscopy (SEM) and Transmission Electron Microscopy (TEM) imaging [46], monitoring the relative movement of interference and diffraction patterns formed from the reflection of monochromatic light by special marks/indentations on the sample surface [121, 36, 112], non contact Atomic Force Microscopy (AFM) [19], X-Ray Diffraction [94], laser vibrometry [59] in-situ RAMAN spectroscopy [96], optical linear encoders [43] and capacitative sensing [118]

Micro tensile testing of thin film materials has been conducted on brittle [59],

ductile and polymer [51] materials sometimes under varying temperatures [53] and different properties like Young's modulus, Poisson's ratio, fracture strength, fracture toughness [139], fatigue [6, 111] and residual stress [59, 39] have been evaluated. SCS, poly-Si, SiO_2, SiN_x [19, 47, 46, 53, 121], various metal films like Au, Ni [128], Pt and permalloy [74, 86] have been tested. The effect of strain rate and fabrication temperature was also studied in some cases [59]. For SCS the elastic moduli measured are in good agreement with values obtained from alternative methods [6, 53, 54]. Measured strength values show a significant scatter and strong dependence on the sample geometry, so a probabilistic rather than a deterministic approach is required [54].

1.4 Thin Film Stresses

Typically MEMS devices are multi layered structures fabricated by surface micro machining of thin films deposited on, usually bulk micro machined, Si wafers which are the most commonly used substrates. Free standing membrane films have also been utilized in certain applications. These metal, ceramic or polymer thin films are deposited by different deposition methods which are based on either physical (PVD) or chemical (CVD) processes.

Most of these methods result in highly constrained polycrystalline structures with high levels of intrinsic stress built in them. These stresses originate from the formation of highly strained regions in the bulk of the film or in the film/ substrate or in the film/ free surface interface during the film deposition process [68]. Certain dynamic processes like recrystallization and inter diffusion also contribute in film straining [68]. The mechanical response, the unusual endurance in yielding and the residual stresses of these polycrystalline thin film materials are closely associated with their grain structure (mean grain size, morphology and texture) [134].

Stress evolution in thin films deposited on oxidized Si substrates, using physical vapor deposition methods (evaporation, sputtering) has been studied for different combinations of substrate- vapor temperatures. In most cases these films grow in the Volmer- Weber growth mode through the formation of islands which as they get larger start to interact with each other forming a continuous film [34].

There are two basic types of micro structure that can result from these processes. Depending on the materials involved and on the ratio of the substrate temperature over the melting temperature of the deposited film either a columnar or an equiaxed grain structure evolves [134, 34].

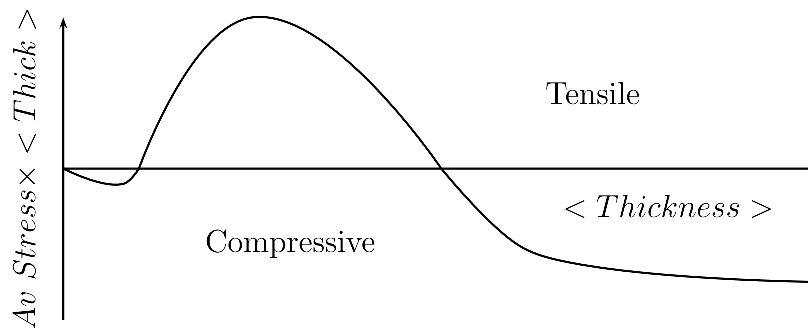

Figure 1.2: Average stress×mean thickness versus mean thickness during film growth on oxidized Si wafers. The features of initial compressive stress, then tensile stress, and then again compressive stress with a plateau are typical for a wide range of materials. After Freund and Suresh [34].

For a wide range of materials it was found that the average film growth stress shows a typical dependence on the mean thickness as depicted in figure 1.2, when deposition under ultra high vacuum conditions takes place.

The succession of compressive- tensile- compressive incremental stress states is due to different mechanisms becoming dominant at different thickness scales. Initially surface effects in the film island/ substrate interface are believed to control the observed compressive average growth stress. These surface mechanisms become less important as the film islands grow and start to interact with each other forming grain boundaries. The excess energy of the grain boundary formation results in straining of the associated film islands, thus causing the film to become tensile stressed. The last compressive stress state is characteristic of a class of high mobility materials (type II materials) with equiaxed grain micro structure but it is also encountered in low mobility (type I) materials deposited on adequately hot substrates [134]. This is mainly attributed to the presence of excess atoms in the formed grain boundaries under these conditions [34].

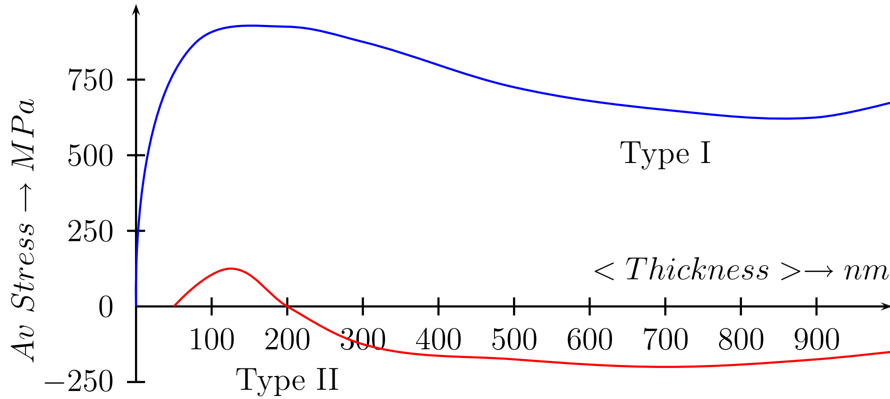

Figure 1.3: Average stress versus mean thickness after film growth on oxidized Si wafers. Type I materials withstand very high intrinsic stresses which, depending on the deposition conditions, can be as high as 1 GPa tensile or compressive. As the substrate temperature rises, stress in Type I materials follows the Type II curve. After Thompson and Carel [134].

Low mobility (type I) materials deposited at low temperatures have a columnar grain structure and can withstand very high intrinsic tensile or compressive strains, the stress nature being determined by the deposition conditions. In figure 1.3 the mean bulk stress as a function of the mean film thickness is depicted for the case of low and high mobility materials.

In sputter deposited type I materials produced under ultra high vacuum conditions, extremely high compressive stresses rise [134]. In type II materials deposited under these conditions compressive stresses also rise. Ultra high vacuum sputtering deposition is a physical process where the mean free path covered by the energetic atoms in the vapor phase is long. These atoms gain high kinetic energies prior to colliding with the free surface of the substrate. These collisions often cause damage on the substrate surface and this is believed to be the main cause of the compressive strains that rise in the films [34]. Another mechanism of secondary importance is the entrapment of Ar atoms in the film bulk during the film growth [34].

Minimization of the total surface, interface energy is the driving force for the formation of grains with a preferred orientation perpendicular to the film plane. Due to the abnormal grain growth these become the predominant grains in the film structure. However there are cases, like during post deposition annealing of the film, where the strain density minimization mechanism controls the grain growth through recrystallization processes and may lead to a different textured micro structure [134, 68]. Especially face centered cubic crystals (f.c.c.) like Au, Ag and Al, which fall in the category of high mobility type II materials, are deposited with a preferential (111) oriented texture directed perpendicular to the substrate plane.

Heat treatment of deposited films on thick substrates can cause grain boundary movement, recrystallization and abnormal grain growth driven by the minimiza-

tion of the strain energy. Post deposition cooling gives rise to thermal strains which are largely fixed by the mismatch between the thermal expansion coefficient of the film and that of the substrate.

$$\sigma_{th} = \frac{E_f}{(1 - \nu_f)} \int_{T_{cryst}}^{T_0} (\alpha_f - \alpha_s)\, dT \tag{1.1}$$

In equation 1.1 σ_{th} is the equiaxed thermal stress that rises in a film with Young's modulus E_f, Poisson's ratio ν_f and coefficient of thermal expansion α_f when it is deposited on top of a substrate with a thermal expansion coefficient α_s and cooled down from temperature T_{cryst} to the ambient temperature T_0

1.4.1 Wafer Curvature Technique

The first attempt to describe the stress distribution in a thin film deposited over a substrate was by G.G. Stoney in 1909 in his famous article [129] where an analytical model of the bending caused on a beam by the deposition of a film on top of it is presented. Stoney's equation is still in use for thin films deposited on isotropic plates, slightly modified by Hoffman who introduced the idea of a biaxial elastic modulus:

$$\sigma_f = \frac{E}{6\,(1 - \nu)} \left(\frac{1}{R} - \frac{1}{R_0} \right) \frac{t_s^2}{t_f} \tag{1.2}$$

E: Young's modulus of the substrate, ν: Poisson's ratio of the substrate, t_s: thickness of the substrate, t_f: thickness of the film .

In equation 1.2 only the elastic properties of the substrate and not those of the film are introduced. This formula relates the residual stress in the film σ_f, with the induced change in the curvature of the substrate after the deposition of the film

and is still in use today due to its simplicity, though it is based on assumptions like uniform film stress distribution and isotropic properties of the substrate that are not always valid.

Recent modifications of equation 1.2 take into account the anistropic properties of the substrate [55], extend the analysis to multilayered composite media [136] and incorporate stress gradient effects in the modelled structures [52].

Two dimensional models accounting for non uniform stress distributions, which also include the mechanical properties of the films and not only those of the substrate, have also been developed [12, 156], however in most cases the resulting partial differential equations are not amenable to analytical solutions.

For the curvature measurements different techniques have been developed based on contact profilometry [152, 153] or on non intrusive optical methods like single or dual wafelength laser interferometry [97, 136, 124, 125, 157, 104, 103, 122, 9, 49, 64] which in certain cases enable real time monitoring of the curvature during film processing. The wafer curvature technique remains a significant method to determine experimentally the residual stresses in thin film materials, though only mean stress data can be obtained.

Static tip deflection of multi layered cantilever beams is another option for determining the residual stress in the films comprising the microfabricated structure. Optical methods based on SEM imaging [66] and optical microscopy [109] have been proposed for the tip deflection measurements.

1.4.2 RAMAN Spectroscopy

Alternative experimental methods to measure directly residual stresses in thin films have been developed like an x-ray diffraction based technique [83, 155] and

Raman spectroscopy [144, 145, 27, 26, 106, 41].

Raman spectroscopy is an optical non destructive method that allows direct stress measurements to be performed in SCS and other materials that are not transparent in UV light with $0.5 - 0.7\ \mu m$ spatial and $10\ MPa$ stress accuracy [13, 26, 27, 78, 137]. The method is based on the shift in the frequency of an inelastically scattered UV photon by a lattice vibrational mode called phonon which is associated to the deformation of the studied material using well established material constants: the so called phonon deformation potentials. Currently the method is successfully used to characterize piezoelectric thin films like AlN and ZnO [78, 117, 137].

The method due to its high accuracy is very well suited for stress studies in MEMS devices and it has already been used for static stress measurements [127, 130, 144, 145, 146, 147] as well as for studying transient heating phenomena in semiconductor devices [70].

In particular with micro Raman spectroscopy spatial resolution in the range of $1\ \mu m$ can be achieved while at the same time stress values as low as $30\ MPa$ can be resolved [144, 131], making the method very useful for high resolution, in situ, residual or dynamic strain measurements on MEMS components. Strains can be converted to stresses once the mechanical properties of the materials are known and a detailed distribution of the induced stresses and stress gradients can be obtained.

In the case of MEMS devices with free standing, moving, mechanical parts, simple knowledge of the residual stresses in the thin films used is not enough, since serious effects like out of plane bending of cantilever structures [45, 154] and shifting of the resonant frequencies of simply supported beams [131] have been reported. Different techniques to either reduce or compensate for the excessive stresses and

finally fabricate flat devices have been proposed, as the use of stress balancing layers at a wafer level [77], the Ar bombardment of the final devices [10] and the film thickness variation [45]. These methods have proven effective in the fabrication of flat devices for many applications, however they do not eliminate the impact of the residual stresses in the operational characteristics and the reliability of MEMS with free standing moving elements. Especially the bombardment of the devices with Ar has been reported to inadvertently diminish the fracture strength of the Si.

1.5 Ferroelectricity- Piezoelectricity- PZT

Piezoelectricity is a property of all, except one, crystal classes with no center of symmetry, which was first observed by the Curie brothers [99]. Two phenomena are associated with this crystal property, the direct piezoelectric effect where the crystal becomes polarized under externally applied stresses and the converse piezoelectric effect, where an external electric field results in the elastic straining of the crystal. MEMS technology makes use of both the direct and the converse effect for sensor and actuation applications respectively.

Pyroelectric crystals are a subclass of piezoelectric materials which possess a spontaneous polarization $\vec{P_S}$ even in the absence of an external electric field. When pyroelectric crystals are uniformly heated or cooled the spontaneous polarization changes and a net surface charge density is generated.

Ferroelectricity is the property of certain pyroelectric crystals to possess at least two equilibrium orientations of the spontaneous polarization vector even in the absence of an external electric field. The spontaneous polarization vector can be switched between the different orientations by an external electric field [23].

Most ferroelectric crystals undergo a phase transition from a high temperature, high symmetry paraelectric phase to a lower symmetry ferroelectric one. The temperature associated with this phase change is called the Curie temperature T_C.

Piezoelectric thin films that have already been successfully incorporated in MEMS devices are AlN, ZnO and a class of ferroelectric ceramics like lead zirconate titanate $Pb(Zr_xTi_{1-x})O_3$, (PZT). PZT ceramics show a rather high piezoelectric response [138, 28] and have already been used in applications demanding high linearity in response and high actuation forces [20, 45, 91]. PZT is a solid solution of $PbTiO_3$ and has a perovskite structure which is depicted in figure 1.4 in (a) the paraelectric cubic phase and (b) in the slightly distorted tetragonal ferroelectric phase. The ferroelectric phase can also adopt a rhombohedral structure if the composition of the solid solution is modified by 50% Zr [23]. There are six different orientations that the spontaneous polarization vector $\vec{P_S}$ can adopt in the tetragonally distorted lattice which become eight in the case of the rhombohedral structure.

Grain formation in PZT thin films is nucleation controlled and results in textured structures with orientations defined by the deposition conditions [138]. These polycrystalline structures are transversely isotropic and appear with no net macroscopical spontaneous polarization when they are deposited with no preferential texture. This is due to the formation of ferroelectric domains which are areas of uniform polarization that are formed to minimize the total free energy of the film during the deposition process.

The spontaneous polarization vectors of the ferroelectric domains are in general randomly distributed canceling each other out, however application of an external electric field can cause them to switch and reorient themselves in directions which tend to be parallel to the direction of the applied field and the film becomes

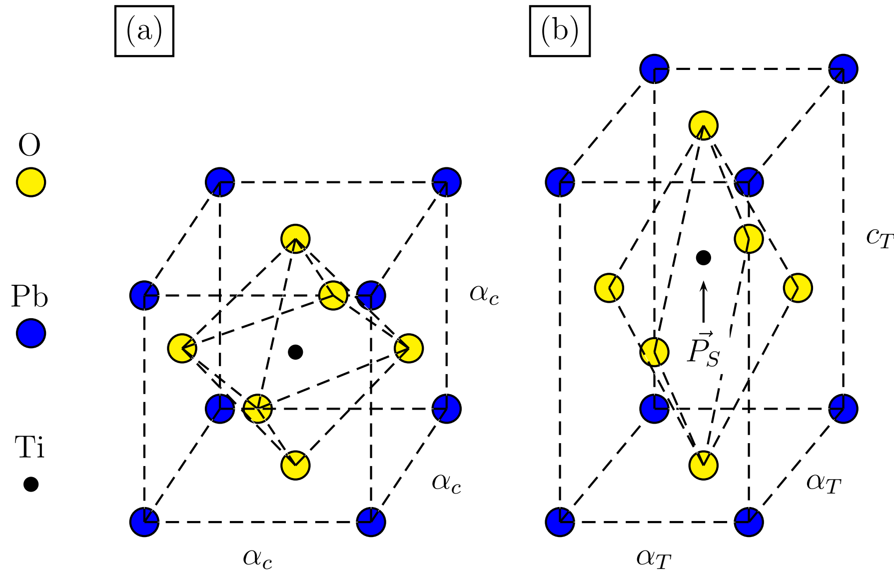

Figure 1.4: Perovskite structure of $\mathrm{PbTiO_3}$ crystal in (a) the paraelectric cubic and (b) the ferroelectric tetragonal phase.

macroscopically poled. The regions between domains of different polarization are called domain walls. Domains with opposite polarizations form a 180° domain wall while domains with polarization vectors perpendicular to each other form a 90° domain wall.

The polarization of a ferroelectric crystal shows a typical hysteretic dependance to external electric fields (figure 1.5) due to the swithing of the ferroelectric domains polarization. The polarization at zero field is called the remanent polarization P_R and the field necessary to zero the polarization is called the coercive field E_C . When most of the domains are oriented to directions which tend to be parallel to the direction of the applied field the saturation polarization P_{SAT} is reached. The elastic response of the ceramic when electrically probed, is linear only when 90° domain wall switching does not occur.

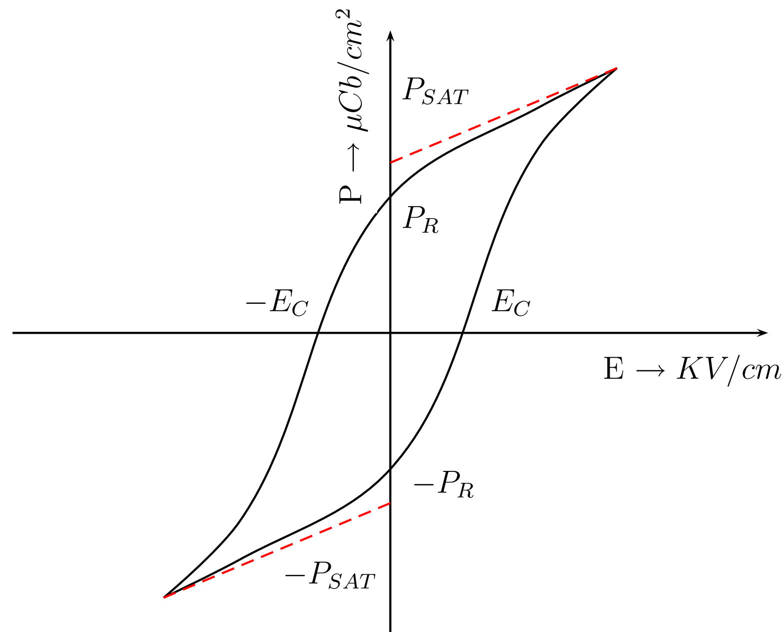

Figure 1.5: Polarization P as a function of the applied electric field E for a typical ferroelectric ceramic. The polarization at zero field P_R is called the remanent polarization and the field E_C necessary to zero the polarization is the coercive field.

PZT films can be deposited on Si substrates by various methods. Sol-gel deposition is a CMOS compatible technique which gives good quality, uniform films at relatively low temperatures, 530 ^oC for x=0.3 and 580 ^oC for x=0.52 near the morphotropic phase boundary if Pt is used as the template layer for the proper nucleation of the perovskite phase. Orientation in this case is influenced by the composition of the sol, the excess lead concentration, the pyrolisis temperature as well as the heating rate of the crystallization step. Pt is believed to promote the formation of the perovskite crystal as it reacts with Pb, forming a metastable

Pt_3Pb intermetallic phase [143] with the desired 111 orientation. Since Pb is a fast diffusing ion which in addition reacts with Si, a thermally grown SiO_2 thin film is usually introduced as a barrier layer between Pt and Si.

1.6 Fatigue

Fatigue is a failure process observed in many materials when they are subjected in a repetitive application of load that may be well below the ultimate tensile strength. When a material is subjected to fluctuating loads the microstructure is irreversibly changed causing the strength of the material to diminish and inevitably the structure to fail pre maturely.

Fatigue failure in metals is believed to originate at surface flaws where points of stress concentration are created. After some cycles of loading a crack is formed which propagates transversely to the principal normal stress due mainly to the motion of dislocations ahead the crack tip.

Fatigue failure of materials can be investigated experimentally by subjecting a test sample in a constant cyclic stress amplitude S and determining the number of loading cycles N until failure. This method is called stress/strain- fatigue life method. In figure 1.6 the graph of the loading waveform as a function of time of a stress- fatigue life test is plotted. The loading conditions are fully characterized when the stress amplitude S, the mean stress σ_m and one of the extreme values σ_{max}, σ_{min} or the ratio $R = \sigma_{min}/\sigma_{max}$ are known.

The cycling load does not need to be fully reversed as figure 1.6 shows. However when an alternating load is superimposed on a mean stress σ_m as in figure 1.6 the maximum applied load should always be kept lower than the fracture strength of the material. The fracture strength of the material obtained from quasi- static

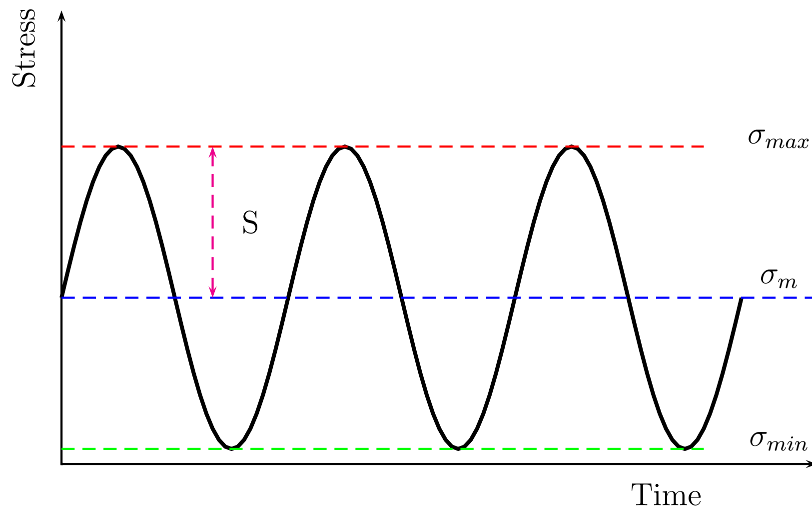

Figure 1.6: Tension- tesion cycle stress for tensile mode fatigue testing.

measurements can be used for this purpose however measurements under comparable experimental conditions are more appropriate.

It has been observed that the frequency and the waveform of the applied load: whether it has a sinusoidal or a triangular shape, can influence the fatigue process when testing is performed under special environmental conditions such as elevated temperature and humidity.

In figure 1.7 three different types of S-N curves are depicted. The first two types of curves (a and b) are typically encountered when the tested materials are metals. Increase in the maximum stress amplitude results in a decrease in the number of cycles to failure in both cases. For some materials however there is a limit called the endurance limit S_e below which no failure occurs no matter how long the sample is cyclically loaded (curve a).

A fundamental difference between ductile and brittle materials like ceramics is that in the latter case the dislocation motion is restricted. Cracks in brittle

materials are in general initiated by flaws or defects in the body of the material, which are usually introduced during processing or by contact damage. Ceramics and brittle materials in general do not exhibit significant cycling fatigue effects and the corresponding S-N curves are typically straight lines almost parralel to the x axis (curve c).

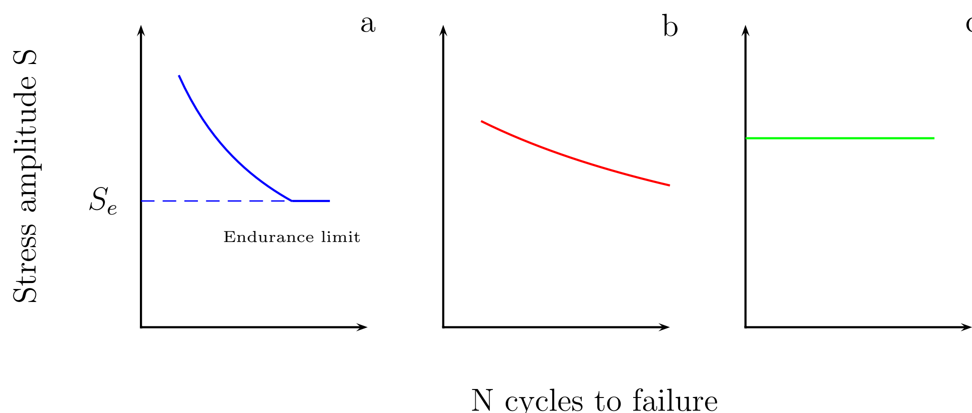

Figure 1.7: Stress S vs number of cycles N to failure (S-N) curves for different types of materials. Curves (a) and (b) are commonly encountered when ductile materials are tested. Ceramics do not have a significant cycling fatigue effect (curve c).

A different approach in studying fatigue is based on the use of concepts and methods of Linear Elastic Fracture Mechanics (LEFM). Within the context of the LEFM theory the notion of the stress intensity factor K as a measure of the driving force for crack propagation is of central importance [5, 48]. Stress intensity factors depend on the loading conditions, the geometry and the length of the crack. They can be either experimentally defined or in some cases analytically calculated. In the most general case of a central crack with length 2α in an infinite plane the

stress intensity factor K_I for the opening mode crack is given in equation 1.3 as a function of the crack length α and the far field applied stress σ_∞:

$$K_I = \sigma_\infty \sqrt{\pi \alpha} \tag{1.3}$$

An important characteristic of the stress intensity factor approach is the existence of a critical stress intensity factor value the *fracture toughness* of the material, K_c which is a measure of the resistance of the material to the propagation of sharp cracks. This type of fatigue study is based on measuring the crack growth rate $d\alpha/dN$ per cycle in pre cracked samples which are subjected to varying fluctuating loads. The crack growth rate per cycle is associated to the stress intensity factor range or crack driving force ΔK, according to equation 1.4:

$$\frac{d\alpha}{dN} = A\Delta K^m \tag{1.4}$$

where A and m are empirical parameters that are material, frequency, environment, stress and temperature dependent and $\Delta K = K_{max} - K_{min}$ is equal to the difference between the maximum and minimum stress intensity factors .

Fracture toughness of a material can be experimentally obtained by tensile testing of pre cracked specially fabricated samples using the compliance calibration method. Fracture toughness of SCS thin films of various orientations have been measured [87] and the reported in the literature values range from $0.7 - 1.3\ MPa.\sqrt{m}$. Lower values of fracture toughness are reported for the closely packed {111} cleavage planes [54].

Equation 1.4 is usually referred to as the Paris equation and it is usually used to fit experimentally measured values of crack growth rates by varying the values of m. Paris equation, fits experimental data for ceramics for very high values of the

exponent m and so in that case the crack growth rate shows a high sensitivity to the maximum applied stress intensity factor.

Bulk Si is a brittle material that is not susceptible to fatigue. Tests on micron-scale structures made from SCS or poly-Si on the other hand revealed a different behavior. In general the published results display similar trends with lower cyclic stresses resulting in larger number of cycles to failure. The S-N curves look more like type b curves in figure 1.7 with [4].

Tests that have been conducted under various loading (tension-tension, resonant vibration) and environmental conditions (temperature and humidity) [6, 74, 14, 88, 87, 89, 90, 22, 57] have shown that both micron-scale SCS and poly-Si display delayed failures under cyclic fatigue loading at applied cyclic stresses as low as half the (single-cycle) fracture strength [4]. Two main classes of different mechanisms to explain such behavior have been suggested. The first class of mechanisms [14, 88, 87, 89, 90, 22] attribute fatigue to a surface effect caused by cracking in the silicon-oxide layer (e.g., reaction-layer fatigue) while the second class of mechanisms identify subcritical cracking in the silicon itself as the cause of thin-film silicon fatigue [57, 58, 56]. Lifetimes are highly dependent on the environmental conditions with samples cycled in vacuum experiencing no fatigue, while humidity and high oxygen atmospheres seem to accelerate failure. The frequency of the applied load on the other hand does not seem to affect the fatigue mechanism.

In ferroelectric ceramics fatigue is manifested not only in the occurence of micro cracks which propagate and lead to physical damage but also as the collapse of the induced polarization which is observed after a number of polarization cycles. The structural and the ferroelectric fatigue phenomena are interrelated, however there are cases where the observed polarization collapse after cycling is reversible and is not accompanied by apparent structural damage.

Mechanical fatigue in PZT 52/48 ceramics have also been investigated using monotonic loading of PZT membranes via means of a bulge testing set up [101, 102, 8]. More recently Kobayashi et al developed a self sensitive micro cantilever for investigating ferroelectric fatigue in piezo MEMS components [65, 63, 67, 66].

1.7 Research Objectives

- Development of piezo- MEMS specific reliability testing methods at both the wafer and the device level to investigate the physics of failure in the micro scale and evaluate the elastic properties of thin film functional materials.
  - Development of a MEMS dynamic stress analysis method, based on time- resolved micro RAMAN spectroscopy. This was undertaken in collaboration with Bristol University for reliability studies of MEMS systems. Piezo actuated cantilever type devices, will be characterized using Laser Doppler Vibrometry and in situ, time- resolved, RAMAN spectroscopy to assess the operational strains that rise under these conditions of operation.
  - To develop tensile testing as a means of characterizing the mechanical properties of functional materials involved in piezo MEMS devices. Appropriate structures, including dog bone shaped structures were investigated and PZT and ZnO were tested under uniaxially applied loads so that elastic properties such as Young's modulus E, Poisson's ratio ν and fracture strength σ_F will be directly evaluated for each one of these materials.
  - To determine the mechanical properties of PZT ceramics as a function of thickness, composition, grain size, poling conditions and temperature. The influence of the Pt/PZT interface on the properties and the

behavior of the ceramic layer. PZT films of various thicknesses, prepared from both sol compositions (Zr/Ti=30/70, 52/48), before and after poling would be tested.

- In addition to static testing, dynamic accelerated tests at resonant frequencies would be performed on prototype piezo activated devices in order to investigate the crack initiation/ propagation mechanisms in different materials. To this end specially designed and developed MEMS devices, fabricated using standard processes with stress concentration points deliberately created on them, would be used as reliability test vehicles. These devices would then be tested under resonant conditions and the change in the resonant frequency as a result of crack propagation would be monitored. Different environmental conditions can be simulated with tests under vacuum or in air.

- Develop a stress elimination scheme for sol- gel deposited ferroelectric stack by removal of the Pt template layer using wafer transfer bonding and dry etching techniques.

- Fabrication of free standing, stress free, cantilever type piezo MEMS devices based on the proposed stress elimination scheme. To this end low stressed electro deposited Ni and PECVD deposited SiN_x films will serve as the alternative structural layers and the potential benefits from their use will be further investigated.

Chapter 2

Experimental Setup

2.1 Tensile Test

2.1.1 Tensile Stage Design

The tensile stage established at Cranfield, was based on the 200N commercial model by DEBEN UK modified for the testing of micro- components by the addition of a new piezo- electric motor. The specific motor, model P-840 from Physik Instrument, is capable of high accuracy movement resolution in the nm range 2 nm, making it ideal for the particular application. The existing commercial model comes standard with a DC motor capable of 3 μm movement resolution and this is retained in the developed stage for the gross positioning of the jaws prior to sample mounting.

There are two available options for the load cell, a 2 N and a 20 N. The force resolution of the kit is equal to 1000:1 so the minimum resolved force with the first cell fitted is 0.002 N. The stage is designed to fit in a Philips XL 30 SEM chamber which is available in Cranfield University. There is also provision for future use of the extra temperature controlling unit which is available for the

specific kit. The applied strain rate is also variable with a minimum value equal to 4 nm/sec. The stage is controlled by an external controlling unit also provided by DEBEN UK. Connection to this external electronics unit is through a special feed through fitted on the SEM chamber. The control unit is connected to a personal computer running windows XP through RS 232 interface. DEBEN UK provides the associated drivers and controlling software for the win XP platform.

Table 2.1: Miniature tensile stage specifications

Load cell	2 N & 20 N
Load cell resolution	1000:1
Piezo-motor travel	30μm
Displacement resolution	4 nm
Strain rate	from 4 nm/sec

In table 2.1 the basic characteristics of the prototype tensile stage are summarized. The choice of the load cells was based on the reported in the literature values for the fracture strength of various materials [150, 148, 81, 60, 59]. The maximum reported value for SiN_x is 7 GPa while for most of the tested materials is in the range of 1 GPa. The maximum applied stress σ was then calculated for different load cells as a function of the cross sectional area A of a sample according to the following simple equation:

$$\sigma = \frac{F}{A} \tag{2.1}$$

A simple rectangular geometry was assumed for the tested samples with width w and height h in the range of 10 $\mu m \leq w \leq 100$ μm and 1 $\mu m \leq h \leq 10$ μm

respectively.

The results are illustrated in figure 2.1. It can be seen that even the 1 N load cell is adequate for applying a maximum stress over 1 GPa for the whole range of the cross sectional areas considered. The 10 GPa limit though is reached by load cells over 5 N.

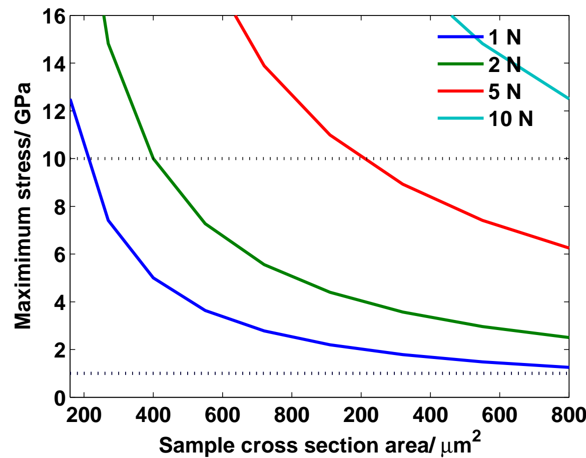

Figure 2.1: Maximum applied normal stress as a function of the cross sectional area of the tested sample for different load cells

During the stage development it was decided that two different types of samples with different dimensions would be fabricated. For the first type of samples a typical tension test with direct application of the load would be performed. For this type of testing two flat horizontal jaws would be used to mount the sample on the stage during application of the tensile load as shown in figure 2.2.

Alternatively vertical jaws can be used for application of compressive load using the appropriate pushing tip as figure 2.3 indicates. This configuration for application of compression can be combined with the horizontal jaws as well.

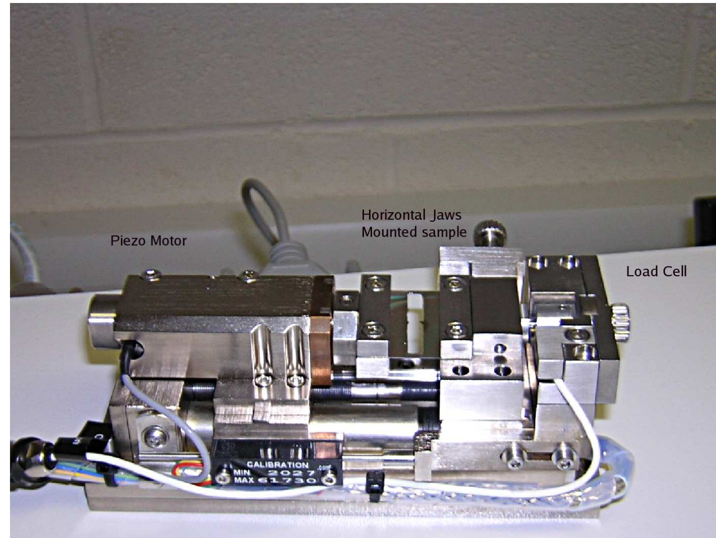

Figure 2.2: Prototype tensile stage kit, equipped with horizontal gripping jaws for conventional tensile testing.

2.1.2 Strain- Displacement measurement

Displacements can be extracted from the extension/ contraction of the piezo motor, provided that the various parts of the stage (load cell, clamping jaws etc) and the piezo element itself are much stiffer than the sample. This may be concluded directly from the proceeding simplified analysis.

Assuming for simplicity a 1-D problem the load-cell, the sample and the piezo electric element may be considered as springs connected in series with equivelant stiffness k_L, k_s and k_p respectively (figure 2.4). The extensional stiffness of a beam of length L and cross sectional area A is equal to $k = EA/L$ where E is the Young's modulus of the material. Assuming that the piezo electric element operates in the linear regime the exerted strain is given by:

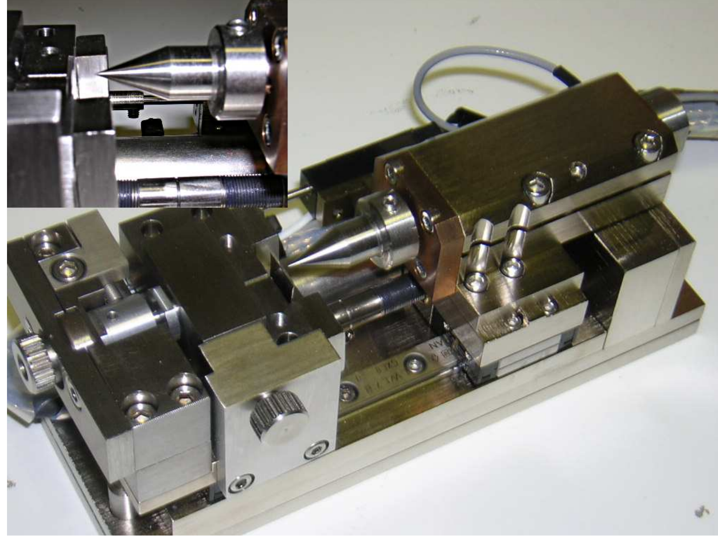

Figure 2.3: Prototype tensile stage kit, equipped with vertical gripping jaws and point tip for bending and crack initiation experiments. In the inset the pushing tip is shown in contact with a metal sample.

$$x_1 = s_{11}^{E_3} T_1 + d_{31} E_3 = \frac{T_1}{E_p} + d_{31} E_3 \tag{2.2}$$

Equation 2.2 is one of the two constitutive equations of a linear piezoelectric material operating in the d_{31} mode, if Voigt notation is adopted [23, 75]. In 2.2, x_1 is the induced strain, T_1 the mechanical stress exerted on the piezoelectric, $s_{11}^{E_3}$ the elastic compliance under conditions of constant applied field, E_p the Young's modulus of the piezoelectric and finally E_3 is the externally applied field.

Substituting in 2.2 the Young's modulus E_p in the denominator of the first term on the right with Lk_p/A one gets:

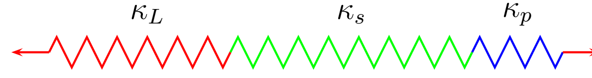

Figure 2.4: Equivalent spring constant of the load cell, the tested sample and the piezo element. The force from the extension/ contraction of the piezo is applied on the load cell and the sample.

$$\underbrace{x_1 L}_{\Delta l_p} = \frac{\overbrace{T_1 A}^{F_p}}{k_p} + d_{31} E_3 L \Rightarrow \Delta l_p = \frac{F_p}{k_p} + d_{31} E_3 L \tag{2.3}$$

In 2.3 Δl_p is the extension/ contraction of the piezo electric element, F_p is the force exerted on the piezo element from the sample which is opposite to the load applied on the sample by the piezo motor. From 2.3 it is evident that:

- For a certain applied voltage (constant field E_p) a longer piezo electric element gives a longer travel distance Δl_p (extension or contraction), albeit in this case at the expense of the displacement resolution due to limitations imposed by the electronic controllers used. It was thus decided to use two piezo elements connected in series.

- A piezo electric element with a high stiffness k_p is desirable, as this eliminates the straining of the piezo element due to the reaction forces exerted on it from the samples, while ensuring the linear dependence of the measured displacement on the applied voltage for a wide range of tested samples. In practice k_p needs to be much higher than the combined stiffness of the used load cell and the tested sample.

When the stiffness of the piezo element is high compared to the stiffness of the sample, the displacement of the piezo element Δl_p may be considered equal to the sample displacement provided that the stiffness of the load cell k_L is infinite, or in practice much higher than the stiffness of the sample. This condition is rarely met and the sample displacement x_s is related to the load cell displacement x_L through the simple equation:

$$\Delta l_p = x_s + x_L \tag{2.4}$$

The ratio x_s/x_L is proportional to the inverse stiffness ratio k_L/k_s since the force F_p from the piezo motor is applied on both the load cell and the sample. The sample displacement x_s is thus calculated from the measured piezo displacement Δl_p in case the load cell stiffness k_L is known according to equation 2.4:

$$x_s = \frac{\Delta l_p}{1 + (k_s/k_L)} \tag{2.5}$$

From 2.5 it is clear that the measured displacement Δl_p and the actual sample displacement x_s may differ signifficantly. In addition the response of both the sample and the load cell may be strongly dependent on the applied load so the stiffness ratio k_s/k_L in 2.5 is no longer a constant.

A way to circumvent all the limitations that are imposed by the finite stiffness of the various parts, is to measure the strain/ displacement directly on the sample using an optical non destructive strain measurement technique, based on digital image correlation.

Digital image correlation (DIC), is an optical, non- contact technique which can be used for the calculation of the strains from a series of consecutive images with sub- pixel resolution [110]. In DIC a speckle pattern on the surface of the

sample is chosen and the reflected light- intensity pattern is monitored during the deformation of the sample. A basic assumption is that the image patterns $f(x, y)$ and $f^*(x^*, y^*)$ of the undeformed and the deformed sample respectively are in a unique and one to one correspondence with the respective sample surface. Should this assumption hold one would be in principle able to deduce the small deformations of the sample surface from the deformations of small subsets of the images, typically $(2M + 1) \times (2M + 1)$ pixels. The method has been further developed and can be used for the analysis of three dimensional displacements as well [21].

The starting point for the foundation of DIC is the large strain formula definition [72].

$$u_{ij} = \frac{1}{2}\left(\frac{\partial u_i}{\partial x_j} + \frac{\partial u_j}{\partial x_i} + \frac{\partial u_i}{\partial x_k}\frac{\partial u_i}{\partial x_l}\right) = \frac{1}{2}\left(u_{i,j} + u_{j,i} + u_{i,k}u_{i,l}\right) \tag{2.6}$$

For a tensile sample which is deforming primarily in the x,y plane u_{zz}, u_{zy} and u_{zx} from equation 2.6 are taken equal to zero. Furthermore the out of plane displacements w are expected to be negligible thus all the derivatives of w with respect to the in plane coordinates should be very small. Under these assumptions the finite strains expected are given by:

$$\epsilon_x = u_{xx} \approx \frac{\partial u}{\partial x} + \frac{1}{2}\left[\left(\frac{\partial u}{\partial x}\right)^2 + \left(\frac{\partial v}{\partial x}\right)^2\right] \tag{2.7}$$

$$\epsilon_y = u_{yy} \approx \frac{\partial v}{\partial y} + \frac{1}{2}\left[\left(\frac{\partial v}{\partial y}\right)^2 + \left(\frac{\partial u}{\partial y}\right)^2\right] \tag{2.8}$$

$$\epsilon_{xy} = u_{xy} \approx \frac{1}{2}\left(\frac{\partial u}{\partial y} + \frac{\partial v}{\partial x}\right) + \frac{1}{2}\left[\left(\frac{\partial u}{\partial x}\right)\left(\frac{\partial u}{\partial y}\right) + \left(\frac{\partial v}{\partial x}\right)\left(\frac{\partial v}{\partial y}\right)\right] \tag{2.9}$$

In addition to the assumptions used for the derivation of equations 2.7- 2.9 it should be further assumed that the reflectivity of the sample surface is not affected or altered in any way during sample testing. This implies that the reflected light intensity pattern f deforms but it does not change its local values due to deformation making tracking of a moving point from the reflected light intensity possible.

The 2-D strains from equations 2.7- 2.9 are fully determined if the derivatives of the in- plane displacements u, v with respect to the in plane coordinates x, y are known. The registration accuracy of displacements depends on the resolution of the used sensor and the magnification of the imaging system. Higher magnifications for a fixed image sensor increase the accuracy albeit at the expense of the field of view area. The other option is the use of a sub- pixel registration algorithm. In [11] the different algorithms that have been developed for the extraction of the displacements and their corresponding derivatives are presented and the three most widely used implementations are reviewed. All these methods calculate displacements/strains of the image subset with a sub pixel resolution mainly by maximizing an appropriate correlation function.

For this work the freely distributable MATLAB code from the group of Kevin J. Hemker at Johns Hopkins University was used [2]. The code is based on the MATLAB function cpcorr.m which performs the calculation following the correlation coefficient curve-fitting method [11, 51]. Initially the normxcorr2.m function calculates the normalized correlation coefficient $C(u, v)$ from equation 2.10 where f, f^*, are the reflected light intensity patterns of the image subset in the undeformed and the deformed image and f_m and f_m^* are the average values of the corresponding ensembles.

From 2.10 a set of $(2M+1)\times(2M+1)$ correlation factors are calculated. Because the minimal unit in a digital image is one pixel, the displacement calculated from

equation 2.10 is an integer multiple of one pixel. The private function findpeak.m finds the local maxima in this discrete set of correlation factors $C\left(u,v\right)$.

$$C\left(u,v\right)=\frac{\sum_{x=-M}^{M}\sum_{y=-M}^{M}\left[f\left(x,y\right)-f_m\right]\left[f^*\left(x+u,y+v\right)-f_m^*\right]}{\sqrt{\sum_{x=-M}^{M}\sum_{y=-M}^{M}\left[f\left(x,y\right)-f_m\right]^2}\sqrt{\sum_{x=-M}^{M}\sum_{y=-M}^{M}\left[f^*\left(x+u,y+v\right)-f_m^*\right]^2}} \tag{2.10}$$

For displacement evaluation with sub pixel resolution a two dimensional quadratic surface 2.11 is fit to subsets comprising of eight points around each local maximum value.

$$C\left(u,v\right)=\alpha_0+\alpha_1 x+\alpha_2 y+\alpha_3 x^2+\alpha_4 y^2+\alpha_5 xy \tag{2.11}$$

The maximization of C with respect to the coordinates x,y is then used to derive the subset displacements u,v from the solution of a linear algebraic system of equations.

$$\frac{\partial C}{\partial x}=\alpha_1+2\alpha_3 x++\alpha_5 y=0 \tag{2.12}$$

$$\frac{\partial C}{\partial y}=\alpha_2+2\alpha_4 y++\alpha_5 x=0 \tag{2.13}$$

The solution of the equations 2.12, 2.13 gives the new positions x,y of the image subset points and thus the displacements u,v. The main advantage of the method is the speed of calculations (low CPU time), however the accuracy is not as high as in the case of the Newton- Raphson iterative method [11]. The accuracy of the

pixel registration algorithms that are typically used in DIC ranges between 0.01 and 0.5 pixel [11].

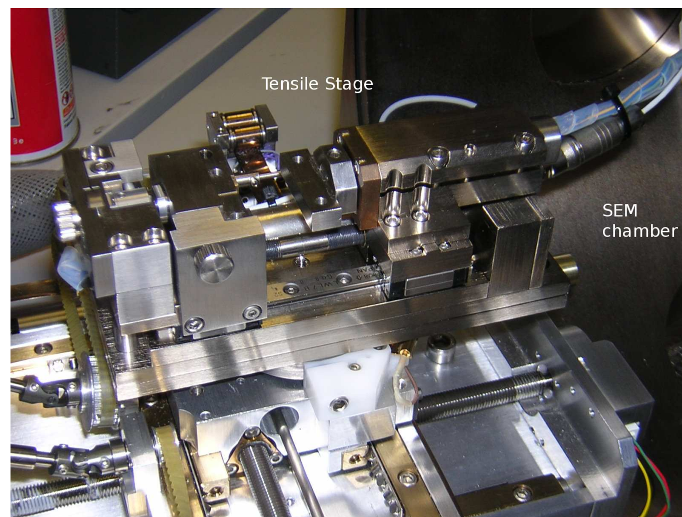

Figure 2.5: The tensile stage kit mounted in the SEM chamber using the specially designed fixture.

In this case the MATLAB based software offers the user control over the size of the correlated subset (M) and the resolution of the marker's positions. The code was slightly modified to produce videos from the captured images showing the test process. Testing was performed in the SEM chamber (figure 2.5) and the images were manually captured using the integrated CCD camera. By using SEM imaging one can achieve high magnifications which further enhance the accuracy of the correlation method while at the same time the way the sample deforms and fractures is monitored.

2.1.3 Fabrication Process

Sample preparation was based on the standard processing used in piezo- MEMS device fabrication. Typical substrates used in this study were four inch, double sided polished, Si wafers of (100) orientation, with 200 nm of thermally grown oxide SiO_2 on both sides. This oxide layer is essential for the proper PZT deposition when the sol-gel method is used, as it serves as a protective layer that prevents Pt, normally used as the template layer for the PZT growth, from interacting with the underlying Si. This thin oxide layer also acts as a barrier layer that limits the diffusion of Pb molecules into the Si during the high temperature crystallization step.

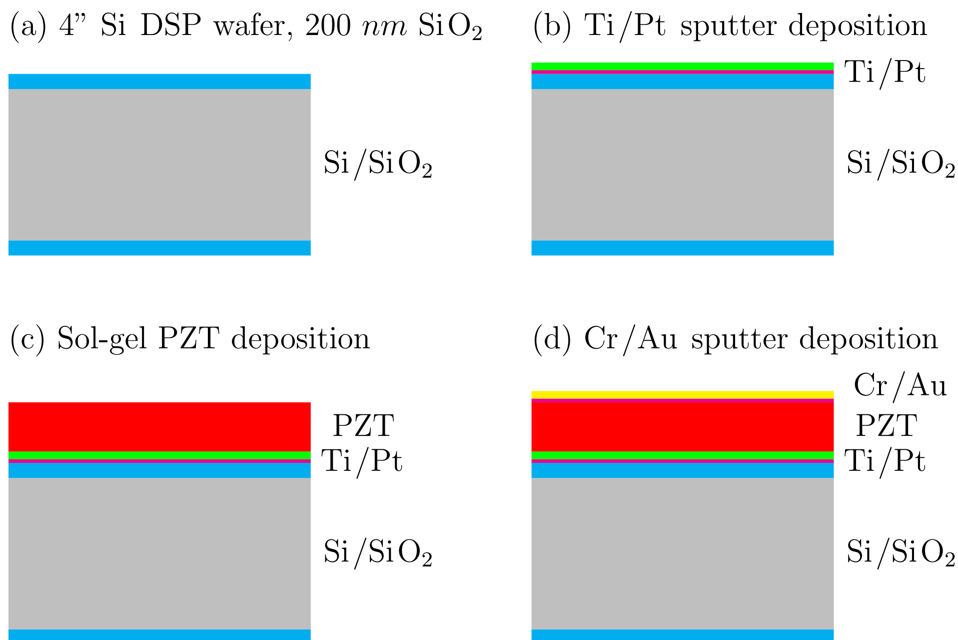

Figure 2.6: Fabrication process. First metallization step (b), deposition of the ceramic (c) and second metallization step (d).

The first processing step is the metallization step. Sol- gel deposited PZT cannot grow properly directly on the oxide layer so a thin metal film is needed. Usually a thin Pt layer is used for that purpose. Pt is essential for the proper PZT crystallization at relatively low temperatures when the sol- gel deposition method is used, as it serves as a template layer for the proper perovskite phase formation [143]. For that reason 100 *nm* of Pt are DC sputtered on the initial wafers using a NORDIKO sputtering system. A thin Ti layer is RF sputter deposited in the same system prior to the Pt deposition in order to improve the adhesion of Pt on the oxide surface [17, 30].

The PZT sols were prepared using the following precursors: lead acetate trihydrate ($Pb(CH_3COO)2.3H_2O$), zirconium propoxide ($Zr(OCH_2CH_2CH_3)_4$) and titanium butoxide ($Ti(OCH_2CH_2CH_2CH_3)_4$). The precursors were stoichiometrically mixed and refluxed in a solution of acetic acid (CH_3COOH) and methanol (CH_3OH). PZT sols with a Zr/Ticomposition of 30/70 and 52/58 were prepared with a 10% or 20% Lead Pb excess respectively. That way Lead loss during pyrolysis and annealing is compensated [84, 143].

Sol gel deposition of the PZT ceramic is a spin and drying process that is repeated until the desired thickness is reached. Each layer is spin- coated on the platinized wafer at 3000 *rpm* for 30 *sec* using an EMS photoresist spinner. Baking and crystallization temperatures depend on the composition of the sol used and on the desired orientation of the final film [84]. For a sol with a composition ratio of Zr/Ti = 30/70 baking for 30 *sec* at 200 ^oC is needed prior to the 5 *min* crystallization anneal at 530 ^oC in air atmosphere. Baking for a sol of a Zr/Ti = 52/48 composition ratio on the other hand is performed at a temperature 300 . . . 350 ^oC for 3 *min* and the gel is then annealed in air at 580 ^oC for 5 *min*. Alternatively ZnO ceramics are rf sputter deposited in a BALZERS system using substrate heating. In that case the metallization step is not that essential and Ti/Au can

also be used.

Finally a metal layer is deposited on top of the ceramic. This layer is needed for the fabrication of the reflective pads that are necessary for the DIC strain measurement method. Au is the most common choice due to its high reflectivity and the fact that can be easily etched using either wet or dry etching techniques. A thin Cr or Ti layer, is also used in that case as an adhesion promoter. So the samples end up with a structure similar to that shown in 2.6.

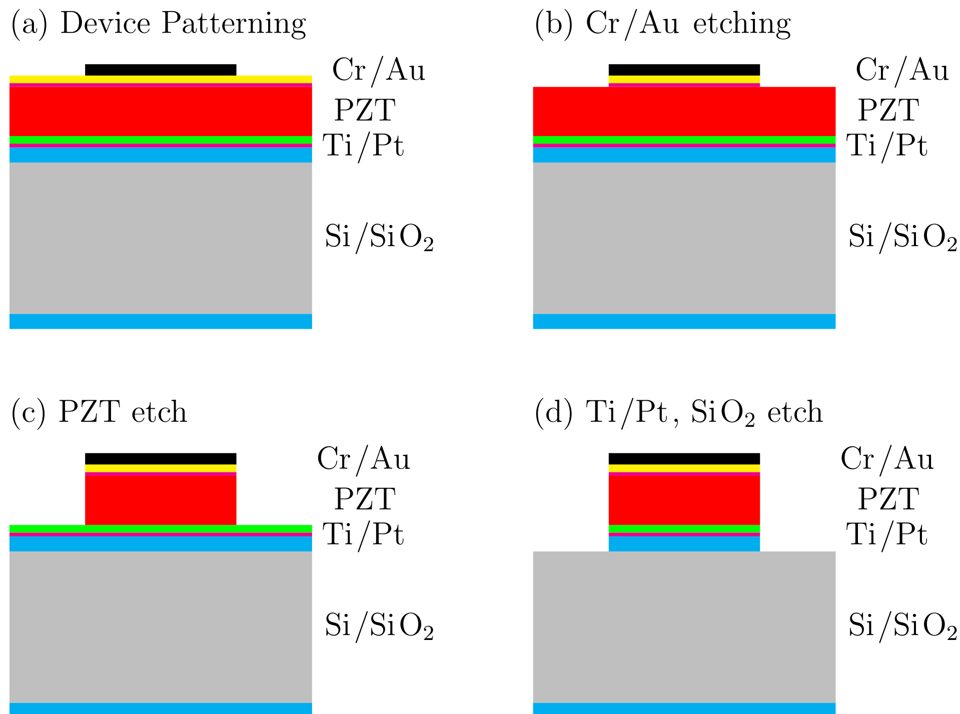

Figure 2.7: First photolithography. Device patterning (a), etching of Cr/Au (b) and PZT layers (c). Etching of bottom electrode and oxide films from the front (d).

The first photolithography step defines the sample layout. Depending on the subsequent etch method the appropriate photo resist is used. If wet etching of

the ceramic is chosen, a positive resist like S1818 or AZ4562 is needed, otherwise AZ5214E negative resist is used and masking of the etched materials is accomplished by electro plating 0.6 μm of Ni. The Ni bath used in this work was made of 450 g/l nickel sulphamate and 30 g/l boric acid. The bath temperature was 50 ^oC and the current density was set at 38 mA/Cm^2. Ni hard masking has proved to be better suited for the dry etching of the ceramics in the RIE as it is not prone to the formation of "fences" due to the re deposition of the etched material. The processing steps following this first photolithography step are presented in figure 2.7.

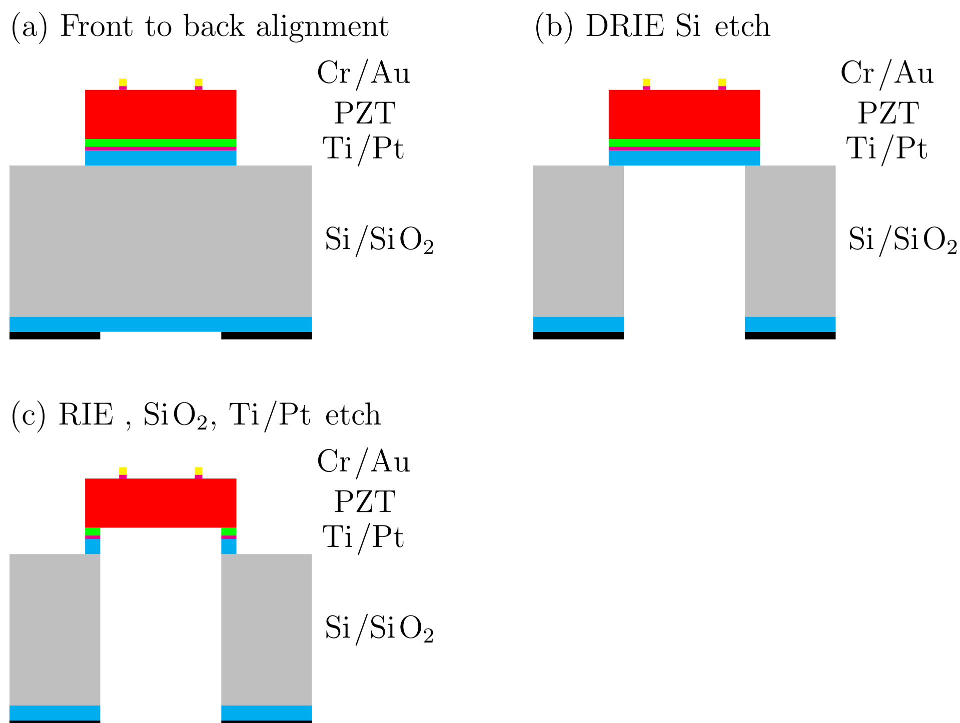

Figure 2.8: Front to back alignment (a) and DRIE Si etch (b). Final release of the structures by RIE etching of the oxide, Ti/Pt layers (c).

The second photolithography step (figure 2.7) defines the Au pads on the top of the samples. These pads define the gauge length on the measured sample and are essential for the optical strain measurement method.

The final photolithography defines the silicon supporting stage through a front to back alignment step. Silicon is etched in the DRIE and the samples are finally released after both the SiO_2 and the metal films are removed completely from the back. In figure 2.8 the release steps following the back patterning of the wafer are schematicaly presented.

2.1.4 Mask Design- Sample Layout

In order to investigate the impact of sample dimensions on measured properties, samples with a variety of geometries were designed. Documents BS EN 62047-1, 2, 3:2006 from British Standard about tensile testing of thin film materials were used as guidelines. Samples with total lengths ranging from 400 μm up to 4 mm and widths between 50 μm and 500 μm were finally designed (table 2.2).

Table 2.2: Sample dimensions.

Mask	Gauge Leng. μm	Parallel Leng. μm	Total Leng. μm	Width μm
	1500	2000	4000	500
1st	1000	1500	4000	350
	500	750	2000	200
2nd	200	300	400	50

In figure 2.9 a single test structure is schematically shown. The tested film depicted in red has been patterned in a dog bone shaped geometry on top of a

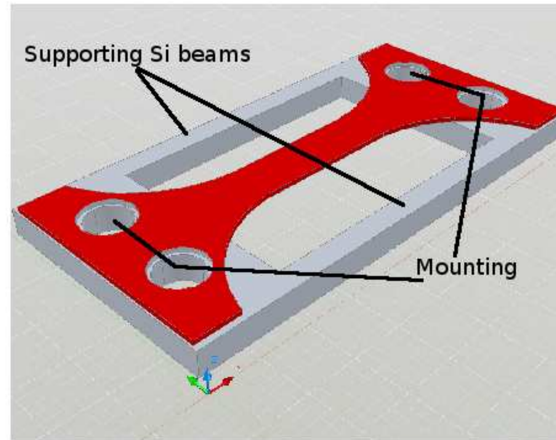

Figure 2.9: Schematics of a dog bone shaped sample geometry attached on a rectangular Si frame. Two pairs of mounting holes are defined on both the tested film and the supporting frame. The Si supporting beams are cut after securing the frame on the tensile stage.

rectangular Si supporting frame. Two pairs of holes have been etched in both the film and the Si frame. These holes are used for gripping the sample on the tensile stage with the horizontal jaws shown in figure 2.2 which are secured in place using the appropriate screws. After mounting the Si frame on the tensile stage the supporting beams are cut leaving the sample free for testing. The distance between the centres of the circular holes is 2 cm and the length of the supporting beams is equal to 2 cm.

In figure 2.10 the computer aided design of the first mask set is shown. There are nine samples in total on each wafer. The nine dog bone shaped samples are deposited on top of three Si frames which are diced from the wafer after completion of the fabrication process.

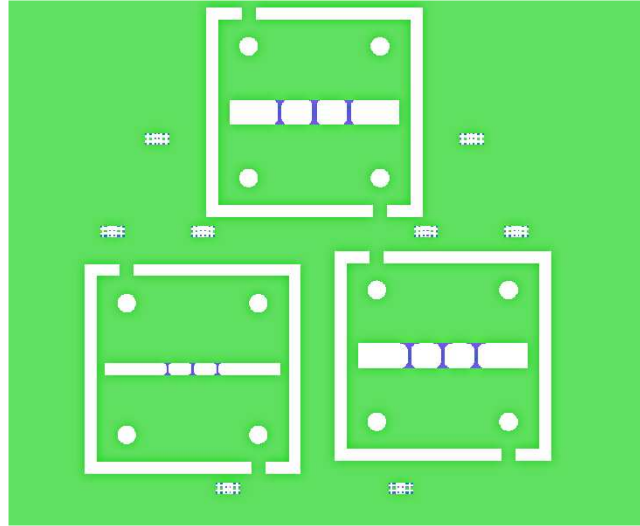

Figure 2.10: Computer Aided Design of the first mask set with the large dog bone shaped structures. There are three silicon frames with three parallel dog bone samples each.

Each frame contains three parallel dog bone structures in order to increase the yield of successfully released devices. The purpose of this design was to increase the yield of the samples per wafer. In figure 2.11 a fabricated sample is shown. In practice the stiffness of the structures on a single frame may vary significantly due partly to deviations that should be expected in the dimensions of surface micromachined devices and partly due to the statistical scatter of the measured mechanical properties. Variations in the sample stiffness could result in the anisotropic, non uni- axial loading of the dog- bone shaped structures thus invalidating the tensile test results. In order to eliminate this risk, it was decided that in case a frame with more than one specimen was mounted on the stage only one of these specimens would be used for testing.

The large samples are tested using the 20 N load cell. The force resolution in this

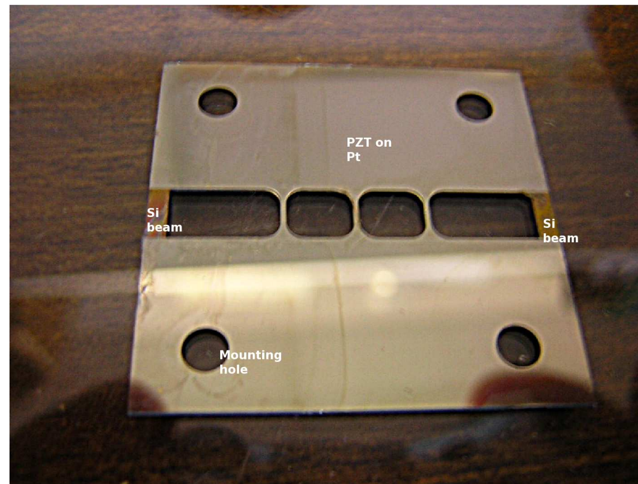

Figure 2.11: Photograph of sample fabricated using the first mask set. The Si supporting beams are cut after mounting the sample on the tensile stage.

case is 0.02 N so for a typical sample with thickness ≈ 1 μm and width between $200 \ldots 500$ μm the stress resolution to be expected is between $40 \ldots 100$ MPa. The sub pixel resolution of the DIC registration algorithm is between 0.01 and 0.5 pixels. The resolution of the CCD sensor which was used to capture the digital images is 712×484 pixels. The displacement resolution is thus defined by the magnification of the imaging system. When a $400\times$ magnification is used the individual pixel length is 0.44 μm and the minimum displacement that can be resolved is between $0.0044 \ldots 0.22$ μm. Under this magnification the field of view is also limited resulting in a measured length ≈ 310 μm. The theoretical strain resolution in that case, assuming that the loading direction coincides with the image width (712 pixels), is limited between $(0.07\% \ldots 0.0014\%)$.

Testing of smaller samples was not possible with the mask set shown in figure 2.10. Handling samples with lengths shorter than 1 mm using these large Si frames would be very difficult as any slight misalignment of the frame on the

tensile stage would result in the sample destruction. In order to circumvent these difficulties a special test structure was designed and is schematically presented in figure 2.12. This silicon stage consist of a moving platform, which is connected through a number of thin silicon beams on a larger stationary frame where the mounting holes are defined. The tested samples are perpendicular to the beams that support the moving frame and are placed in symmetric places around the platform's plane mid axis, having one end attached on the moving platform (see inset figure in 2.12). When a uniaxial compressive load is applied on the free end of the platform, the supporting beams bend resulting in the application of tension on the samples.

A second mask set (figure 2.13) with seven test structures like the one presented in figure 2.12 was designed. In five of these silicon stages there is a small moving frame with four samples and six supporting beams. There is also one stage with six samples and one with six samples and six counter samples which can be used for the evaluation of the residual stress in the thin film. This last type of stage uses eight parallel beams in total to support the larger platform needed for the twelve samples (figure 2.14). In total thirty eight samples can be fabricated and tested on each wafer.

The response of the Si frame- sample system under the application of an external force can be approximated by that of parallel connected springs with stiffness k_s for the sample and k_{b_y} for the beams. A simple analysis based on Euler- Bernoulli beam theory was performed to define the geometry and the number of supporting beams needed for each stage. The stiffness of the beams in the direction of the applied load should be comparable to the sample stiffness. At the same time platform movement should be totally constrained in the two other directions.

In a first simplified approach, samples under uniaxial tensile loading contribute a spring constant equal to $k_s = (E_s \times A)/l_s$, where A is the cross sectional area, l_s

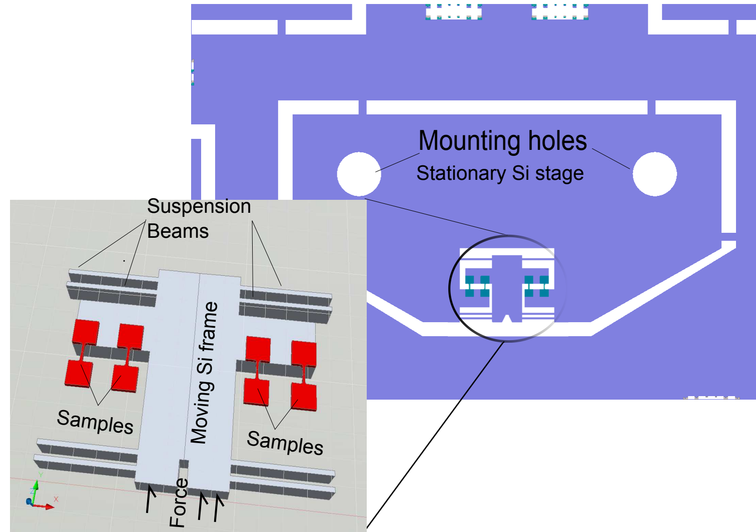

Figure 2.12: Schematics of a test structure. There are four dog bone shaped samples bridging the gap between the fixed and the moving part of the Si frame. The two parts of the frame are connected through parralel Si suspension beams, the fixed part is mounted on the load cell using the mounting holes and a compression load is applied on the moving part using the special pushing tip.

the length and E_s the Young's modulus of the tested structure. Assuming a value of 70 GPa for the Young's modulus of the thin film PZT and a sample thickness of 1 μm the stiffness of each sample is equal to $k_s = 8.75\ kN/m$.

The suspension silicon beams on the other hand are oriented along the $< 110 >$ direction with an equivalent Young's modulus $E_{Si} = 168\ GPa$. Under the assumptions of Euler- Bernoulli beam theory the spring constant of a cantilever beam with length l_b, width w_b and thickness t_{Si} in the three directions x, y, z are:

$$k_{b_x} = \frac{E_{Si} w_b^3 t_{Si}}{l_b^3}, k_{b_y} = \frac{E_{Si} w_b t_{Si}}{l_b}, k_{b_z} = \frac{E_{Si} w_b t_{Si}}{l_b^3} \tag{2.14}$$

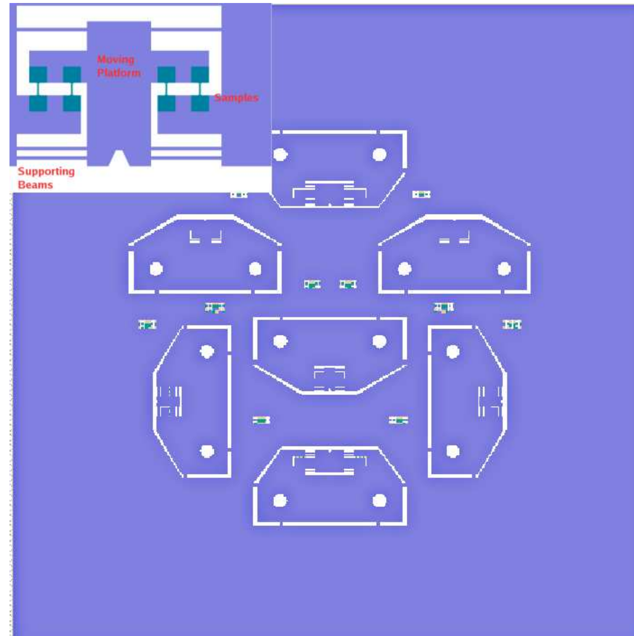

Figure 2.13: Schematic of the second mask design. There are 38 small dog bone samples in total which are attached on 7 different stages. Five of the stages come with 4 samples attached, there is one stage has 6 samples and one stage comes with 6 samples and 6 counter samples. In the inset the moving platform with the 4 samples and the 6 supporting beams is shown.

with the convention that y is considered as the longitudinal and z as the vertical direction. In that case x- direction corresponds to the loading direction.

The thickness of the suspension beams is defined by the thickness of the wafer. Typical values are 425 μm and 525 μm. Widths and lengths were the parameters that could be varied during the frame design in order to achieve the desired stiffness compatibility between the samples and the beams. Since the role of the beams is also to constrain the frame movement in the y and z directions, only combinations of lengths and widths that give high enough spring constant k_{b_y} and

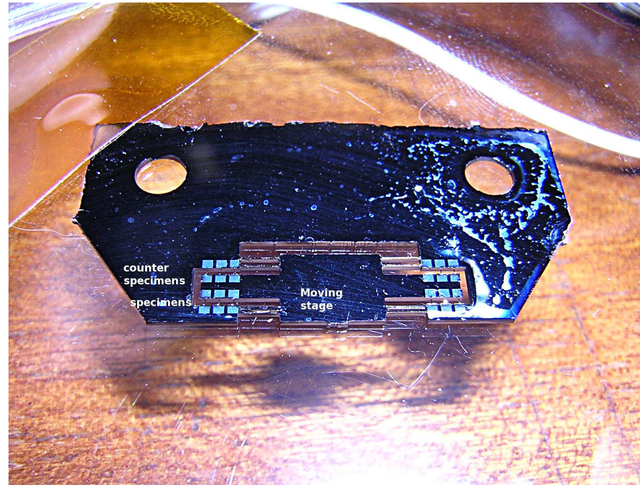

Figure 2.14: Silicon frame with 6 samples and 6 counter samples for the evaluation of the residual stress. This platform requires 8 supporting beams instead of the 6 used in the simpler stages with the 4 samples.

k_{b_z} are accepted. Combinations of beam lengths between 1800 μm and 2200 μm and widths between 100 μm and 150 μm were considered.

The ratios of the sample stiffness k_s over the calculated beam spring constants k_{b_x}, k_{b_y}, k_{b_z} for the different values of lengths and widths considered, are plotted in figure 2.15 α. Since high anisotropy is desired, only triplets (x, y, z) with x close to one and y, z tending to small values close to zero are acceptable. In β the sum of stiffness ratios is plotted as a function of the beam length and width. Based on the comment made previously the optimal combinations correspond to the red colored area of the plot. It was finally decided to use beams with length 2200 μm and width 100 μm.

The total number of suspension beams needed for a specific frame is related to the total number of attached samples. Based on the previous analysis it was decided

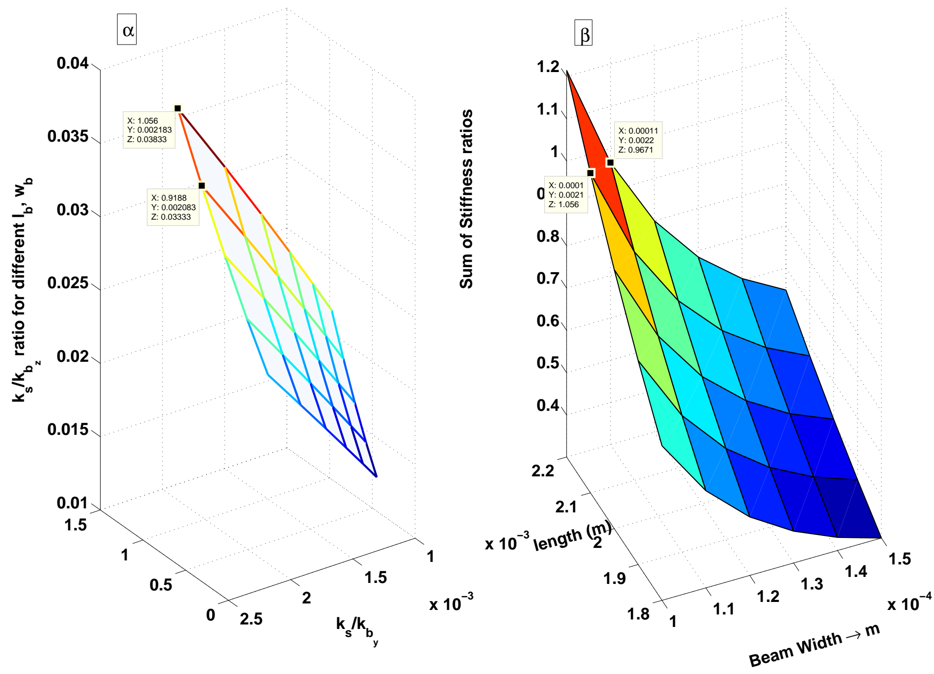

Figure 2.15: Calculated sample stiffness in the x,y and z direction relative to the stiffness of a $< 110 >$ oriented Si beam is plotted in α, assuming a beam thickness equal to $525\ \mu m$ and variable lengths, widths. Sum of ratios of sample stiffness over beam stiffness in the x, y and z direction is plotted in β as a function of the beam width and length.

to use six beams for the smaller frames with the four attached specimens and eight beams for the larger frames which accommodate six samples. The high anisotropy of the structure was further investigated using ANSYS (App B-1). This model calulates the deformation of the Si frames under the application of their own weight. The calculation is performed assuming anisotropic material for increased accuracy.

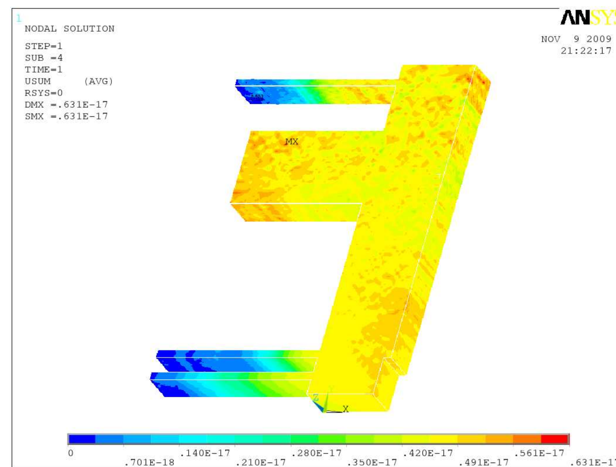

Figure 2.16: Deformation of a 425 μm thick small Si frame under the action of gravity.

In figure 2.16 the deformation of a 425 μm thick Si frame under the action of the gravitational field is presented. The geometric symmetry of the structure around the lognitudinal axis was taken into account so half the structure is modeled. The displacement in the z axis as well as the deformation due to gravity is negligible. This was also confirmed in the case of small frames made from thicker (525 μm) wafers as expected. Larger frames with six supporting beams give larger deformations compared to the small ones but still small enough to be neglected (figure 2.17).

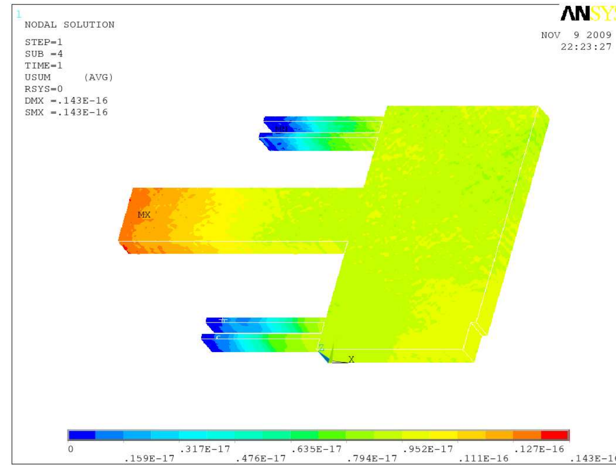

Figure 2.17: Deformation of a $525\ \mu m$ thick large Si frame under the action of gravity.

Next the approximation of the supporting beams by simple linear springs of equivalent spring constant k_{b_y} in the direction of the applied load was calculated using ANSYS.

In figure 2.18 the displacement in the y direction of a Si suspension beam is plotted as a function of the applied force for the two different cases of interest. A linear fit was applied to the data and the stiffness of the beam in the direction of loading was found equal to $k_{b_y} = 6585\ N/m$ for the thick beam and equal to $k_{b_y} = 5294\ N/m$ for the thinner one very close to the values derived from the analytical expressions in 2.14.

The maximum force was chosen equal to $0.1\ N$ as in this case the displacement of the beam in the direction of the applied load and thus the displacement of the Si frame exceeds $15\ \mu m$. This displacement translates to a strain of the $400\ \mu m$ long specimens $\approx 3.8\%$ much higher than the strain levels a brittle ceramic is expected

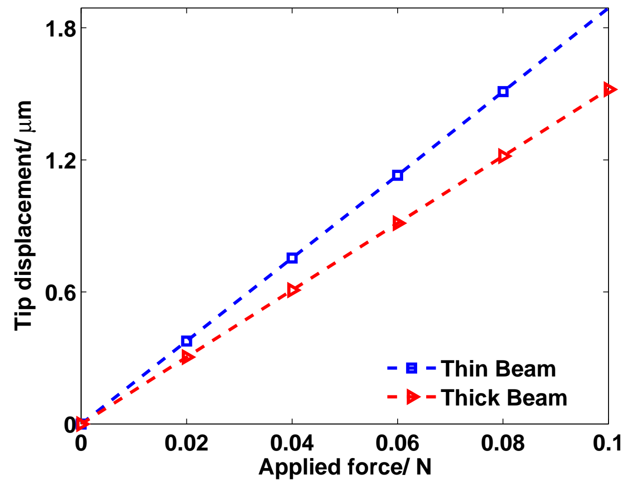

Figure 2.18: Tip displacement of a 525 μm and a 425 μm thick Si suspension beam as a function of the applied force. In both cases the response of the beams is well within the linear limits.

to sustain.

In addition the deformation of the Si frames due to the traction exerted on them from the sample anchor pads, for these levels of sample straining were found using ANSYS to be in the nm range (figure 2.19). This is three orders of magnitude less than the deformation of the actual sample which can thus safely be considered equal to the frame displacement.

Each time a sample fractures during testing an abrupt change in the stiffness of the structure is expected. Provided the conditions presented in the previous discussion are met, the change in the stiffness of the structure before and after fracture of a sample can be used for the evaluation of the sample Young's modulus if the sample geometry is taken into account.

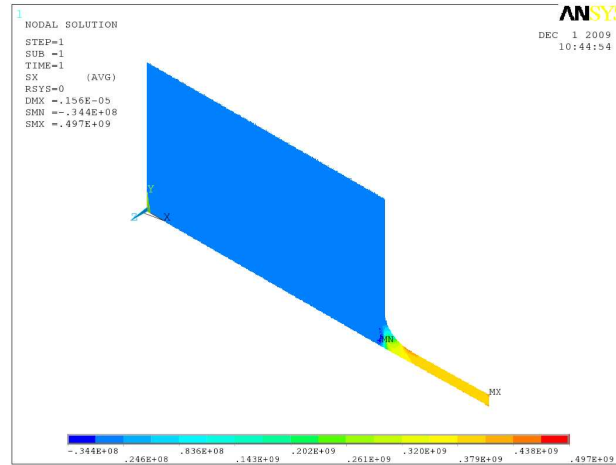

Figure 2.19: Surface traction exerted from the sample pad on the Si frame.

Finally the residual stress in the films can be evaluated from the special test structures where pairs of samples and counter- samples have been fabricated. In this case the stress is assumed homogeneous in all the specimens and the counter specimens resulting in a zero applied force on the moving frame. During testing as the moving frame is pushed, specimens are strained while at the same time stress in the counterspecimens is relieved, assuming an initial state of tensile residual stress in the tested film. When the strain in the counter specimens is totally relaxed, the beams buckle and there is an abrupt change in the total stiffness [59]. On the other hand, starting with an initial state of compressively stressed beams, a sudden increase in the total stiffness is expected when the specimens are stetched enough to cancel the residual strain. The frame displacement where the change in the total stiffness due to the buckling/ stretching of the counter specimens is observed, may be used for the evaluation of the residual stress in the tested film.

The force resolution when the 2 N load cell is used is $2mN$ so the stress resolution

for a typical sample in this case is 40 MPa. The displacement of the pushing tip is measured using DIC with a resolution between $0.0044 \ldots 0.22$ μm when images with a 400× magnification are used.

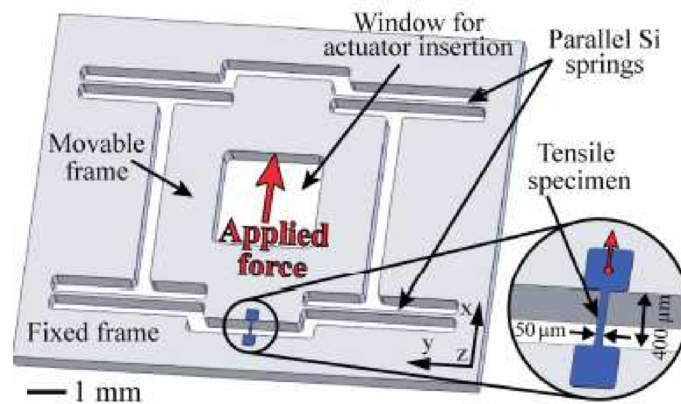

Figure 2.20: Schematics of IMTEK test structure courtesy of Dr Joao Gaspar.

A number of wafers were measured at IMTEK in Freiburg using the wafer scale micro tensile setup that has been developed there. This fully automated method allows the fast acquisition of load-elongation data from 26 samples processed on a single silicon substrate which are tested sequentially without removing them from the wafer. Performing the test at the wafer level also facilitates sample handling, thus rendering the method ideal for brittle material characterization.

In figure 2.20 an IMTEK test structure is schematically depicted. The micro tensile sample is bridging the gap between the inner moving Si frame and the outer fixed part of the structure which are connected by four suspension Si beams. The rectangular window in the movable frame is provided for the insertion of the actuator which is used for applying the load.

The wafer is attached on a vacuum chuck which is mounted on a special motorized $xy\theta$ stage. This stage enables accurate positioning and alignment of the 26

samples to the loading tip of the external actuator [39, 40]. This PZT actuator is equipped with a force sensor offering a $1mN$ force resolution. A programmable xyz actuation head is used for connecting the loading tip to the PZT actuator and enables positioning of the tip in the special actuation window provided in the test structures. A laser deflection sensor is used for the displacement measurements. The displacement resolution is 10 nm. For a typical sample with length 400 μm, width 50 μm and a thickness of $\approx$ 1 μm the achieved resolution in stress and strain measurements are 20 MPa and 0.0025% respectively.

2.2 Stress Elimination Scheme by the Removal of Pt Template Layer

A technique, for the elimination of the thermal stress in sol gel deposited ferroelectric stacks by the complete removal of the SiO_2 and the Pt under layers was proposed. The idea is to attach the wafer by its top face to a second wafer and to remove the initial substrate and the highly stressed films using dry etching techniques. At this point processing of the device structure can be resumed using low stress bottom electrode and structural layers.

The feasibility of this technique was investigated using 4” wafers containing the same Au/PZT/Pt/SiO_2 layer structure as described earlier. The main steps in the process are illustrated in figure 2.21. The attachment of the two wafers was carried out using a newly developed transfer bonding technique [98] the key features of which are the relatively low bonding temperature, the ability to bond any kind of wafer material, the high tolerance to 3D surface topographies and the wide range of polymers that can be used for the adhesive layer, including benzocyclobutene (BCB) [100] and photoresists such as SU8 and the mr-I 9000

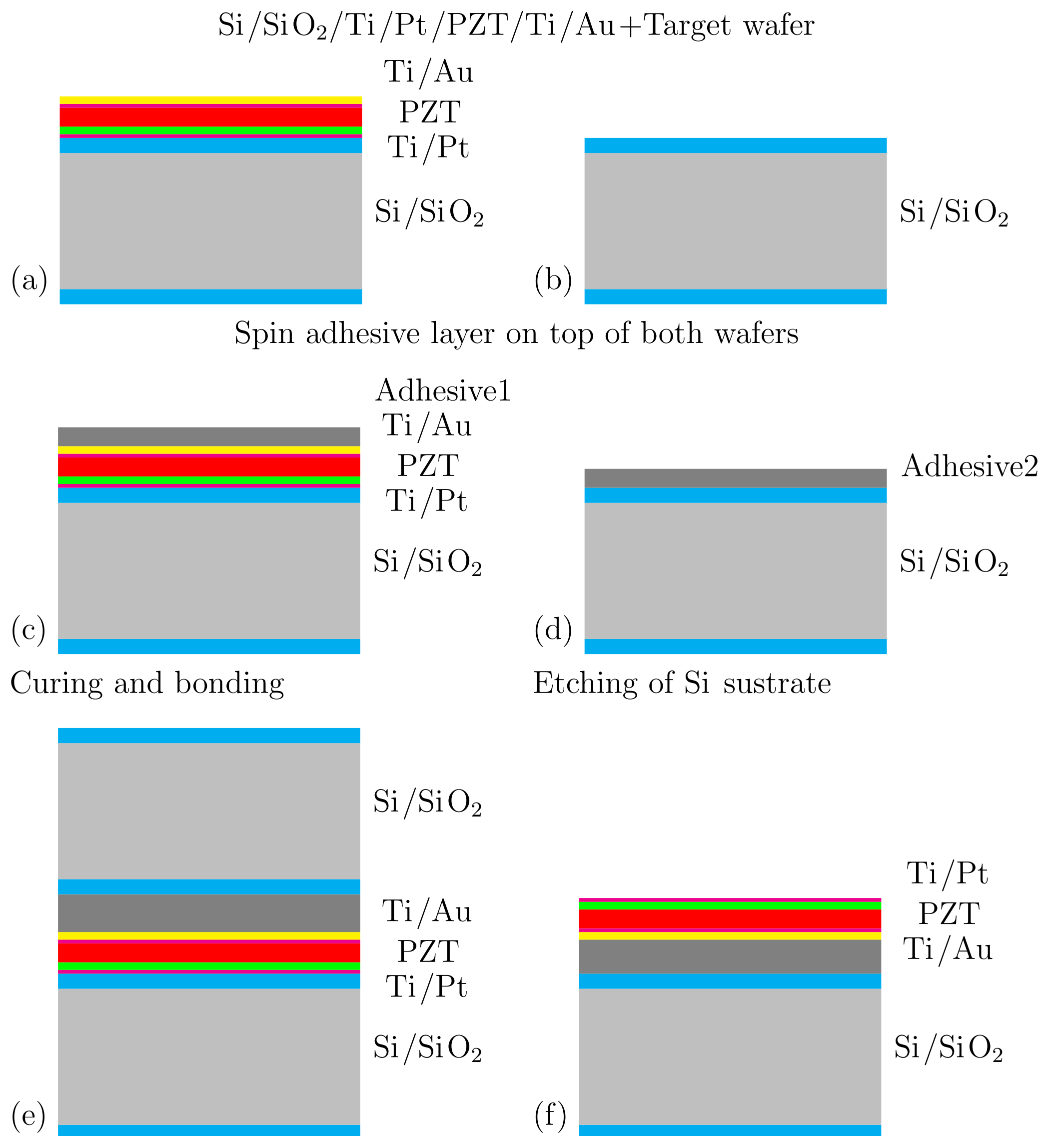

Figure 2.21: Stress elimination scheme based on adhesive wafer bonding.

nano-imprint series resist from Microresist Technology GmBH [108] used in the current work. The adhesive was spun onto the wafer (figure 2.21(c)) and also onto a second wafer (figure 2.21(d)) with spin speed adjusted to give a nominal thickness of 2.5 μm. Then, using a Karl Suss SB6 substrate bonding tool, the wafers were bonded together (figure 2.21(e)) at a chuck pressure of 4 bar and a curing temperature of 350 ^oC for 50 min [108].

2.2.1 Fabrication of stress free microcantilever

The released stack on top of the adhesive layer that resulted from the removal of the initial Si substrate in the DRIE (figure 2.21(f)), had the Ti/Pt electrode replaced by a 8 nm/100 nm thick Ti/Au film which was rf- sputter deposited. In figure 2.22 the process steps involved in device fabrication based on the stress elimination scheme are presented.

After having the Ti/Pt layer replaced by Ti/Au 2.22(a) the stacks are patterned using AZ 5214E negative resist and a low stress Ni film with a nominal thickness of 1 μm which is electroplated on top of them as figure 2.22(b) illustrates. Ni serves as the device new structural layer and at the same time it is used as the hard mask during the dry etching of the rest of the films in the RIE.

After completion of the RIE etch of the metal and the ceramic films the devices are released by etching the adhesive layer using high power O plasma etch in the DRIE. Monitoring the DRIE etch process closely is crucial in order to leave a sufficiently thick adhesive layer close to the beam anchor to serve as support for the released device.

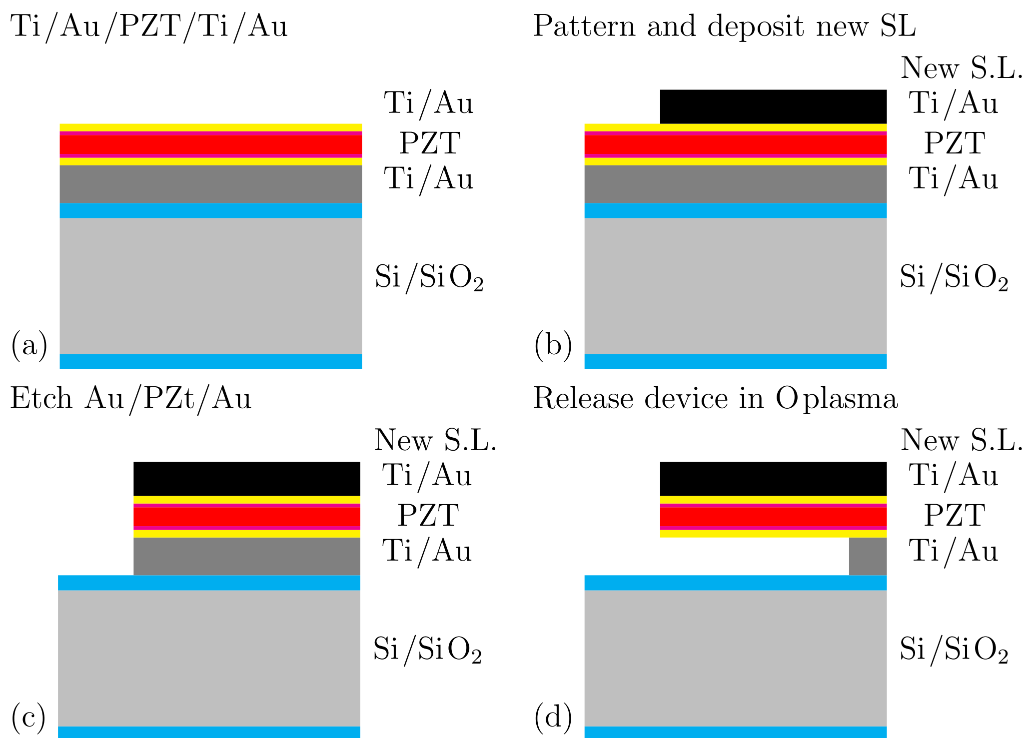

Figure 2.22: Design rules for fabrication of cantilever type device based on the stress elimination scheme. In (b) the new structural layer (Ni, SiN_x) is deposited on top of the back etched ferroelectric stack (a). The films are etched using the appropriate masking material (c) and the devices are finally released by etching the adhesive layer in high power isotropic O plasma (d)

.

2.3 Piezo MEMS Reliability Testing

2.3.1 Mask Design

A set of masks was designed and drawn using the Computer Aided Design Auto-Cad software suite for the purpose of device level reliability testing of piezo MEMS components. The mask set contained a total of five masks to produce a range of cantilever and bridge type devices that can be used for both static and dynamic characterization. PZT bimorph type devices may be fabricated using this mask set in conjuction with typical Si wafers, following the fabrication process that was specially developed for this purpose. The masks are described below in order of use:

1. Top Electrode, the mask for the top electrode of the structures was a dark field mask to be used with a positive resist.
2. PZT, the mask for the patterning of the PZT, was a light field mask used with a positive resist.
3. Bottom Electrode, the mask used to define the bottom electrode of the device. This was a light field mask to be used with a positive resist.
4. Front Etch, this mask was used to pattern both the oxide of the top of the wafer and the underlying Si of the device layer. The mask was also a dark field mask.
5. Back Etch, was the final mask which was used to pattern the back of the wafer. This mask is also a dark field mask.

Two different types of devices have been designed. Cantilever type beams for static tip deflection measurements and time resolved micro RAMAN dynamic

stress measurements and clamped- clamped bridge type devices for accelerating fatigue testing. The devices are attached on special frames which can be diced from the wafer so the structures can be individually tested.

Table 2.3: Geometry of F1-3 cantilevers and BBS1-8 bridge type PZT bimorphs.

Device type	Length (μm)	Width (μm)
F1	1400	340
F2	1600	270
F3	3000	250
BBS1-4	400	100
BBS5-8	450	50

The cantilever structures are named and numbered F1-3 while the naming convention for the bridge type devices is BBS1-8. The names are etched on the device die so the dies can be easily identified. In table 2.3 the dimensions of the different types of structures as they are defined in the CAD file are presented. The length of the BBS devices is the length of the transducer beam on the top. Both types of the BBS structures share a 1 mm long structural layer.

2.3.2 Fabrication Process

The micro cantilevers were fabricated using surface and bulk micro machining techniques on a Si on insulator (SOI) wafer. The thickness of the Si structural layer can be varied between $2 \ldots 10$ μm and it is covered with a 200 nm thick SiO_2 film which is primarily intended in preventing the Pt bottom electrode from interacting with Si. The thickness of the buried oxide, which serves as the etch

stop layer during the back etching of the Si in the DRIE was 1 μm (figure 2.23(a)). Thickness of both the buried and the surface oxide can be customized to the needs of a specific application.

The transducer element is a $Pb\,(Zr_xTi_{1-x})\,O_3$ (PZT) film deposited by sol gel deposition on top of a Ti/Pt thin layer, serving as the bottom electrode for the excitation of the PZT as well as the template layer for the proper perovskite phase crystallization. This 100 nm thick Pt film is RF magnetron sputtered at room temperature on top of an underlying 8 nm Ti adhesion layer. The ceramic is subsequently deposited by a sol-gel method: a spin and drying process which was repeated until the desired thickness which is measured using a DEKTAK surface profiler is reached (figure 2.23(b)).

Finally the Pt top electrode with a thin (8 nm) Ti adhesion layer is deposited by a lift-off bi-layer process, using LOR2A and S1818 to pre-pattern the top of the PZT (figure 2.23(c)).

The PZT, Pt and SiO_2 layers of the stack are successively dry etched using Reactive Ion Etching (RIE) and the cantilevers are finally released by dry etching the Si using Deep Reactive Ion Etching (DRIE), (figure 2.23(d), (e) and (f)). PZT is etched using a CHF_3/Ar/O mixture while for Si etch, SF_6 is used.

The process flow for fabricating PZT bimorph type devices using this mask set is slightly altered. Instead of SOI wafers, plain Si (100) oriented wafers are used as substrates. Following the process flow developed for the fabrication of the dog bone shaped samples a blanket Pt film is sputter deposited on top of the ceramic. This serves as the intermediate electrode of the bimorph structure and is also the template layer for the sol gel deposition of the second PZT film.

In figure 2.24 the process of building a double ferroelectric stack for the purpose of PZT bimorph fabrication is presented. The fabrication process follows the design

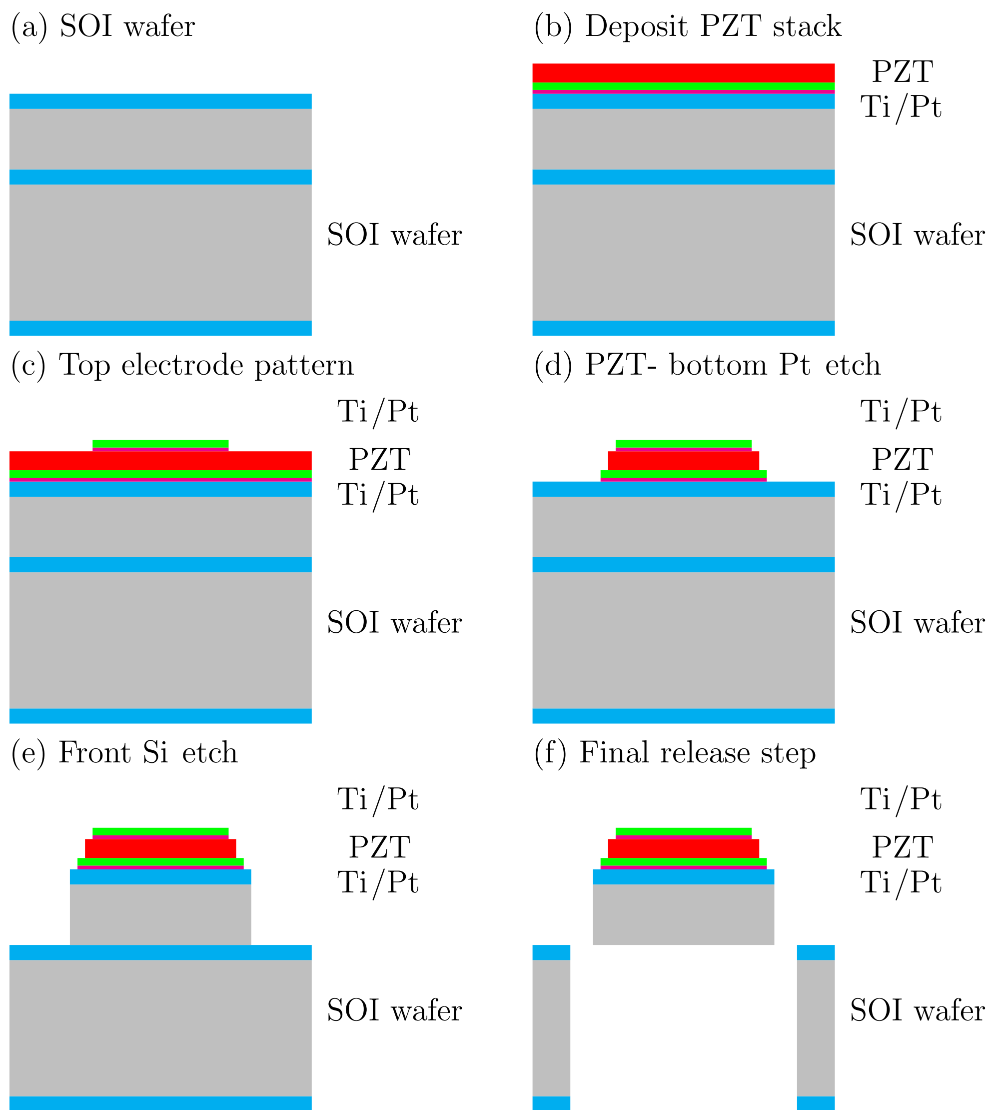

Figure 2.23: PZT stack deposition on SOI wafer (a) and (b). Top electrode deposition (c) and PZT, bottom electrode patterning and etching (d). Device layer etch (e) and final release (f).

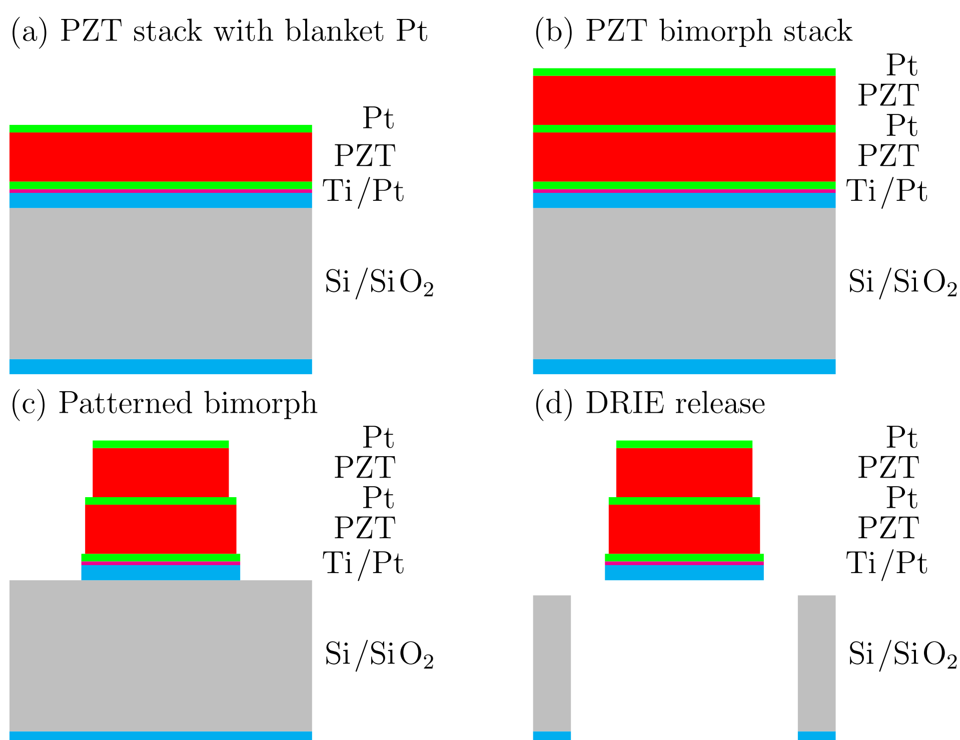

Figure 2.24: Fabrication process of the PZT bimoprhs. A second PZT stack is deposited by means of sol gel deposition on top of the initial stack (b). AZ-5214E negative resist is combined with the mask sets and electroplated Ni is used as the masking material for the dry etching (c). After the DRIE release (d) the $\mathrm{SiO_2}$ is RIE etched. The bottom Pt electrode can be etched as well.

rules depicted in figure 2.23 for the case of the cantilevers. In the bimorph case the top electrode is not deposited by a lift off process but is rf sputtered in a blanket form instead. The top electrode mask defines both the top electrode and the top PZT film so it is combined with a negative resist and a Ni hard masking layer is deposited by electrodeposition.

After the top Pt electrode and the top PZT layer are dry etched in the RIE, the Ni mask is wet etched using $FeCl_3$. The PZT mask is now used to pattern the mid Pt electrode which is also etched in the RIE. The wafer is then covered by a Ti-Auseed layer for Ni electro deposition and the bottom electrode mask combined with a negative resist are used to define the geometry of the lower stack.

After the Ni plating, the lower PZT film is dry etched in the RIE and the Ni and Au layers are removed by wet etching. The thin Ti film is then dry etched in the RIE and the front etch mask is used to define the geometry of the bimorph bottom electrode. The back etch in the DRIE is common in the two process flows.

After release of the bridge type structure the thermally grown SiO_2 layer is dry etched in the RIE. There is the option of etching further in the RIE and removing the Pt bottom electrode for the testing the mechanical fatigue of the ceramic.

2.3.3 Composite Piezoelectric Beam Model

Stoney's equation 1.2 can be used to caclulate the bow induced in a wafer by the residual stress in a film which is deposited on one of the wafer surfaces. The equation is only valid when the substrate thickness is much larger that the thickness of the deposited film. The analysis of Timoshenko for the static deflection of a bimetallic thermostat [135] is applicable in the case of beams with layers of comparable thickness.

More recently, analytical relations for multi layered composite media, comprising of either only elastic [136] or elastic and piezoelectric materials, were proposed [142, 25, 109]. The analysis used here generally followed the treatment by Pulskamp et al [109] which was based on the well known Bernoulli-Euler beam bending equation:

$$\underbrace{\frac{d^2y/dx^2}{\sqrt{\left(1+(dy/dx)^2\right)^3}}}_{\kappa} = \frac{M\,(x)}{EI} \tag{2.15}$$

In equation 2.15, y is the vertical deflection along the lognitudinal direction x of a composite beam, under conditions of pure bending. The incompatibility of strains that rise between adjacent layers during heat treatment due to differential thermal expansion, or the strains that rise in the case of composites comprising of piezoelectric and elastic layers result in moments $M\,(x)$ that act around the neutral axis of the beam. The term on the left gives the beam curvature κ and the denominator EI in the right term is the beam flexural rigidity.

Based on the assumptions of the theory of laminated composites a system of algebraic equations which connect the curvature κ and the strain ϵ_o of the beam neutral axis with the force F and the bending moment M induced in the layers of the composite are derived. In the 1-D case of a beam this system is simplified to:

$$\left\{ \begin{array}{c} F \\ M \end{array} \right\} = \left[\begin{array}{cc} (EA)_{tot} & (ES)_{tot} \\ (ES)_{tot} & (EI)_{tot} \end{array} \right] \left\{ \begin{array}{c} \epsilon_o \\ \kappa \end{array} \right\} \tag{2.16}$$

In equation 2.16 assuming that w is the beam width, z is the thickness direction and h the distance from the neutral axis or any other reference axis:

- $(EA)_{tot} = \int_{-h/2}^{h/2} w(z)\, E(z)\, dz$ is the composite extensional stiffness
- $(EI)_{tot} = \int_{-h/2}^{h/2} w(z)\, E(z)\, z^2 dz$ is the composite flexural stiffness
- $(ES)_{tot} = \int_{-h/2}^{h/2} w(z)\, E(z)\, zdz$ is a coupling stiffness term
- $F = \int_{-h/2}^{h/2} w(z)\, E(z)\, \epsilon(z)\, dz$ is the total force
- $M = \int_{-h/2}^{h/2} w(z)\, E(z)\, \epsilon(z)\, zdz$ is the total bending moment

If it is further assumed that the layers have uniform properties and all the calculations are performed with respect to the neutral axis of the beam the integrals are greatly simplified to summations over the thickness of the individual layers.

In the Appendix A-1 the MATLAB m file that was used for the implementation of the model is presented. The m file calculates the vertical deflection as a function of the distance along the beam, under the action of the bending moment due to the residual stresses in the films comprising the beam. The mechanical properties and the dimensions of the films are the input parameters of the model. The composite Young's modulus and moment of inertia with respect to the beam's width are calculated as well as the position of the beam's neutral axis. In both cases the elastic properties of the films were assumed to be constant and equal to their bulk values while stress gradients in the films were assumed negligible. The equation is solved numerically using a Runge-Kutta method of fourth order accuracy.

The Appendix A-2 contains the modifications one has to introduce in the composite model to account for the strains generated by the piezoelectric layer. In both cases the simplified ordinary differential equation resulting from the definition of the curvature when the displacements are assumed small, is analytically integrated.

All calculations are performed with respect to the position of the beam neutral axis. The resulting strain ϵ_o should thus always be equal to zero. This is another way to cross check the validity of the calculation.

2.3.4 Device Modelling

The starting point for this analysis is the model of composite structures derived previously. In this case the force and moment used as inputs in the final matrix equation result from the change in the dimensions of the constrained piezoelectric layer due to the converse piezoelectric effect. In the appendix A-2 the necessary modifications in the initial code of the MATLAB model are presented. The beam dimensions are those of the tested F1 sample.

The non piezoelectric materials were assumed homogeneous with mechanical properties presented in table 2.4. These were taken from [1]. For the piezo electric film the properties of PZ23 material taken from Ferroperm catalogue (Appendix C-1) were used.

A 2-D model of the multi layered piezo actuated F1 type beam was also developed using ANSYS FEA commercial package. The code is presented in Appendix A-4. Coupled field 4 node 2-D PLANE13 elements with the plane strain option activated, were used to model the piezoelectric film. For the rest of the layers the 4 node 2-D PLANE182 structural solid elements with the plane stress option selected, were chosen. The material properties of these layers were those of table 2.4. The elements of the stiffness matrix for the ferroelectric film were derived from the plane stress modulus of the PZ23 ceramic (see App A-4 material properties section). The e_{ij} parameters were also calculated in this case from the d_{ik}, c_{kj} coefficients.

Table 2.4: Material properties of the non piezo electric layers used in device modeling. For the piezo electric film the properties of PZ23 ceramic from Ferroperm catalogue were used.

Layer	Young's modulus GPa	Poisson's ratio	Density gr/m^{-3}
Si	155.00	0.230	2.330
SiO_2	78.36	0.170	2.201
Ti	119.70	0.310	4.480
Pt	167.40	0.303	21.400

The analysis was also performed using quadratic elements. In this case the 8-node PLANE223 coupled field elements were used to simulate the piezoelectric film while the 8-node PLANE183 elements were used for the elastic layers.

In figure 2.25 the tip deflections predicted from the analytical and the ANSYS numerical model are plotted as a function of the applied voltage. Both the results of the linear and the non linear analysis are depicted. The linear solution of both finite element models were in good agreement with the results anticipated from the analytical problem. Results of the non linear ANSYS analysis on the other hand varied depending on the types of elements used. The linear solution of the FEM for the static tip deflection to be expected when 5 $Volts$ are applied at the ferroelectric film is 21.8 μm (figure 2.26).

For the harmonic analysis a three dimensional model of the beam was developed. The batch file is presented in Appendix A-3. The 3-D finite element model takes into account finite size effects which are either related to the device design, like the 5 μm inset between the adjacent layers, or arise during the fabrication process,

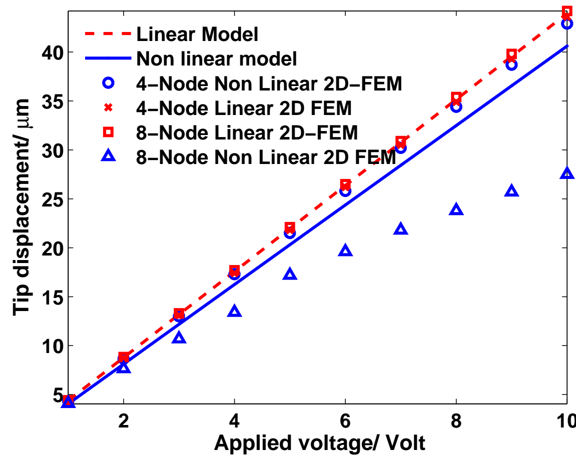

Figure 2.25: Tip deflection of a 1400 μm long piezo actuated cantilever Si beam as a function of the applied field calculated by different models. Thickness of the Si structural layer is $10\mu m$

like the over etching of the beam anchor. In this analysis the coupled field 8 node SOLID5 elements were employed for modeling the piezoelectric layer. The non piezoelectric films were modeled using either the SOLID45 or the more advanced SOLSH190 elements which are better suited for simulating thin film structures. The geometric symmetry of the beam around the longitudinal axis is taken into account to reduce the model dimensions and save CPU time.

Convergence of the solution in this case was checked by altering the mesh size and by using two different types of elements for modelling the structural layer. Results from using the 8 node continuous structural elements SOLID45 and SOLSH190 with a meshsize equal to 10 μm were identical. Refinigng the mesh further did not alter the calculated displacements. The continuity of the un averaged stress field in the deformed structure was also checked and no abrupt changes were found. The linear solution is slightly lower than the one predicted from the 2-D analysis,

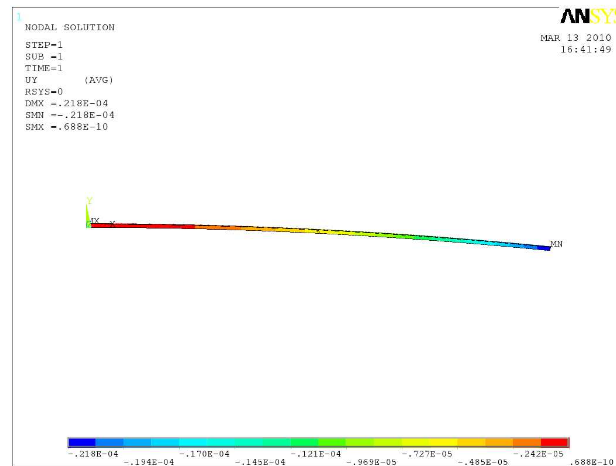

Figure 2.26: Static tip deflection of a multilayered piezo activated cantilever derived from ANSYS 2D non linear finite element analysis. The applied voltage is 5 $Volts$.

a result to be expected in the 3-D case due to the stress stiffening effect which arises from the piezoelectric strain in the transverse axis. The same applies to the non linear solution of the 3-D model which is slightly lower than 17 μm as figure 2.27 depicts.

A model of the PZT bridge type bimorph device was then derived from the multimorph 3-D model by substituting the Si structural layer by a PZT layer of 1 μm thickness and by eliminating the thermal oxide. This model is a simplified version of the model of the micro cantilever which takes advantage of the structure symmetry along both the transverse and the lognitudinal axis. The three dimensional, four node, linear SOLID5 elements with the couple field analysis capability were used to simulate the PZT layers. The Pt thin layers were modelled by the linear SHELL181 elements.

In table 2.5 the first four results of the modal analysis performed using ANSYS

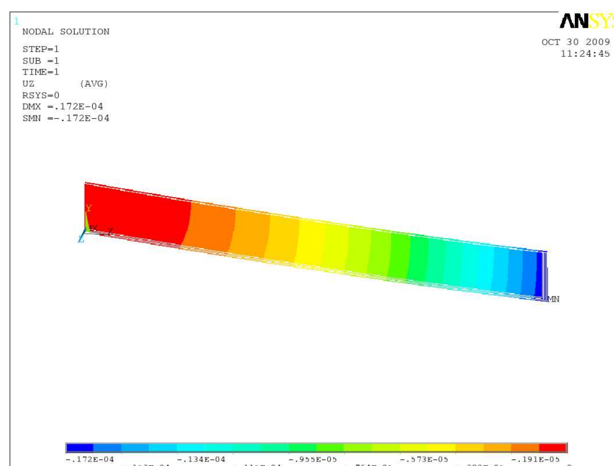

Figure 2.27: Static tip deflection of a multilayered piezo activated cantilever derived from . The applied voltage is 5 $Volts$.

in the frequency range $1 \ldots 200\ kHz$ as they are calculated for the different types of cantilevers and bridge type structures are presented.

Harmonic analysis was also performed and the dynamic stress maps of the vibrating bridge type bimorphs were obtained under conditions of resonance. Interest was focused on the first modal shape of the bimoprh beams and on the dynamic stress that is expected to rise in the lower structural PZT layer. The amplitude of the applied sinusoidal voltage was limited to 2 $Volts$, low enough to ensure that domain switching will not occur and thus the piezoelectric response of the PZT transducer will be linear.

In figure 2.28 the first modal shape of a BBS1-4 type device modelled using ANSYS is depicted. The results of the harmonic analysis for the BBS5-8 devices are presented in 2.29. The maximum deflection is 140 μm for the former and 136 μm for the latter.

Table 2.5: The first four resonant frequencies of the piezoactuated cantilever devices and of the bridge type bimorphs used for dynamic measurements, as they were calculated using ANSYS FEA for the frequency range $1 \ldots 200\ kHz$. The properties of the PZT film were taken from FERROPERM catalogue (material PZ24).

PZT type	1st (kHz)	2nd (kHz)	3rd (kHz)	4th (kHz)
F1	6.067	37.989	106.560	145.700
F2	4.560	29.700	82.378	162.120
F3	1.202	7.258	23.128	36.810
BBS1	7.927	42.557	99.879	170.640
BBS5	6.727	37.018	90.772	166.078

In figure 2.30 the deflection profile of a vibrating BBS1-4 bridge type PZT bimorph is plotted in blue. The maximum displacement is 140 μm and it is located in the middle of the beam. The red curve in 2.30 is the calculated stress intensity in the lower PZT surface as a function of the distance from the beam anchor. The maximum stress is close to 300 MPa and is located in the middle of the beam at a distance 500 μm away from the beam anchor. When a sinusoidal field with a frequency equal to the first resonant frequency of the device is applied on the top PZT element the stress in the lower layer fluctuates between the maximum tensile and compressive value. By controlling the amplitude of the applied signal the maximum stress that rise in the lower PZT layer is controlled.

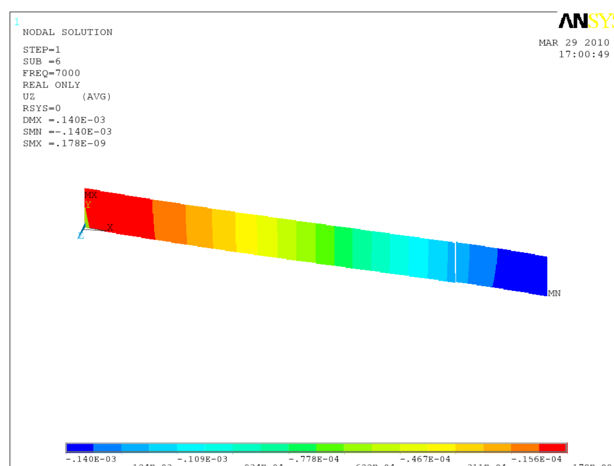

Figure 2.28: First modal shape of a BBS1-4 type device respectively calculated using ANSYS 3D linear finite element analysis. The applied voltage is $2\ Volts$.

2.3.5 Laser Doppler Vibrometer

The resonant frequencies and the modal shapes of the vibrating devices can be experimentally measured using laser Doppler vibrometry. This is an optical, non contact, non destructive method that enables velocity and out of plane displacement measurements of periodic motion with high spatial resolution in a wide range of frequencies [18]. In figure 2.31 the scanning vibrometer set up that was used for these measurements is depicted.

The system is a Polytech Microscope Scanning Vibrometer (MSV 300) which consists of:

- the scanner unit with the scanner head containing the interferometer
- the scanner unit controller

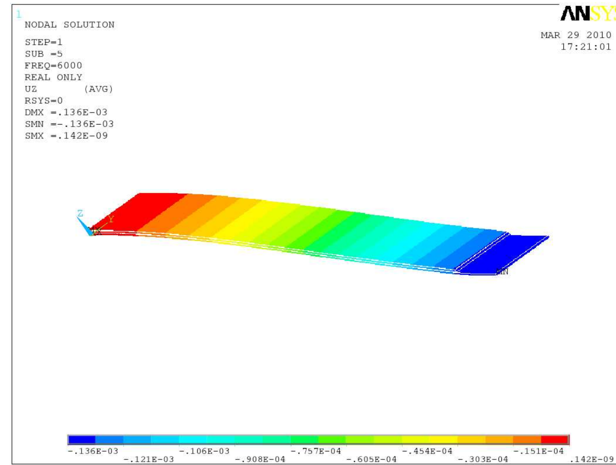

Figure 2.29: First modal shape of a BBS5-8 type device respectively calculated using ANSYS 3D linear finite element analysis. The applied voltage is $2\ Volts$.

- the vibrometer controller
- a workstation loaded with the appropriate software which is connected with all the units via GPIB interface

The scanner is connected to an optical microscope through a special microscope adapter. In this case an Olympus optical microscope equipped with four lenses of $\times 1.25$, $\times 5$, $\times 10$ and $\times 20$ magnification is used. Accuracy of the out of plane displacement measurements is within the pm range and the maximum area that can be scanned with the $\times 1.25$ lens is $320 \times 240\ \mu m^2$. The in plane spatial resolution is $1\ \mu m$.

The kit is also capable of accessing the planar vibrational characteristics of micro structures when the planar motion analyzer PMA-300 with the micro motion an-

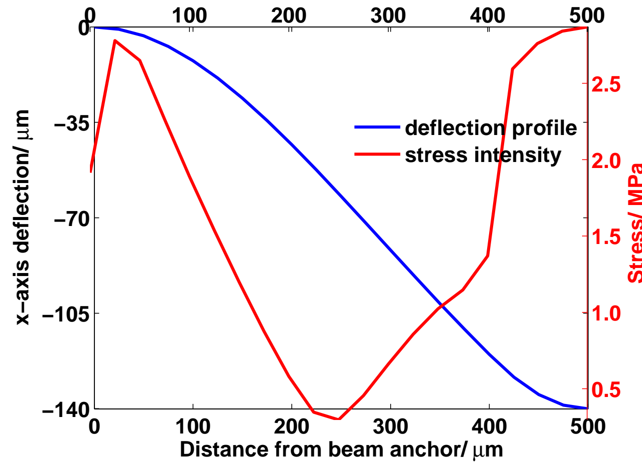

Figure 2.30: Maximum deflection profile of a BBS1-4 bridge type bimoprh at the first resonant frequency. In red the stress intensity profile in the lower PZT structural layer. Note the different y-axis.

alyzer MMA-300 module are used. This planar motion detection method is based on correlating digital images captured through stroboscopic video techniques.

A Hewlett Packard HP 33120A function/ arbitrary waveform generator with a maximum output amplitude of 9.9 $Volts$ is used for driving the measured devices.

2.3.6 Electric- Ferroelectric Characterization

The dielectric permittivity ϵ_d and the dielectric loss $\tan\delta$ of the ferroelectric films are measured using a Weyne Kerr precision component analyser model 6425 depicted in figure 2.32.

The component analyzer is capable of performing impedance, phase angle, inductance, capacitance, DC and AC resistance, quality factor, dissipation factor and

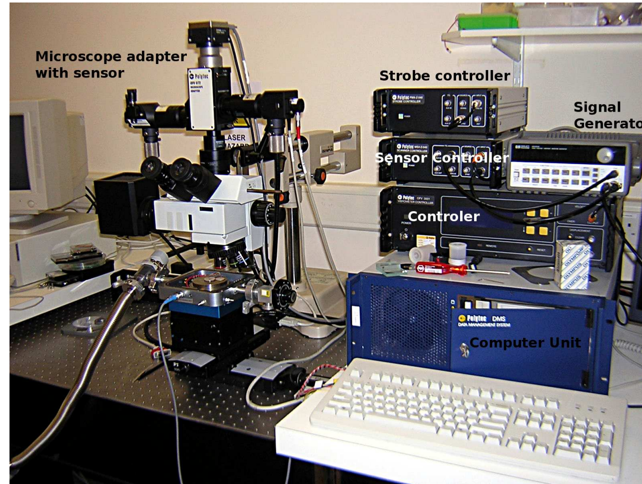

Figure 2.31: PSV Polytec Laser Doppler Vibrometer set up.

admittance measurements in the frequency range up to 300 kHz. The driving voltage used in this study had a fixed amplitude $V_{ac} = 100\ mVolts$ and samples were characterized at 10 kHz, 100 kHz, 200 kHz and 300 kHz.

The dielectric permittivity/ constant of the film is derived from the capacitance of the ferroelectric capacitor which in the case of a MEMS device is formed between the bottom and top metal layers. On unpatterned ferroelectric films deposited on Pt the capacitors are formed by depositing a Cr-Au top electrode in the form of dots with a diameter $d \approx 0.75\ mm$. The thickness of this Au layer is $\approx 100\ nm$. The Cr layer only serves as an adhesion promoter so it does not need to be thicker than 10 nm. These are deposited either by rf sputtering or by evaporation. Access to the Pt bottom electrode in this case is gained by partially etching the PZT film using wet etching in buffered HF. The etched step is measured in DEKTAK surface profiler and the thickness l of the film is thus derived.

The dielectric constant of the film ϵ_f is then calculated from the measured capacitance C, assuming an ideal capacitor, according to the equation:

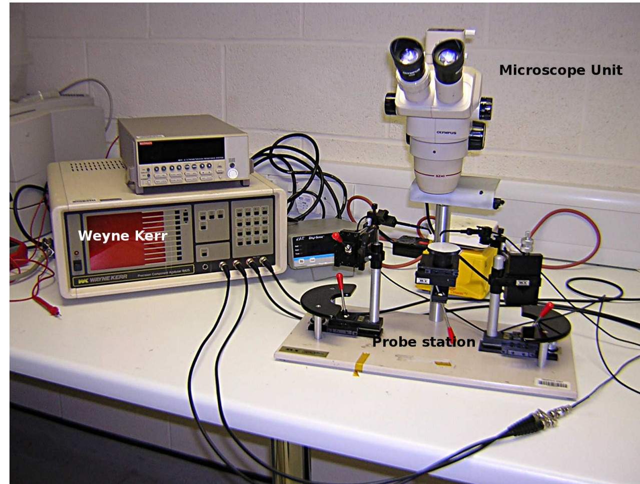

Figure 2.32: Weyne Kerr precision component analyser model 6425 with probe station and optical microscope.

$$\epsilon_f = \frac{4Cl}{\epsilon_0 \pi d^2} \tag{2.17}$$

In equation 2.17 $\epsilon_0 = 8.854 \times 10^{-12}\ F/m$ is the vacuum permitivity, d the diameter of the top electrode and l the film thickness. The AC ripple voltage can be superimposed on an externally applied DC voltage and measurements under conditions of constant bias can be obtained.

The polarization hysteresis of the ferroelectric capacitors is measured using the precision tester RT66A by Radiant technologies depicted in figure 2.33. The tester is also capable of measuring the remanent polarization curve, the leakage current and the small signal capacitance of a ferroelectric capacitor as a function of the applied voltage. The frequency, shape and polarity characteristics of the driving pulse are all user defined. For these tests a bipolar square pulse was chosen.

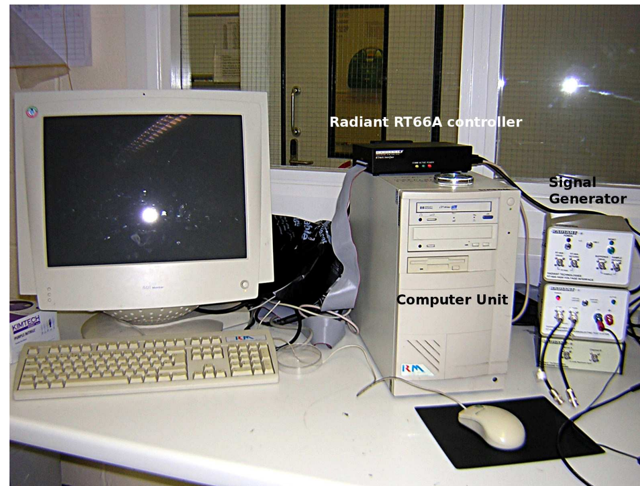

Figure 2.33: Radiant RT66A set up for ferroelectric characterization.

The period of the driving signal is 10 ms and the amplitude was varied between $15 \ldots 19$ $Volts$.

The maximum amplitude of the driving signal is limited to 19 $Volts$ unless an external amplifier, not shown in 2.33 is used. The tested samples were connected to the tester via the probe station with the integrated optical microscope shown in 2.32.

PZT films are contact poled by applying a DC voltage for 10 min at an elevated temperature. A hotplate is set at 130 ^oC and the film or the device to be poled is positioned on the hotplate surface. The probe station is connected to a DC voltage generator and a DC voltage between $10 \ldots 20$ $Volts$ is applied on the film for 10 min.

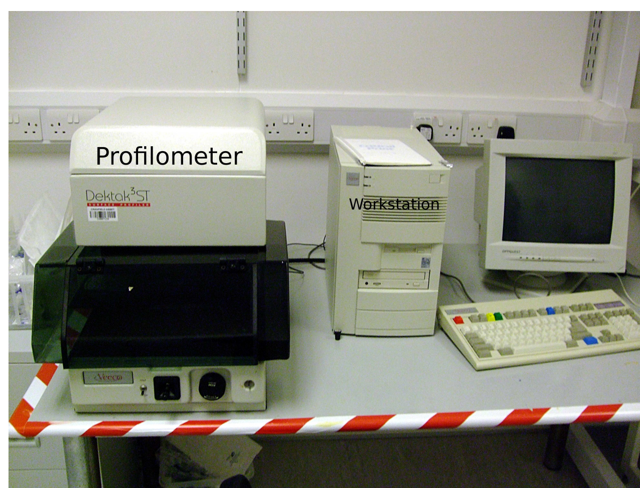

Figure 2.34: Veeco DEKTAT surface profilometer.

2.3.7 Stress Measurements

A Veeco DEKTAK surface profilometer shown in figure 2.34 was used for the wafer curvature measurements. The contact force of the profilometer stylus and the length of the performed scan are configured by the user. For these measurements the stylus force was set at 30 mg and the scan length at 50000 μm the maximum available option.

A special, Al made, jig is affixed to the stage of the profilometer to ensure that the scan is along the same path each time the wafer is measured. The jig is designed to accomodate both 50 mm and 100 mm wafers. Prior to the measurement process the stylus of the Dektak is aligned with the aligning hole provided on the base plate figure 2.35. The wafer to be measured is then placed on the three contact points provided by ball bearings figure 2.35. The wafer is then pushed into contact with the posts and the flats aligned to the reference groove figure 2.35 at the back of the holder. When the wafer is repeatedly measured after processing it is ensured that the difference between the scanned paths is negligible.

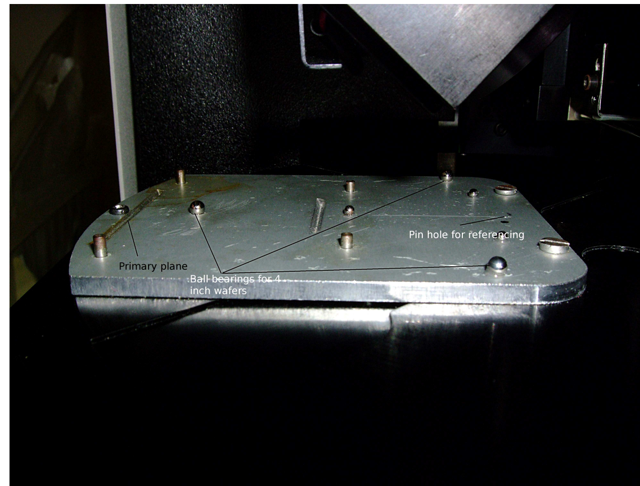

Figure 2.35: The Al made jig used for keeping the wafers leveled during curvature measurements. The pin hole and the groove used for referencing are labelled. The ball bearings where the 100 mm wafers are placed are also illustrated

A Renishaw inVia Raman spectrometer in the $z\,(x-)\,z$ backscattering geometry was used for the RAMAN spectroscopy measurements. The long axis of the cantilever was aligned to the x direction. Laser pulses were generated by modulating the output of a diode pumped solid state 532 nm laser source. With this set up well defined pulses of variable width and delay times can be generated. For these measurements laser pulse lengths were set between $1.3 - 16$ μs and duty cycles of 5-10% were used. These parameters are expected to extend the temporal resolution limit, allowing measurements of higher frequency devices.

The laser is focused through a 50 0.55NA objective lens on the back of the exposed (100) Si backside (figure 2.36) for a short time during each voltage cycle. During this time the scattered light is collected through the same objective and is analyzed. By controlling the time delay between the cantilever driving voltage and optical pulses the entire duty cycle is sweeped. The achieved lateral spatial

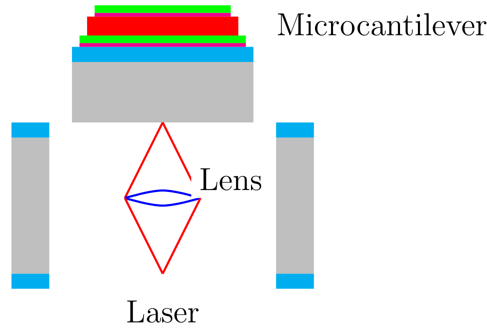

Figure 2.36: Schematic of the microcantilever and the objective lens set up used for the dynamic stress measurements.

resolution is ≈ 0.50.7 μm. The Raman scattered light is collected from a depth of 0.5 μm and the power density of the incident on the sample light was kept below $0.1 mW/\mu m^2$ to prevent heating. The devices were mounted on a computer controlled XYZ stage with 0.1 μm step precision.

Chapter 3

Tensile Testing

3.1 First Mask Set

The first mask set was used for PZT, Ni and Liquid Crystal Polymer testing. Defining the sample dimensions with accuracy is a major concern when miniature testing is performed. Micro fabrication processes offer limited control on the definition of the sample dimensions. A 10% variation in the thickness of the deposited films is normally expected. Etched surfaces on the other hand, are never perfectly vertical and smooth and a rough topography often with considerable inclination relative to the wafer top surface, is encountered. Test results can be seriously compromised due to these limiting factors. To address this issue the thickness of each sample was individually measured using a DEKTAK surface profiler. During this characterization step, the inclination of the sample side walls was also checked to make sure they remain vertical to the wafer surface.

3.1.1 PZT Testing

PZT films with 30/70 and 52/48 compositions were deposited by sol- gel on twelve platinized wafers with thicknesses ranging from 600 nm up to 1.1 μm. The ceramic

was etched in buffered HF solution and a 10% variation in thickness between samples of the same wafer was confirmed.

The wafers were then prepared for the DRIE Si etch step. The supporting Si rectangular frames were defined at the back of the wafers using a 13 μm thick photoresist layer as the masking material. Initially no backing wafer was introduced between the etched wafers and the He cooled chuck in the DRIE chamber. That way the wafers are more effectively cooled.

The process was closely monitored and the etched depth was frequently measured until 300 μm of Si were removed. The wafers were then removed from the DRIE chamber and they were attached on a backing wafer. For the initial tests a thin layer of photoresist was spun on top of both the sample and the backing wafer which would then be kept in contact on top of a hotplate until a firm bond was established. The DRIE process was then resumed.

Finally the SiO_2 and the Pt underlayers were etched in the RIE. The backing wafer was then removed by leaving the samples overnight in an acetone bath to dissolve the adhesive resist layer. It was observed that the yield of successfully fabricated dog bone shaped samples was high however one should be extremely cautious in removing the processed wafer from the acetone beaker as slight vibrations could cause sample fracture. The processed samples were then given a high power O plasma clean to remove any resist residue from the top. This residue was formed from the resist surface which was exposed to the plasma chemistry during the Si DRIE etch and had become insoluble to acetone. Some of the samples broke during loading in the DRIE chamber for this cleaning step probaly due to vibrations caused by the high vacuum pumps.

Finally the Si frames were diced from the wafers and the samples were ready for testing. Some samples broke during dicing however the most tricky step of all

was the cutting of the Si supporting beams after having mounted and secured the frames on the tensile stage with the horizontal jaws. The stiffness of the Si suspension beams was identified as a potential problem because a high force was applied in order to cut them causing a severe vibration of the frame.

More wafers were prepared and the tests were repeated. The acetone release and the high power O plasma clean steps were eliminated by simply attaching the sample wafers on the backing wafers using three tiny drops of resist or in some cases no resist at all. That way more samples were released for testing. At the same time the thickness of the suspension beams was halved making cutting them easier. The results were once again disappointing with the samples fracturing when the suspension beams were cut.

Sample fracture also occured when focused ion beam (FIB) was employed for cutting the Si suspension beams. Possible misalignement of the stage jaws due to poor manufacturing tolerances lead to the samples being overloaded and fail prematurely when released.

It is known that metal films have been successfully measured using this type of sample layout so a composite structure, where the metal films under the ceramic were preserved, was fabricated. Finally one large dog-bone shaped structure was successfully released after mounting on the stage jaws and testing in the SEM was performed (figure 3.1).

Initial check using SEM imaging revealed a defect close to one of the alignment marks. This defect which is clearly shown in 3.2 was expected to coincide with the initiation point of the final fracture crack. The sample though fractured almost immediately after the tensile load was applied, at a point outside the defined gauge length. The exact fracture point is also shown in 3.2 while in the inset figure the crack profile is shown under higher magnification.

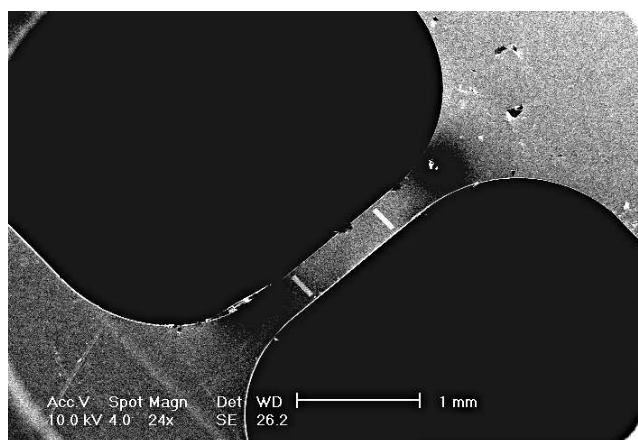

Figure 3.1: SEM micrograph of a released composite Pt/PZT sample fabricated using the first mask set in the SEM chamber.

Following this observation it was decided to try even thicker films so three wafers were prepared: two with PZT films with thickness 2 μm and 2.4 μm respectively and one with a 3 μm thick ZnO ceramic.

These trials were also unsuccessful and so a different route was followed. Si beams with a thickness of 30 μm: comparable to the supporting beam thickness, were prepared to investigate the feasibility of this type of testing using the specific stage. At the same time the DIC strain measurement method would be tested and validated and any problems associated with poor alignment of the sample to the applied load would be identified as Si was not expected to break during testing.

Releasing these thick silicon dog bone shaped structures was indeed successful and in figure 3.3 a released silicon beam in the chamber is shown. Measuring lines are introduced to define the region of interest.

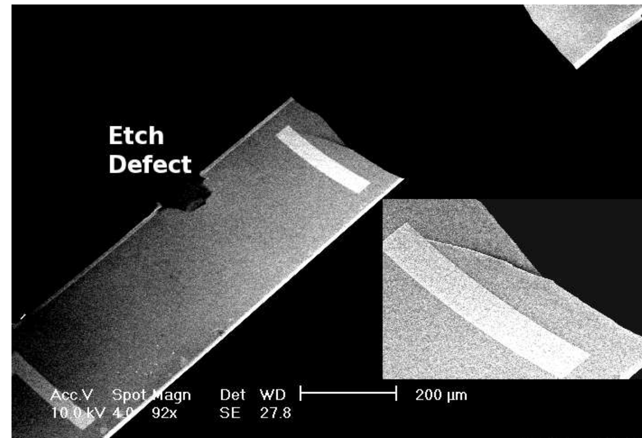

Figure 3.2: SEM micrograph of the tested sample. In the inset the cracked beam is shown under higher magnification.

3.1.2 Electro Plated Ni Testing

Our next test was performed on Ni films prepared by electro plating. The thickness of the fabricated Ni samples was 1.5 μm. In figure 3.4 the initial unstrained image of one Ni sample is shown. The sample is covered by a thin layer of resist which was meant to keep the wafer bonded on the backing wafer during the Si etch in the DRIE chamber. After the SiO_2 and the Pt films were etched in the RIE, the bonded wafers are left in acetone overnight where the resist dissolves. When the surface of the resist is exposed to the plasma species during etching, it gets hardened and it is not perfectly removed when acetone is used. High power O_2 plasma is known to be very effective in removing this hardened resist layer, loading these samples in the DRIE though caused them to break so it was decided to perform the measurement without removing it.

The results from testing one Ni dog bone shaped structurs that was successfully released are plotted in figure 3.5 (α). The strains were extracted using the DIC

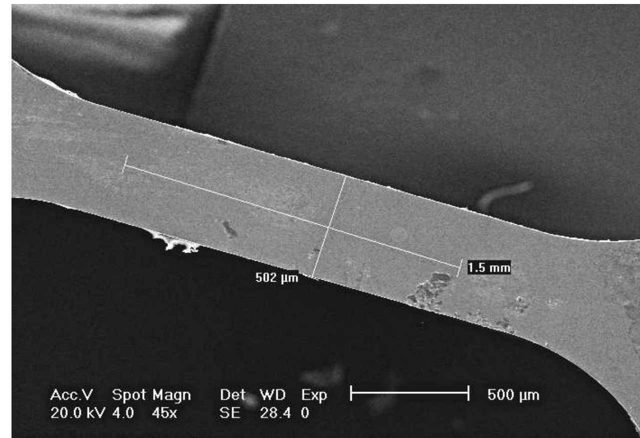

Figure 3.3: SEM micrograph of a dog bone Si structure. Silicon was used after the initial unsuccessful experiments with the ceramics in order to test the method with thicker samples.

optical method. A mean value of $E = (97 \pm 5)\, GPa$ was calculated for the Young's modulus of the tested Ni, from the inclination of the linear fit of the load vs strain curves in figure 3.5 (β). The transverse strain was also extracted and the Poisson's ratio was calculated equal to $\nu = 0.37$.

Previous work on the effect the electroplating conditions have on the grain structure and the mechanical properties of the Ni plated thin films, showed a strong dependence of the Young's modulus on both the current density and the bath temperature for a certain type of plating solution [79, 128, 62]. The samples in this work were fabricated using a solution made of 450 g/l nickel sulphamate and 30 g/l boric acid. The bath temperature was 50 ^oC and the current density 38 mA/Cm^2. The calculated Young's modulus is in good agreement with the results presented in [79, 128, 62], when similar deposition conditions were used.

In the foregoing analysis the Ni Young's modulus was derived from the applied

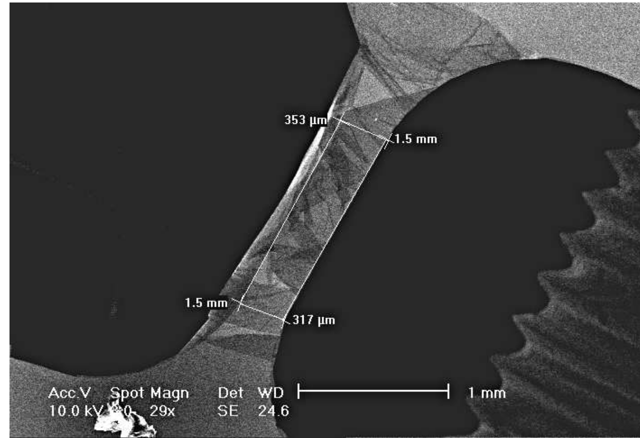

Figure 3.4: SEM micrograph of a Ni plated sample. Burnt resist residue still present.

stress σ and the measured strain ϵ using the simple equation $E = \sigma/\epsilon$. The applied stress was derived by dividing the applied force F with the width $w = 500\ \mu m$ and the thickness $t = 1.5\ \mu m$ of the sample. The uncertainty of the force measurement was $\delta F = 0.02\ N$. Assuming a relative uncertainty of 1% in thickness measurement $\delta t = 0.0015\ \mu m$ and a 1 μm uncertainty in the width measurements $\delta w = 1\ \mu m$ the uncertainty in the calculated stress σ is:

$$\delta\sigma = \sqrt{\frac{\delta \mathrm{F}^2}{t^2 w^2} + \frac{F^2 \delta \mathrm{t}^2}{t^4 w^2} + \frac{F^2 \delta \mathrm{w}^2}{t^2 w^4}} \tag{3.1}$$

For the maximum applied force $F \approx 0.7\ N$ the uncertainty in the applied stress $\delta\sigma$ from equation 3.1 is 28 MPa. The uncertainty in ϵ as discussed in chapter 2 is expected to range between $0.0014 \ldots 0.07\%$. Based on that the uncertainty δE in the calculated Young's modulus is:

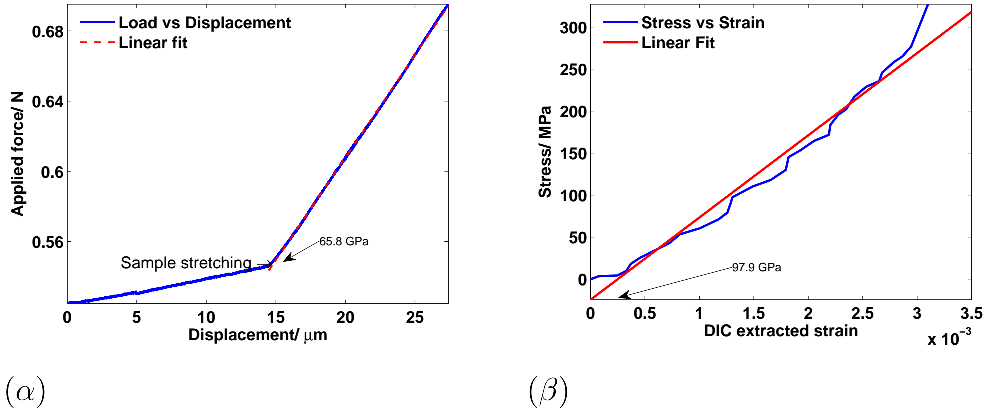

(α) (β)

Figure 3.5: Load vs displacement data (α) and Stress vs strain data (β) for the electro plated Ni samples. The strain data in (β) was extracted using digital image correlation techniques. From the inclination of the linear fitted line the young's modulus is evaluated.

$$\delta\epsilon = \sqrt{\frac{\delta\sigma^2}{\epsilon^2} + \frac{\delta\epsilon^2\sigma^2}{\epsilon^4}} \tag{3.2}$$

Equation 3.2 gives $8\ GPa \leq \delta E \leq 18\ GPa$ depending on the uncertainty $\delta\epsilon$ of the measured strains. The relative uncertainty $\delta E/E$ is thus rather high ranging between 8% and 19%.

3.1.3 LCP- LCP Au Composite Testing

Next tests were performed on liquid crystalline polymer (LCP) circuit material from Rogers corporation. The LCP films of the ULTRALAM 3000 family were

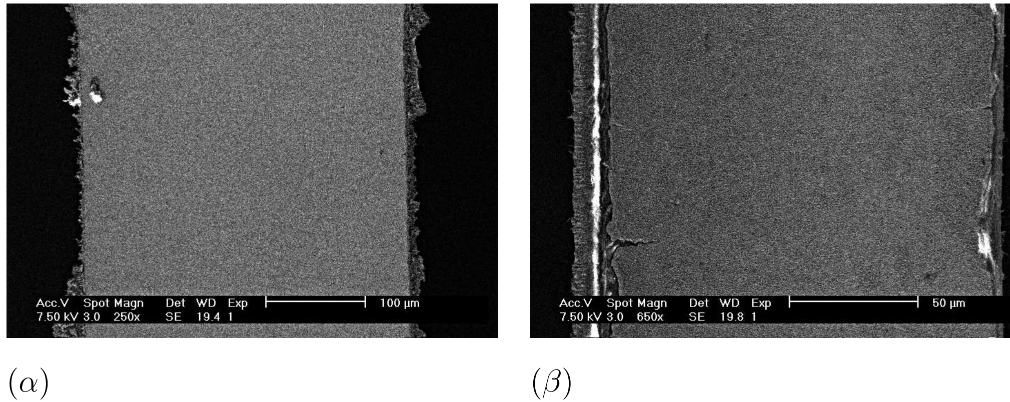

(α) (β)

Figure 3.6: SEM micrograph of the top surface of the LCP dog bone shaped structure (α) and the LCP-Au composite (β) samples.

developed for single layer and multilayer substrate constructions. These laminates come in the form of rectangular sheets covered with a thin layer of Cu [3].

The samples were fabricated by dry etching the 50 μm thick LCP in high power O plasma. The sample geometry was defined using AZ5214E negative resist and masked by a 1 μm thick sputtered Au film. The etch mask was wet etched in KI-I solution prior to sample testing (figure 3.6) (α) .

For the LCP-Au composites the Au film was not wet etched as figure 3.6 (β) depicts. In figures 3.7, 3.8 the load displacement graph and the resulting from the DIC analysis stress- strain curve are presented for the case of the LCP and the LCP-Au composite sample respectively.

Young's modulus for the LCP sample agrees well with the value reported by the manufacturer (2.25 GPa) [3]. The same applies to the composite structure if a simple model of two parallel connected springs is assumed to describe the response of the LCP-Au sample. This simple model is presented in detail for the PZT case

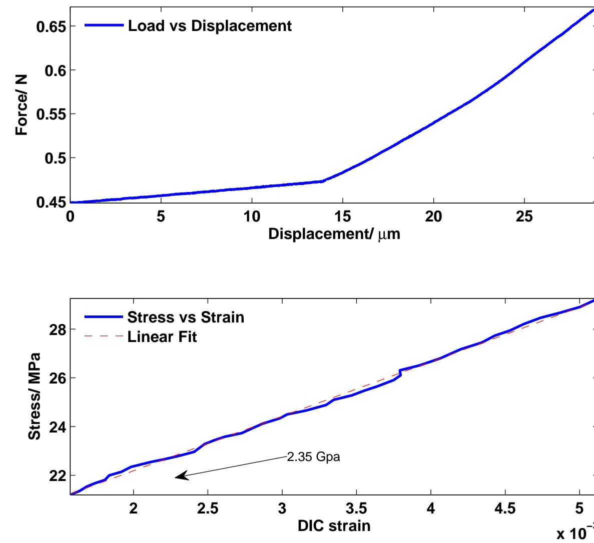

Figure 3.7: Load vs displacement (top) and Stress vs DIC extracted strain data (bottom) for the LCP samples. From the inclination of the linear fitted line the young's modulus is evaluated.

in equation 3.5. Following a similar analysis and assuming a Young's modulus of 70 GPa for the Au film, the composite modulus is found equal to 3.68 GPa close to the extracted value, even if further corrections due to sample bending are not accounted for.

The uncertainty of the method in extracting the Young's modulus of the LCP film is estimated by applying the same reasoning as in the case of the Ni film. The main difference in this case is the thickness $t = 50$ μm of the sample. From equation 3.1 the uncertainty in calulating the stress σ is estimated $\delta\sigma = 1$ MPa. Finally from 3.2 the uncertainty in the E calculation is derived for the range of uncertainties $0.0014\% \leq \delta\epsilon \leq 0.07\%$ in the measured strain. The relative uncertainty in the

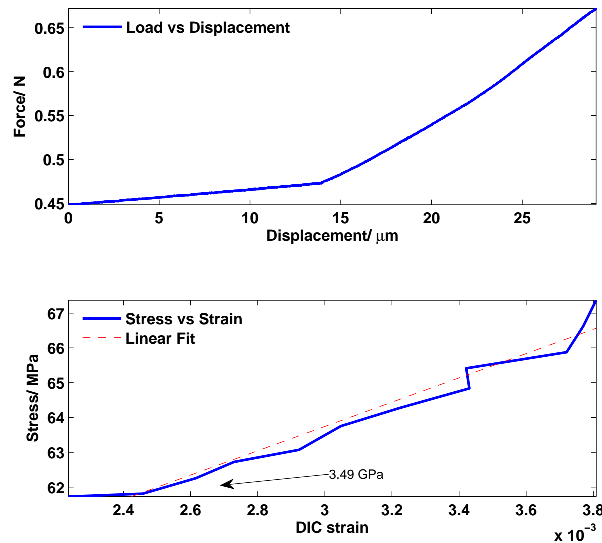

Figure 3.8: Load vs displacement (top) and Stress vs DIC extracted strain data (bottom) for the Au covered LCP samples. From the inclination of the linear fitted line the young's modulus is evaluated.

calculation of E was found to be between 10% :when the lowest uncertainty in the strain measurement is considered, and 50% when the strain uncertainty is high.

3.2 Second Mask Set

3.2.1 PZT Testing

Following the difficulties experienced during Ni testing, initial wafers processed using the second mask set were simply attached to the backing wafer for the DRIE etch step. Yield of structures after completion of this dry etch step was rather

high, but almost all devices broke when it was attempted to remove the oxide and Pt layers in the RIE. This was attributed to the way the RIE reactor pump is engaged, causing a severe vibration of the sample. The test was repeated with a new sample and this time it was attempted to control the pump out rate to avoid this shock vibration, however the yield of released structures did not improve.

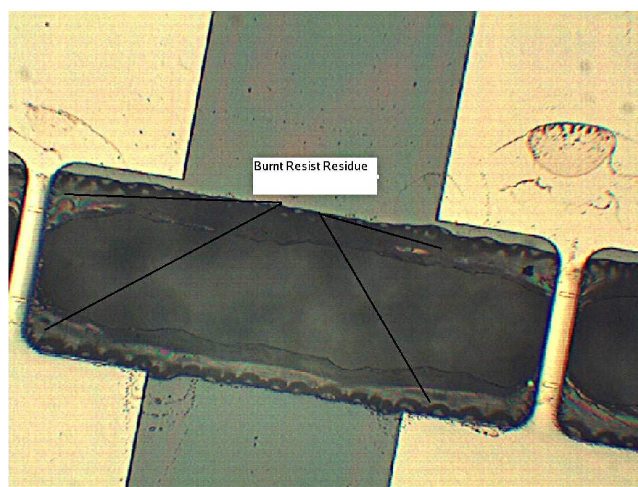

Figure 3.9: Released small dog bone shaped PZT structures on silicon frame. There is still a thin layer of hardened resist covering the devices.

Subsequent wafers were bonded on backing wafers using photoresist, a method used successfully with the larger samples. Use of resist improved the yield of devices but on the other hand removing the hardened resist from the top of the structures proved once again rather difficult. In figure 3.9, an optical micrograph of two released small samples is presented. The thin hardened resist layer is also clearly visible.

Attempts to etch this resist layer using high power O_2 plasma resulted in device failure, an outcome also encountered with the larger samples. Measuring the small samples with the thin resist layer on, using SEM imaging, showed that most of

the ceramic beams were already cracked and were kept in place by the polymer layer. On the other hand measuring these composite structures gave unusually high values for the applied strain.

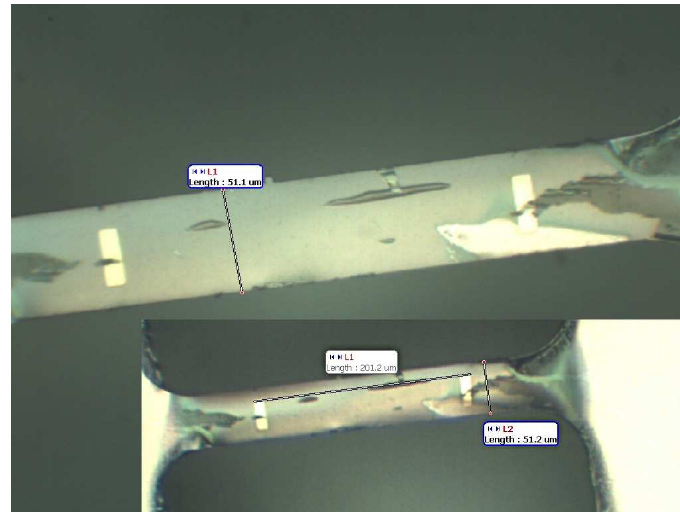

Figure 3.10: Optical micrograph of one of the PZT dog bone shaped samples that was successfully released using high O_2 DRIE plasma etching. In the inset a micrograph at smaller magnification is illustrated.

After several unsuccessful attempts, finally a Si frame containing two dog bone shaped PZT structures was fabricated. Following the process flow previously described, using a thin resist layer to protect the samples during the dry RIE etching many samples were finally released and a high power oxygen plasma was used for the removal of the burnt resist residue.

After one hour of etching in the high power oxygen plasma one frame with two samples on, was retrieved from the DRIE chamber. In figure 3.10, one of the PZT samples that were finally tested is shown. The resist was almost totally removed from the top surface of both these samples.

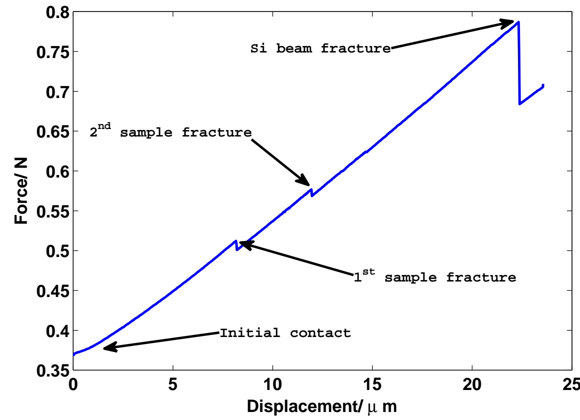

Figure 3.11: Experimental Load vs Displacement curve for the two tested PZT samples. The initial non linear part of the curve is due to the time needed for the pushing tip to come into firm contact with the moving frame. At sample fracture an abrupt fall is observed.

The stationary frame was mounted on the tensile stage and a compressive load was applied on the inner, moving frame until both samples failed. The monitored load versus displacement curve is shown in figure 3.11. The initial part of the curve is not linear due to the time needed for the establishment of contact between the load tip and the moving frame.

After this initial lag the load starts increasing linearly with the displacement of the piezo motor. Each time a sample breaks an abrupt fall is observed in the load curve due to the stiffness of the load cell. The stiffness of the moving frame- sample system is expected to decrease each time a sample breaks and this is realized by the change in the inclination of the load vs displacement curve.

From the change in the inclination of the load displacement curve the Young's modulus of the tested samples can be evaluated. Furthermore, the negative incli-

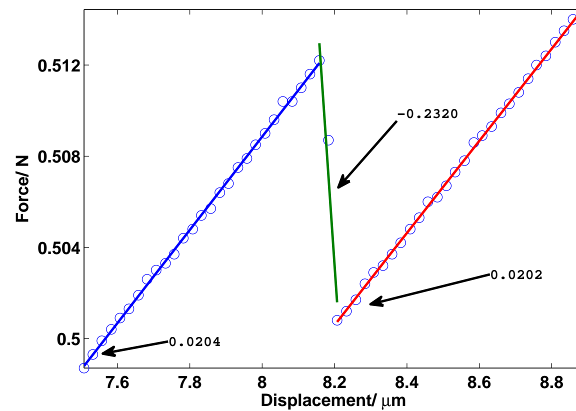

Figure 3.12: Detail of the load vs displacement curve in the region of the first sample fracture. Graphical evaluation of the sample Young's modulus from the change in the curve inclination.

nation of the small curve which connects the two parts of the load displacement curve before and after the fracture of a sample may be used for the evaluation of the load cell stiffness.

Finally the fracture strength of the sample is evaluated from the change in the applied load immediately after the sample fracture. To this end the vertical distance between the two curves, before and after the sample failure is plotted. The second part of the experimental curve is linearly fitted and extrapolated to the displacement value where the sample fracture occurs.

The regions of the load vs displacement curve that correspond to the fracture of the two samples are plotted in figures 3.12 and 3.14 respectively. The experimental points of the three parts of the curve were linearly fitted for the calculation of the curve inclination. The calculated values are truncated to the third decimal point and plotted on the graph.

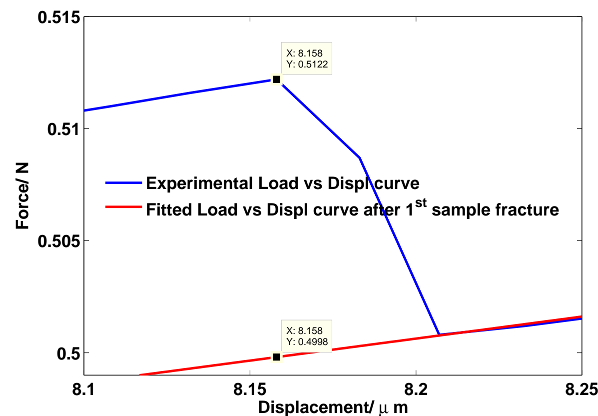

Figure 3.13: Graphical calculation of the fracture strength of the first sample from the load vs displacement curve.

In both cases a small decrease in the curve inclination after the fracture of the sample is monitored, which in the case of the second sample is very small. The negative inclination of the load cell loading curve which corresponds to the stiffness of the cell is not constant implying a non linear response during loading.

Based on the simplified theoretical analysis of the parallel connected springs, the Young's modulus for the first sample is evaluated from the graph equal to 27 GPa.

The fracture strength of the ceramic samples was also evaluated graphically. In figures 3.13 and 3.15 the regions of interest of the load versus displacement curve are plotted. The part of the curve after sample fracture is fitted linearly and extrapolated down to the displacement value which corresponds to the sample fracture, as the red line indicates. The vertical distance beatween the actual load where the fracture occurs and the extrapolated red curve is used for the evaluation of the fracture strength. The fracture strength values that were calculated for the two samples were 350 MPa and 270 MPa respectively.

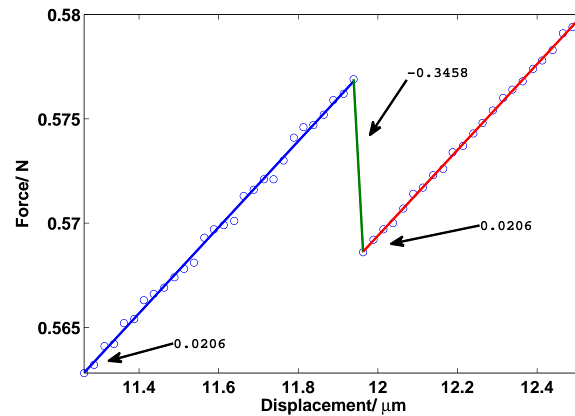

Figure 3.14: Detail of the load vs displacement curve in the region of the second sample fracture. Graphical evaluation of the Young's modulus of PZT from the change in the curve inclination.

SEM micrographs of the fractured samples are presented in figures 3.16 and 3.17. Both samples fractured at points close to the pads attached on the stationary Si frame. Due to the poor accuracy of the front to back mask alignment process, both samples were slightly displaced towards the moving frame. The pads attached on the stationary part of the frame were not in perfect contact with the frame surface and this exposed region which appears buckled in the image, is also loaded altering the stiffness of the tested sample. A finite element model was developed to account for this effect and will be discussed in detail.

In addition both the released samples were attached on the same side of the frame, so testing was performed under conditions of asymmetric loading. This is especially true for the sample positioned in the far outer side of the frame.

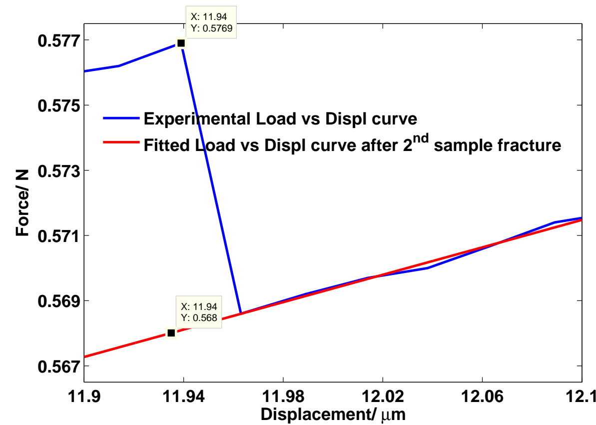

Figure 3.15: Graphical calculation of the fracture strength of the second sample from the load vs displacement curve.

3.2.2 Si **Frame Stiffness**

In the previous analysis the load cell stiffness was evaluated from the negative inclination of the load versus displacement curve of the piezoelectric motor in the sample fracture region. The stiffness of the frame was calculated theoretically based on the assumptions of Euler Bernoulli linear beam theory.

Three different measurements of the frame displacement were performed first in the back left supporting beam, then under the same magnification in the back right beam in order to identify possible misalignments in the application of the load. Finally the displacement in the point of the tip contact was measured at 800x magnification for increased accuracy.

Displacements were calculated using the digital image correlation method and were then combined with the applied force values measured by the tensile stage. The experimental data were fitted with a linear model and the stiffness of the

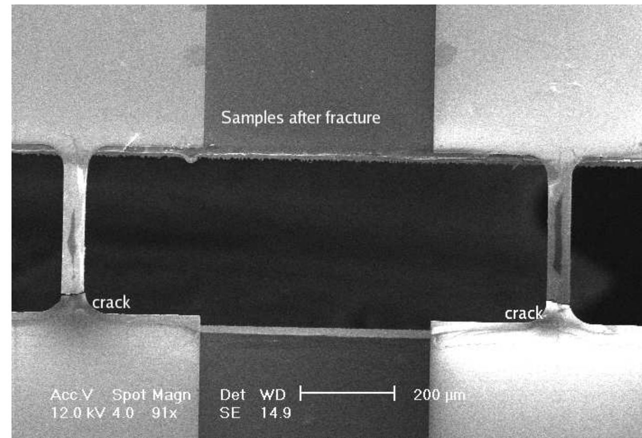

Figure 3.16: SEM micrograph of the fractured samples of PZT after testing. Both samples cracked at points close to the pad attached on the stationary frame. Part of the anchors is released and this results in non uniform loading of the suspended part.

frame was evaluated from the inclination of the curve.

Initially a rectangular grid of markers, covering the whole area of the unstrained beam was used. The new position of each marker is calculated during image correlation in each one of the successive images and finally the data for both the x and the y direction for each image are saved.

In figure 3.18 the position of the markers in the 18th image are plotted as a function of their initial position. Green dots show the projection of the displaced markers in the direction of the applied load. In total 19 images were captured during this test and the S- shaped form of the markers projection resembles the deformed shape to be expected for a beam with ends fixed on two parallel surfaces moving relative to each other.

The displacement values for the markers at the moving end of the beam: y-

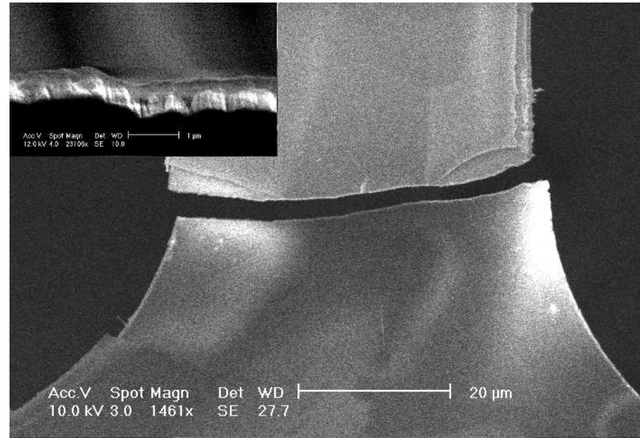

Figure 3.17: SEM micrograph of the cracked region in one of the tested samples. In the inset a cross section of the cracked area under higher magnification is presented. The crack appears transgranular.

position at 100 pixel in figure 3.18, were converted in μm and the applied force vs displacement curve for the moving frame is plotted in figure 3.19 (α).

A linear fit of the experimental values is also plotted in figure 3.19. From the inclination of the straight red line the stiffness of the frame in the direction of the applied load is calculated equal to 1.71×10^4 N/m and the corresponding stiffness of each supporting beam, assuming they are identical is 2.85×10^3 N/m.

Similar reasoning applied on the back right beam gives an equivalent spring constant of 2.67×10^3 N/m for the Si suspension beams. The experimental values are quite different from the 6.31×10^3 N/m value which was theoretically predicted for a beam of this geometry.

To increase the accuracy of the displacement measurement, images of the tip-frame contact point were captured at a much higher magnification. The resulting

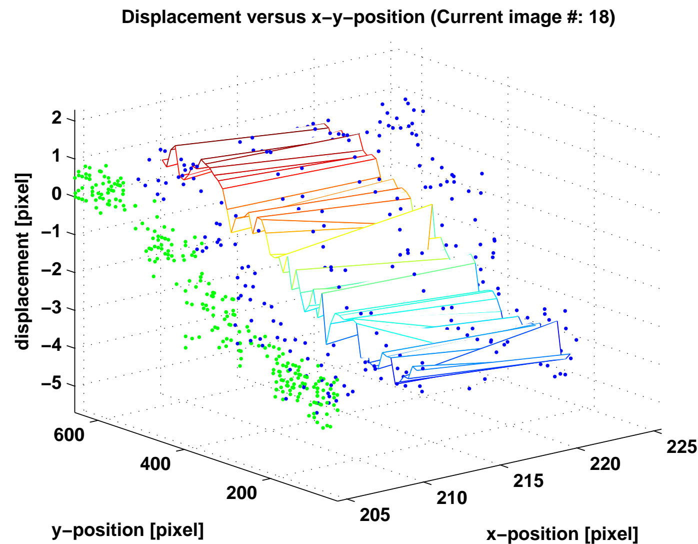

Figure 3.18: Marker displacement as a function of marker position. Green dots show the marker displacement in pixels in the y axis, parallel to the direction of the applied load.

load vs displacement curve is plotted in 3.20. Derivation of the beam stiffness from the inclination of the red line, yielded a value of $2.71 \times 10^3\ N/m$ consistent to the previously reported ones.

The discrepancy between the theoretically predicted and the experimentally obtained stiffness value was further investigated using SEM imaging (figure 3.21) to determine whether the actual geometry of the fabricated beams differed considerably from the designed one. It was found that the dimensions of all six suspension beams were quite different from the initial design.

Thicknesses varied between $75 - 83\ \mu m$, up to 25% less than the initial design. Differences in lengths were not that high with measured values ranging from $2.08 - 2.110\ mm$ approximately 5% less than the targeted value. The edges also look

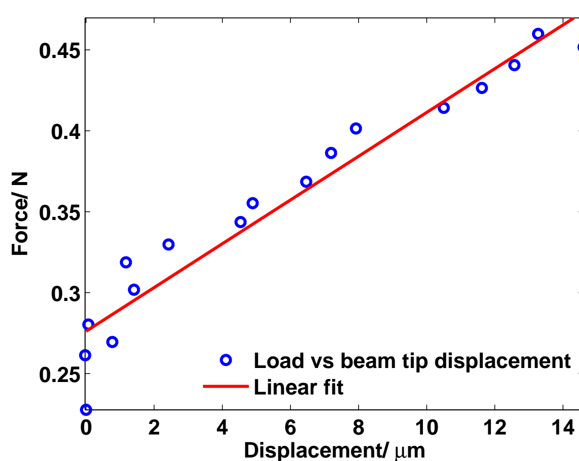

Figure 3.19: Force vs displacement measured on the back left suspension beam of the moving Si frame. The red line corresponds to the linear fit of the experimental data.

rounded giving a cross section quite different from a rectangle.

3.3 IMTEK Samples

Alignment and placement of samples was leading to delays in the programme and so it was decided to contact the group of Professor Oliver Paul at Department of Microsystems Engineering (IMTEK), University of Freiburg, Germany was contacted and a collaboration established. Professor Oliver's group has extensive expertise on brittle material testing [59] and their on wafer tensile testing method was successfully demonstrated on specimens made of poly Si [36, 39].

This method is perfectly suited for brittle material testing as the special silicon frames which the specimens are attached to, do not need to be diced and removed

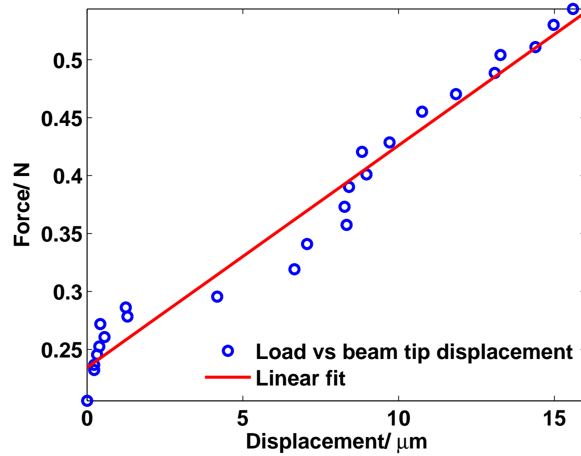

Figure 3.20: Force vs displacement measured on the back right suspension beam of the moving Si frame. The red line corresponds to the linear fit of the experimental data.

from the wafer for testing. A high accuracy positioning system moves the actuator head over the clamped wafer and the samples are strained to fracture: the whole process being monitored in situ by CCD imaging. Twenty two out of the twenty six suspended frames have only one test sample attached thus ensuring alignment to the external load is always good. In the remaining four frames a counter specimen opposite to the measured sample were fabricated aimed at estimating the residual strain in the tested film.

As part of this collaboration fourteen wafers, with different films and film thicknesses were fabricated as listed in table 3.1. Here an IMTEK design and mask was used, although the fabrication process was identical to the one developed in Cranfield and described earlier. On wafer testing was performed on 26 samples with a geometry similar to that of the samples in Cranfield's second mask set (figure 3.24).

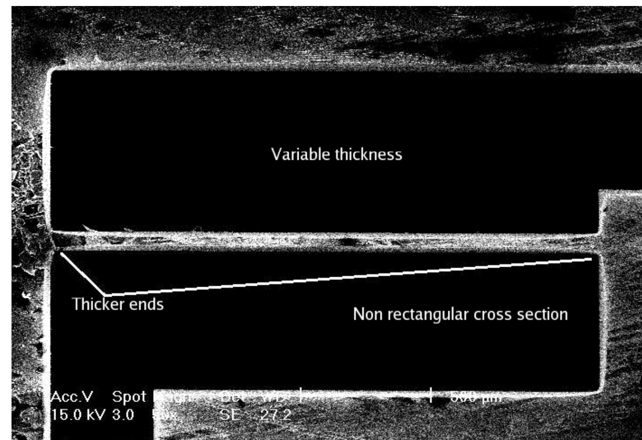

Figure 3.21: SEM micrograph of one of the Si suspension beams. The beam thickness is not constant thoughout the beam length as a result of the DRIE etch process. The edges also appear rounded.

Wet etching of the ceramic in buffered HF was used to pattern the dog bone shaped samples but it was soon realized that for these small samples with a width of only 50 μm the inevitable undercut would cause the cross section layout to become trapezoidal as the SEM image 3.22 illustrates. It was thus decided to fabricate in parallel a number of samples by dry etching the ceramic in the RIE using electro plated Ni as the masking material. This improved the side wall layout of the samples as the SEM micrographs in 3.23 show. The effect of fabrication process on the ceramic fracture strength would thus be investigated.

Efforts to release the samples for testing were not successful. Etching the oxide and the Pt from the back of the suspended samples at IMTEK also resulted in their destruction. One sample did survive and was measured though in this case the stiffness of the suspended silicon frame was found to be rather high, limiting the accuracy of the test.

Table 3.1: Samples fabricated for on wafer testing at IMTEK.

Film	Composition	Orientation	Thickness μm
PZT	30/70	(111)	0.35(2)/0.7/1.1/1.5
PZT	52/48	(111)	0.5/1.0/1.5
PZT	52/48	(100)	0.5/1.0(2)/1.5
ZnO			2.0/2.5

In figure 3.25 the applied force is plotted versus the measured displacement for the only sample that has been released and measured. The applied force for a 5 μm displacement of the combined sample, frame system is 1.5 N which is rather high. This implies that the frame stiffness is not comparable to the sample stiffness limiting the accuracy of the meaurement.

Fabrication of dog bone shaped structures for tensile testing of piezoelectric ceramics, proved rather challenging showing a rather poor yield of successfully released devices. In order to circumvent the difficulties related to the device fabrication and handling it was decided to test composite structures where the SiO_2, Pt under layers would not be etched prior to the testing.

The elastic properties of the tested ceramics would then be extracted from the experimental values obtained for the composite structure. Two reference wafers were prepared and patterned for the determination of the oxide/ Pt films contribution to the total response of the tested composite. To this end both these reference wafers were fabricated following the same process flow developed for the fabrication of the actual samples, the only difference being the wet etching of the ceramic layers after the completion of the sol gel deposition step. This way all

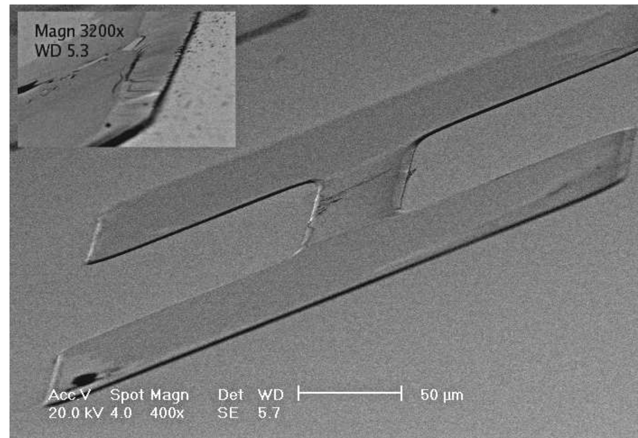

Figure 3.22: SEM micrograph of a dog bone shaped structure that has been wet etched. In the inset the pronounced undercut of the side walls is illustrated.

the structural changes that take place during PZT crystallization in the oxide/ Pt system and could possibly alter the mechanical response of the films, would be taken into account.

All the wafers had Si partially etched from the back using DRIE at Cranfield prior to sending them at IMTEK for the final release of the tested dog- bone shaped structures. The released samples after thorough cleaning and drying were inspected under the microscope and their actual dimensions were optically defined, as deviations in both the parallel length and width due to the etching process are to be expected. In figure 3.26 a SEM micrograph of a released sample is illustrated. From this it is clear that slight overetching of the silicon substrate during the DRIE process results in part of the anchor pads of the device to be released as well, thus altering the geometry of the tested sample. These overetched parts of the beam anchor that were hanging over the Si frame were also individually measured so the extracted material property values could be appropriately corrected afterwards.

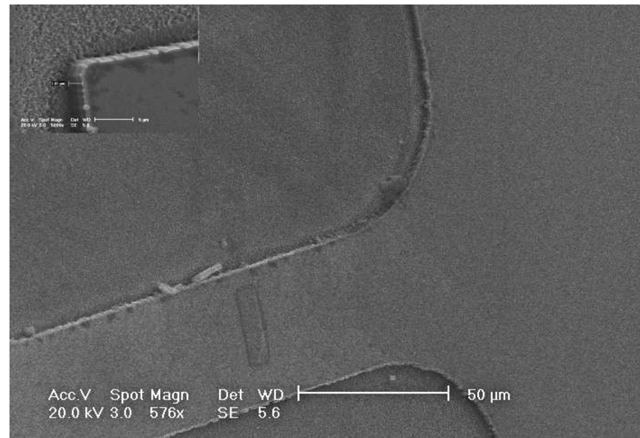

Figure 3.23: SEM micrograph of a dog bone shaped structure that has been dry etched using Ni hard masking. In the inset the almost perfectly vertical side walls are shown.

Yield of PZT devices improved, however all the ZnO and SiO_2/Pt reference specimens broke and were not measured.

3.3.1 Data Processing

The IMTEK wafers were mounted on the tensile kit where the samples could be batch tested. The loading tip position was controlled in all three directions and after an initial calibration all samples on a wafer were sequentially measured. The tip applied a linearly increasing load to each one of the samples by pushing the suspended silicon frame up to a predefined maximum displacement set at the piezo electric motor. A 200 N load cell is used for loading and the applied force is constantly monitored as a function of time. Displacement of the loading tip is optically measured, by the reflection of a laser beam on the tip surface.

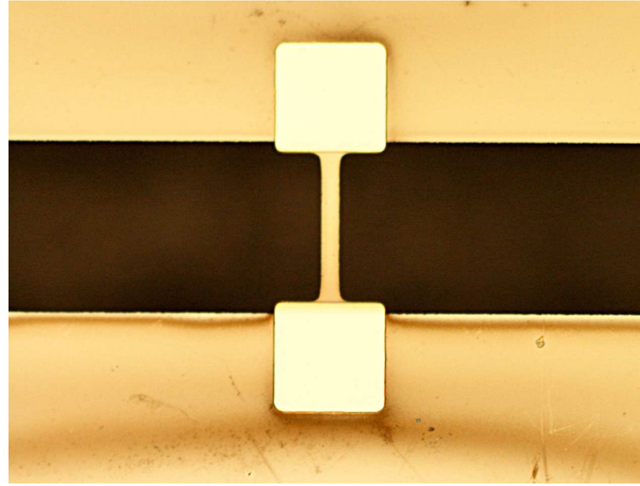

Figure 3.24: Optical micrograph of a released dog bone shaped structure fabricated using mask set from IMTEK.

The force versus time data is automatically plotted by the software and a text file is generated containing the measured force (F_{meas}) and displacement (d_{meas}) data as a function of the experimental time. At this point and prior to data processing the experimental values of force and displacement are calibrated using equations 3.3 and 3.4 respectively.

$$F = \beta F_{meas} \tag{3.3}$$

$$d = d_{meas} - \beta F_{meas}\left(\frac{1}{\kappa_{\tau}} + \frac{1}{\kappa_{\beta}}\right) \tag{3.4}$$

In equation 3.3 F is the force applied on the moving Si frame if the geometry of the loading tip is taken into account while d in 3.4 is the actual displacement of the frame under the application of the force F if the straining of the loading tip and that of the block where the sample is attached on is subtracted.

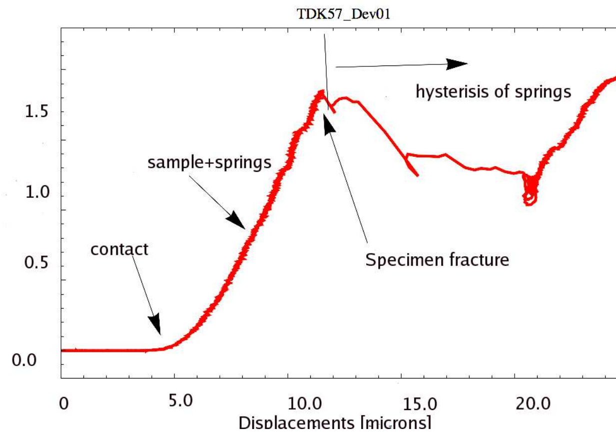

Figure 3.25: Force vs displacement curve for a PZT 30/70 sample measured at IMTEK.

These corrections are necessary since the load is applied on the sample through a vertical loading rod which forms a 90° angle with the load cell. These equations take into account the finite stiffness of this rod κ_τ and that of the block where the sample is attached on κ_β, as well as the effect of the bending moment that the vertical loading rod applies on the load cell (parameter β). These parameters were experimentally defined [38]: $\kappa_\tau = 150.44\ mN/\mu m$, $\kappa_\beta = 1454.42\ mN/\mu m$ and $\beta = 1.01146$.

The calibrated force data is plotted as a function of the experimental time in figure 3.27. During the horizontal parts of the graph no contact between the tip and the frame is established. After the initial contact at the left part of the graph, the force increases until sample fracture which is manifested in the graph by an abrupt fall in the monitored load. The tip pushes the frame further up to a predefined maximum displacement, the force increases following a linear and then a non linear cubic curve as it should be expected for a spring loaded above the limit of linear response. Once the maximum displacement is reached, the force

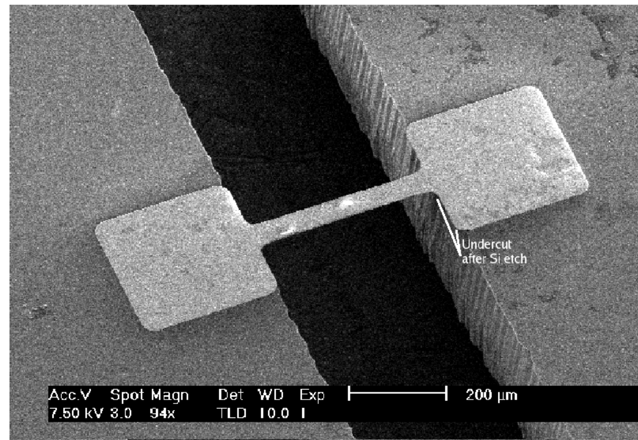

Figure 3.26: SEM micrograph of a released dog bone shaped structure fabricated using IMTEK mask set. The released part of the anchor pad due to Si overetching is visible.

remains constant until the data is saved and the tip starts moving backwards.

If none of the supporting beams fractures during testing, the resulting graph for the loading and the unloading of the Si frame should be symmetric and the final part of the graph should also be horizontal. In practice a drift of the load cell with time is observed most of the times so the data that correspond to the free movement of the tip are fitted by the red line in the graph and the recorded force values are accordingly corrected.

In figure 3.28 the actual force F is plotted as a function of the frame displacement d during the loading (blue curve) and the unloading (red curve) of the sample. The initial contact point, the sample fracture point as well as the parts of the graph corresponding to the linear and the non- linear response of the suspension beams are specially annotated on the same figure.

The part of interest where the sample fracture occurs is zoomed in, in figure 3.29.

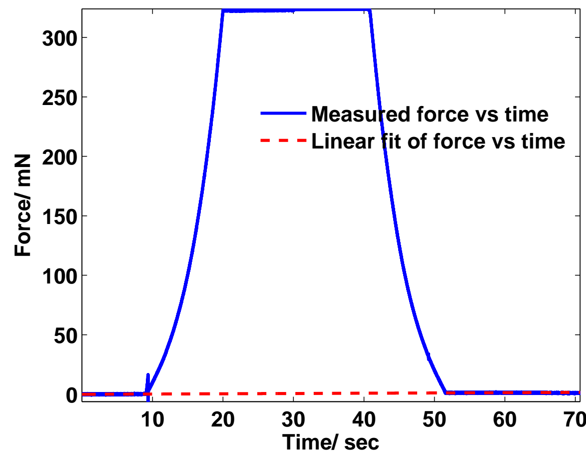

Figure 3.27: Calibrated force values vs experimental time. Load cell drift is also estimated by the inclination of the red line which corresponds to the linearly fitted horizontal parts of the load cell curve.

From this magnified graph five data points are chosen for the linear fit of the data which is subsequently used for the extraction of the material parameters. The residual strain is estimated from the distance traveled by the frame between the point of contact with the loading tip and the buckling of the counter- specimen which is followed by an increase in the inclination of the graph. This is only happening in the four frames with the specimen counter- specimen pairs. Defining the point of counter- specimen buckling is a bit arbitrary as figure 3.29 depicts.

The fitted data are plotted in figure 3.30 (red, dashed lines). The Young's modulus of the tested structure is evaluated from the change in the total stiffness before and after the sample fracture.

In figure 3.31 a micrograph of a fractured composite sample is depicted. The crack in the ceramic does not coincide with the under layer fracture surface. Pt is

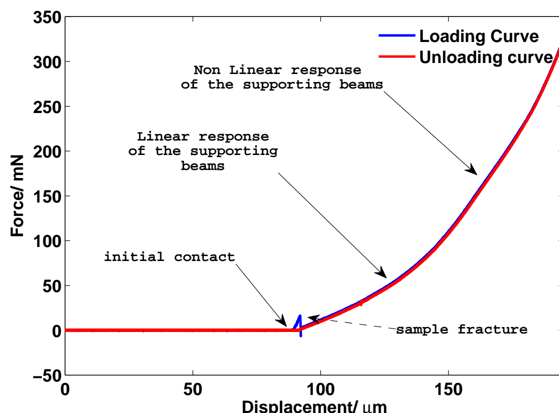

Figure 3.28: Calibrated force values vs displacement during sample loading (blue line) and unloading (red line).

bending upwards due to the high residual tensile stress built during the annealing of the pzt. In the inset a details of the columnar structure of the cracked ceramic are visible under high magnification.

The results of the foregoing analysis are presented in table 3.2. The first two columns contain information relevant to the tested wafer (composition of the ceramic and device number). In the next six columns the dimensions of the tested sample and the mean dimensions of the two suspended anchor parts are presented. The lengths and widths were optically measured prior to testing. The thickness of the PZT ceramic was individually measured during device fabrication. Finally in the last three columns the graphically determined Young's modulus, fracture strength and residual stress of the composite dog bone samples are presented. It should be mentioned once again that the residual stress measurement is only performed in certain samples which are designed in pairs for this purpose.

Table 3.2: Specifications of the tested samples. The dimensions (L_{sam}, w_{sam}) of the tested structure as well as the mean length and the mean width (L_{anc}, w_{anc}) of the two suspended anchor parts were optically measured. In the last three columns the composite Young's modulus, the fracture strentgh and the residual stress which were graphically determined are presented.

PZT comp	Dev no	L_{sam} μm	w_{sam} μm	L_{anc} μm	w_{anc} μm	t_{PZT} μm	t_{SiO_2} μm	E_{comp} GPa	σ_{fr} MPa	σ_{res} MPa
52/48	1	405.6	49.1	29.4	295	0.67	0.2	62.1	148	-
"	9	402.1	50.3	28	298	0.67	0.2	41	276	55
"	19	399.8	49.2	31.2	302	0.74	0.2	41	301	34
"	2	403.3	45.6	20.9	300	1.48	0.2	40.8	288	-
"	3	405.6	45.6	23.8	300	1.42	0.2	38.6	297	-
"	6	404.5	45.6	26	303	1.44	0.2	40.8	336	-
"	7	404.5	46.3	27.9	297	1.43	0.2	29.9	325	-
"	8	405.3	46.8	26.7	300	1.38	0.2	30	264	-
"	12	404.5	46.8	27.9	305	1.42	0.2	39	299	-
"	18	405.6	45.6	26.5	300	1.48	0.2	42	254	-
"	22	405	45.6	23.9	300	1.52	0.2	33.8	265	-
"	14	398	47.6	28.9	297	0.37	1	44.8	194	-
30/70	2	398.8	49.6	22.9	300	0.39	1	59.1	456	-
"	3	402	49.3	19	302	0.38	1	59	381	-
"	9	400	49	31	300	0.39	1	67.5	432	86
"	19	400	50.1	30.9	302	0.38	1	44	338	75

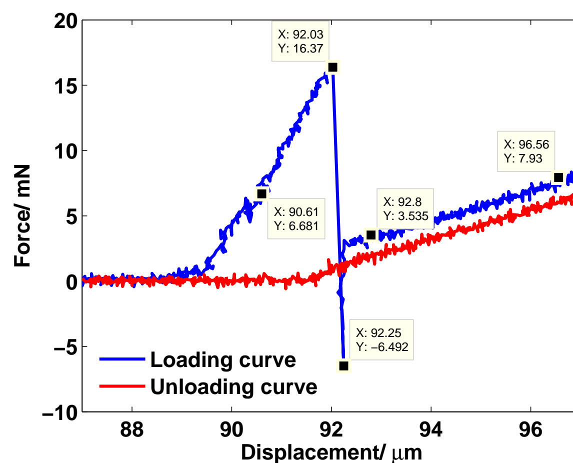

Figure 3.29: Calibrated force values vs displacement during sample loading (blue line) and unloading (red line) magnified for the graphical evaluation of the sample Young's modulus and fracture strength.

3.4 Equivalent Spring Constant of Composite Samples

The Young's modulus of the ceramic was evaluated from the spring constant of the composite sample, using a simplified mechanical model as the one shown in figure 3.32.

In this model each one of the films comprising the composite structure is represented by a spring with a specific spring constant. The three springs have a common initial length L_0 and are connected in parallel, so under the application of an external force F they are all displaced by the same amount. The equivalent composite spring constant is then:

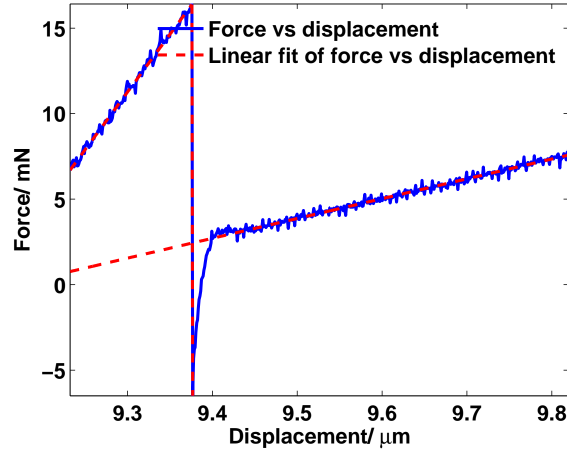

Figure 3.30: Graphical evaluation of the sample Young's modulus and fracture strength. Red lines correspond to the linear fit of the experimental values.

$$\begin{aligned} \kappa_{comp} &= \kappa_1 + \kappa + \kappa_3 \\ \frac{E_{comp}A_{comp}}{L} &= \frac{E_1 A_1}{L} + \frac{E_2 A_2}{L} + \frac{E_3 A_3}{L} \\ E_{comp}t_{comp} &= E_1 t_1 + E_2 t_2 + E_3 t_3 \end{aligned} \tag{3.5}$$

One should be very careful with the terms entering equation 3.5. As it was stated before the dimensions of most samples were slightly different from the designed ones. Even more important, due to over etching of the Si frame in the DRIE, in most samples part of the sample anchor is also released (figure 3.26).

This suspended part with length L_{susp}, width w_{pad} and thickness t_{sam} is also strained during testing and thus contributes to the overall stiffness of the sample which responds like a system of two springs connected in series. The first spring has an equivalent constant $k_{sam} = E_{sam}w_{sam}t_{sam}/L_{sam}$ and the second one, due to the contribution of the overhang anchor $k_{anc} = E_{sam}w_{pad}t_{sam}/L_{susp}$. The load

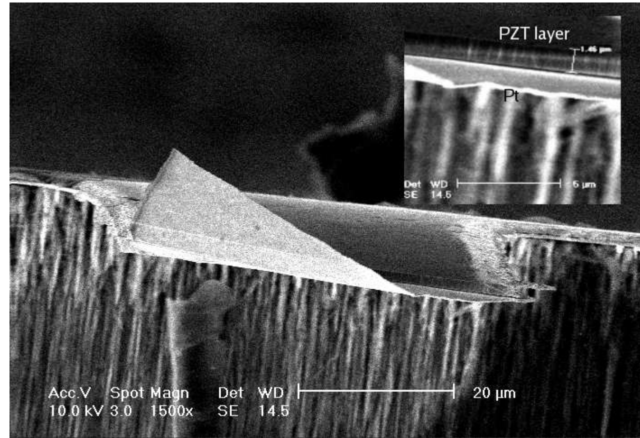

Figure 3.31: SEM micrograph of the cross section of a tested sample. In the inset the PZT layer over the Pt / oxide underlayer is shown under higher magnification.

on the second part is not uniformly applied. The overall stiffness k in this case is given by [38]:

$$k_{tot} = \frac{E_{sam} w_{sam} t_{sam}}{L_{sam} \left[1 + 2\gamma \left(L_{susp} / L_{sam} \right) / \left(w_{pad} / w_{sam} \right) \right]} \tag{3.6}$$

In equation 3.6 γ is a constant which is defined by finite element modelling. The FEM model takes into account the non uniform loading of the suspended part as well as finite size effects arising from the rounded corners of the sample [38]. The mean value for γ calculated at IMTEK using a wide range of mechanical and geometrical parameters as inputs in COMSOL MULTIPHYSICS commercial fem package is 4.79.

The model was further extended to account for materials with different mechanical properties than those tested at IMTEK and for samples with the geometry of those fabricated at Cranfield.

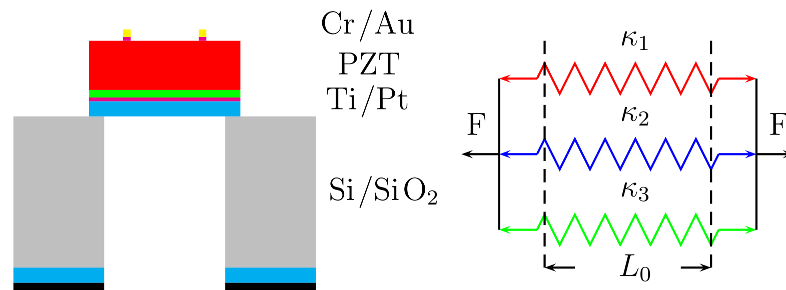

Figure 3.32: Layer structure of the tested devices and the simple mechanical equivelant of the three parallel connected sprigs.

In the appendix B-2 the ANSYS model of a single layer dog bone shaped structure with a suspended anchor part is presented. This model takes advantage of the symmetry boundary conditions across the longitudinal and the transverse axis of the tested geometry in order to save CPU time and calculates the extension of the sample for different cases of elastic and geometrical parameters when a force of 0.02 N is applied. This force was chosen from the load cell force versus displacemnt graphs as representative of the mean force where sample fracture occurs.

The simulations were run for a wide range of input parameters. Young's moduli were varied between $10 \ldots 80\, GPa$, sample lengths between $395 \ldots 405\ \mu m$, sample widths between $45 \ldots 50\ \mu m$, suspended anchors lengths between $0 \ldots 40 \mu m$ and widths between $295 \ldots 305\ \mu m$. For all these combinations the equivalent spring constant k_{tot} in equation 3.6 were derived from the ratio of the applied force $f = 0.02\ N$ over the sample displacement calculated from the finite element model. The mean γ is in this case $\bar{\gamma} = 5.38 \pm 0.25$, higher than that calculated at

IMTEK due to the lower stiffness materials considered.

The Young's modulus of the PZT samples tested at Cranfield were then corrected by entering into 3.6 this value of γ.

In the appendix B-3 a more general model of a composite dog bone shaped sample with a layer structure SiO_2/Pt/PZT is presented. This model was derived from the single layer one. The elastic properties of the ceramic were varied as in the single layer model while those of the SiO_2 and Pt under layers were assumed constant (Young's moduli 70 GPa, 170 GPa and Poisson's ratio 0.2, 0.38 respectively).

The thickness and the elastic moduli of the three layers comprising the composite are different, resulting in the neutral axis of the structure not coinciding with the mid axis. When an axial load is thus applied to the composite a bending moment is also generated causing it to bend. The direction of bending (upwards or downwards) is defined by the displacement of the composite neutral axis relative to the mid axis.

This response was confirmed by the simulations where the maximum displacement of the structure in the direction perpendicular to the applied force was found to be much larger than the displacements in the in plane directions. However the planar stress is uniformly applied in the direction of the applied force and is much larger than the out of plane stress so the assumption of uniform planar loading is still valid.

This is clearly shown in figure 3.33 where ANSYS was used to calculate the displacement of a composite dog bone structure with a 0.2 μm thick SiO_2 and a 0.75 μm thick PZT layer on top of the 0.1 μm thick Pt bottom electrode. On the first column the calculated displacments in the three directions are illustrated. The force is applied in the x- direction. In the second column the calculated mean

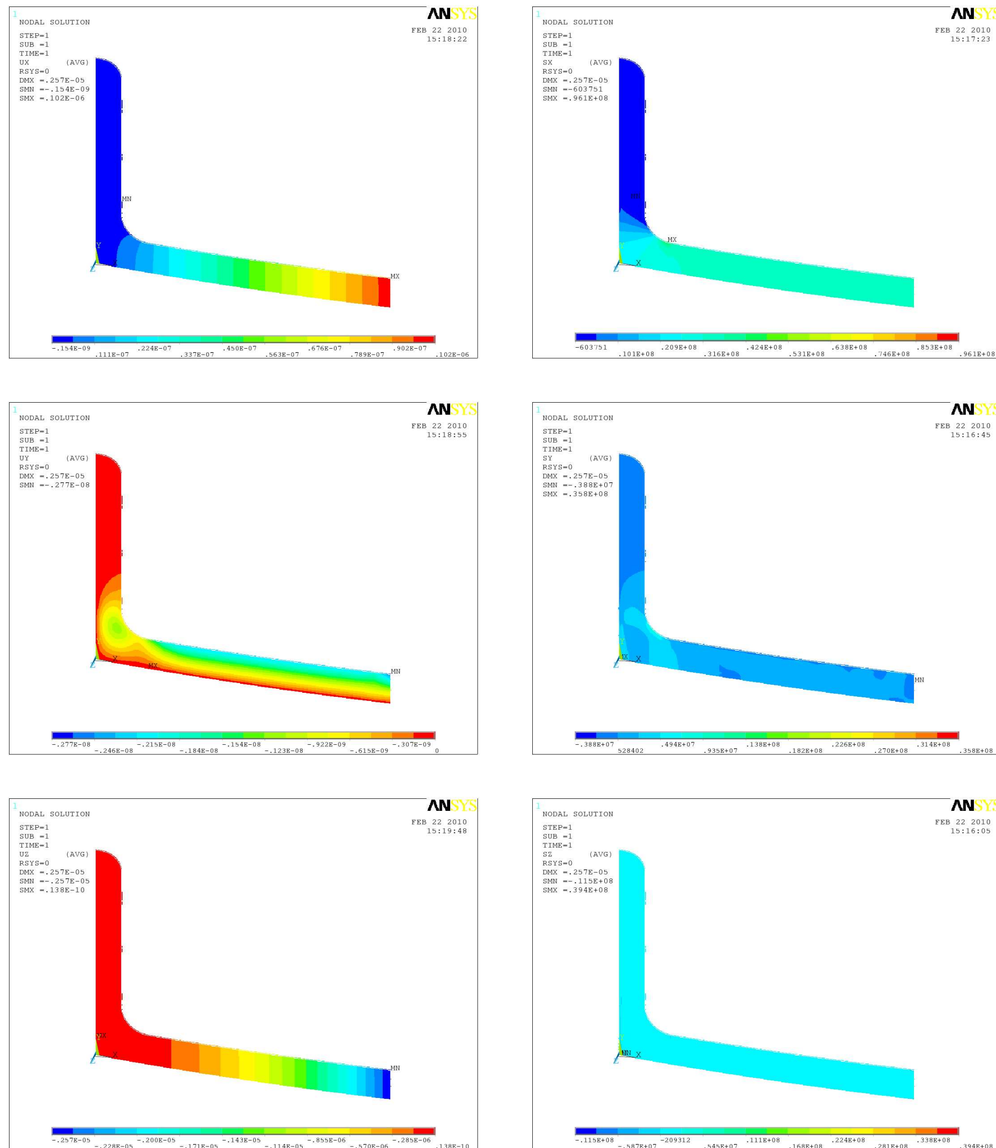

Figure 3.33: ANSYS model of the composite dog bone structure in the case of the thinner oxide and ceramic films used. On the first column the displacement in the x, y and z direction under an applied force of $0.02\ N$ is depicted. Next to each displacement the mean stress in the corresponding direction is presented.

stress is depicted. The mean stress in the x direction is uniform and much higher in magnitude than the stress in the other two directions. Especially the out of plane stress (z- direction) is much lower than the stresses that rise in- plane. The same applies to the principal stresses.

The equivalent spring constant was calculated using ANSYS from the ratio of the applied force $F = 0.02\ N$ over the displacement of the structure in the x-direction. Different geometries and combinations of elastic moduli were tested. In addition to the sample dimensions, the thickness of both the ceramic and the oxide layer were varied. It was observed that the value of γ was very sensitive in the variation of the relative thickness of the layers comprisisng the composite and the assumed modulus for the PZT while on the other hand changes in the rest of the dimensions (assuming a constant total thickness and a specific Young's modulus for the PZT) did not alter it signifficantly.

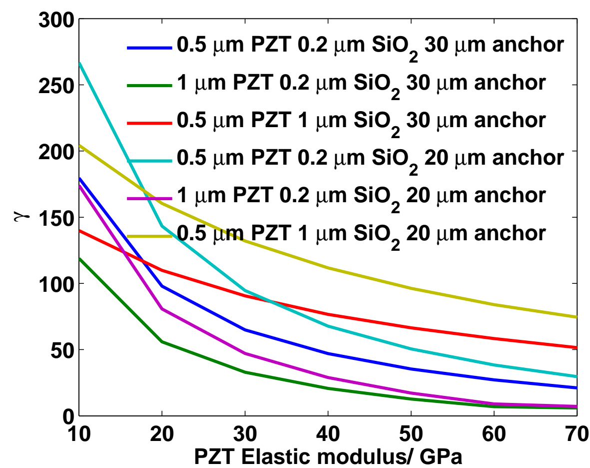

Figure 3.34: γ constant as a function of the assumed PZT Young's modulus for different cases of composite structures and different lengths of the suspended anchor part.

In figure 3.34 the γ constant is plotted as a function of the assumed PZT elastic modulus for different cases of composite structures. The plots correspond to the most characteristic cases of the samples tested and represent the limiting cases that were modelled: the rest of the curves for a sample with a specific layer structure but different lengths and widths fall within these limiting cases and are not plotted.

The correction factor γ becomes very large when the ceramic elastic modulus is assumed smaller than 30 GPa, as can be clearly seen in figure 3.34. When these high γ values are introduced into equation 3.6 the corresponding k_{tot} yield Young's moduli from equation 3.5 which are all much larger than the elastic modulus of the bulk pzt $E_{bulk} \approx 70\ GPa$. Since it was expected that the calculated moduli for different γ should not vary considerably it was decided to exclude the values which correspond to assumed moduli in the range $10, \ldots 20\ GPa$. The mean γ used in equation 3.6 for the calculation of the composite modulus from the graphically determined k_{tot} was $\bar{\gamma} = 40 \pm 5$.

3.5 Elastic Properties and Fracture Strength of PZT Ceramic

In figure 3.35 the histograms of the ceramic Young's modulus extracted from equations 3.5 after the correction 3.6 has been applied are depicted. Assuming that the data are normally distributed a normal distribution function with a mean value $\mu = (57 \pm 8)\ \ GPa$ and a standard deviation $\sigma = (29 \pm 6)\ \ GPa$ is fitted to the experimental results.

The 95% confidence intervals for the mean value of the Young's modulus of the ceramic E is also calculated from the data equal to $(41 \leq E \leq 73)\ \ GPa$. The

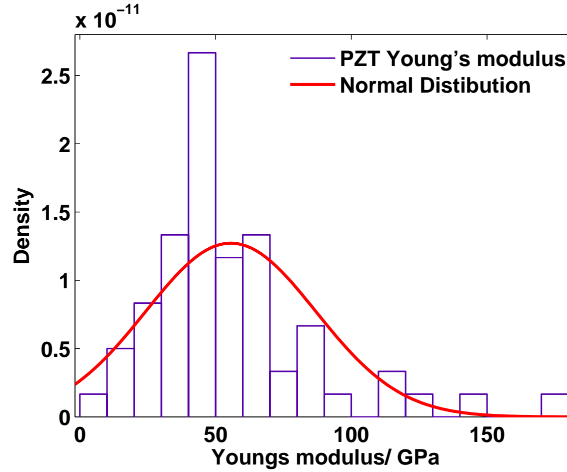

Figure 3.35: Histogram of PZT Young's modulus data obtained from testing IMTEK and Cranfield samples. A normal distribution function.fits the experimental data.

mean Young's modulus of the ceramic is thus $E = (57 \pm 16)\ GPa$ with a 95% likelihood ratio assuming a Gaussian distribution for the measured data.

In figure 3.36 the calculated strength data for the two different types of composite samples, those having a 1 μm thick SiO_2 layer and those having a thinner 0.2 μm oxide layer, are plotted. The cumulative fracture probability is also modelled by a Weibull distribution. The samples with the thinner oxide appear to fracture easier in a less brittle manner than those with the thicker oxide.

For a more reliable and accurate comparison the 95% confidence intervals of both the mean tensile strength $\tilde{\sigma_f}$ and the weibull modulus m are calculated. For the composites with the thicker oxide $\tilde{\sigma_f} = 394^{+78}_{-65}\ MPa$ and $m = 5.1^{+5.8}_{-2.7}$ and for those with the thinner oxide layer $\tilde{\sigma_f} = 295^{+23}_{-21}\ MPa$ and $m = 8.3^{+5.2}_{-3.2}$ respectively.

It is thus not possible to draw a definite conclusion about the relative fracture strength and Weibull modulus of the two different types of samples.

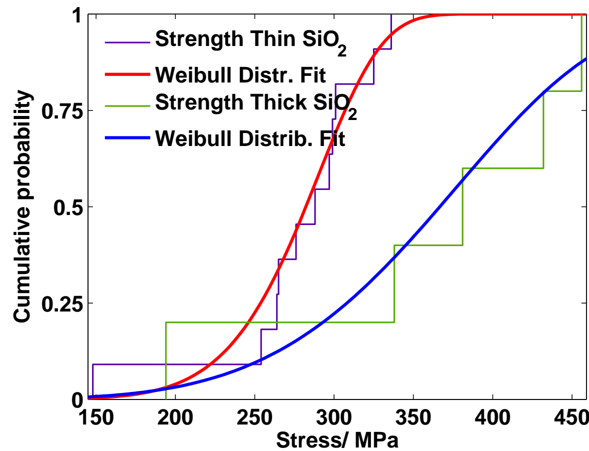

Figure 3.36: Cumulative fracture probability of a composite $\mathrm{SiO_2/Pt}/PZT$ structure as a function of the measured tensile strength for two different types of samples.

So far the mechanical properties of sol gel deposited thin film ferroelectric ceramics have been probed using bulge testing [8, 50] and nanoindentation [50]. The biaxial modulus $E/\left(1-\nu^2\right)$ is extracted in the case of the bulge testing, however in [50] a finite element model is used to extract the Young's modulus of the film from the bulge data. This is achieved by simulating the deformation profile of the tested membranes under conditions of constant air pressure, for different values of the PZT Young's modulus and Poisson's ratio.

It is expected that these findings should compare well with the results of this work as the fabrication process and the annealing conditions used in both cases are similar to ours. This should in principle result in similar micro structures with comparable mean grain sizes [101].

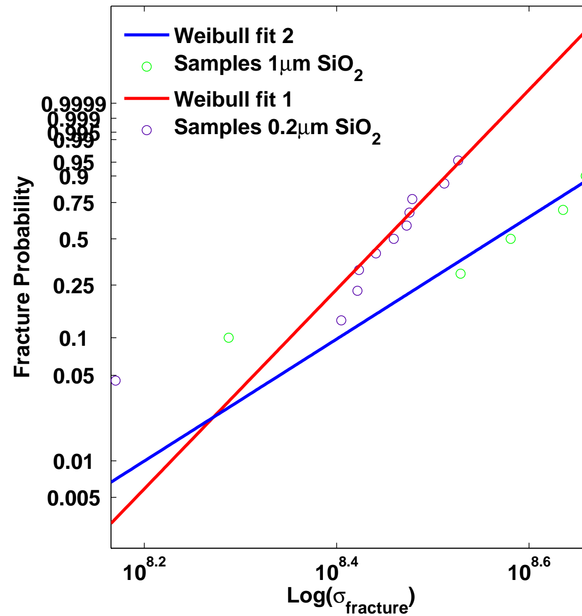

Figure 3.37: Fracture probability of a composite $SiO_2/Pt/PZT$ structure as a function of the measured tensile strength for two different types of samples.

It was decided to perform bulge testing on PZT (30/70) membranes as well and use the results as a reference for comparison with the findings of these different previous works. These membranes are fabricated by bulk micromachining of the back side of the Si substrates with KOH solutions [40]. The Si_3N_4 is deposited by low pressure chemical vapor deposition and serves both as the etch mask and the etch stop layer. Long rectangular membranes are patterned on one side of the wafer.

Problems were encountered with the poor adhesion of the Ti/Pt bottom electrode on top of the Si_3N_4 surface. It was thus decided to use TiO_2 instead of pure Ti. After depositing the 15 nm thick Ti film using rf- sputtering the wafer was annealed

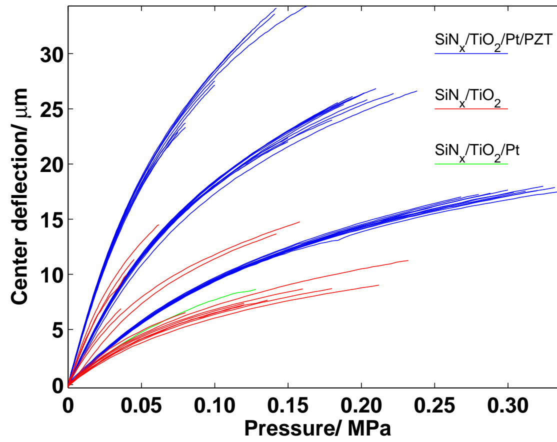

Figure 3.38: Deflection profiles of different membranes as a function of the applied pressure. Blue lines correspond to the full ferroelectric stack while the red and the green ones were obtained from the reference wafers.

in air at 700 ^oC for 3 min using rapid thermal annealing. This resulted in the oxidation of the Ti film and the formation of a TiO_2 layer with the anatase phase and a thickness measured ≈ 30 nm. A 750 nm thick PZT (30/70) film was finally deposited by spin casting on top of the rf sputtered Pt bottom electrode.

To increase the yield of successfully released membranes it was decided to keep the underlayers and thus measure the response of the composites with a layer structure SiN_x/ TiO_2/ Pt/ PZT. In order to be able to extract the material properties of the PZT film from the deflection profiles of the composite membranes two more wafers were prepared one covered with TiO_2 and the other with both TiO_2 and Pt [37].

In figure 3.38 the deflection profiles of the different membranes as a function of the applied pressure are plotted. Three different sets of curves are depicted. The

blue curves correspond to the response of the composite membranes, the red ones to the SiN_x/ TiO_2 membranes and the green to the SiN_x/ TiO_2/ Pt membranes.

In all three samples the front surface was partially attacked by the KOH resulting in a number of broken membranes. Especially in the Pt coated wafer only one membrane was finally measured.

In table 3.3 the results from the micro tensile testing are summarized. For comparison the results from IMTEK bulge testing and the findings of [8, 50] are also included. Note that the tensile strength $\tilde{\sigma_F}$ MPa, weibull modulus m and residual stress σ_R MPa results in the first two lines refer to composite structures and are not directly comparable to the bulge test findings. In addition the calculated confidence bounds are not the same in each method.

Two different approaches were adopted for processing the bulge data at IMTEK. Starting from the mechanical properties of the Si_3N_4 film the response of the Si_3N_4/ TiO_2 membranes was analyzed and the properties of the TiO_2 layer were derived. The process was repeated with the Si_3N_4/ TiO_2/ Pt and Si_3N_4/ TiO_2/ Pt/ PZT membranes and the properties of the Pt and the ceramic film were sequentially evaluated. However, only one Si_3N_4/ TiO_2/ Pt membrane had survived the wet etching process so the accuracy in evaluating the properties of the Pt film was limited. In addition the uniformity of the TiO_2 film thickness was poor so the calculations were repeated assuming the literature values for both the oxide and the Pt films.

The results of this analysis are also included in the table of results 3.3. This second approach rendered results for the biaxial modulus that are in good agreement with the findings in [8]. The calculated residual stress however appears larger than the stress defined by the wafer curvature technique 4.3.

The Young's modulus derived from this work is in good agreement with the results

in [50]. The mean value found here is $\approx 16\%$ higher. The discrepancy is likely due to the calculation of the γ correction factor in 3.5. The fem model that was developed for this purpose assumed isotropic properties for all the layers in the composite. It is known however that PZT thin films are tranversely isotropic. In addition the elastic properties of both the Pt and the SiO_2 films were not varied during the evaluation of γ.

The uncertainty in extracting the Young's modulus E using this method is calculated from equation 3.2. The uncertainty of the measured stress $\delta\sigma$ is calculated from equation 3.1 where $w = w_{sam}$ and $t = t_{sam}$. The strains are extracted from the measured displacements $\epsilon = d/L$. The uncertainty in measuring displacements in this case is $\delta d = 10\ nm$. Assuming a 1 μm uncertainty in defining all the lateral parameters (L, w) and a 1% relative ucertainty in defining the sample thickness the uncertainty $\delta\epsilon$ for a typical displacement $d = 10\ \mu m$ (figure 3.30) is:

$$\delta\epsilon = \sqrt{\left(\frac{\delta d}{L}\right)^2 + \left(\frac{d\delta L}{L^2}\right)^2} = 6.7 \times 10^{-5} \tag{3.7}$$

For a maximum force $F = 15\ N$ (figure 3.30) the uncertainty in the stress from equation 3.1 is $\delta\sigma = 21\ MPa$. Finally from equation 3.2 the uncertainty in the calculation of E is $\delta E = 1.7\ GPa$. These values represent the 7%, 5.25% and 2.98% of the calculated fracture strength σ_f and the Young's modulus E of the two kinds of tested samples which are presented in the first two rows of table 3.3.

Table 3.3: Young's modulus/ plane strain modulus $E/\ E_{ps}$, fracture strength/ strain $\tilde{\sigma_F}\ \epsilon_F$, weibull modulus m and residual stress/ strain $\sigma_R/\ \epsilon_R$ evaluated using micro tensile and bulge testing.

Details	Method	$E\ GPa$	$E_{ps}\ GPa$	$\tilde{\sigma_f}\ MPa$	$\epsilon_f\%$	m	$\sigma_R\ MPa$	$\epsilon_R\%$
Thin oxide	Tensile	$41-73$		295^{+23}_{-21}		$8.3^{+5.2}_{-3.2}$	45 ± 15	
Thick oxide	Tensile	$41-73$		394^{+78}_{-65}		$5.1^{+5.8}_{-3.7}$	81 ± 8	
IMTEK	Bulge		96 ± 29	220		1.9	6 ± 29	
IMTEK*	Bulge		162 ± 29	664		3.2	94 ± 29	
Hong et al [50]	Bulge	49.6 ± 5.8						
Hong et al [50]	Nanoindentation	49.0 ± 15.2						
Bahr et al [8]†	Bulge		158		0.89 ± 0.05			0.1
Bahr et al [8]‡	Bulge		154		0.8 ± 0.1			0.1

* Mechanical properties of the TiO_2 and Pt films were taken from the literature.

†Film thickness 350 nm.

‡Film thickness 500 nm.

Chapter 4

Residual Stress Elimination Scheme

4.1 Sample Preparation

For the layer stress measurements single sided polished four inch, Si wafers, with (100) orientation were used. The Si substrate was 400 μm thick and it was coated with a 0.2 μm thick thermally grown SiO_2 film. The 100 nm thick, Pt template layer was DC sputter deposited at room temperature, in a Nordiko sputtering system on top of a 8 nm thick Ti adhesion promoting layer. This was followed by the deposition of the $PbZr_xTi_{1-x}O_3$, PZT film, by sol-gel deposition. Sols with compositions $x = 0.3,\ 0.52$ were processed.

For the first samples the sol-gel deposition process was repeated ten times, giving PZT films of a Zr/Ti = 30/70 composition with a thickness of 1 μm. The final step was the RF magnetron sputtering of the top electrode which in this case consisted of a 100 nm thick Au layer on top of a thin Ti film.

The wafer curvature technique has been used to investigate the stress in these SiO_2/Ti/Pt/PZT/Au transducer structures. The radius of curvature of the stack was measured using a DEKTAK surface profiler before and after the deposition of each individual layer and from equation 1.2 the corresponding stress was calcu-

lated. The scan length was set equal to 50000 μm, the maximum available. The wafer was positioned at a special stage designed to keep it levelled and ensure scans are performed between the same points around the wafer center each time. The direction of the scan path was perpendicular to the primary flat of the wafer. A second scan parallel to the direction of the primary flat was also performed at certain samples to check the validity of the assumption that the film stress is uniformly distributed in the plane.

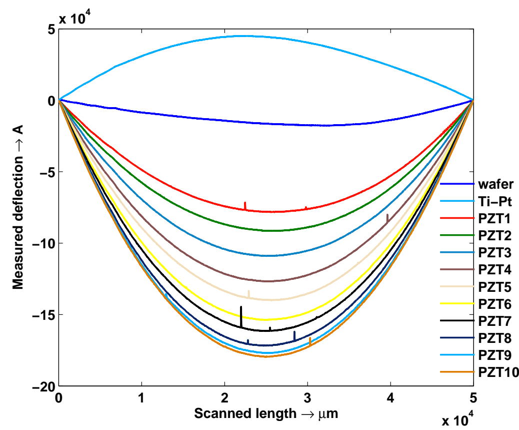

Figure 4.1: Wafer deflection measured using a DEKTAK surface profiler after layer by layer film deposition. The data is plotted as a function of the scanned length.

The measured deflection of the wafer is exported in text format as a function of the scanned data. In figure 4.1 the measured deflection of a wafer as a function of the scanned length is plotted after each layer has been deposited. A fifth order polynomial fit is applied on the data and the radius of curvature is calculated as a function of the scanned length by differantiation. The radius of curvature at half the scan length, which coincides with the center of the wafer, was used as input in equation 1.2. This was chosen as a reference point for all scans as the assumption of constant curvature across the full scan length does not hold ideally.

In the table 4.1 the stress in each layer as it is calculated for a PZT(30/70) coated wafer after each layer is deposited, is shown. In the first column the results from the scans perpendicular to the primary flat are presented while the second one contains the results from the scan directed parallel to the primary flat.

Table 4.1: Layer stress calculated after the deposition of each film on a Si wafer when scans are performed perpendicular to the primary flat (s1) and parallel to that (s2). In the last column the relative difference as a percentage of s1 is calculated.

Layer	Stress (GPa) s1	Stress (GPa) s2	$\|(s1-s2)/s1\|$
Ti/Pt	−0.830	−0.988	20
PZT1	1.589	1.677	6
PZT2	−0.018	0.000	100
PZT3	0.093	0.073	21
PZT4	0.000	0.073	N/A
PZT5	0.013	0.023	77
PZT6	0.098	0.148	50
PZT7	0.101	0.151	50
PZT8	0.094	0.160	70
PZT9	0.084	0.190	126
PZT10	−0.128	−0.080	38
Ti/Au	−0.237	−0.143	40

From table 4.1 it can be seen that the as deposited Ti/Pt bottom electrodes have a high compressive stress close to 1 GPa. The as deposited Ti/Au top electrodes also have compressive stress though considerably lower. This is typical for high mobility metals deposited by sputter deposition under conditions of ultra high vacuum.

The PZT stress data show a high tensile value, over 1.5 GPa, for the first layer of the ceramic, all subsequent layers having values in the range of 100 MPa. Assuming a value of 70 GPa for the PZT Young's modulus the tensile stress value for the first layer should give rise to strains of 2.2%, much higher than the strain-to-failure of 0.1% [104] that should be expected for ceramics. The low tensile stress of the rest PZT layers has been identified in previous works as well and is mainly attributed to the shrinkage of the material during the baking and the crystallization step.

As PZT crystallization is a high temperature process alterations in Ti/Pt residual stress have been reported [124, 125, 152, 107] due to interactions between the adjacent films and/or annealing out of the as-deposited stress. Process induced changes were investigated by comparing the stresses in the layers as measured during the building of the PZT stack with those measured for the same layers during their sequential removal.

In general the order of magnitude of the stress results derived from scans perpendicular to the primary flat of the sample are in good agreement with those derived from scans parallel to this flat.

4.2 Layer Stress Measurements

After completion of the stacks, the layers were removed by two different methods. In most samples, Au was wet etched in a KI- I solution. The underlying Ti layer, was dry etched using reactive ion etching (RIE). PZT was removed in a buffered HF solution, with the back oxide of the wafer protected with a photoresist layer. Pt bottom electrode was wet etched using a combination of HCl and HNO_3 acid at 60 ^oC (aqua- regia solution), while for the underlying Ti layer the same as

before dry etch process was adopted. Finally the back of the wafer was once more covered with photoresist and the SiO_2 from the front was wet etched in a 10% HF solution.

Table 4.2: Layer stress calculated after etching of the films comrising the ferroelectric stacks using dry etching (S1) and wet etching (S2) techniques. The layer stress during stack fabrication are also presented in columns 1 (for sample S1) and 3 (sample S2). The PZT ceramic had a composition of $Zr/Ti = 30/70$

Layer	S1 (GPa)	S1 etch	S2 (GPa)	S2 etch (GPa)
Ti/Au	−0.284	−0.278	−0.240	-0.225
PZT10	−0.102	−0.049	0.090	
PZT9	0.980	0.247	0.102	
PZT8	0.120	0.207	0.086	
PZT7	0.095	−0.366	0.124	
PZT6	0.150	0.190	0.004	+0.054
PZT5	0.102	−0.180	0.200	
PZT4	0.097	0.185	0.065	
PZT3	0.085	−0.049	0.050	
PZT2	0.090	0.060	0.060	
PZT1	1.578	−0.186	1.485	
Ti/Pt	−0.932	0.442	−0.980	+0.877
SiO_2	N/A	−0.075	N/A	-0.165

For one of the samples only dry etching techniques were employed. The Au and the Pt top and bottom metal electrodes were etched by a physical process based on Ar bombardment. This recipe ensures the highly selective etch of the metal

layers over the underlying thin oxidized Ti layer. The PZT ceramic is also etched using a physical process based on CHF_3-Ar bombardment. The selectivity of this latter recipe over the bottom Pt electrode is low causing excessive etch of the film especially around the edge of the wafer, thus limiting the accuracy of the calculations for this layer.

All samples were finally wet etched in HF and a last measurement of the radius of curvature of the bare Si substrate was obtained.

In table 4.2 the stress data that were calculated during this stripping process are presented. The stress of the Ti/Au top electrode has not changed since this layer has not undergone any thermal treatment. The PZT film on the other hand has a low tensile stress equal to 54 MPa as it was calculated in the case of sample s2, where the ceramic was wet etched.

For sample s1, the PZT film was dry etched in ten successive steps, each step resulting in the removal of around 100 nm of material. In this latter case the etch rate was not homogeneous throughout the top surface of the wafer resulting in faster etching of the ceramic towards the edge of the sample thus rendering the individual layer calculations unreliable. However, a calculation of the PZT film stress using as the initial radius of curvature R_0 in equation 1.2 the measured value after the removal of the Ti/Au top electrode and as the final value the measured R after the complete etch of the PZT, results in a tensile value of 75 MPa which is in good agreement with the result obtained from sample s2.

In the table of results 4.3, the mean stress per layer from different types of samples are presented. For the calculation of the mean stress scans performed at directions perpendicular and parallel to the primary flat were considered. In the second column results from five standard wafers used for deposition of PZT (52/48) are presented. In the third column results from ten standard wafers used as substrates

for PZT (30/70) growth are presented and finally column 4 contains results from a SiN_x coated Si wafer where PZT (30/70) was deposited. In the latter case the Pt bottom electrode was deposited after oxidizing the Ti adhesion layer by rapid thermal annealling (RTA) .

Table 4.3: Layer stress calculated after etching the films comrising a ferroelectric stack, when standard oxidized Si wafers are used as substrates (column 2 for PZT 52/48 and 3 for PZT 30/70) and when low stress PECVD SiN_x coated wafers are used for PZT 30/70 deposition (column 4).

Layer	$(\bar{\sigma_f} \pm \delta\sigma_f)\ GPa$	$(\bar{\sigma_f} \pm \delta\sigma_f)\ GPa$	$\sigma_f\ GPa$
Ti/Au	$-(0.31 \pm 0.05)$	$-(0.28 \pm 0.03)$	-
PZT	0.15 ± 0.03	0.06 ± 0.01	0.072
Ti/Pt	1.05 ± 0.12	0.88 ± 0.12	0.75
TiO_2	-	-	0.23
SiO_2	$-(0.17 \pm 0.04)$	$-(0.17 \pm 0.04)$	-
SiN_X	-	-	

It is clear, finally, that only the residual stress in the Ti/Pt bottom electrode had changed during PZT crystallization. This change, from compressive to tensile, is mainly attributed to the annealing out of the original compressive stress and the subsequent introduction of a purely thermal stress due to the large thermal expansion coefficient mismatch between Pt and the Si substrate. This thermal stress which arises in the Pt film during PZT crystallization, ignoring other interactions and assuming bulk values for the film properties, is given by equation 1.1. Assuming $E_f = 170\ GPa$ and $\nu_f = 0.39$ for the elastic modulus and Poisson's ratio of bulk Pt and $\alpha_f = 9 \times 10^{-6}\ deg^{-1}$, $\alpha_s = 2.5 \times 10^{-6} deg^{-1}$ for the thermal

expansion coefficients of bulk Pt and bulk Si respectively, equation 1.1 for a temperature range from $T_0 = 30\ ^oC$ to $T_{cryst} = 530\ ^oC$, gives a thermal stress equal to $0.91\ GPa$, close to the value of $0.88\ GPa$ obtained experimentally and consistent with previous works.

Assuming a composite film with a layer structure SiO_2- Ti- Pt- PZT a calculation of the overall residual stress is performed using the wafer curvature technique. In this case the initial radius of curvature that enters equation 1.2 is the one calculated from the DEKTAK scan on top of the completed stack, while the final one is derived from the scan on top of the Si substrate after the oxide etch. The total thickness is the sum of thicknesses $\approx 1.3\ \mu m$. This way a residual stress for the composite structure between $100 \ldots 120\ MPa$ is calculated. Compared to the results of the tests in table 3.3, using the special specimen, counter- specimen pairs this is a much higher stress value.

There are other changes that take place during processing, such as Ti diffusion into the Pt as well as formation of TiO_2 [126, 30, 85] which since the Ti layer is extremely thin have been assumed to have little effect on the calculated stress. Another value from table 4.2 that needs to be noted is the relatively high compressive stress in the thermally grown SiO_2 [92].

The uncertainty in calculating stress using the wafer curvature technique is estimated from equation 1.2. Typical values for the measured radius of curvature range between $4\times10^7 \ldots 10^8\ \mu m$ with an uncertainty $\delta R = 10^6\ \mu m$. Measurements are performed on layers of films with a thickness $t_f \approx 0.1\ \mu m$. The uncertainty in film thickness measurements is 1%. The substrate thickness is $t_s = (425 \pm 10)\ \mu m$.

$$\frac{E}{6\left(1-\nu\right)}\sqrt{\frac{t_s^4\delta R_0^2}{R_0^4 t_f^2}+\frac{t_s^4\delta R^2}{R^4 t_f^2}+\frac{\left(-\frac{1}{R_0}+\frac{1}{R}\right)^2 T_s^4\delta t_f^2}{t_f^4}+\frac{4\left(-\frac{1}{R_0}+\frac{1}{R}\right)^2 t_s^2\delta t_s^2}{t_f^2}} \qquad (4.1)$$

Using these values a stress $\sigma = 940\ MPa$ is calculated from equation 1.2 with an uncertainty $\delta\sigma = 105\ MPa$ derived from 4.1. The relative uncertainty is thus $\approx 11\%$. Assuming a range between $9 \times 10^7 \ldots 10^8\ \mu m$ for the radius of curvature a stress $\sigma = 70\ MPa$ is calculated from equation 1.2 with an uncertainty $\delta\sigma = 12\ MPa$ from equation 4.1. The relative uncertainty in this case is thus larger $\approx 17\%$.

4.3 Stress Elimination Scheme by the Removal of Pt Template Layer

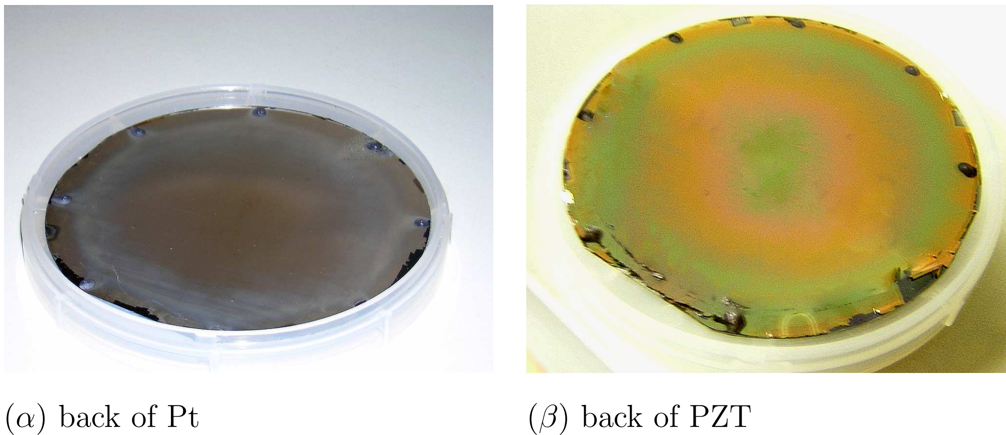

(α) back of Pt (β) back of PZT

Figure 4.2: Exposed back of α the Pt and β the PZT film after completion of the back etching process.

These results clearly identify a largely fixed stress in the PZT stack localized in the Pt and (to a lesser extent) SiO_2 layers below the PZT. Based on these findings the feasibility of the stress elimination technique was investigated using 4" wafers containing the same Au/PZT/Pt/SiO_2 layer structure as described earlier.

Table 4.4: Layer stress calculated after deposition of each film comrising a ferroelectric stack (column 2), after etching of each film following the completion of the stack (column 3) and finally after etching of the films following the release of the stack from the Si subtrate using wafer bonding (column 4).

	Measured Layer Stress (GPa)		
Layer	Sample fabrication	PZT stack etch	After initial Si etch
Ti/Au	−0.310	−0.310	−0.225
PZT	0.227	0.054	0.021
Ti/Pt	−0.830	0.877	−0.267
SiO_2	-	−0.162	-

The SiO_2 and Pt films were then removed using plasma etching to expose the back surface of the PZT: figure 4.2 (α) shows the Pt surface, exposed after the removal of the SiO_2 layer and figure 4.2 (β) the PZT surface after Pt etch.

The effects on the stress in the remaining layers caused by the removal of the silicon substrate were measured by the wafer curvature technique and the results are presented in the last column of table 4.4 [42]. Once the Pt is released from the substrate the Pt layer is under a low compressive stress while the PZT is again under tensile stress, though less than in the initial stack. This can be explained by assuming that removal of the Si eliminates the force constraining the Pt, dictated by the difference in thermal expansion coefficients (equation 1.1), so allowing the Pt film to relax. As expected the stress in the Au top electrode is unaltered.

The back surface of a ferroelectric stack which has undergone the stress elimination

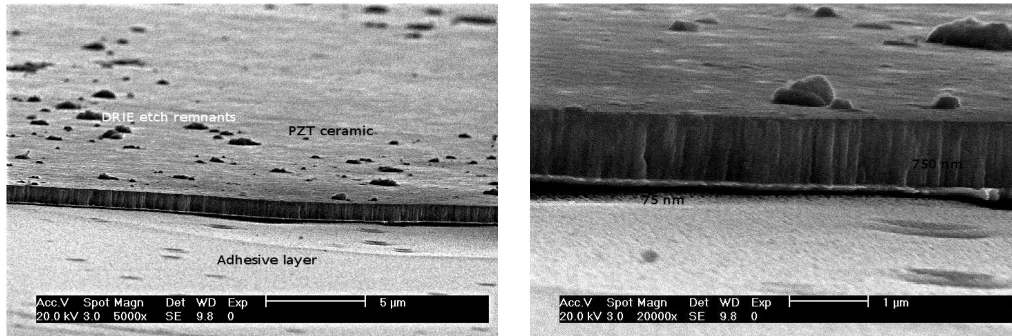

(α) (β)

Figure 4.3: Cross sectional view of the back etched ferroelectric stack (α). Columnar grain structure of the ceramic (β).

process is investigated using SEM imaging. In figure 4.3 (α) a SEM micrograph of the ferroelectric stack on top of the adhesive layer is depicted.

In figure 4.3 (β) a cross sectional view of the ceramic is shown under higher magnification. The Cr/Au film which was sputter deposited on the top of the ceramic is now visible in contact with the adhesive layer at the bottom of the image. The columnar grain structure of the PZT film is also visible. In both (α) and (β) there are some visible structures on the top of the ceramic.

The composition of these structures was investigated using energy dispersive X-ray spectroscopy (EDX analysis). In figure 4.4 (α) the area of the ceramic that was scanned is depicted. The two points where the beam of the X-rays was focused are annotated by spectrum 1 and 2. In figure 4.4 the results of the analysis performed on point 1 are plotted. A similar graph was obtained from the analysis of the second point. Clearly these structures mainly consist of Si. Traces of Pt and Ti are also detected. These findings suggest that these structures are the result of

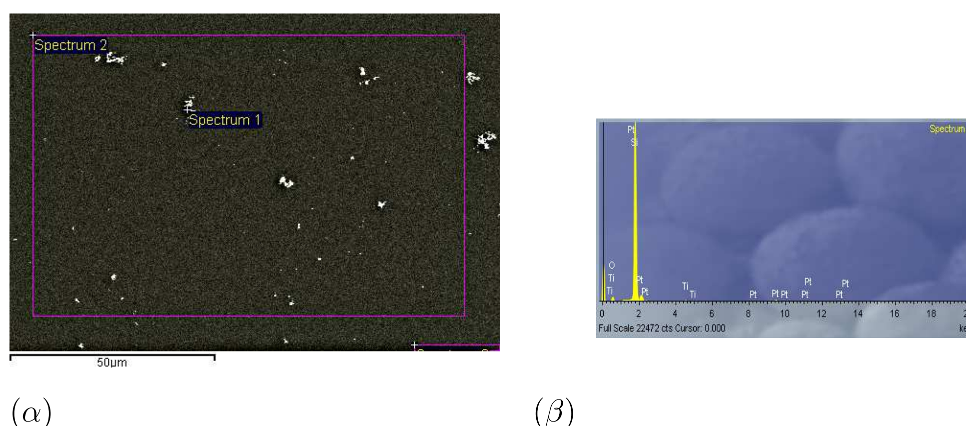

(α) (β)

Figure 4.4: Sem micrograph of the area of the ceramic where the EDX analysis was performed. The points of interest are shown. In (β) the results of the analysis from point 1 are plotted.

the partial etch of the Si substrate in the DRIE chamber.

4.4 Device Fabrication

4.4.1 Residual Stress Induced Deflection of a Cantilever Beam

In order to demonstrate the effectiveness of the Pt layer removal technique in lowering stress and hence distortion in piezoelectric microstructures a comparison has been made of the tip deflections to be expected from two micromachined cantilevers, one composed of the above Au/PZT/Pt/SiO_2/Si structure and the other with the Pt, SiO_2 and Si layers removed and replaced by low stress Au and SiN_x for the bottom electrode and structural layers, respectively, giving a Au/PZT/Au/SiN_x structure.

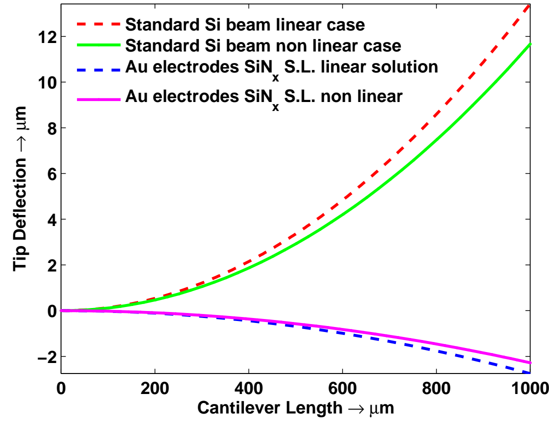

Figure 4.5: Linear and non linear model of the tip deflection due to residual stress to be expected for a typical Si beam with a Au top electrode and for a beam fabricated based on the stress elimination method where the Pt layer has been replaced by a Au film and a low stress SiN_x film is introduced to serve as the structural layer.

The stress values used for the Au, PZT, Pt and SiO_2 were those which had been measured on the real structure during etch back i.e. those given in column 4 table 4.4. The SiN_x was assumed to have negligible stress with Young's modulus $E = 290\ GPa$ and was given the same thickness (10 μm) as the Si structural layer: a 10 μm beam width was assumed in both cases.

The resulting beam tip deflections as a function of beam length are given in figure 4.5 which also shows for comparison the result to be expected in the limit of small displacements. In this latter case it is assumed that the beam's curvature is small and an ordinary differential equation of second order is analytically solved. It can be seen that the assumption of small displacements is not valid for the full range of beam lengths investigated in the present work but both approximate solutions show clearly the great reduction in beam deformation achievable by replacement

of the high stress layers. The calculations were performed running in MATLAB the m file from the Appendix A-1.

4.4.2 Fabrication Process

Fabrication of free standing stress- free devices, based on the stress elimination scheme was attempted. During the PZT etching in the RIE, a process with a relatively slow etch rate $\approx 3\ nm/min$ which is based on fluorine chemistry, it was observed that the etch rate would deteriorate in time practically becoming zero after three hours. It is believed that contamination of the chamber walls due to the formation of Ni, F compounds affected the gas chemistry in the reactor. The etch rate of the process improved considerably after the chamber walls were thoroughly clean by mechanical means. However, sample processing was aborted to avoid causing Ni contamination of the ICP chamber.

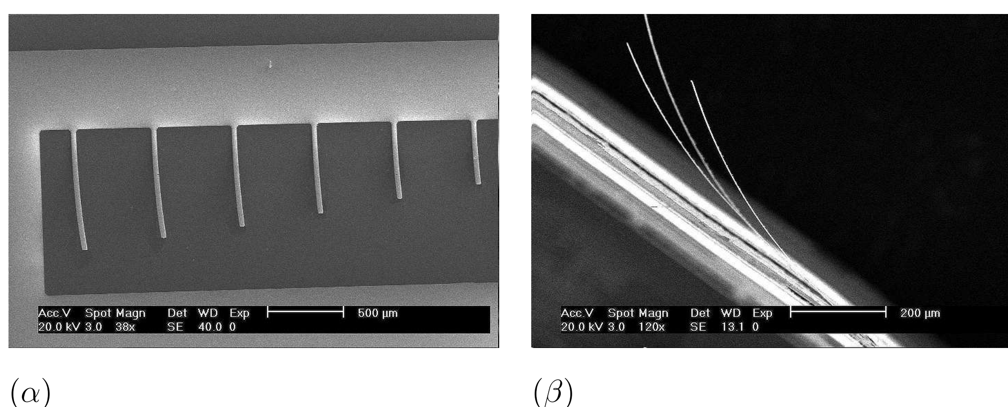

(α) (β)

Figure 4.6: SEM micrographs of the released beams fabricated based on the stress elimination scheme. Sputter deposited Al is used as the structural layer.

Two more wafers were prepared and sent to KTH in Sweden where the adhesive bonding was performed. One of the wafers was sent back to Cranfield where the initial substrate was etched in the DRIE. Instead of Ni, 750 nm of Al were rf- sputter deposited on top of the released ferroelectric stack. Cantilever type structures were patterned using AZ 5214E negative resist. The stress in the Al film was found equal to 285 MPa compressive using the wafer curvature technique. In figures 4.6 (α) and 4.6 (β) the released beams that were fabricated using rf sputtered Al are depicted. Due to the unbalanced residual stresses the beams bend upwards: a result actually anticipated due to the high stress in the Al film on one hand and the actual thickness of the film on the other. According to the simple model used in our calculations, for flat structures a ten times thinner Al film should have been used.

The method however enables the fabrication of cantilever type devices with the transducer element positioned under the structural film. This can be very important in case maximum downward deflection is desirable. Conventional PZT actuated devices cannot take advantage of the high piezoelectric response of the ceramic in both the upward and the downward direction. This is because an increase of the applied field over a certain limit results in domain switching and probing of the nonlinear response of the piezoelectric strain. The direction of the maximum deflection in that case is controlled by the position of the PZT film relative to the structure neutral axis.

4.5 Ferroelectric- Electric characterization

In parallel with the device fabrication, ferroelectric capacitors were formed by depositing a top electrode in the form of Cr- Au dots on top of the processed ferroelectric stacks. The thickness of the Au top electrodes is ≈ 100 nm and the diame-

ter is $d = 750\ \mu m$. The tested stacks had a layer structure Au/Cr/PZTCr/Au and the adhesive layers used during the stress elimination process were benzocyclobutene- based polymer (BCB) and photo resist of the MRI-9000 family. The tested ceramic had a composition ratio of Zr/Ti = 30/70 in both cases.

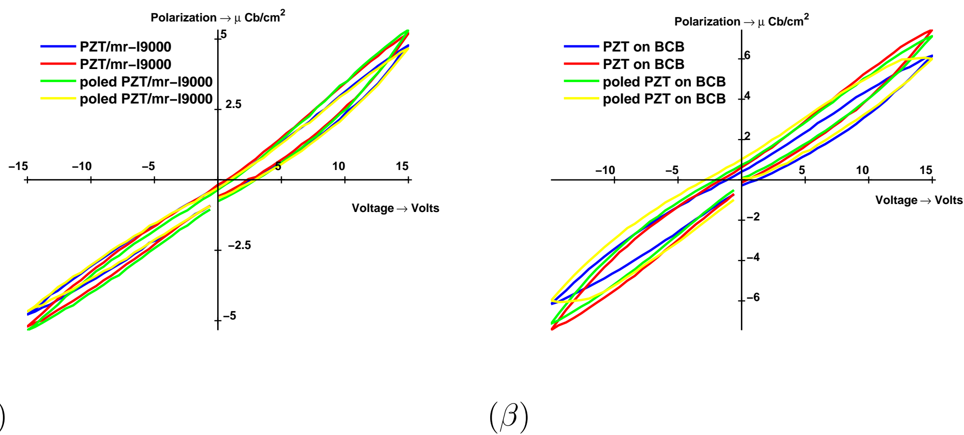

(α) (β)

Figure 4.7: Polarization vs field (P-E) hysteresis loops of a ferroelectric stack which has been wafer transfered using (α) MRI-9000 and (β) BCB as the bonding layer. The wafer on which the stack was initially deposited on has been etched from the back. Loops before and after poling of the stack are illustrated.

In figures 4.7 (α) and 4.7 (β) the hysterisis loops that were obtained from testing both samples are plotted. In both cases the ferroelectric response of the films has deteriorated. No switching occurs although a high enough field is applied on the tested capacitors.

Poling of the films was attempted by applying a voltage of 10 $Volts$ at a constant temperature $T = 130\ ^oC$ for 10 $mins$. After poling was completed the ferroelectric capacitors were connected back to the rt66a set up and had their ferroelectric response probed again, however without success.

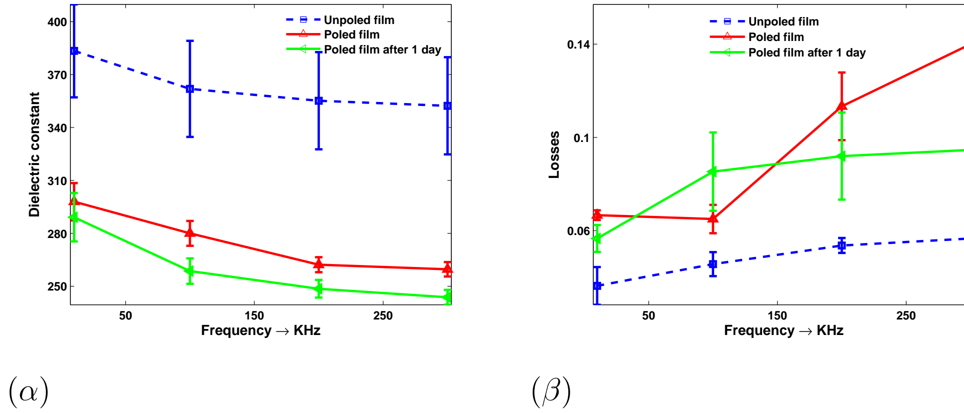

Figure 4.8: Dielectric constant (α) and dielectric loss (β) of a PZT 30/70 film with a sputter deposited $\mathrm{Cr/Au}$ top electrode, after stress elimination.

The dielectric permittivity and the dielectric loss of the ferroelectric films were also measured using the weyne kerr presicion component analyser. The capacitors were measured before and immediately after the poling process. One more measurement was performed after 24 hours had elapsed from poling. A number of capacitors are measured each time and the mean dielectric constant and loss are plotted in figure 4.8 (α) and (β) respectively.

The dependence of the dielectric permittivity on the frequency of the applied signal and the poling conditions is mainly controlled by extrinsic processes like domain- wall pinning and defect displacement [23, 61]. The dielectric loss on the other hand is controlled by various mechanisms however the observed increase after heat treatment of the capacitors is attributed to the higher mobility of the charge carriers.

There is a monotonic increase of the loss with the frequency which is believed to

originate from the contribution of the Pt bottom electrode high resistivity in the formula used by the weyne kerr analyzer in the extraction of the loss parameters from the impedance measurements.

4.6 Polarization Collapse

Interest was thus focused on the possible alterations that may have occurred in the area of the Cr-Au blanket electrode which was in contact with the adhesive layer. To this end ferroelectric capacitors, having Cr-Au top electrodes were fabricated. The capacitors were characterized before and after a 1 hr anneal at 350 ^oC in air.

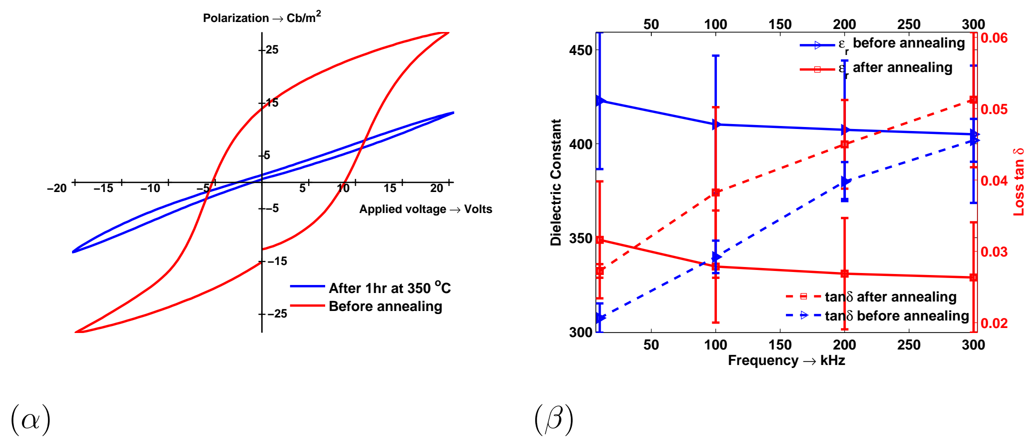

(α) (β)

Figure 4.9: Polarization vs field (P-E) hysteresis loops (α) and dielectric permittivity- loss as a function of frequency (β) obtained before and after heat treatment of a PZT 30/70 film deposited on a standard wafer when Cr/Au is used as the top electrode. Annealing time is 1 hr at 350 ^oC.

In figure 4.9 (α) the polarization versus field hysteresis loops obtained before and after annealing the ferroelectric capacitors are plotted in red and blue respectively.

In 4.9 (β) the dielectric permittivity- loss measured before and after treatment as a function of frequency are plotted. Note the double y- axis used in this case.

In figure 4.9 (α) the blue curve obtained from the heat treated capacitor resembles a Lissajous figure to be expected from a linear lossy dielectric [75]. The observed decrease in the measured dielectric permittivity may be explained by the formation of a thin dielectric layer between the top Au film and the underlying ceramic. This layer is formed during the heat treatment of the capacitor due to the oxidation of the thin Cr layer [93] and thus contributes in the measured capacitance after annealing, as a capacitor connected in series with the initial ferroelectric ceramic. The resulting capacitance is less than the capacitance of the individual (ferroelectric- dielectric) films.

This is further supported by the change in the mean dielectric constant as a function of frequency given in table 4.5. The relative change does not vary much with the frequency of the applied signal.

Table 4.5: Calculated mean dielectric permittivity of the ferroelectric capacitors with a Cr/Au top electrode before and after heat treatment for $1\ hr$ at $350\ ^oC$ as a function of frequency. The relative change does not depend on the frequency.

Frequency kHz	10	100	200	300
ϵ_r before	422	410	407	405
ϵ_r after	349	335	331	329
$\Delta\epsilon_r/\epsilon_r$	0.1730	0.1829	0.1867	0.1877

Assuming that the thickness of the dielectric layer is of the same order as the

thickness of the Cr film $\approx 10\ nm$ and the dielectric permittivity of the $\mathrm{Cr\,O_2}$ is close to the bulk value then ignoring any other alterations, the relative decrease in the measured capacitance due to the two capacitors connected in series is:

$$\frac{1}{C_{meas}} = \frac{1}{C_{pzt}} + \frac{1}{C_{\mathrm{Cr\,O_2}}} \Rightarrow C_{meas} = \frac{C_{pzt}C_{\mathrm{Cr\,O_2}}}{C_{pzt} + C_{\mathrm{Cr\,O_2}}} \tag{4.2}$$

In equation 4.2 $C_{pzt} = \epsilon_{pzt}\epsilon_0 A/l_{pzt}$ is the capacitance of the ceramic layer which has thickness l_{pzt}, dielectric permittivity ϵ_{pzt} and $C_{\mathrm{Cr\,O_2}} = \epsilon_{\mathrm{Cr\,O_2}}\epsilon_0 A/l_{\mathrm{Cr\,O_2}}$ is the capacitance of the formed oxide layer. A is the area of the top electrode which is common for both layers. The measured capacitance corresponds to a fictitious capacitor with thickness $l_{pzt} + l_{\mathrm{Cr\,O_2}} \approx l_{pzt}$ and permittivity ϵ.

By substituting C_{pzt}, $C_{\mathrm{Cr\,O_2}}$, and C_{meas} in 4.2 one obtains for the measured permittivity ϵ after the heating treatment:

$$\epsilon = \frac{\epsilon_{pzt}\epsilon_{\mathrm{Cr\,O_2}}}{\epsilon_{pzt}\frac{l_{\mathrm{Cr\,O_2}}}{l_{pzt}} + \epsilon_{\mathrm{Cr\,O_2}}} \xrightarrow{\frac{l_{pzt}}{l_{\mathrm{Cr\,O_2}}} \approx 0.01} \epsilon < \epsilon_{pzt} \tag{4.3}$$

The decrease in the measured permittivity calculated from 4.3 might not however explain the observed one. Other mechanisms like the rise of internal bias fields during annealing cannot be excluded.

Optical micrographs of the top Cr/Au dots captured using digital imaging before 4.10 (α) and after 4.10 (β) heat treatment show structural damage at the top surface.

New samples were prepared using PZT (30/70) ceramic with sputter deposited Ti/Pt and Pt dots serving as the top electrode of the ferroelectric capacitors. The results of these tests are depicted in figure 4.11.

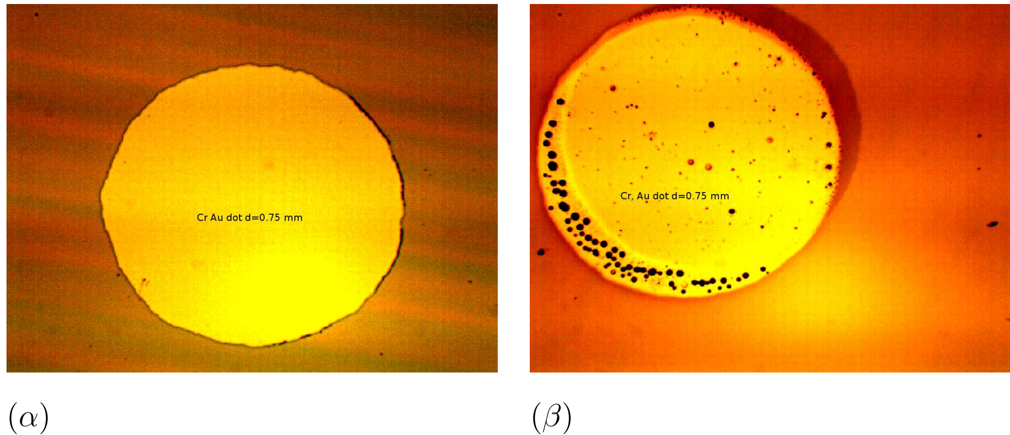

(α) (β)

Figure 4.10: The sputter deposited Cr/Au dots serving as top electrodes of the ferroelectric stack (α) show apparent signs of damage after heat treatment (β).

In 4.11 (α1) the polarization vs field hysteresis loops of the capacitors with the Ti/Pt top electrodes obtained before and after treatment are plotted. The results of the electrical characterization of these capacitors are depicted in 4.11 (β1). After treatment the ferroelectric response has deteriorated and the dielectric permittivity has decreased. However no structural damage was observed on the top electrode this time. Once again the Ti adhesion layer is oxidized during the annealing forming a thin TiO_2 dielectric layer between the PZT ceramic and the Pt top electrode.

In 4.11 (α2) the polarization vs field hysteresis loops of the capacitors with the Pt top electrodes obtained before and after treatment are plotted. The results of the electrical characterization of these capacitors are depicted in 4.11 (β2).

Contrary to the previous findings heat treatment in this case resulted in a pinched, slightly displaced to the negative field axis, hysteresis loop followed by an increase

in the dielectric permittivity. Pinched hysteresis loops are associated with the displacement of defects which interact with the domain walls and result in abnormal domain switching [23].

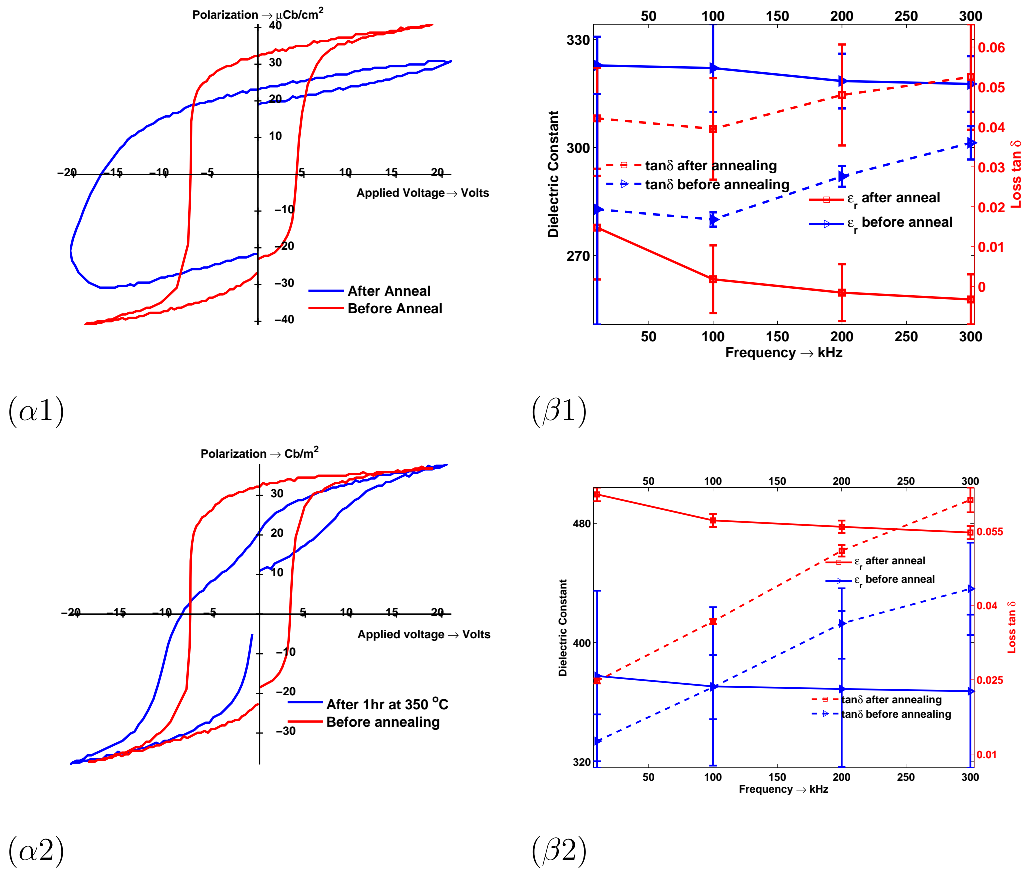

Figure 4.11: Polarization vs field (P-E) hysteresis loops (left column) and dielectric permittivity ϵ and loss $\tan\delta$ (right column) of a ferroelectric capacitor formed by a PZT 30/70 film with a sputter deposited $\mathrm{Ti/Pt}$ (top) and Pt (bottom) top electrode, before and after heat treatment.

Heat treatment of the PZT (30/70) ceramic affected both the film- top electrode

interface as well as the bulk of the film. This has been observed previously in capacitors that have been annealed in reduction atmospheres though in that case it is the creation of oxygen vacancies that poses restrictions on the domain wall movement. Heat treatment is also associated with the rise of internal bias fields in the film that can cause alterations or even suppression of polarization switching. In that case the hysteresis appears displaced or constricted.

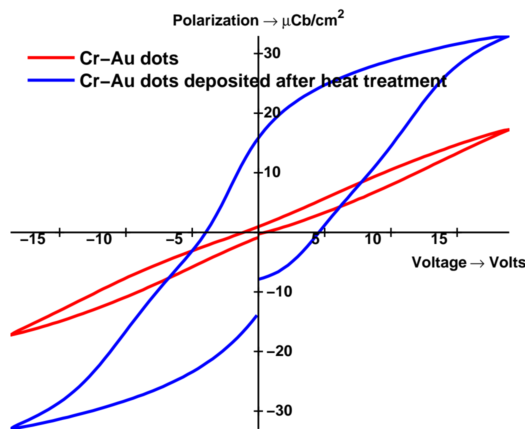

Figure 4.12: Polarization vs field (P-E) hysterisis loops of a PZT 52/48 film with a (111) orientation. The film is deposited on a standard wafer and the Cr/Au top electrodes are deposited prior to the heat treatment (red) and after the heat treatment (blue line). Clearly damage occured in the electrode area.

Testing was then performed on ferroelectric capacitors fabricated from PZT 52/48 ceramic. In figure 4.12 the polarization versus field hysteresis loop of a heat treated ferroelectric capacitor with a Cr- Au top electrode is plotted in red. After testing a new set of top electrodes was deposited by rf sputtering Cr- Au dots on the free surface of the same sample. The result of the newly formed capacitors are plotted in blue on the same graph.

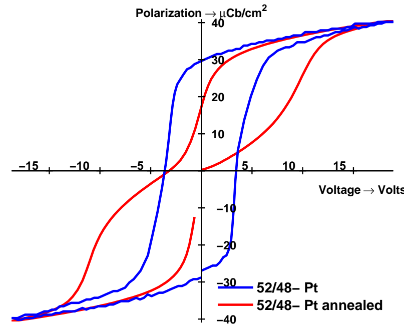

Figure 4.13: Polarization vs field (P-E) hysteresis loops before and after heat treatment of a (100) oriented PZT 52/48 film deposited on a standard wafer when Pt is used as the top electrode.

In figure 4.13 the polarization versus field hysteresis loop of a PZT 52/48 ferroelectric capacitor with a Pt top electrode is plotted before and after annealing. The ferroelectric hysteresis obtained after annealing is pinched and slightly shifted to the negative field axis. Once again displacement of defects in the domain wall area occurs during heat treatment, resulting in abnormal domain switching of the pinned walls in the heat treated films. Surface related phenomena should not be excluded as the result of depositing new electrodes after treatment in 4.13 (α) suggests.

It has been reported that the suppressed polarization switching in fatigued or heat treated ferroelectric films may be recovered by application of a sufficiently high DC electric field or by annealing the film at temperatures higher than the Curie temperature. In our case annealing of the bonded ferroelectric stacks at temperatures over 600 ^oC was not desirable. It was thus decided to investigate the effect of exposing the stack to a high temperature anneal prior to the adhesive bonding.

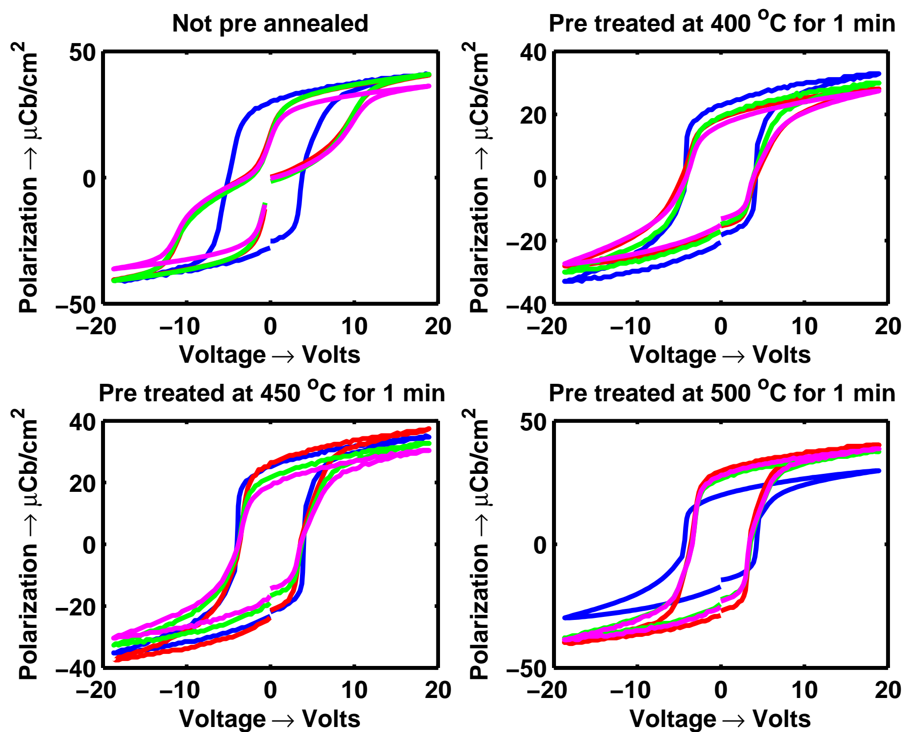

Figure 4.14: Polarization vs field hysterisis loops of PZT 52/48 films deposited on a standard wafer with a (111) orientaion using sputter deposited Pt as the top electrode. All four samples were annealed at $350^{o}C$ for $1\ hr$. The top right and both the bottom loops were obtained from samples that have been heat treated before for $1\ min$ at temperatures between $400\ ^{0}C$ and $500\ ^{o}C$.

Tests were performed on ferroelectric capacitors that were fabricated by rf sputter depositing Pt dots on top of a PZT 52/48 ceramic. The wafer was then cleaved in four pieces. Three of the pieces were given an extra anneal for 1 min at temperatures between $400 \ldots 500\ ^oC$. All four pieces were then heated in a hot plate for 1 hr at 350 ^oC. In figure 4.14 the polarization versus field hysteresis loops for each sample before and after the 1 hr treatment are depicted. It is clear that the high temperature anneal prevents the polarization suppression.

A ferroelectric stack was fabricated by spin coating a platinized Si wafer with a 1 μm thick PZT 52/48 film. The film had a (111) orientation. A blanket Pt layer was deposited by rf sputtering on top of the PZT ceramic and the stack was annealed for 20 min at 450 ^oC. A thin Cr layer was rf sputtered on top of the Pt layer and the wafer was send to KTH for bonding. The thin Cr layer improves adhesion of the adhesive layer on the Pt top electrode. The sample was bonded on an auxilliary wafer and was sent back to Cranfield where the initial Si substrate was dry etched in the DRIE.

In figure 4.15 (α) the polarization versus field hysteresis loop of this sample is depicted in red. For comparison the hysteresis of the same stack before sending it to Sweden is also plotted in blue. It can be seen that the loop is slightly distorted. The inclination of the curve in the saturation points become larger implying a larger dielectric permittivity. At the same time the loop becomes broader indicating a higher dielectric loss. These results are confirmed by the electrical measurements in (β).

The polymer film serving as substrate in this case is less stiff than the standard Si wafers usually used for PZT growth. The measured dielectric permittivity is thus expected to differ from the permittivity of the constraint film. It is known that the dielectric permittivity of a piezoelectric material measured under conditions of constant strain ϵ^x, is related to the permittivity of the material measured under

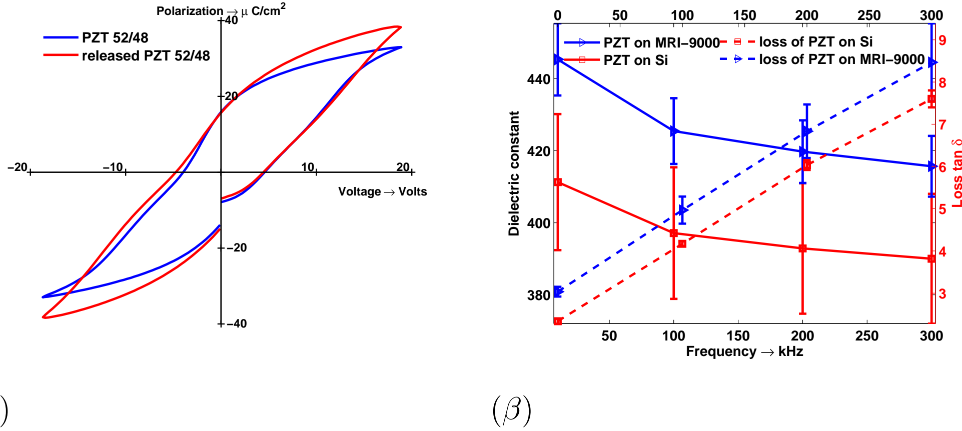

(α) (β)

Figure 4.15: Hysteresis loop of a (111) oriented PZT 52/48 film which has undergone the stress elimination process with sputter deposited Pt serving as the top electrode (red curve). The hysteresis loop of the same film before processing is also plotted for comparison (blue curve). In (β) the dielectric permittivity- loss of the film before and after processing are plotted as a function of frequency.

conditions of constant stress ϵ^T:

$$\epsilon^x = \epsilon^T \left(1 - \frac{d^2}{s^E \epsilon^T}\right) \tag{4.4}$$

In equation 4.4 a one dimensional case has been considered for simplicity. d, s^E are respectively the piezoelectric constant and the stiffness under constant field of the material. The ratio $d^2/s^E\epsilon^T$ is called the piezoelectric coupling of the piezoelectric material, it is always positive resulting in the permittivity of the clamped film ϵ^x to be lower than the permittivity of the unconstraint material ϵ^T.

In this case the film is not totally constrained but clamped on a compliant material. The constitutive equations of the piezoelectric film in the one dimensional

case take the form:

$$x = s^E T + d^T E \quad (4.5)$$

$$D = d^E T + \epsilon^T E \quad (4.6)$$

In equations 4.5 and 4.6 s^E is the compliance of the piezoelectric film measured under conditions of constant field, ϵ^T is the permittivity in the unconstratint state, d^E and d^T are the piezoelectric coefficients measured under conditions of constant field and constant stress respectively.

The film is attached on a substrate with a compliance s_1 and thickness t_1. If the thickness of the piezoelectric layer is t_2 then the strain compatibility and the static equilibrium conditions are:

$$x = s_1 T_1 \quad (4.7)$$

$$T_1 t_1 = T t_2 \quad (4.8)$$

Where T_1 is the stress that rise in the adhesive layer. Substituting in 4.7 X_1 from 4.8 and setting equal to 4.5 the stress X is derived in 4.9 and from that the dielectric displacement D (equation 4.10):

$$T = \frac{d^T}{-s_1 \frac{t_2}{t_1} - s^E} E \quad (4.9)$$

$$D = \underbrace{\epsilon^T \left(1 - \frac{d^T d^E}{\left(s_1 \frac{t_2}{t_1} + s^E \right) \epsilon^T} \right)}_{\epsilon^{const}} E \quad (4.10)$$

In equation 4.10 ϵ^{const} is an expression of the permittivity of the partially constraint film. In the case of a very compliant substrate with $s_1 \rightarrow \infty$ from 4.10 one gets $\epsilon^{const} = \epsilon^{T}$. On the other hand in the case of a very stiff substrate $s_1 = 0$ and the expression of the dielectric permittivity gives $\epsilon^{const} = \epsilon^{x}$ as should be expected.

Chapter 5

Dynamic Measurements

Dynamic stress analysis of MEMS devices operating at resonance was performed in collaboration with Bristol university, using a technique based on time-resolved micro-Raman spectroscopy. In this study piezo actuated Si cantilevers were used as test vehicles for the evaluation of the dynamic strains that rise in the structural layer of a resonating MEMS device.

Accelerated fatigue testing of PZT bimorph devices was also performed. The devices had a clamped clamped bridge type geometry and the maximum deflection at resonance was monitored as a function of time.

5.1 Device fabrication

5.1.1 Microcantilevers

The micro cantilevers used in this study were fabricated using surface and bulk micromachining techniques on a Si on insulator (SOI) wafer. The fabrication process is presented in detail in chapter 2. The thickness of the Si structural layer was 10 μm and it was covered with a 200 nm thick SiO_2. The thickness of the

buried oxide, which serves as the etch stop layer during the back etching of the Si in the DRIE was 1 μm.

The transducer element was a 1 μm thick Pb $(Zr_{0.3}Ti_{0.7})\,O_3$ (PZT) film deposited on top of a Ti/Pt thin layer. This 100 nm thick Pt film was RF magnetron sputtered at room temperature on top of an underlying 8 nm Ti adhesion layer. X-ray diffraction confirmed that the PZT film was well crystallized with the expected (111) orientation.

Finally the Pt top electrode with a thin (8 nm) Ti adhesion layer was deposited by a lift-off bi-layer process, using LOR2A and S1818 to pre-pattern the top of the PZT. The thickness of the top electrode was varied in order to achieve a null total bending moment due to the residual stresses in the films of the PZT stack and end up with flat structures [109].

The PZT, Pt and SiO_2 layers of the stack were successively dry etched using Reactive Ion Etching (RIE) and the cantilevers were finally released by dry etching the Si using Deep Reactive Ion Etching (DRIE). PZT was etched using a CHF_3/Ar/O mixture while for Si etch, SF_6 was used. Three different types of devices: named F1-3, were fabricated and BCB bonded for testing. The dimensions of the Si structural layer are presented in table 2.3.

The devices were diced from the wafer and then attached on BCB frames using wire bonding in order to facilitate handling and excitation for further testing. A rectangular window was opened in the BCB frames prior to having the device dies attached on them. This window provides access to the UV RAMAN laser to the exposed Si base of the piezo actuated cantilevers. Figure 5.1 (α) depicts a device die attached on a BCB stage. The wires that connect the device electrode pads to the Cu covered BCB lines are barely visible. In the inset the rectangular window drilled in the back of the BCB frame is shown under higher magnification.

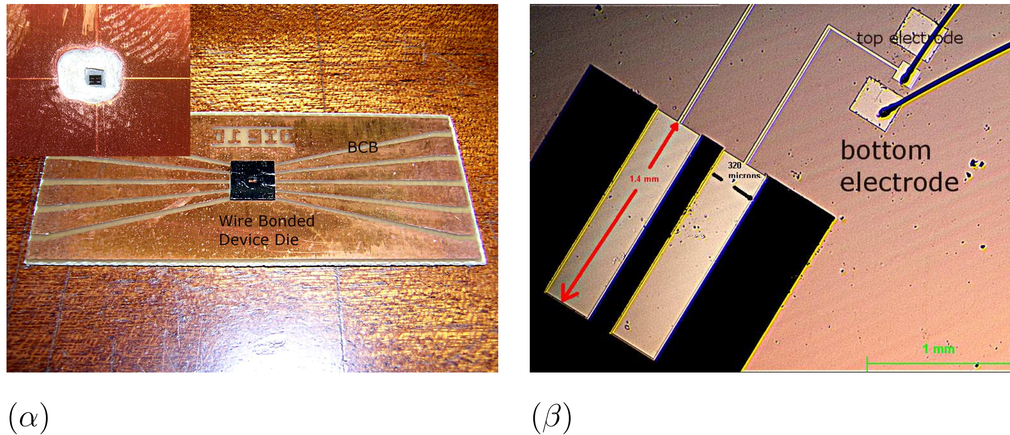

(α) (β)

Figure 5.1: Optical micrographs of (α) the BCB wire- bonded Si cantilevers that were used for RAMAN spectroscopy and (β) the same cantilevers under higher magnification. The wire bonded pads that provide access to the top and bottom electrode are also illustrated.

In figure 5.1 (β) an optical micrograph of the actual devices is shown where the beams dimensions are clearly illustrated. The electrode pads are also shown with the wires for the electrical connection attached on them.

5.1.2 PZT bimorphs

PZT bimorphs were fabricated following the process flow presented in chapter 2. For the purpose of this study the thickness of both the lower and the upper PZT (30/70) ceramic film was $\approx 750\ nm$. Following our previous findings on the deleterious effects that heat treatment had on the ferroelectric properties of a PZT stack: depending on the top electrode configuration used, it was decided that no adhesion layer would be introduced between PZT and Pt electrodes. This

severely compromised the adhesion of the Pt film on top of the PZT causing it to de laminate and blister when it was attempted to deposit the second PZT layer on top of it.

In order to improve the adhesion of the Pt film on top of the lower PZT layer a series of annealing trials were performed to establish the optimal processing conditions prior to the deposition of the second PZT layer. This heat treatment was expected to anneal out the high compressive stress in the as deposited Pt film and possibly remove any trapped Ar atoms.

After completion of the first PZT layer a Pt blanket layer was sputter deposited with the expected $< 111 >$ orientation. The wafer was cleaved in nine smaller pieces which served as samples for the annealing trials. Tests were contacted at temperatures between $400 \ldots 700^oC$ for 10 min, 15 min and 20 min. In every case PZT growth on top of these processed stacks proceeded without problems so a post deposition anneal at 450^oC for $15 - 20$ min was decided.

The sol gel deposition was then resumed and the second PZT layer was deposited on top of the stack. On top of that second PZT film another blanket Pt layer was rf sputter deposited. The whole bimorph stack was heat treated at 530^oC for 20 min so all three Pt electrodes would end up with the same thermal tensile strain built in them for stress balancing purposes. This is because the released devices are designed to be symmetrical around the mid Pt electrode so it is expected that the neutral axis will coincide with the mid axis and the resulting bending moments from the top and bottom Pt electrodes would be counter balanced.

This annealing step also enhanced the adhesion of the Pt top electrode prior to the electro plating of the Ni hard masking. Electro plating conditions were further optimized by decreasing the current density as it was observed that the Pt top electrode would peel of when Ni electro plating was performed under conditions of

high current density. The Pt top electrode and the PZT layer of the upper stack were successively dry etched using Reactive Ion Etching (RIE). After patterning and dry etching the mid electrode a Ti/Au seed layer was rf sputter deposited on top of the wafer prior to the second Ni hard masking. The rest of the layers were dry etched in the RIE and the devices were finally released by dry etching the Si using Deep Reactive Ion Etching (DRIE). Two different types of devices were finally released for testing, five of the BBS type (BBS1-5) and six of the BS type (BS1-6).

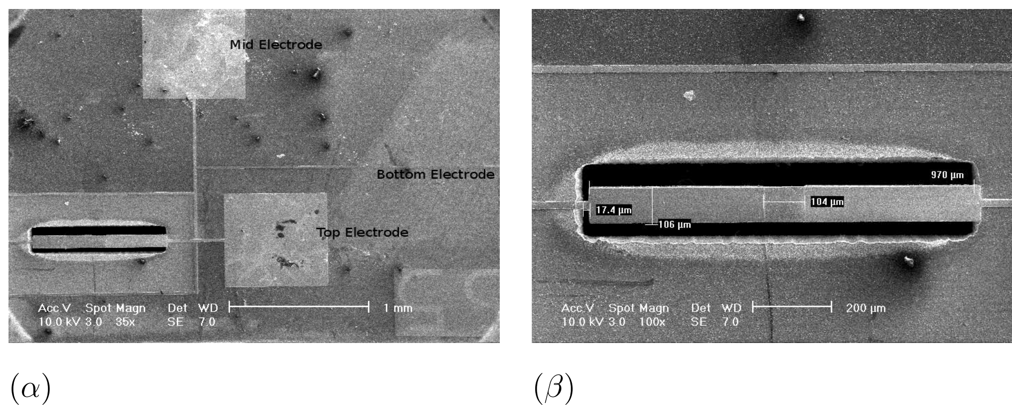

(α) (β)

Figure 5.2: SEM micrograph of a PZT bimorph (α) and the released beam under higher magnification (β). The left anchor has been over etched.

Figure 5.2 depicts a SEM micrograph of device die BBS5. The three electrode are annotated in (α) while in (β) the actual device is depicted under higher magnification. The left anchor of the beam is suspended as can be clearly seen in (β). This is a result of the DRIE isotropic etching combined with the poor alignment accuracy of the KARL SUSS front to back aligner. This was observed in all the released devices. It was expected that the amount of stress that would rise in these

short ligaments during bimorph testing would possibly cause them to fracture pre maturely invalidating the result of the test.

It was thus decided to repeat the fabrication of bimoprhs. Extra care was taken with the front to back alignement step and the DRIE back side Si etching in order to eliminate the appearance of these over etched beam anchors. Once again results were disappointing revealing a limitation in the mask design and the accuracy of the alignment that could be achieved. The mask set design needs to be revised in order to eliminate the risk of over etching the anchor of the beams. However we proeceeded with testing as this is the first attempt to fabricate PZT bimoprhs and interest in probing the ferroelectric and the dielectric properties of these films was high.

5.2 Electric- Ferroelectric Characterization

After the beams were successfully released, the PZT film was poled by direct application of a constant DC voltage (20 $Volts$) at an elevated temperature (130 ^{o}C) for 10 min. In figure 5.3 the polarization hysteresis curves as a function of the applied field are shown before and after device poling, as they were obtained using an RT66A bridge.

The electric properties of the piezoelectric film were investigated using a Wayne Kerr network analyzer where the dielectric loss and the relative permittivity of the film were measured in a range of frequencies 5.4. It can be seen that after poling both the remanent polarization and the coercive field of the PZT film increased significantly. The loop is slightly shifted towards the negative voltage axis. This is possibly caused by the rise of an internal bias field during poling.

In figures 5.5 and the polarization versus field hysteresis loops of the top (blue

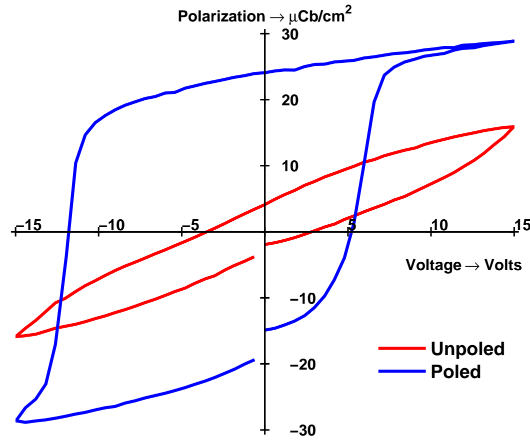

Figure 5.3: Polarization versus field (P-E) ferroelectric hysteresis loop of the device PZT film before and after poling.

curve) and the bottom (red) PZT layer of the bimorph structure are plotted. The loops are very similar to each other.

The dielectric permittivity as a function of the frequency is plotted in 5.6 for three different devices. The corresponding dielectric loss $\tan\delta$ as a function of frequency is also plotted in the same graph.

For frequencies above 100 kHz the dielectric loss $\tan\delta$ becomes extremely high. This is believed to result from the way the top electrode is defined on top of the PZT ceramic. Due to the limitations imposed by the total number of masks that could be designed, the top electrode and the underlying PZT film of the bimorphs are defined by the same mask. There is thus no inset between the Pt top electrode and the ceramic and this can contribute to the resistive loss of the device.

An additional contribution to the high resistive loss observed at higher frequencies comes from the long transmission lines which are combined with large area

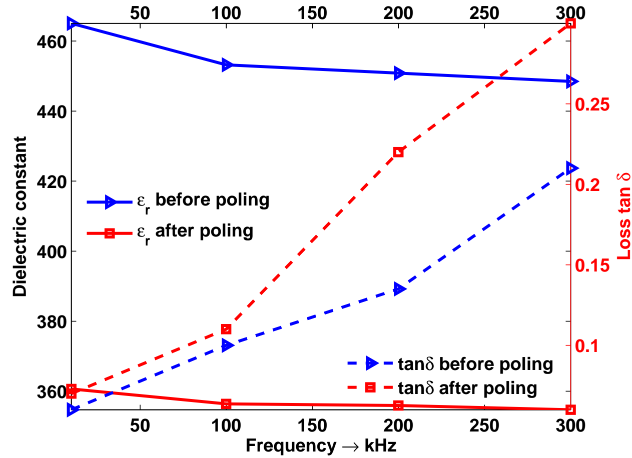

Figure 5.4: Dielectric permittivity- loss as a function of frequency before and after PZT poling. Note double y- axis.

electrode pads for easy probing of the three device electrodes. The large overall area of the Pt bottom electrode results in a rather high resistance which obviously affects the way the weyne kerr presicion component analyzer extracts the loss parameters from the measured impedance.

5.3 Laser Doppler Vibrometry

The devices were further characterized using Laser Doppler Vibrometry (LDV). In this case the Polytech Gmbh, PSV 3000 Laser Doppler Vibrometer was used and all the measurements were carried out using the simple beam configuration. In this, at least three reference points on the sample surface are defined before the measurement and all the measured values are calculated with respect to the values obtained for these points.

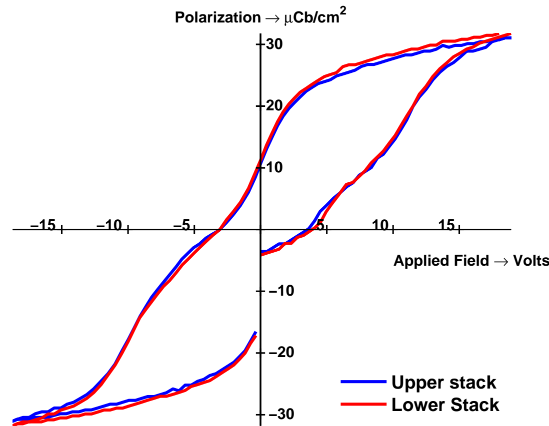

Figure 5.5: Polarization versus field ferroelectric hysteresis loop of the bimorph top and bottom PZT film.

At first a fast scan was performed using the periodic chirp mode to define the resonant frequencies of each beam. Frequencies between zero and 200 kHz were scanned using complex averaging to improve the signal to noise ratio and enhance the resolution of the measurement. The frequency range was divided to 6400 intervals, the maximum number of sample points allowed in this operational mode. In table 5.1 the first three resonant frequencies of each type of device, as defined using the LDV set up are presented.

For each normal mode a HEWLETT PACKARD 33120A high frequency generator was used to excite the device with a sinusoidal waveform of 5 $Volts$ amplitude and a scan was perform to define the corresponding modal shape. Apart from the F1 type of cantilevers which fit well in the field of view of the available lenses only a small portion of the F2 and F3 beams close to the tip was scanned. The measured frequencies are in good agreement with the modal analysis results presented in table 2.5. The devices were sent to Bristol University where only the type F1

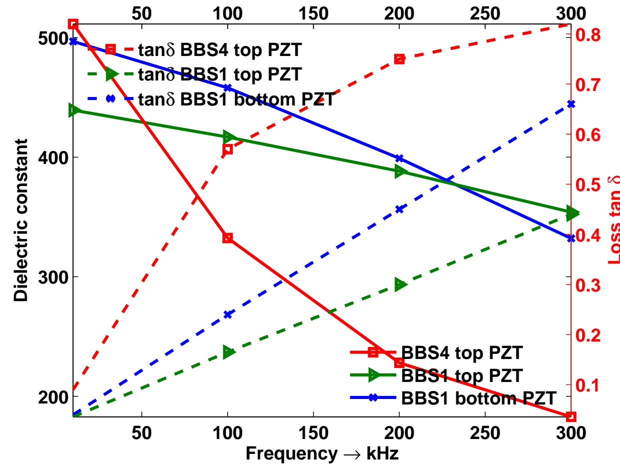

Figure 5.6: Dielectric permittivity and dielectric loss of the bimorph top and bottom PZT film.

devices were finally characterized.

In figures 5.7 and 5.8 the first and the second mode of resonance of the measured F1 type device are shown respectively, while in table 5.2 the measured resonant frequencies and the corresponding tip deflections are summarized. The quality factor Q of the device at each mode of resonance as it was evaluated from the spectral response for each resonant frequency is also presented.

The modal shapes and the resonant frequencies of the PZT bimoprh structures were also measured using the LDV. The devices were probed using the HEWLETT PACKARD 33120A signal generator operating at the periodic chirp mode. The signal amplitude was limited at 1 $Volt$ as there were concerns about the endurance of the overecthed anchors. The scanned range of frequencies was limited between $1 \ldots 200$ kHz and the measured resonant frequencies are summarized in table 5.3.

The agreement between the measured and the calculated resonant frequencies in

Table 5.1: Resonant frequencies of the piezoactuated cantilevers F1-3 used for dynamic stress evaluation measured using LDV.

Device type	1st (kHz)	2nd (kHz)	3rd (kHz)	4th (kHz)
F1	6.094	37.890	106.500	145.700
F2	4.688	29.500	82.560	161.900
F3	1.219	7.125	22.904	36.781

Table 5.2: Resonant frequencies and tip deflections measured by LDV. Quality factors were also evaluated from the FWHM of the spectral response.

	1st Resonant mode	2nd Resonant mode
Frequency (KHz)	6.094	37.89
Tip deflection (μm)	22.5	5
Q	273	460

this case is poor. This is the result of the fabricated devices being considerably different than the modeled designs. Due to the over etching of one of the beam anchors the final bridges are no longer symmetric and this introduces extra modes of resonance with more complex deflection profiles. In addition the finite element model did not take into account any stress stiffening effects which are expected to alter the resonant frequencies. Tensile stress is known to cause the first resonant frequency of a bridge type device to shift to higher values while compressive stress has an opposite effect.

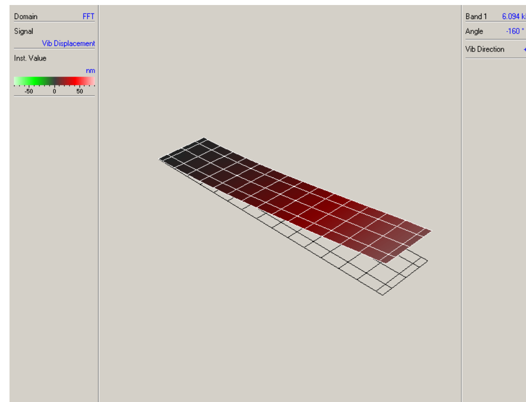

Figure 5.7: First resonant mode of the cantilever beam used for RAMAN stress measurements. The resonant frequency is 6.094 KHz

5.4 Accelerated Fatigue Testing

Poor accuracy of the front to back alignment process, combined with a mask design that did not provide adequate space between the border of the back etch area and the signal transmission lines resulted in part of the beam anchor to be over etched exposing a small part of the transmission line. This can be clearly seen in figure 5.9 (α) where an SEM micrograph of the bridge type bimorph structure (BBS5) is depicted under high magnification. A thin ligament $\approx$ 30 μm long which is already broken can be clearly seen.

Most of these overetched parts broke during the attempts to release the individual device dies. Even those that survived the dicing process broke during the resonant frequency measurements in the LDV.

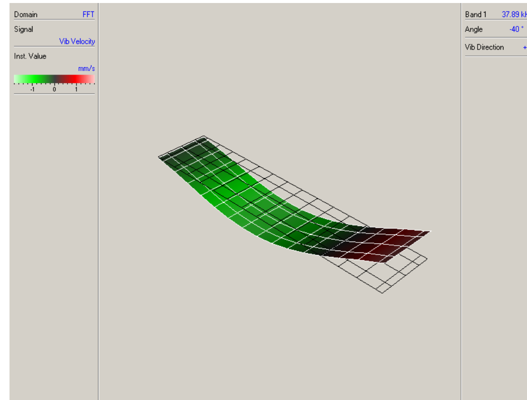

Figure 5.8: Second resonant mode of the cantilever beam used for RAMAN stress measurements. The resonant frequency is 37.890 KHz

An example of a beam that failed prematurely during the vibrometry measurements is depicted in figure 5.9 (α). In 5.9 (β) the crack area is shown under higher magnification. Cracking was initiated in the upper left edge of the beam at the point of contact with the wafer. After a critical length was reached it propagated through the ceramic layers following an almost straight line.

This is further supported by the SEM micrographs of the bimorph beam that are depicted in figures 5.10 (α) and (β). These images were captured from the back side of the bimorph devices. In 5.10 (α) a general view of the back of the device is depicted while in (β) interest is focused on the crack area. The Pt bottom electrode has delaminated along the area of the free crack propagation.

In figures 5.11 (α) and (β) SEM micrographs of the cracked surface are depicted. The columnar grain structure of the PZT ceramic is clearly seen.

Table 5.3: Resonant frequencies of the PZT bimorph devices measured using LDV.

Dev	1st (kHz)	2nd (kHz)	3rd (kHz)	4th (kHz)	5th (kHz)	6th (kHz)
BBS2	22.72	43.28	76.75	103.40	149.60	186.30
BBS3	23.69	45.03	76.50	106.40	152.90	190.20
BBS5	11.38	28.00	47.06	55.81	67.91	103.70
BBS5	39.72	53.66	75.00	93.25	121.30	156.10

The periodic chirp signal that was used to define the resonant frequencies, causes the beam to vibrate in a number of modes of vibration thus complicating the loading conditions at the anchor. Cracking on the other hand advanced very fast so no stress versus number of cycles data can be extracted.

5.5 RAMAN Results

An initial scan on an inactive cantilever was performed and the static stress in the Si substrate was found to be negligible compared to a reference bulk sample $< 6.5\ MPa$. The cantilevers were then driven at resonance using the same conditions as described above and the dynamic stresses that rise in the Si substrate were measured across the longitudinal axis of the samples using Raman spectroscopy as a function of time.

In figures 5.12 and 5.13 the data for a cantilever beam vibrating at the first and second resonant frequency respectively, are plotted as a function of time for different points across the longitudinal axis. The dynamic stresses oscillate between tensile and compressive during each cycle with a $\pi/2$ phase shift relative

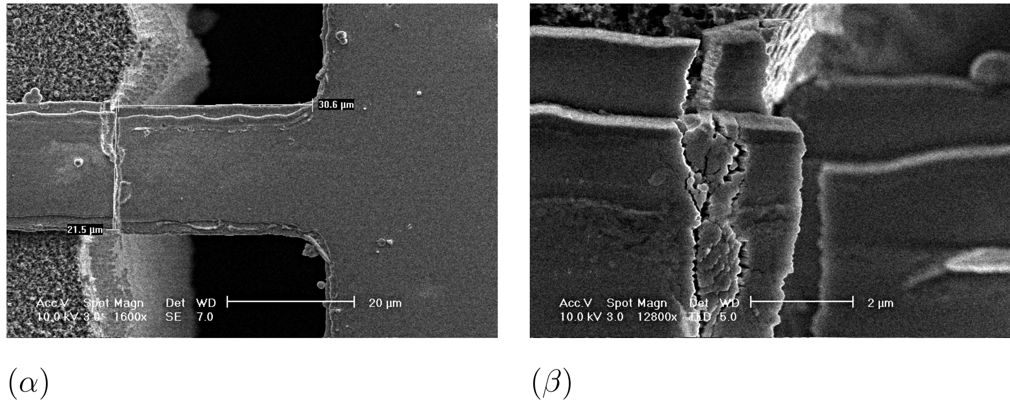

(α) (β)

Figure 5.9: SEM micrograph of the broken anchor of a PZT bimorph (α). Detail of the crack initiation area (β).

to the applied sinusoidal voltage, as was expected for a damped forced oscillator.

The maximum stress amplitude is between 150 MPa and 200 MPa with a 30 MPa resolution for both modes of resonance and it is generated at the cantilever base where the maximum curvature occurs. In the second mode of resonance an additional point of maximum stress and of opposite sign relative to the sample's base stress, is observed at an inflection point located 700 μm away from the cantilever base.

A more detailed analysis performed in the maximum stress points of both resonant modes for longer integration times, improved further the stress resolution to 10 MPa. The maximum values obtained from this more detailed measurement were 120 MPa for the cantilever base point in both modes and 180 MPa for the inflection point of the second resonant mode.

From figures 5.12 (α) and (β) the maximum stress locations which are at $x = 0$ for the first-order mode, and $x = 0$, $x = 700$ μm for the second-order were identified.

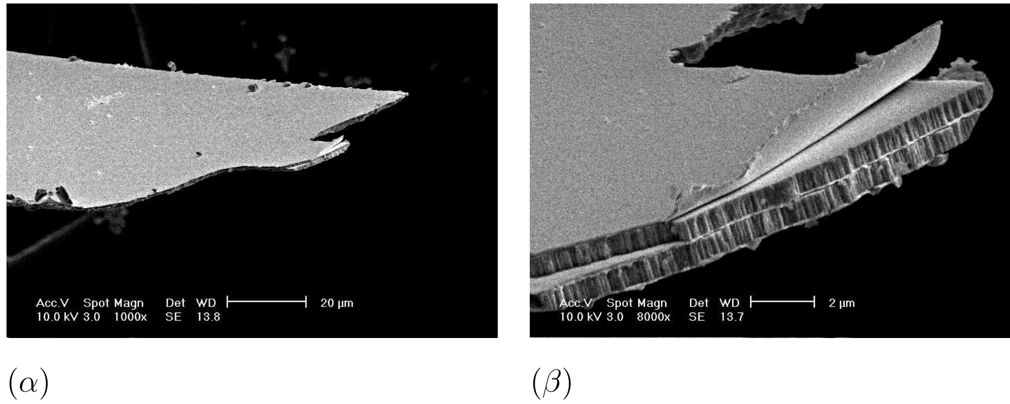

(α) (β)

Figure 5.10: SEM micrograph of the bottom of the PZT bimorph after failure (α). The cracked area under higher magnification (β).

Figure 5.14 (α) shows the dynamic stress measured at the microcantilever base for the first order resonant mode. The stress evolution is sinusoidal and has an amplitude of $120 \pm 10\ MPa$. It was observed that the phase of the stress response lags the driving voltage by $\pi/2$, a characteristic of resonant operation. In figure 5.14 (β) the stress measured for the microcantilevers second order resonant mode, which is also sinusoidal, and has an amplitude of $120 \pm 10\ MPa$ at the microcantilever base and $180 \pm 10\ MPa$ at x=700 μm is depicted. The stress responses at x=0 and x=700 μm are opposite in sign due to the opposite microcantilever bending at these points illustrated in figure 5.12 (β) .

5.6 Device Modelling

It was attempted to combine the dynamic stress maps with the deflection measurements using this 3-D finite element ANSYS model. Measured quality factors

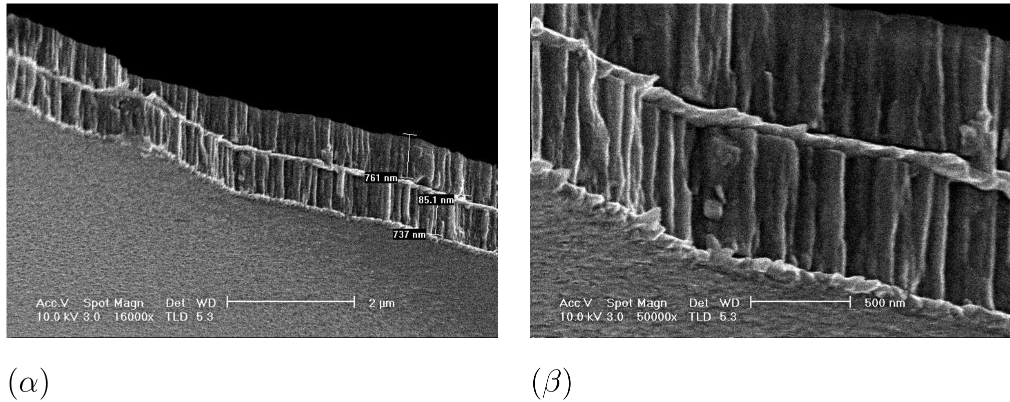

(α) (β)

Figure 5.11: SEM micrograph of the cracked area (α). Detail of the crack (β).

were used as input in the model and the only adjustable parameters were the piezoelectric film properties. Modal analysis was performed for the different types of PZT ceramics from ferroperm and the resulting resonant frequencies for the first three resonant modes are outlined in table 5.4.

Good agreement was obtained between the measured (table 5.1) and the calculated resonant frequencies in the case of the PZ24 ceramic. A harmonic analysis was performed using PZ24 mechanical and piezoelectric parameters as inputs in the ANSYS model. A global damping ratio was calculated for each one of the first two resonant modes from the experimentally defined quality factors in table 5.2, $\xi = 1/2Q$ namely 0.0018 for the first and 0.001 for the second mode.

ANSYS harmonic analysis overestimated considerably the maximum deflection at resonance. For the first mode of resonance a maximum deflection of 136 μm is derived from the model while for the second mode of resonance the calculated maximum tip deflection is $\approx$ 40 μm. These results differ considerably from the measured maximum deflections which were 22.5 μm and 5 μm at the first and the second resonant modes respectively.

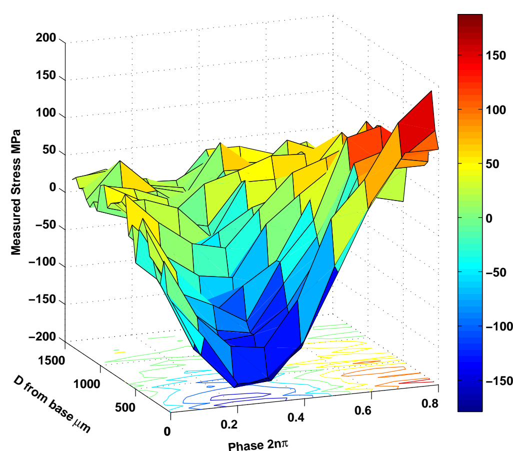

Figure 5.12: Dynamic stress map of the micro cantilever vibrating at the 1st resonant frequency

The next step was to calculate the stress profile along the length of the cantilever when the beam is displaced at the maximum position of each resonant mode. The modelled dynamic stresses would then be compared to the experimentally measured ones.

In figure 5.15 (α) the calculated (solid lines) stress profiles along the length of a cantilever vibrating at the first and the second resonant frequency are plotted, assuming a PZT film with the mechanical and the piezoelectric properties of the PZ24 Ferroperm ceramic. The experimentally measured dynamic stress along the length of the cantilever, which was measured using RAMAN spectroscopy is also plotted (single points) for comparison.

The calculated stress profiles follow in general the distribution of the experimental stress measurements. However, agreement between the calculated and the experimental values is poor. ANSYS results for the first resonant mode underestimate

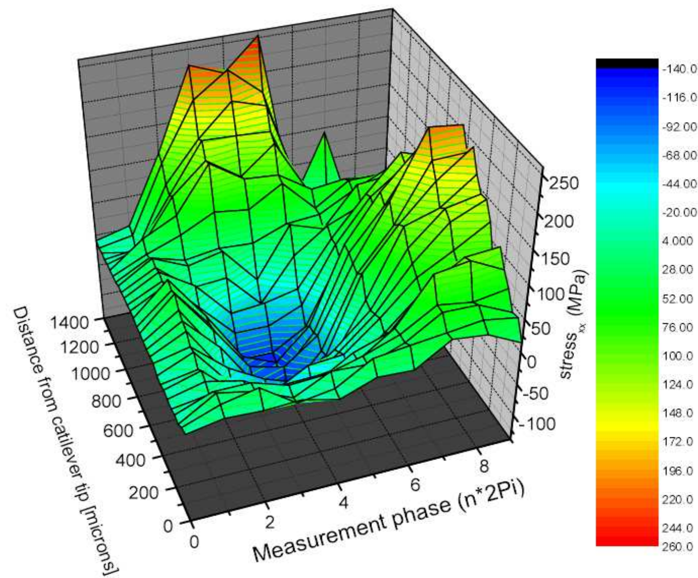

Figure 5.13: Dynamic stress of the micro cantilever vibrating at the 2nd resonant frequency

the actual stress levels. The simulated stresses in the case of the second modal shape on the other hand underestimate the maximum value in the area of the deflection point by as much as 100 MPa.

Assuming the piezoelectric coefficients of the PZ24 ceramic for the PZT film, very good agreement could be obtained between the FEA results and the measured resonant frequencies however the agreement between the calculated and the measured stresses was less good. Even more so the calculated maximum deflections overestimated considerably the measured ones.

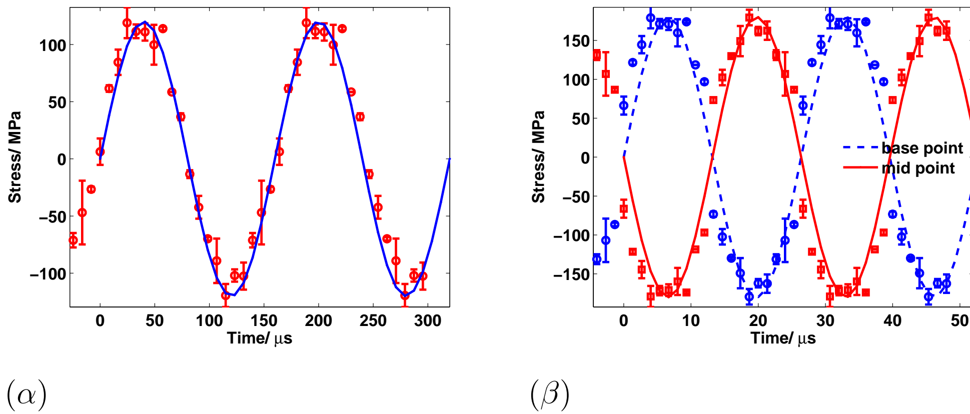

(α) (β)

Figure 5.14: Dynamic stress at the base of the micro cantilever vibrating at the 1st (α) and 2nd (β) resonant frequency as a function of time.

The harmonic analysis was repeated assuming the PZ34 and PZ46 properties for the PZT film. The choice was based on the observation that the resonant frequencies calculated in table 5.4 in the case of these ceramics were close enough to the measured ones. In figure 5.15 (β) the calculated stress profiles along the length of a resonating cantilever with a PZ34 ceramic layer are plotted. The calculated maximum tip deflections in this case were 22 μm and 5.2 μm for the first and the second resonant mode respectively. Once again it was not possible to achieve good agreement between all the calculated and the measured properties of interest (resonant frequency, maximum deflection and dynamic stress).

Uncertainties in other simulation parameters like the exact dimensions, the mechanical properties and the damping ratio of the individual layers comprising the beam also affect the accuracy of the calculation. Another serious limitation of the finite element model is that only linear materials are considered in the harmonic analysis, however domain switching and as a result non linear straining of the PZT

Table 5.4: Resonant frequencies of type F1 piezoactuated cantilever used for dynamic stress measurements, calculated using ANSYS FEA for different types of PZT film. The properties of the different types of film were taken from FERROPERM catalogue.

PZT type	1st (kHz)	2nd (kHz)	3rd (kHz)
PZ21	5.791	36.254	101.850
PZ23	5.888	36.864	103.550
PZ24	6.067	37.989	106.560
PZ26	5.950	37.251	104.620
PZ27	5.824	36.463	102.420
PZ28	5.960	37.316	104.790
PZ29	5.844	36.590	102.760
PZ34	6.326	39.611	111.180
PZ46	6.187	38.742	108.760
PZ26b	6.006	37.604	105.620

ceramic, is likely to occur under the excitation voltage used in these experiments.

The observed discrepancy between the modelled and the measured dynamic stress needs to be further investigated. So far dynamic stresses that rise in resonating structures used for studying fatigue in micro structures were modelled using finite elements. This method based on time- resolved, micro RAMAN spectroscopy may be used instead to measure directly and more accurately the dynamic stress at least in Si based MEMS components.

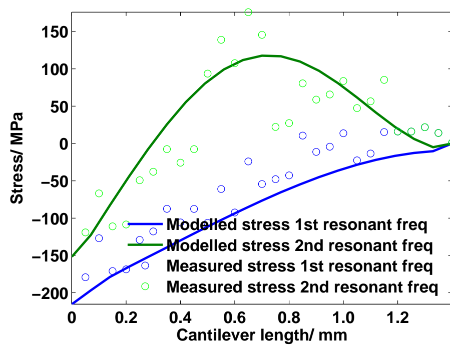

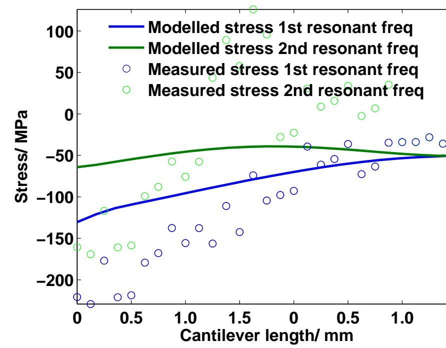

(α) (β)

Figure 5.15: Calculated versus measured stress profiles for the 1st and 2nd resonant frequency using PZ24 parameters (α) and PZ34 parameters (β).

Chapter 6

Discussion- Conclusions- Recommendations for Future Work

6.1 Discussion

Mechanical testing of piezo ceramics in thin film form has been attempted by various researchers. The most commonly used methods include bulge testing, instrumented nano indentation and resonance tets. These methods were briefly reviewed in the first chapter of this thesis. The advantages of each method concerning sample preparation, sample handling and the type of material properties that can be extracted from the experimental data were also presented. Here a brief comparison between the different methods, including the micro tensile testing method that was developed during this study, is attempted.

The main advantage of instrumented nano indentation is that no special test structures are required. Tests are performed directly on the films of interest making sample preparation and data aquisition easy and fast. Interpretation of the results is also straightforward since the sample geometry is quite simple without the complications and uncertainties of micro fabricated structures. The

tip of the nanoindenter can be used as a top electrode and the moduli of the films under conditions of constant electric field can be measured. However for large penetration depths in thin film testing the geometry of the indenter tip as well as the substrate stiffness need to be taken into account. Furthermore the Poisson's ratio of the specimen needs to be assumed when the nanoindentation is used for the evaluation of the Young's modulus.

Bulge testing is also performed at a wafer scale, usually using highly automated test jigs. Data aquisition is fast however sample preparation is more complicated compared to the simple films used with instrumented nano indentation. The film diaphragms used for testing are relatively easy to fabricate by simply depositing the film of interest usually on one side of a Si substrate wafer. The other side of the wafer is then patterned and the Si is etched using bulk micro machining techniques until the membranes are released. The side of the wafer where the film is deposited must be properly shielded in order to protect it from the KOH etchant. This is especially true when PZT membranes are fabricated as it was found during this study. It was observed that the KOH etchant could cause signifficant corrosion to the ceramic unless the process was closely monitored. Apart from the plane strain modulus, the fracture strength and the residual stress in the films, the fracture energy of the film- substrate interface can be evaluated using the bulge test. As is the case with the nanoindentation test, the Poisson's ratio needs to be assumed in case the Young's modulus of the material is calculated.

Finally in dynamic tests special test structures like cantilever or clamped- clamped bridge type beams are fabricated. The first resonant frequency of a beam is measured which in the case of a free standing cantilever type beam is a function of the density ρ and the Young's modulus of the material. For bridge type beams the first resonant frequency also depends on the residual stress built in the beam. Frequency measurements should be carried out under vacuum conditions as air

damping can cause the resonant frequency of the micro fabricated beam to shift. Fabricating free standing PZT ceramic beams with a thickness $t \approx 2\ \mu m$ using sol-gel deposition involves some processing steps that can be rather time consuming. Furthermore issues related to finite size effects that normally arise during micro processing can result in structures with a geometry considerably different than the initial design thus making interpretation of the results more difficult.

Use of micro tensile testing for mechanical characterization of brittle materials is fairly new. This was the first time that the method was applied to PZT ceramic films. Samples can be very fragile making sample handling and mounting on the tensile stage very difficult. Keeping the sample axis aligned to the external load is also a major concern. These obstacles are overcome by depositing the tested films on special frames made usually from Si. The most recent designs include frames with a stationary and a moving part where the external load is applied. The use of these special Si made frames facilitates sample handling and ensure that alignment to the external load is achieved during micro fabrication. IMTEK's recent design eliminates the need for dicing the Si frames from the wafers thus making possible to perform tensile testing in a highly automated way.

During this study three different configurations were tested. Releasing the dog bone shaped samples proved rather difficult. Samples were very fragile and were breaking at different steps of the fabrication process. It was thus decided to fabricate samples with the Pt and SiO_2 underlayers preserved. That way the yield of the successfully released samples improved however the calculation of the film properties became more complicated and extra assumptions concerning the properties of the underlayers are needed. Attempts to assess the mechanical response of the underlayers as well as the properties of composites with a layer structure $SiO_2/Pt/ZnO$ were unsuccessful. It is believed that the low yield of successfully measured samples is mainly caused by the reduced stiffness of the

special Si frames where the samples are deposited on. As a consequence of the DRIE isotropic etching the Si suspension beams end up 25% thinner than the initial design. This makes the frames compliant and is likely to cause pre mature failure of the devices.

6.2 Conclusions

- A method for probing the mechanical response of thin film materials based on miniature tensile testing is presented. The tensile stage was developed in collaboration with DEBEN UK. It is a commercial 200K model made by DEBEN which was specially modified for testing samples in the micron scale. The stage can be fitted with two different types of mounting jaws for performing conventional tensile testing or bending tests. The option of low frequency cyclic loading is also available.

- Strains are extracted directly from the deformation of the sample surface by correlating digital images captured using SEM imaging techniques. The freely distributable MATLAB code from Johns Hopkins University was used as the basis for the DIC method.

- Test samples of different dimensions were designed and fabricated. The smaller ones come mounted on a specially designed Si frame with an inner moving stage and an outer stationary part which facilitates sample handling. Studied are thin film materials used in piezo MEMS fabrication like PZT and ZnO ceramics. LCP, LCP-Au composite structures as well as electro plated Ni were also tested.

- The extracted Young's moduli of the LCP, LCP-Au composite and electro plated Ni samples agree well with the literature. The Poisson's ratio of the

electro- plated Ni is also estimated equal to $\nu = 0.37$. The Young's modulus of the electro plated Ni is expected to vary with the deposition conditions which control the film micro structure.

- Yield of successfully released ceramic samples is rather poor, even when they are deposited on top of the specially designed Si frames. Results from testing two PZT samples lead to a Young's modulus of $27 \pm 7\ GPa$. The fracture strength of the two samples is 270 MPa and 350 MPa respectively. It should be noted that this is a very small of samples for a reliable statistical analysis. In addition, the geometry of the tested samples is found to depart from the mask design. This is due to the over etching of the Si substrate during the DRIE process which exposes part of the sample anchor resulting in a non uniform straining of the the tested specimen.

- A finite element model of the sample geometry was developed using ANSYS parametric design language. The model accounts for finite size effects rising from the geometry of the sample and the fabrication process. Based on the results of the simulations a correction is applied to the experimental data. According to this the actual modulus is 15% higher.

- In collaboration with IMTEK in Freiburg composite structures comprising of SiO_2/Pt/PZT were tested using their wafer scale tensile test set up. Sixteen samples of both 52/48 and 30/70 compositions were successfully released. Bulge testing was also performed on PZT membranes in order to check the validity of the tensile testing results.

- A finite element model of the composite dog bone shaped samples is developed using Ansys parametric design language. The model is based on the one that was developed to simulate the sample geometries designed at Cranfield. This model assumes that all three materials are homogeneous

with the properties of the Pt and SiO_2 underlayers being constant. Based on the results of the simulations a correction is applied to the experimental data.

- A statistical analysis is performed using the data from the two samples tested at Cranfield and the sixteen samples tested at IMTEK. The 95% confidence interval for the Young's modulus of the ceramic is 57 ± 16 GPa almost 25% less than the value of 70 GPa reported for the bulk. This is a direct consequence of the small mean diameter of the grains in the film microstructure. Compared to the findings of nanoindentation this result is $\approx$ 16% higher. It is believed that this discrepancy is mainly due to the assumptions used in the fem model that calculates the applied correction in the experimental data. A more refined model should take into account the transverse isotropic properties of the PZT layer and allow fluctuations in the properties of the underlayers as well. Bulge testing results on the other hand are in good agreement with the literature.

- The composite structures that were tested at IMTEK come in two different configurations. In eleven of them the thickness of the underlying SiO_2 film is 0.2 μm while in the remaining five the oxide thickness is equal to 1 μm. The 95% confidence interval for the fracture strength and Weibull modulus of the samples with the thinner oxide is 295^{+23}_{-21} and $8.3^{+5.2}_{-3.2}$ respectively. The corresponding data for the samples with the thinner oxide are 394^{+78}_{-65} and $5.1^{+5.8}_{-3.7}$. The samples with the thinner oxide appear to fracture easier in a less brittle manner than those with the thicker oxide however no definite conclusion may be drawn from this data.

- The residual stress in the composites was also estimated. From analyzing two samples with a thin oxide underlayer a residual stress equal to $45 \pm$

15 MPa is found. On the other hand the residual stress in the samples with the thicker oxide is found equal to 81 ± 8 MPa.

- Stresses in ferroelectric stacks are also measured using the wafer curvature technique. The results are in good agreement with the literature and a very high tensile stress in the Pt bottom electrode is confirmed.

- A technique to eliminate stress in sol- gel deposited ferroelectric stacks, based on transfer wafer bonding is developed. Cantilevers based on this scheme are fabricated, using rf- sputter deposited Al as the structural layer. The resulting structures are not flat however the method may be used for fabricating beams having the PZT layer under the structural layer in cases that maximum downward deflection from a piezo activated cantilever is desired.

- Heat treatment during bonding is causing the ferroelectric properties of the stack to deteriorate. This is investigated by exposing samples with different top electrode configurations in the same conditions as the bonded wafers. Ferroelectric stacks using Pt as both the top and bottom electrode are the least influenced.

- A ferroelectric stack with a layer structure Pt- PZT (52/48)- Pt is successfully bonded and transfered to a new wafer substrate using MR-I9000 photoresist. The measured dielectric permittivity is higher than that of the constraint film. This is attributed to the higher compliance of the adhesive layer where the film is now attached on.

- A method based on time- resolved micro- RAMAN spectroscopy has been developed and tested on piezo- actuated micro cantilevers. Dynamic stress maps are obtained as a function of time for a cantilever vibrating at the first

and the second resonant frequency. It is attempted to combine these results with the modal shapes defined with laser doppler vibrometry.

- A finite element model of the vibrating microcantilever is developed using ANSYS parametric design language. The model attempts to combine the results from the LDV and the RAMAN experiments by varying the properties of the piezoelectric layer that are used as inputs in the model. No perfect agreement between the calculated and the experimental values of all three properties of interest (resonant frequencies, maximum deflection and stress) could be obtained. Non linear response of the pzt material as well as uncertainties in other parameters are believed to be the cause.

- A process flow is presented for the micro fabrication of PZT bimoprh structures. Based on this process flow, bridge type bimorphs have been designed and fabricated for the purpose of PZT ceramic fatigue testing.

6.3 Recommendations for Future Work

- Refine model of multi layered composite to account for possible variations in the properties of the SiO_2 and Pt layers. In this extended finite element model transverse isotropic properties for the PZT film should be used as input.

- Investigate possible mechanisms of dielectric loss in ferroelectric stacks that have been processed for stress elimination purposes.

- Revise design of the piezo actuated bridge type PZT bimorphs to eliminate the risk of over etching part of the bridge anchor.

- Investigate dynamic crack growth in ceramics by introducing a stress concentration notch in the bridge type PZT bimorphs using focused ion beam

milling. The pre cracked samples will be actuated and the resonant frequency will be monitored as a function of time. As the crack propagates the stiffness of the structure changes so a shift in the resonant frequency is expected.

- Investigate dynamic crack growth in Si by fabricating bridge type PZT actuated devices on SOI wafers. An extra mask is needed to introduce a notch in the bridge by means of etching.

- Investigate ferroelectric fatigue in conjunction with the accelerated mechanical testing. This could be realized by reversing the operation of the bridge type structures by applying the driving signal in the bottom PZT layer and using the top smaller pads for sensing.

- Investigate mechanical properties of PZT ceramics in thin film form under conditions of constant external fields.

References

[1] http://matweb.com.

[2] http://www.mathworks.com/matlabcentral/fileexchange/12413.

[3] www.rogerscorporation.com.

[4] Alsem, D., Pierron, O., Stach, E., Muhlstein, C., and Ritchie, R. Mechanisms for fatigue of micron-scale silicon structural films. *Advanced Engineering Materials 9* (2007), 15–30.

[5] Anderson, T. *Fracture Mechanics: Fundamentals and Applications.* CRC Press, 1991.

[6] Ando, T., Shikida, M., and Sato, K. Tensile-mode fatigue testing of silicon films as structural materials for mems. *Sensors and Actuators A: Physical 93*, 1 (2001/8/25), 70–75.

[7] Arsdell, W. V., Brown, S., Inc, E. F. A. A., and Phoenix, A. Subcritical crack growth in silicon mems. *Microelectromechanical Systems, Journal of 8*, 3 (1999), 319–327.

[8] Bahr, D., Crozier, B., Richards, C., and Richards, R. Defects and failure modes in pzt films for a mems microengine. In *Materials Research Society Symposium Proceedings* (2001).

[9] Berfield, T., Ong, R., Payne, D., and Sottos, N. Residual stress effects on piezoelectric response of sol-gel derived lead zirconate titanate thin films. *Journal of Applied Physics 101*, 2 (2007), 024102.

[10] Bifano, T., Johnson, H. T., Bierden, P., and Mali, R. K. Elimination of stress-induced curvature in thin film structures. *Journal of Microelectromechanical Systems 11* (2002), 592–597.

[11] Bing, P., Hui-min, X., Bo-qin, X., and Fu-long, D. Performance of sub-pixel registration algorithms in digital image correlation. *Measurement Science and Technology 17* (2006), 1615–1621.

[12] Blech, I. A., Blech, I., and Finot, M. Determination of thin-film stresses on round substrates. *Journal of Applied Physics 97*, 11 (2005), 1–7.

[13] Bonera, E., Fanciulli, M., and Batchelder, D. N. Combining high resolution and tensorial analysis in raman stress measurements of silicon. *Journal of Applied Physics 94*, 4 (2003), 2729–2740.

[14] Brown, S., van Arsdell, W., Muhlstein, C., Assoc, F. A., and Framingham, M. Materials reliability in mems devices. *Solid State Sensors and Actuators, 1997.TRANSDUCERS'97 Chicago., 1997 International Conference on 1* (1997).

[15] Bryzek, J., Roundy, S., Bircumshaw, B., Chung, C., Castellino, K., Stetter, J. R., and Vestel, M. Marvelous mems. *Circuits and Devices Magazine, IEEE 22*, 2 (2006), 8–28.

[16] Cammarata, R. C. Surface and interface stress effects in thin films. *Progress in Surface Science 46*, 1 (1994), 1–38.

[17] Cao, J.-L., Solbach, A., Klemradt, U., Weirich, T., Mayer, J., Horn-Solle, H., Bottger, U., Schorn, P. J., Schneller, T., and

Waser, R. Structural investigations of pt/ti electrode stacks for ferroelectric thin film devices. *Journal of Applied Physics 99*, 11 (2006), 114107.

[18] Castellini, P., Martarelli, M., and Tomasini, E. P. Laser doppler vibrometry: Development of advanced solutions answering to technology's needs. *Mechanical Systems and Signal Processing 20*, 6 (2006/8), 1265–1285.

[19] Chasiotis, I., and Knauss, W. A new microtensile tester for the study of mems materials with the aid of atomic force microscopy. *Experimental Mechanics 42*, 1 (2002), 51–57. Cited By (since 1996): 54.

[20] Cheng, S. L. Design and performance of a piezoelectric microgyroscope. In *Technical digest of IEEE Transducers* (1999).

[21] Chu, T. Three dimensional displacement measurement using digital-image- correlation and photogrammic analysis. *Experimental Mechanics* (1990), 10–16.

[22] Connally, J., and Brown, S. Micromechanical fatigue testing. *Experimental Mechanics 33*, 2 (1993), 81–90.

[23] Damjanovic, D. Ferroelectric, dielectric and piezoelectric properties of ferroelectric thin films and ceramics. *Rep.Prog.Phys 61*, 1267-1324 (1998), 97–98.

[24] Despont, M., Drechler, U., Yu, R., Pogge, H. B., and Vettiger, P. Wafer-scale microdevice transfer/interconnect: Its application in an afm-based data-storage system. *Journal of Microelectromechanical Systems 13* (2004), 895–901.

[25] DeVoe, D. L., and Pisano, A. P. Modeling and optimal design of piezoelectric cantilever microactuators. *Journal of Microelectromechanical Systems 6*, 3 (1997), 266–270. Cited By (since 1996): 66.

[26] Dombrowski, K. F., Dietrich, B., Wolf, I. D., Rooyackers, R., and Badenes, G. Investigation of stress in shallow trench isolation using uv micro-raman spectroscopy. *Microelectronics and Reliability 41*, 4 (2001), 511–515. Cited By (since 1996): 4.

[27] Dombrowski, K. F., Wolf, I. D., and Dietrich, B. Stress measurements using ultraviolet micro-raman spectroscopy. *Applied Physics Letters 75*, 16 (1999), 2450–2451. Cited By (since 1996): 14.

[28] Dubois, M., and Muralt, P. Measurement of the effective transverse piezoelectric coefficient e31,f of aln and pb(zrx,ti1-x)o3 thin films. *Sensors and Actuators A: Physical 77* (1999), 106–112.

[29] Dudley, D., Duncan, W., and Slaughter, J. Emerging digital micromirror device (dmd) applications. In *Proc. SPIE* (2003), vol. 4985, pp. 14–25.

[30] Ehrlich, A., Weib, U., Walter, H., and Gebner, T. Microstructural changes of pt/ti bilayer during annealing in different atmospheres-an xrd study. *Thin Solid Films 300* (1997), 122–130.

[31] Feynman, R. There's plenty of room at the bottom. *Journal of Microelectromechanical Systems 1* (1992), 60–66.

[32] Fitzgerald, A. M., Iyer, R. S., Dauskardt, R. H., and Kenny, T. W. Subcritical crack growth in single-crystal silicon using micromachined specimens. *J.Mater.Res 17*, 3 (2002), 684.

[33] Freund, L. B. A surface chemical potential for elastic solids. *Journal of the Mechanics and Physics of Solids 46*, 10 (10/1 1998), 1835–1844.

[34] Freund, L. B., and Suresh, S. *Thin Film Materials Stress, Defect Formation and Surface Evolution.* Cambridge University Press, UK, 2003.

[35] Gad-El-Haq, M. *The MEMS Handbook*. CRC Press, 2002.

[36] Gaspar, J., Nurcahyo, Y., Ruther, P., and Paul, O. Mechanical characterization of silicon nitride thin-films using microtensile specimens with integrated 2d diffraction gratings. In *Micro Electro Mechanical Systems, 2007. MEMS. IEEE 20th International Conference on* (2007), pp. 223–226.

[37] Gaspar, J., Ruther, P., and Paul, O. Mechanical characterization of thin-film composites using the load- deflection response of multilayer membranes - elastic and fracture properties. In *Materials Research Society Symposium Proceedings* (2006).

[38] Gaspar, J., Schmidt, M., Held, J., and Paul, O. Wafer- scale microtensile testing of thin films. Accepted for publication by Journal of Microelectromechanical Systems.

[39] Gaspar, J., Schmidt, M., Held, J., and Paul, O. High-throughput wafer-scale microtensile testing of thin films. In *Micro Electro Mechanical Systems, 2008. MEMS 2008. IEEE 21st International Conference on* (2008), pp. 439–442.

[40] Gaspar, J., Schmidt, M., Held, J., and Paul, O. Reliability of mems materials: Mechanical characterization of thin films using the wafer scale bulge test and improved microtensile techniques. In *Material Research Society Symposium Proceedings* (2008).

[41] Gerlach, G., Suchaneck, G., Koehler, R., Sandner, T., Padmini, P., Krawietz, R., Pompe, W., Frey, J., Jost, O., and Schoenecker, A. Properties of sputter and sol-gel deposited pzt thin films for sensor and actuator applications: preparation, stress and space charge distribution, self poling. *Ferroelectrics 230*, 1 (1999), 411.

[42] Gkotsis, P., Kirby, P. B., Saharil, F., Oberhammer, J., and Stemme, G. Thin film crystal growth template removal: Application to stress reduction in lead zirconate titanate microstructures. *Applied Physics Letters 91* (2007), 163504.

[43] Greek, S., Ericson, F., Johansson, F. Fürtsch, M., and Rump, A. Mechanical characterization of thick polysilicon films: Young's modulus and fracture strength evaluated with microstructures. *Journal of Micromechanics and Microengineering 9* (1999), 245–251.

[44] Greek, S., Ericson, F., Johansson, S., and Schweitz, J. In situ tensile strength measurement and weibull analysis of thick film and thin film micromachined polysilicon structures. *Thin Solid Films 292* (1997), 247–254.

[45] Gross, S. J. Micromachined switches and cantilever actuators based on piezoeletric lead zirconate titanate (pzt), 2004.

[46] Haque, M., and Saif, M. In-situ tensile testing of nano-scale specimens in sem and tem. *Experimental Mechanics 42*, 1 (2002), 123–128. Cited By (since 1996): 33.

[47] Haque, M. A., and Saif, M. T. A. A review of mems-based miroscale and nanoscale tensile and bending testing. *Experimental Mechanics 43*, 3 (2003), 248–255. Cited By (since 1996): 13.

[48] Hertzberg, R. *Deformation and Fracture of Engineering Materials.* Wiley, 1976.

[49] Hong, E., Smith, R., Krishnaswamy, S., Freidhoff, C., and Trolier-McKinstry, S. Residual stress development in

pb(zr,ti)o3/zro2/sio2 stacks for piezoelectric microactuators. *Thin Solid Films 510*, 1-2 (2006), 213–221.

[50] Hong, S., Kim, M., Lee, S., and Lee, C. Characterization of deformation behaviors and elastic moduli of multilayered films in piezoelectric inkjet head. *Journal of Microelectromechanical Systems 17* (2008), 1155–1163.

[51] Hua, T., Xie, H., Pan, B., Qing, X., Dai, F., and Xiqiao Feng, X. A new micro-tensile system for measuring the mechanical properties of low-dimensional materialsfibers and films. *Polymer Testing 26* (2007), 513–518.

[52] Huang, S., and Zhang, X. Extension of the stoney formula for film-substrate systems with gradient stress for mems applications. *Journal of Micromechanics and Microengineering 16*, 2 (2006), 382.

[53] Ikeda, T., Sugano, K., Tsuchiya, T., and Tabata, O. Tensile testing of single crystal silicon thin films at 800 c using ir heating. *Solid-State Sensors, Actuators and Microsystems Conference, 2007.TRANSDUCERS 2007.International* (2007), 571–574.

[54] Jadaan, O., Nemeth, N., Bagdahn, J., and Sharpe, W. Probabilistic weibull behavior and mechanical properties of mems brittle materials. *Journal of Materials Science 38*, 20 (2003), 4087–4113.

[55] Janssen, G. C. A. M. Stress and strain in polycrystalline thin films. *Thin Solid Films 515*, 17 (2007/6/13), 6654–6664.

[56] Kahn, H., Avishai, A., Ballarini, R., and Heuer, A. Surface oxide effects on failure of polysilicon mems after cyclic and monotonic loading. *Scripta Materialia 59*, 9 (2008), 912 – 915. Viewpoint set no. 44.

[57] Kahn, H., Ballarini, R., and Heuer, A. Dynamic fatigue of silicon. *Current Opinion in Solid State and Materials Science 8*, 1 (2004), 71–76.

[58] Kahn, H., Chen, L., Ballarini, R., and Heuer, A. Mechanical fatigue of polysilicon: Effects of mean stress and stress amplitude. *Acta Materialia 54*, 3 (2006), 667–678.

[59] Kamiya, S., Kuypers, J. H., Trautmann, A., Ruther, P., and Paul, O. Process temperature dependent mechanical properties of polysilicon measured using a novel tensile test structure. *Microelectromechanical Systems, Journal of 16*, 2 (2007), 202–212.

[60] Kapels, H., Aigner, R., and Binder, J. Fracture strength and fatigue of polysilicon determined by a novelthermal actuator [mems]. *Electron Devices, IEEE Transactions on 47*, 7 (2000), 1522–1528.

[61] Kholkin, A., Taylor, D., and Setter, N. Poling effect on the piezoelectric properties of lead zirconate titanate thin films. In *Applications of Ferroelectrics, 1998. ISAF 98. Proceedings of the Eleventh IEEE International Symposium on* (1998).

[62] Kim, S., and Kang, S. Sensitivity of electroplating conditions on youngs modulus of thin film. *Japanese Journal of Applied Physics 47* (2008), 7314–7316.

[63] Kobayashi, T., Ichiki, M., Kondou, R., Nakamura, K., and Maeda, R. Degradation in the ferroelectric and piezoelectric properties of pb (zr, ti) o 3 thin films derived from a mems microfabrication process. *Journal of Micromechanics and Microengineering 17*, 7 (2007), 1238.

[64] Kobayashi, T., Ichiki, M., Noguchi, T., and Maeda, R. Deflection of wafers and cantilevers with pt/lno/pzt/lno/pt/ti/sio_2 multilayered structure. *thin Solid Films 516* (2008), 5272–5276.

[65] Kobayashi, T., Kondou, R., Nakamura, K., Ichiki, M., and Maeda, R. Sensing property of self-sensitive piezoelectric microcantilever utilizing $pb(zr_{0.52}/ti_{0.48})o_3$ thin film and $lanio_3$ oxide electrode. *JAPANESE JOURNAL OF APPLIED PHYSICS PART 1 REGULAR PAPERS SHORT NOTES AND REVIEW PAPERS 46*, 10B (2007), 7073.

[66] Kobayashi, T., Maeda, R., and Itoh, T. A fatigue test method for pb (zr, ti) o 3 thin films by using mems-based self-sensitive piezoelectric microcantilevers. *Journal of Micromechanics and Microengineering 18*, 11 (2008), 115007.

[67] Kobayashi, T., Maeda, R., and Itoh, T. The influence of dc bias on the displacement and sensor output of self-sensitive piezoelectric microcantilevers. *Journal of Micromechanics and Microengineering 18*, 3 (2008), 35025.

[68] Koch, R. The intrinsic stress of polycrystalline and epitaxial thin metal films. *JOURNAL OF PHYSICS CONDENSED MATTER 6* (1994), 9519–9519.

[69] Komatsubara, M., Namazu, T., Nagai, Y., Inoue, S., Naka, N., Kashiwagi, S., and Ohtsuki, K. Raman spectrum curve fitting for estimating surface stress distribution in single-crystal silicon microstructure. *Japanese Journal of Applied Physics 48*, 4 (2009), 04021.

[70] Kuball, M., Riedel, G., Pomeroy, J., Sarua, A., Uren, M., Martin, T., Hilton, K., and Wallis, D. Time-resolved nanosecond

sub-micron resolution thermal analysis of high-power AlGaN/GaN HFETs. *phys. stat. sol.(a) 204*, 6 (2007), 2014–2018.

[71] Lafontan, X., Pressecq, F., Beaudoin, F., Rigo, S., Dardalhon, M., Roux, J. L., Schmitt, P., Kuchenbecker, J., Baradat, B., Lellouchi, D., Le-Touze, C., and Nicot, J. M. The advent of mems in space. *Microelectronics Reliability 43*, 7 (2003/7), 1061–1083.

[72] Landau, L., and Lifshitz, E. Course of theoretical physics. In *Theory of Elasticity*. Butterworth Heinemann, 2006.

[73] Laser, D. J., and Santiago, J. G. A review of micropumps. *Journal of Micromechanics and Microengineering 14* (2004), 35–64.

[74] Li, X., Ding, G., Wang, H., Ando, T., Shikida, M., and Sato, K. Mechanical properties of electrodeposited permalloy thin film measured by using a tensile test. *Solid-State Sensors, Actuators and Microsystems Conference, 2007.TRANSDUCERS 2007.International* (2007), 555–558.

[75] Lines, M., and Glass, A. *Principles and Applications of Ferroelectric and Related Materials*. Clarendon Press, 1977.

[76] Ljungcrantz, H., Hultman, L., Sundgren, J., Johansson, S., Schweitz, N. K. J., and Shute, C. Residual stresses and fracture properties of magnetron sputtered ti films on si microelements. *Journal of Vacuum Science & Technology A: Vacuum, Surfaces, and Films 11* (1993), 543.

[77] Lu, J., Kobayashi, T., Zhang, Y., Maeda, R., and Mihara, T. Wafer scale lead zirconate titanate film preparation by sol-gel method using stress balance layer. *Thin Solid Films 515*, 4 (2006/12/5), 1506–1510.

[78] Lughi, V., and Clark, D. R. Defect and stress characterization of aln films by raman spectroscopy. *Applied Physics Letters 89*, 24 (2006), 1911–1914.

[79] Luo, J. K., Flewitt, A. J., Spearing, S. M., Fleck, N. A., and Milne, W. I. Young's modulus of electroplated ni thin film for mems applications. *Materials Letters 58*, 17-18 (2004), 2306 – 2309.

[80] Madou, M. *Fundamentals of Microfabrication.* CRC Press, UK, 2000.

[81] Malhaire, C., Ignat, M., Dogheche, K., Brida, S., Josserond, C., and Debove, L. Realization of thin film specimens for micro tensile tests. *Solid-State Sensors, Actuators and Microsystems Conference, 2007.TRANSDUCERS 2007.International* (2007), 623–626.

[82] Malhaire, C., Seguineau, C., Ignat, M., Josserond, C., Debove, L., Brida, S., Desmarres, J. M., and Lafontan, X. Experimental setup and realization of thin film specimens for microtensile tests. *Review of Scientific Instruments 80* (2009), 023901.

[83] Maniguet, L., Ignat, M., Dupeu, M., Backmann, J., and Normandon, P. X-ray determination and analysis of residual stresses in uniform films and patterned lines of tungsten. In *Materials Research Society Symposium* (1993).

[84] Marshall, J. M., Corkovic, S., Zhang, Q., Whatmore, R. W., Chima-Okereke, C., Roberts, W. L., Bushby, A. J., and Reece, M. J. The electromechanical properties of highly [100] oriented pzt (52/48) thin films. *Integrated Ferroelectrics 80*, 1 (2006), 77–85.

[85] Millon, C., Malhaire, C., and Barbier, D. Control of ti diffusion in pt/ti bottom electrodes for the fabrication of pzt thin film transducers. *Materials Science in Semiconductor Processing 5* (2003), 243–247.

[86] Modlinski, R., Puers, R., and De Wolf, I. Micro- tensile tests to characterize mems. Tech. rep., IMEC, Kapeldreef 75, 3001 Leuven Belgium, 2007.

[87] Muhlstein, C., Brown, S., and Ritchie, R. High-cycle fatigue of single-crystal silicon thin films. *Microelectromechanical Systems, Journal of 10*, 4 (2001), 593–600.

[88] Muhlstein, C. L., Brown, S. B., and Ritchie, R. O. High-cycle fatigue and durability of polycrystalline silicon thin films in ambient air. *Sensors and Actuators A: Physical, 94*, 3 (11/20 2001), 177–188.

[89] Muhlstein, C. L., Howe, R. T., and Ritchie, R. O. Fatigue of polycrystalline silicon for microelectromechanical system applications: crack growth and stability under resonant loading conditions. *Mechanics of Materials, 36*, 1-2 (0 2004), 13–33.

[90] Muhlstein, C. L., Stach, E. A., and Ritchie, R. O. A reaction-layer mechanism for the delayed failure of micron-scale polycrystalline silicon structural films subjected to high-cycle fatigue loading. *Acta Materialia, 50*, 14 (8/16 2002), 3579–3595.

[91] Muralt, P., and Baborowski, J. Micromachined ultrasonic transducers and acoustic sensors based on piezoelectric thin films. *Journal of Electroceramics 12*, 1-2 (2004), 101–108. Cited By (since 1996): 4.

[92] Murray, P., and Carey, G. Determination of interfacial stress during thermal oxidation of silicon. *Journal of Applied Physics 65* (1989), 3667–3670.

[93] Nam, H., Cho, S., Yee, Y., Lee, H., Kim, D., Bu, J., and Hong, J. Fabrication and characteristics of piezoelectric pzt cantilever for high speed atomic force microscopy. *Integrated Ferroelectrics 35* (2001), 185–197.

[94] Namazu, T., Inoue, S., Takemoto, H., and Koterazawa, K. Mechanical properties of polycrystalline titanium nitride films measured by xrd tensile testing. *IEEJ Transactions on Sensors and Micromachines 125* (2005), 374–379.

[95] Namazu, T., Isono, Y., and Tanaka, T. Evaluation of size effect on mechanical properties of single crystal silicon by nanoscale bending. *Microelectromechanical Systems, Journal of 9* (2000), 450–459.

[96] Namazu, T., Nagai, Y., Naka, N., Kashiwagi, S., Ohtsuki, K., and Inoue, S. In-situ raman spectroscopic surface stress measurement of single crystal silicon microstructures subjected to uniaxial tensile loading. In *Solid-State Sensors, Actuators and Microsystems Conference, 2007. TRANSDUCERS 2007. International* (2007).

[97] Nie, M., Huang, Q. A., and Li, W. Measurement of residual stress in multilayered thin films by a full-field optical method. *Sensors and Actuators, A: Physical 126*, 1 (2006), 93–97. Cited By: 0.

[98] Niklaus, F., Stemme, G., Lu, J. Q., and Gutmann, R. J. Adhesive wafer bonding. *Journal of Applied Physics 99* (2006), 1–24.

[99] Nye, J. F. *Physical properties of crystals: their representation by tensors and matrices.* Oxford University Press, USA, 1985.

[100] Oberhammer, J., and Stemme, G. Bcb contact printing for patterned adhesive full-wafer bonded 0-level packages. *IEEE Journal of Microelectromechanical Systems 14*, 2 (2005), 419.

[101] Olson, B., Randall, L., Richards, C., Richards, R., and Bahr, D. Relationships between microstructure and reliability in pzt mems. In *Materials Research Society Symposium Proceedings* (2001).

[102] Olson, B., Skinner, J., Richards, C., and Bahr, D. Optimization of thermal processing and chemistry in the fabrication of a pzt based mems power generation. In *Materials Research Society Symposium Proceedings* (2002).

[103] Ong, R., Berfield, T., Sottos, N., and Payne, D. Sol-gel derived pb(zr,ti)o3 thin films: Residual stress and electrical properties. *Journal of the European Ceramic Society 25*, 12 (2005), 2247–2251.

[104] Ong, R., Payne, D., and Sottos, N. Processing effects for integrated pzt: Residual stress, thickness, and dielectric properties. *Journal of the American Ceramic Society 88*, 10 (2005), 2839–2847. M3: doi:10.1111/j.1551-2916.2005.00641.x.

[105] Osterberg, P. M., and Senturia, S. D. M-test: A test chip for mems material property measurement using electrostatically actuated test structures. *Journal of Microelectromechanical Systems 6* (1997), 107–118.

[106] Padmini, P., Krawietz, R., Koehler, R., and Gerlach, G. Preparation and stress evaluation of ferroelectric thin films of pzt based pyroelectric sensors. *Ferroelectrics 228*, 1 (1999), 79–89.

[107] Polcawich, R., Dubey, M., Pulskamp, J., Piekarski, B., Conrad, J., Piekarz, R., and Zakar, E. Stress analysis of sio_2/ta/pt/pzt/pt stack for mems application. Tech. rep., Army Research Laboratory, 2000.

[108] Populin, M., Decharat, A., Niklaus, F., and Stemme, G. Thermosetting nano-imprint resists: Novel materials for adhesive wafer bonding. pp. 239–242.

[109] Pulskamp, J. S., Wickenden, A., Polcawich, R., Piekarski, B., Dubey, M., and Smith, G. Mitigation of residual film stress deformation in multilayer microelectromechanical systems cantilever devices. *Journal of Vacuum Science & Technology B: Microelectronics and Nanometer Structures 21* (2003), 2482.

[110] Ranson, W., Sutton, M., Peters, W., and Chu, T. Applications of digital- image- correlation techniques to experimental mechanics. *Experimental Mechanics* (1985), 232–244.

[111] Read, D. Tension- tension fatigue of copper thin films. *International Journal Fatigue 20* (1998), 203–209.

[112] Read, D. Young's modulus of thin films by speckle interferometry. *Measurement Science and Technology 9* (1998), 676–685.

[113] Rebeiz, G. M. *RF MEMS: theory, design, and technology.* John Wiley and Sons, 2003.

[114] Romig, A. J., Dugger, M., and McWhorter, P. Materials issues in microelectromechanical devices: Science, engineering, manufacturability and reliability. *Acta Materialia 51*, 19 (2003), 5837–5866. Cited By: 16.

[115] Saif, M., and MacDonald, N. A millinewton microloading device. *Sensors & Actuators: A. Physical 52* (1998), 65–75.

[116] SAMPSELL, J. B. Digital micromirror device and its application to projection displays. *Journal of Vacuum Science & Technology B: Microelectronics and Nanometer Structures 12* (1994), 3242.

[117] SARUA, A., KUBALL, M., AND NOSTRAND, J. E. V. Phonon deformation potentials of the e2 (high) phonon mode of alxga1-xn. *Applied Physics Letters 85*, 12 (2004), 2217–2219.

[118] SHARPE, W., JACKSON, K., HEMKER, K., AND XIE, Z. Effect of specimen size on youngs modulus and fracture strength of polysilicon. *Journal of Microelectromechanical Systems 10* (2001), 317–326.

[119] SHARPE, W. N., AND BAGDAHN, J. Fatigue testing of polysilicon- a critical review. *Mechanics of Materials, 36*, 1-2 (0 2004), 3–11.

[120] SHARPE, W. N. J. Tensile testing at the micrometer scale: Opportunities in experimental mechaniques. *Society of Experimental Mechaniques 43*, 3 (2003), 228–237.

[121] SHARPE JR, W., YUAN, B., AND EDWARDS, R. L. A new technique for measuring the mechanical properties of thin films. *Journal of Microelectromechanical Systems 6*, 3 (1997), 193–198. Cited By (since 1996): 156; Export Date: 6 July 2007; Source: Scopus.

[122] SHEPARD, J., TROLIER-MCKINSTRY, S., HENDRICKSON, A., AND ZETO, R. Properties of pzt thin films as a function of in-plane biaxial stress. Tech. rep., 1996.

[123] SONTHEIMER, A. B. Digital micromirror device (dmd) hinge memory lifetime reliability modeling, 2002. Cited By (since 1996): 3.

[124] SPIERINGS, G. A. C. M., DORMANS, G. J. M., MOORS, W. G. J., ULENAERS, M. J. E., AND LARSEN, P. K. Stresses in pt/pzt/pt thin-film

stacks for integrated ferroelectric capacitors. *Journal of Applied Physics 78* (1995), 1926–1933.

[125] Spierings, G. A. C. M., Dormans, G. J. M., Moors, W. G. J., Ulenaers, M. J. E., and Larsen, P. K. Stresses in pt/pzt/pt thin-film stacks for integrated ferroelectric capacitors. *Journal of Applied Physics 78* (1995), 1926–1933.

[126] Sreenivas, K., Reaney, I., Maeder, T., Setter, N., Jagadish, C., and Elliman, R. Investigation of pt/ti bilayer metallization on silicon for ferroelectric thin film integration. *Journal of Applied Physics 75* (1994), 232.

[127] Starman, L. A., Lott, J. A., Amer, M. S., Cowan, W. D., and Busbee, J. D. Stress characterization of mems microbridges by micro-raman spectroscopy. *Sensors & Actuators: A.Physical 104*, 2 (2003), 107–116.

[128] Stephens, L., Kelly, K., Simhadri, S., McCandless, A., and Meletis, E. Mechanical property evaluation and failure analysis of cantilevered liga nickel microposts. *Journal of Microelectromechanical Systems 10*, 3 (2001), 347–359. Source: Scopus.

[129] Stoney, G. G. The tension of metallic films deposited by electrolysis. *Proceedings of the Royal Society of London.Series A 82*, 553 (1909), 172–175.

[130] Strikar, V. T., and Spearings, S. M. A critical review of microscale mechanical testing methods used in the design of microelectromechanical systems. *Society of Experimental Mechaniques 43*, 3 (2003), 238–247.

[131] Strikar, V. T., Swan, A. K., Unlu, M. S., Goldberg, B. B., and Spearing, S. M. Micro-raman measurement of bending stresses in micromachined silicon flexures. *Journal of Microelectromechanical Systems 12*, 6 (2003), 779–787.

[132] Su, Q. X., Kirby, P., Komuro, E., Imura, M., Zhang, Q., and Whatmore, R. Thin-film bulk acoustic resonators and filters using zno and lead zirconium titanate thin films. *IEEE Transactions on Microwave Theory and Techniques 49*, 4 (2001), 769.

[133] Tabata, O., Tsuchiya, T., Gaspar, J., and Oliver, P. *Advanced Micro and Nanosystems*. WILEY-VCH Verlag GmbH & Co, 2008.

[134] Thompson, C. V., and Carel, R. Stress and grain growth in thin films. *Journal of the Mechanics and Physics of Solids 44*, 5 (1996/5), 657–673.

[135] Timoshenko, S. Analysis of bi-metal thermostats. *Journal of the Optical Society of America 11* (1925), 233–242.

[136] Townsend, P. H., Barnett, D. M., and Brunner, T. A. Elastic relationships in layered composite media with approximation for the case of thin films on a thick substrate. *Journal of Applied Physics 62* (1987), 4438.

[137] Trodahl, H., Martin, F., Muralt.P., and Setter, N. Raman spectroscopy of sputtered aln films: E2 (high biaxial) biaxial strain dependence. *Applied Physics Letters 89*, 6 (2006), 1905–1908.

[138] Trolier-Mckinstry, S., and P., M. Thin film piezoelectrics for mems. *Journal of Electroceramics 12*, 1-2 (2004), 7–17. Cited By (since 1996): 20.

[139] Tsuchiya, T., Tabata, O., Sakata, J., and Taga, Y. Specimen size effect on tensile strength of surface-micromachinedpolycrystalline silicon thin films. *Microelectromechanical Systems, Journal of 7*, 1 (1998), 106–113.

[140] van Spengen, W. M. Mems reliability from a failure mechanisms perspective. *Microelectronics Reliability 43*, 7 (2003/7), 1049–1060.

[141] Wang, L. P., Wang, Y., Deng, K. K., Zou, L., Davis, R. J., and Trolier-McKinstry, S. Design, fabrication, and measurement of high-sensitivity piezoelectric microelectromechanical systems accelerometers. *Journal of Microelectromechanical Systems 12*, 4 (2003), 433–439.

[142] Weinberg, M. Working equations for piezoelectric actuators and sensors. *Microelectromechanical Systems, Journal of 8*, 4 (1999), 529–533.

[143] Whatmore, R. W., Huang, Z., and Zhang, Q. Low temperature crystallization of lead zirconate titanate thin films by a sol-gel method. *Journal of Applied Physics 85* (1999), 7355–7361.

[144] Wolf, I. D. Micro-raman spectroscopy to study local mechanical stress in silicon integrated circuits. *Semiconductor Science and Technology 11*, 2 (1996), 139–154. Cited By (since 1996): 128.

[145] Wolf, I. D., and Maes, H. E. Mechanical stress measurements using micro-raman spectroscopy. *Microsystem Technologies 5*, 1 (1998), 13–17. Cited By (since 1996): 7.

[146] Wolf, I. D., Pozzat, G., Pinardi, K., Howard, D. J., Ignat, M., Jain, S. C., and Maes, H. E. Experimental validation of mechanical stress models by micro-raman spectroscopy. *Microelectronics Reliability 36*, 11-12 SPEC. ISS. (1996), 1751–1754. Cited By (since 1996): 13.

[147] Wolf, I. D., Senez, V., Balboni, R., Armigliato, A., Frabboni, S., Cedola, A., and Lagomarsino, S. Techniques for mechanical strain analysis in sub-micrometer structures: Tem/cbed, micro-raman spec-

troscopy, x-ray micro-diffraction and modeling. *Microelectronic Engineering 70*, 2-4 (2003), 425–435. Cited By (since 1996): 5.

[148] Yamaji, Y., Sugano, K., Tabata, O., and Tsuchiya, T. Tensile-mode fatigue tests and fatigue life predictions of single crystal silicon in humidity controlled environments. *Micro Electro Mechanical Systems, 2007.MEMS.IEEE 20th International Conference on* (2007), 267–270.

[149] Yang, J., Gaspar, J., and Paul, O. Fracture properties of lpcvd silicon nitride and thermally grown silicon oxide thin films from the load-deflection of long si_3n_4 and si_3n_4/sio_2 diaphragms. *Microelectromechanical Systems, Journal of 17* (2008), 1120– 1134.

[150] Yi, T., and Kim, C.-J. Measurement of mechanical properties for mems materials. *Measurement Science and Technology*, 8 (1999), 706–716. ID: 0957-0233-10-8-305.

[151] Yu, H. G., Zou, L., Deng, K., Wolf, R., Tadigadapa, S., and Trolier-McKinstry, S. Lead zirconate titanate mems accelerometer using interdigitated electrodes. *Sensors and Actuators A: Physical 107*, 1 (10/1 2003), 26–35.

[152] Zhan, L., Tsaur, J., and Maeda, R. Residual stress study of sio2/pt/pb(zr,ti)o3/pt multilayer structure for micro electro mechanical system applications. *Japanese Journal of Applied Physics 42* (2003), 1386–1390.

[153] Zhang, L., Ichiki, M., and Maeda, R. Residual stresses in pt bottom electrodes for sol-gel derived lead zirconate titanate thin films. *Journal of European Ceramic Society 24* (2004), 1673–1676.

[154] Zhang, N.-H. Thermoelastic stresses in multilayered beams. *Thin Solid Films 515*, 23 (9/14 2007), 8402–8406.

[155] Zhao, Z., Hershberger, J., Yalisove, S., and Bilello, J. Determination of residual stress in thin films: a comparative study of x-ray topography versus laser curvature method. *Thin Solid Films 415*, 1 (2002), 21–31.

[156] Zhu, M., and Kirby, P. B. Governing equation for the measurement of nonuniform stress distributions in thin films using a substrate deformation technique. *Applied Physics Letters 88*, 17 (2006).

[157] Zohni, O., Buckner, G., Kim, T., Kingon, A., Maranchi, J., and Siergiej, R. Investigating thin film stresses in stacked silicon dioxide/silicon nitride structures and quantifying their effects on frequency response. *Journal of Micromechanics and Microengineering 17*, 5 (2007), 1042–1051.

Appendices

A-1 MATLAB model of the static tip deflection of a multimorph beam due to thin film residual stress. Linear and nonlinear case

```
function linear_nonlinear
%Material properties
%--------------------------------------------------------------------
E=[168 69 170 50 77]*1e9;         %Young's moduli of layers
nu=[0.065 0.3 0.38 0.28 0.42];     %Poisson's ratio of layers
stress=[0 -0.165 0.877 0.054 -0.225]*1e9;    %residual stress
E_new=E./(1-(nu.^2));         %Plane stress Young's modulus
%--------------------------------------------------------------------
b=1e-4;                                   % beam width in microns
thick=[10 0.2 0.108 1 0.108]*1e-6;    %film thicknesses
area=b*[thick sum(thick)];     %film area and total area
n=size(thick);
idx=n(2);
for i=1:idx,
if b/thick(i)>400,
    E(i)=E_new(i)
end
end
%position of beam's neutral axis
%--------------------------------------------------------------------
mid_axis=[thick(1)/2 cumsum(thick(1:end-1))+thick(2:end)/2];
neutral_axis=sum(E_new.*area(1:end-1).*mid_axis)/sum(E_new.*area(1:end-1));
%new coordinates, neutral axis reference
%--------------------------------------------------------------------
y=[0 cumsum(thick)]-neutral_axis;       %film interface limits
y_centr=(cumsum(thick)-(thick/2))-neutral_axis;    %centroids
%stiffness, rigidity calculations, moment of inetria, young's modulus
%--------------------------------------------------------------------
EA_tot=sum(E.*area(1:end-1));
i=1:5;
sy(i)=y(i+1)+y(i);
ssy(i)=y(i+1).^2+y(i+1).*y(i)+y(i).^2;
ES_tot=sum(E.*area(1:end-1).*sy)/2;
EI_tot=sum(E.*area(1:end-1).*ssy)/3;
A=[EA_tot ES_tot;ES_tot EI_tot];
```

```
E_comp=sum(thick.*E/sum(thick));
I_comp=sum((b*(thick.^3)/12)+area(1:end-1).*(y_centr.^2));
%total force, total moment
%--------------------------------------------------------------------
forces=stress.*area(1:end-1);
moment_tot=sum(forces.*y_centr);
force_tot=sum(stress.*area(1:end-1));
moment=sum(stress.*area(1:end-1).*sy)/2;
%Solution of the matrix eaquation for the strain and
%curvature in the linear model
%--------------------------------------------------------------------
cause=[force_tot
    moment];
result=inv(A)*cause;
L=(0:5:3000);
defl=result(2)*(L.^2)*1e-6/2;
plot(L,defl,'r--',...
    'Linewidth',2)
hold on
k=moment_tot/(E_comp*I_comp)
%Nonlinear model
%--------------------------------------------------------------------
lspan = [0; 3e-3];
y0 = [0; 0];
[t,y] = ode45(@f,lspan,y0);
plot(t*1e6,y(:,1)*1e6,'g');
title('Static beam tip deflection ');
xlabel('Beam length L \rightarrow \mum');
ylabel('Tip deflection \rightarrow \mum');
%--------------------------------------------------------------------
function dydt = f(t,y)
dydt = [            y(2)
         k*(1+y(1)^2)^(3/2) ];
end   % End nested function f
%--------------------------------------------------------------------
hold off
end
```

A-2 Modification of MATLAB model for verification of ANSYS 2-D analysis

```
%MATLAB linear and non linear model of a multilayered piezo actuated
%cantilever. The model includes Ti layers and is derived from the pre
%vious model if we change the material properties section with the fo
%llowing lines and index i range from 1:5 to 1:7.
%Material properties
%------------------------------------------------------------------
E=[155 78.36 119.7 167.4 67.5 119.7 167.4]*1e9;%Si,SiO2,Ti,Pt,PZT,Ti,Pt
nu=[0.23 0.17 0.31 0.303 0.394 0.31 0.303];   %Poisson's ratio
Eel=5e6; %electric field =volt/pzt thickness
d31=(-2.3e-10)*(1+nu(5))
stress=[0 0 0 0 d31*Eel*E(5) 0 0]*1e9; %induced stresses in films
E_new=E./(1-(nu.^2));        %Youngs modulus for small width/thickness
%beam dimensions
%-------------------------------------------------------------------
b=3.4e-4;                                      %beam width in microns
thick=[10 0.2 0.008 0.1 1 0.008 0.1]*1e-6;%film thicknesses in microns
```

A-3 ANSYS Finite Element Model of a multimorph piezoelectricaly actuated beam

```
!!***This program is modelling a multi- layered pzt actuated beam**!!
/FILENAME,Multimorph_10mic_5Volts_5_mic_pzt
/UNITS, SI
/prep7
!!***********************Basic Units*******************************!!
mm=1e-3
um=1e-6
eps_0=8.854e-12
FRQSTR=1.0E3                  ! SHIFT POINT FOR EIGENVALUE EXTRACTION
FRQEND=200E3                   ! UPPER BOUND FOR FREQUNECY EXTRACTION
modes=5
subs=100
pi=3.1415
!!*****************Define material parameters*********************!!
! * Silicon (s=silicon)
```

```
dens_s=2330                                   !Density in kg/m^3
young_s=155e9                               !Young's modulus in Pa
poiss_s=0.23      !Poisson's ratio
damp_si=1.0e-5    !Q=60000 at 100kHz
! * PZT (p=PZT) Ferroperm PZ23
dens_p=7700                                 !Density in kg/m^3
c11_p=157e9                                   !C11_p in N/M^2
c12_p=109e9                                   !C12_p in N/M^2
c13_p=97.7e9                                !C13_p in N/M^2
c33_p=123e9                                 !C33_p in N/M^2
c44_p=25.7e9                                 !C44_p in N/M^2
e31_p=-1.93
e33_p=15.5
e24_p=10.81
eps11_p=1529*eps_0                                 ! In F/m^2
eps33_p=759*eps_0                                  ! In F/m^2
damp_pzt=1.0e-3   !damping of PZT
loss_pzt=0.013   !dielectric loss of pzt
! * Silicon Dioxide (so)
dens_so=2201
young_so=78.36e9
poisson_so=0.17
! * Platinum (pt)
dens_pt=21400
young_pt=167.4e9
poisson_pt=0.303
! * Titanium (ti)
dens_ti=4480
young_ti=119.7e9
poisson_ti=0.31
!!*************************Mesh paramters**************************!!
meshsize=35*um
tol=1e-15
!!************Define geometrical  structural parameters************!!
pztlen=1.4*mm
beam_w=170*um                                         !beam width
beam_t=10*um                              !beam substrate thickness
pzt_th=1*um
so_thick=0.2*um
pt_thick=0.1*um
ti_thick=0.01*um
step=5*um
!!*******************material reference number********************!!
```

```
! Material 1 = Silicon
! material 2 = PZT
! Material 3 = Silicon Dioxide
! Material 4 = Platinum
! Material 5 = Titanium
!!******************Element type used***************************!!
ET, 1, PLANE42
ET, 2, SOLSH190             !LAYERED SOLID-SHELL ELEMENT (SiO2, Pt)
ET, 3, SOLID5, 3             !For the piezoelectric film
ET, 4, SOLID45 !For the Silicon structural layer
!!!!!*****************************************************!!!!!
!!********************Real Constants***************************!!
!!!!!*****************************************************!!!!!
!R,3,so_thick               !Thickness of SiO2
!R,4,pt_thick               !Thickness of Pt
!!*******************Material declaration**********************!!
!******************Silicon material
MP, EX,   1, young_s                  !MP,prop,mat no.,parameter name
MP, DENS, 1, dens_s
MP, NUXY, 1, poiss_s
!MP, DMPR, 1, damp_si
!*******************PZT Material
MP, DENS, 2, dens_p
MP, LSST, 2, loss_pzt
!MP, DMPR, 2, damp_pzt
TB, ANEL, 2
TBDATA, 1, c11_p
TBDATA, 2, c12_p
TBDATA, 3, c13_p
TBDATA, 7, c11_p ! c22=c11
TBDATA, 8, c13_p ! c23=c13
TBDATA, 12, c33_p
TBDATA, 16, (c11_p-c12_p)/2 ! c66=0.5*(c11-c12)
TBDATA, 19, c44_p
TBDATA, 21, c44_p ! c55=c44
TB, PIEZ, 2
TBDATA, 3, e31_p
TBDATA, 6, e31_p ! e32=e31
TBDATA, 9, e33_p
TBDATA, 14, e24_p
TBDATA, 16, e24_p ! e15=e24
MP, PERX, 2, eps11_p
MP, PERY, 2, eps11_p
```

```
MP, PERZ, 2, eps33_p
!******************Silicon Dioxide material
MP, EX, 3, young_so                  !MP,prop,mat no.,parameter name
MP, DENS, 3, dens_so
MP, NUXY, 3, poisson_so
!******************Platinum material
MP, EX, 4, young_pt                  !MP,prop,mat no.,parameter name
MP, DENS, 4, dens_pt
MP, NUXY, 4, poisson_pt
!***************** Platinum material
MP, EX, 5, young_ti                  !MP,prop,mat no.,parameter name
MP, DENS, 5, dens_ti
MP, NUXY, 5, poisson_ti
!!****************************Geometry*****************************!!
RECTNG,0,PZTLEN,0,BEAM_W
RECTANG,PZTLEN-STEP,PZTLEN,0,BEAM_W
RECTANG,0,PZTLEN,0,STEP
RECTANG,PZTLEN-2*STEP,PZTLEN,0,BEAM_W
RECTANG,0,PZTLEN,0,2*STEP
RECTANG,PZTLEN-3*STEP,PZTLEN,0,BEAM_W
RECTANG,0,PZTLEN,0,3*STEP
AOVLAP,ALL
!***************************Create 2-D mesh
ESIZE,MESHSIZE
MSHAPE,0,2D
AMESH,ALL
!*********************Create Si Str. layer**************************!
type,4
mat,1
esize,,5
mshkey,1
mshape,0,3d
vext,all,,,,,beam_t
!************************Create SiO2 layer**************************!
ASEL,S,Loc,Z,beam_t
TYPE,2
mat,3
esize,,1
mshkey,1
mshape,0,3d
vext,all,,,,,SO_THICK
!*********************Create bottom Ti layer************************!
ASEL, S, Loc, Z, beam_t+SO_THICK
```

```
ASEL, U, LOC, X, (pztlen-step), pztlen
ASEL, U, LOC, Y, 0, step
TYPE,2
mat,5
esize,,1
mshkey,1
mshape,0,3d
vext,all,,,,,ti_thick
!*********************Create bottom Pt layer************************!
ASEL,S,Loc,Z,beam_t+SO_THICK+ti_thick
ASEL, U, LOC, X, (pztlen-step), pztlen
ASEL, U, LOC, Y, 0, step
TYPE,2
mat,4
esize,,1
mshkey,1
mshape,0,3d
vext,all,,,,,pt_thick
!***************************Create  PZT layer***********************!
ASEL,S,Loc,Z,beam_t+SO_THICK+pt_thick+ti_thick
ASEL, U, LOC, X, pztlen-(2*step),pztlen
ASEL, U, LOC, Y, 0, 2*step
TYPE,3
mat,2
esize,,2
mshkey,1
mshape,0,3d
vext,all,,,,,pzt_th
!***********************Create top Ti layer*************************!
ASEL,S,Loc,Z,beam_t+SO_THICK+pt_thick+pzt_th+ti_thick
ASEL,U,LOC,X,pztlen-(3*step),pztlen
asel,u,loc,y,0,3*step
TYPE,2
mat,5
esize,,1
mshkey,1
mshape,0,3d
vext,all,,,,,ti_thick
!************************Create top Pt layer************************!
ASEL,S,Loc,Z,beam_t+SO_THICK+2*ti_thick+pzt_th+pt_thick
ASEL,U,LOC,X,pztlen-(3*step),pztlen
asel,u,loc,y,0,3*step
TYPE,2
```

```
mat,4
esize,,1
mshkey,1
mshape,0,3d
vext,all,,,,,pt_thick
NUMMRG,KP,tol,,,,
!!Apply Boundary Conditions!!!!
NSEL,S,LOC, X, 0       !select nodes at the anchor
NSEL,R,LOC, Z, 0, beam_t !exclude PZT (optional)
D, ALL, UX, 0          !!Constain all movements
D, ALL, UY, 0
D, ALL, UZ, 0
NSEL, S,  LOC, Y, beam_w     !!Symmetry condition lognitudinal axis
dsym, symm, y, ,
!!********************APPLY LOAD***********************************!!
! Define the coupling sets of the electrode
! Apply voltage on the electrode
! * Define the first couple set of the bottom electrode
NSEL,S, LOC, z, beam_t+so_thick+pt_thick,
NSEL,S, LOC, z, beam_t+so_thick+pt_thick,
! * Ground bottom electrode
*GET,node_g,NODE,,NUM,MIN
CM,ground,NODE
CP,NEXT, VOLT, ALL
D,node_g, VOLT, 0
! * Define the second couple  set of the top electrode
NSEL,S , LOC, z, pzt_th+beam_t+so_thick+pt_thick,
NSEL,S , LOC, z, pzt_th+beam_t+so_thick+pt_thick,
*GET,node_s,NODE,,NUM,MIN
CM,signal,NODE
CP, NEXT, VOLT, ALL
D,node_s, VOLT, 5
Allsel,all,all
SAVE
FINISH
!!-----------------------------------------------------------------!!
!!!!!!!!!!!!!!!!Solution of static analysis problem!!!!!!!!!!!!!!!!
/SOL
ANTYPE,0
NLGEOM,1
NSUBST,5,1000,1
AUTOTS,1
/STATUS,SOLU
```

```
ESEL,U,TYPE,,1
SOLVE
FINISH
/POST1
PLDISP,0
!!--------------------Modal Analysis------------------------------!!
/SOLUTION
ANTYPE,MODAL                           ! MODAL ANALYSIS
MODOPT,LANB,MODES,FRQSTR,FRQEND,,ON    ! BLOCK LANCZOS SOLVER
MXPAND,,,,YES                          ! EXPAND MODE
ALLSEL, ALL
ESEL, U, TYPE,,1
SOLVE
FINISH
SAVE
!!----------------------Harmonic Solution-------------------------!!
/COMFIG, NRES, 10000 !Number of results allowed
/SOLU !Solution processor
EQSLV, SPARSE, 1E-13 !Symmetric and Unsymmetrisc
!sparse matrix solver
ANTYPE, HARMIC !Type of analysis
HROPT, FULL !Full harmmonic analysis
HROUT, ON !Print solution as real and imaginary
OUTRES, ALL, ALL !Saves all of the solution data
HARFREQ, FRQSTR, FRQEND !Frequency range for solution
NSUBST, subs !sampling rate
KBC, 1 !step boundary condition
DMPRAT, 0.0044 !Global damping ratio (LDV)
ALLSEL, ALL,
ESEL,U, TYPE,,1
SOLVE
FINISH
SAVE
```

A-4 2-D analysis of a piezo actuated multi layered Si beam.

```
!!****2-D model of a multimorph piezoelectrically actuated beam****!!
/FILENAME,2D cantilever model
```

```
/UNITS, SI
/prep7
!!****************************Basic Units**************************!!
Same as for the 3-D model
!!***************Define material parameters***********************!!
! * PZT (p=PZT) Ferroperm PZ23
dens_p=7700                                       !Density in kg/m^3
c11_p=138.4e9                             !C11_p=E/(1-v^2) in N/M^2
c12_p=89.99e9                             !C12_p=vE/(1-v^2)in N/M^2
c13_p=89.99e9                         !C13_p=C12_p  in N/M^2
c33_p=138.4e9                          !C33_p=C11_p   in N/M^2
c44_p=48.4e9                            !C44_p=E/2(1+v)  in N/M^2
e31_p=0.2814                                         !eij=(dik)(Ckj)
e33_p=22.3617
e24_p=20.3856
eps11_p=1529*eps_0                                        ! In F/m^2
eps33_p=759*eps_0                                       ! In F/m^2
!!********************Mesh paramters******************************!!
Same as for the 3-D model
!!*************Define geometrical  structural parameters***********!!
pztlen=1.4*mm
beam_t=10*um
pzt_th=1*um
so_thick=0.2*um
pt_thick=0.1*um
ti_thick=0.01*um
!!***************material reference number*************************!!
Same as for the 3-D model
!!*********************Element type used***************************!!
ET, 1, PLANE183
KEYOPT, 1, 3, 0                    !Plane Stress condition
ET, 2, PLANE223, 1001,,0
KEYOPT, 2, 3, 2                    !Plane Strain Condition
!!********************Material declaration*************************!!
! * PZT Material use either anelastic either homog data
MP, DENS, 2, dens_p
MP, LSST, 2, loss_pzt
!MP, DMPR, 2, damp_pzt
MP, EX, 2, 67.5e9
MP, NUXY, 2, 0.394
TB, PIEZ, 2
TBDATA, 2, e31_p
TBDATA, 5, e33_p
```

```
TBDATA, 8, e24_p
MP, PERX, 2, eps11_p
MP, PERY, 2, eps2_p
!Same as for the 3-D model for the rest of the materials
!!***************************Geometry****************************!!
k,1,0,0,0
k,2,pztlen,0,0
k,3,pztlen,beam_t,0
k,4,0,beam_t,0
k,5,0,beam_t+so_thick,0
k,6,pztlen,beam_t+so_thick,0
k,7,0,beam_t+ti_thick+so_thick,0
k,8,pztlen,beam_t+ti_thick+so_thick,0
k,9,0,beam_t+ti_thick+pt_thick+so_thick,0
k,10,pztlen,beam_t+ti_thick+pt_thick+so_thick,0
k,11,0,beam_t+pzt_th+ti_thick+pt_thick+so_thick,0
k,12,pztlen,beam_t+pzt_th+ti_thick+pt_thick+so_thick,0
k,13,0,beam_t+pzt_th+2*ti_thick+pt_thick+so_thick,0
k,14,pztlen,beam_t+pzt_th+2*ti_thick+pt_thick+so_thick,0
k,15,0,beam_t+pzt_th+2*ti_thick+2*pt_thick+so_thick,0
k,16,pztlen,beam_t+pzt_th+2*ti_thick+2*pt_thick+so_thick,0
A,1,2,3,4
A,4,5,6,3
A,5,7,8,6
A,7,9,10,8
A,9,11,12,10
A,11,13,14,12
A,13,15,16,14
!************************Mesh control******************************!
lesize,1,,,140
lesize,3,,,140
lesize,2,,,5
lesize,4,,,5
lesize,5,,,1
lesize,6,,,140
lesize,7,,,1
lesize,8,,,1
lesize,9,,,140
lesize,10,,,1
lesize,11,,,1
lesize,12,,,140
lesize,13,,,1
lesize,14,,,2
```

```
lesize,15,,,140
lesize,16,,,2
lesize,17,,,1
lesize,18,,,140
lesize,19,,,1
lesize,20,,,1
lesize,21,,,140
lesize,22,,,1
!*************************Meshing******************************!
asel,s,,,1,
type,1
mat,1
mshape,0,2d
amesh,all
asel,s,,,2,
type,1
mat,3
mshape,0,2d
amesh,all
asel,s,,,3,
type,1
mat,5
mshape,0,2d
amesh,all
asel,s,,,4,
type,1
mat,4
mshape,0,2d
amesh,all
asel,s,,,5,
type,2
mat,2
mshape,0,2d
amesh,all
asel,s,,,6,
type,1
mat,5
mshape,0,2d
amesh,all
asel,s,,,7,
type,1
mat,4
mshape,0,2d
```

```
amesh,all
NUMMRG,KP,tol,,,,
!!******************Apply Boundary Conditions**********************!!
NSEL,S,LOC, X, 0     !select nodes at the anchor
D, ALL, UX, 0         !!Constain all movements
D, ALL, UY, 0
!!****************************Apply Load***************************!!
NSEL,S, LOC, y, beam_t+so_thick+ti_thick+pt_thick,
NSEL,S, LOC, y, beam_t+so_thick+ti_thick+pt_thick,
! * Ground bottom electrode
*GET,node_g,NODE,,NUM,MIN
CM,ground,NODE
CP,NEXT, VOLT, ALL
D,node_g, VOLT, 0
NSEL,S , LOC, y, pzt_th+beam_t+so_thick+ti_thick+pt_thick
NSEL,S , LOC, y, pzt_th+beam_t+so_thick+ti_thick+pt_thick
*GET,node_s,NODE,,NUM,MIN
CM,signal,NODE
CP, NEXT, VOLT, ALL
D,node_s, VOLT, 5
Allsel,all,all
FINISH
!!****************************Solution*****************************!!
!Same as 3-D model
```

B-1 ANSYS finite element model of a small Si frame for tensile testing of ceramics.

```
FINISH
/CLEAR
/FILENAME,Silicon frame final Sub11
/OUTPUT,TERM
/UNITS, SI
/SHOW
/PREP7
!*                        INPUT VARIABLES                            *
b_thick=425e-6                                  !Silicon Beam Thickness
b_length=2200e-6                                   !Silicon Beam Length
b_width=80e-6                                       !Silicon Beam Width
```

```
b_spac2=200e-6                                      !Lower Beams spacing
st_height=1.5e-3                                 !One Third Stage Height
st_width1=1.8e-3                                        !Stage Width1
st_width2=2e-3                                          !Stage Width2
tol= 0.100e-8
!*                        ELEMENT TYPES                                 *
ET, 1, PLANE42 !PLANE42 is used for 2-D modeling of solid structures.
ET, 2, SOLSH190
!*                      MATERIAL PROPERTIES                             *
! * Silicon (s=silicon)
dens_s=2330                                          !Density in kg/m^3
c11_s=165.7e9                                     !Young's modulus in Pa
c12_s=63.9e9
c44_s=79.6e9
!!**********************Material declaration***********************!!
! * Silicon material
TB, ANEL, 1
TBDATA, 1, c11_s
TBDATA, 2, c12_s
TBDATA, 3, c12_s
TBDATA, 7, c11_s ! c22=c11
TBDATA, 8, c12_s ! c23=c13
TBDATA, 12, c11_s
TBDATA, 16, c44_s ! c66=c44
TBDATA, 19, c44_s
TBDATA, 21, c44_s ! c55=c44
!*            DRAW THE HALF STAGE WITH 4 BEAMS                          *
K,1,0,0,0
K,2,(st_width2-(2e-4))/2,0,0
K,3,(st_width2-(2e-4))/2,5e-4,0
K,4,st_width2/2,5e-4,0
K,5,st_width2/2,3*st_height,0
K,6,0,3*st_height,0
K,7,0,3*st_height-(2e-4),0
K,8,-b_length,3*st_height-(2e-4),0
K,9,-b_length,3*st_height-(3e-4),0
K,10,0,3*st_height-(3e-4),0
K,11,0,2*st_height+600e-6,0
K,12,-st_width1,2*st_height+600e-6,0
K,13,-st_width1,2*st_height-400e-6,0
K,14,0,2*st_height-400e-6,0
K,15,0,st_height-(9e-4),0
K,16,-b_length,st_height-(9e-4),0
```

```
K,17,-b_length,st_height-(1e-3),0
K,18,0,st_height-(1e-3),0
K,19,0,st_height-(1.2e-3),0
K,20,-b_length,st_height-(1.2e-3),0
K,21,-b_length,st_height-(1.3e-3),0
K,22,0,st_height-(1.3e-3),0
!*                CREATE LINES FROM KEYPOINTS                      *
L,1,2,,
L,2,3,,
L,3,4,,
L,4,5,,
L,5,6,,
L,6,7,,
L,7,8,,
L,8,9,,
L,9,10,,
L,10,11,,
L,11,12,,
L,12,13,,
L,13,14,,
L,14,15,,
L,15,16,,
L,16,17,,
L,17,18,,
L,18,19,,
L,19,20,,
L,20,21,,
L,21,22,,
L,22,1,,
!*                        CREATE AREA                              *
FLST,2,26,4
FITEM,2,1
FITEM,2,2
FITEM,2,3
FITEM,2,4
FITEM,2,5
FITEM,2,6
FITEM,2,7
FITEM,2,8
FITEM,2,9
FITEM,2,10
FITEM,2,11
FITEM,2,12
```

```
FITEM,2,13
FITEM,2,14
FITEM,2,15
FITEM,2,16
FITEM,2,17
FITEM,2,18
FITEM,2,19
FITEM,2,20
FITEM,2,21
FITEM,2,22
AL,ALL,Z,
!*                      CREATE MESH                             *
ASEL,S, Loc, z,0
TYPE, 1        ! Eleent type: plane13 piezoelectric coupled element
MAT, 1         !
ESIZE,40E-6    ! Element size for the mesh element onto the 2D geom
MSHAPE,0,2D    ! Use quadrilateral-shaped elements to mesh
MSHKEY,0  ! Use mapped meshing
AMESH, ALL     ! Mesh all areas
!*                          CREATE VOLUME                       *
TYPE, 2              ! 1=PLANE13 2=SOLID45 3=SOLID5(PZT) 4=PLANE42
MAT, 1
ESIZE, ,15            ! Element size to be affected
ASEL, S , LOC, Z, 0-tol,0+tol
VEXT, ALL, , , , ,b_thick
NUMMRG,KP,tol,,,,
save
!!Apply Boundary Conditions!!!!
NSEL,S,LOC, X, -b_length      !select nodes at the anchor
D, ALL, UX, 0          !Constain all movements
D, ALL, UY, 0
D, ALL, UZ, 0
NSEL,S,LOC, X, st_width2/2     !Symmetry condition
dsym,symm,x,,
allsel,all,all
/SOL
ANTYPE,0
ACEL,0,0,10
/STATUS,SOLU
ESEL,U, TYPE,,1
SOLVE
FINISH
/SOL
```

```
ANTYPE,0
ACEL,0,0,10
NLGEOM,1
NSUBST,5,1000,1
AUTOTS,1
/STATUS,SOLU
esel,u,type,,1
SOLVE
FINISH
```

B-2 ANSYS finite element model of a single layer dog bone shaped structure with anchor part

```
!!**This program is modelling a dog bone shaped structure**!!
/FILENAME, Equivalent length of a dog bone structure
/UNITS, SI
/prep7
!!************************Basic Units********************************!!
mm=1e-3
um=1e-6
eps_0=8.854e-12
!!*****************Define material parameters***********************!!
! * pzt (anisotropic properties of material)
dens_p=7850                                        !Density in kg/m^3
c11_p=148.1e9                               !C11_p in N/M^2
c12_p=98.1e9                                  !C12_p in N/M^2
c13_p=107.2e9                                !C13_p in N/M^2
c33_p=146.3e9                                 !C33_p in N/M^2
c44_p=25.5e9                                  !C44_p in N/M^2
! * Silicon Dioxide (so) (homogeneous material)
dens_so=2201
young_so=170e9
poisson_so=0.2
! * Platinum (pt) (homogeneous material)
dens_pt=21440
young_pt=170e9
poisson_pt=0.38
!!************************Mesh paramters***************************!!
tol=1e-9
```

```
!!***********Define geometrical  structural parameters*************!!
PI=3.14159265359
beam_length=200*um
anchor_lenght=30*um
beam_w=25*um                                        !beam width
anchor_width=150*um
pzt_th=1*um
so_thick=1*um
pt_thick=1*um
radius1=20*um
radius2=15*um
COSSIN=cos(45.0*PI/180.0)
!!******************material reference number*********************!!
! material 1 = PZT
! Material 2 = Silicon Dioxide
! Material 3 = Platinum
!!***********************Element type used************************!!
ET, 1, Shell181        !for very thin layers
ET, 2, SOLID5          !For the tested film
ET, 3, PLANE13         !For meshing areas and plane stress condition
!!!!!**********************************************************!!!!!
!!*********************Material declaration**********************!!
!!!!!**********************************************************!!!!!
! * Pzt material
MP, DENS, 1, dens_p
TB, ANEL, 1
TBDATA, 1, c11_p
TBDATA, 2, c12_p
TBDATA, 3, c13_p
TBDATA, 7, c11_p ! c22=c11
TBDATA, 8, c13_p ! c23=c13
TBDATA, 12, c33_p
TBDATA, 16, (c11_p-c12_p)/2 ! c66=0.5*(c11-c12)
TBDATA, 19, c44_p
TBDATA, 21, c44_p ! c55=c44
! * Silicon Dioxide material
MP, EX, 2, young_so                  !MP,prop,mat no.,parameter name
MP, DENS, 2, dens_so
MP, NUXY, 2, poisson_so
! * Platinum material
MP, EX, 3, young_pt                  !MP,prop,mat no.,parameter name
MP, DENS, 3, dens_pt
MP, NUXY, 3, poisson_pt
```

```
!!***************************Geometry****************************!!
k,1, 0, 0, 0
k,2, anchor_lenght+radius1, 0, 0
k,3, anchor_lenght+beam_length, 0, 0
k,4, anchor_lenght+beam_length, beam_w, 0
k,5, anchor_lenght+radius1, beam_w, 0
k,6, anchor_lenght, beam_w+radius1, 0
k,7, anchor_lenght, beam_w+anchor_width-radius2, 0
k,8, anchor_lenght-radius2, beam_w+anchor_width, 0
k,9, 0, beam_w+anchor_width, 0
k,10,0, beam_w+anchor_width-radius2, 0
k,11,0, beam_w+radius1, 0
k,12, anchor_lenght+radius1,beam_w+radius1,0
k,13, anchor_lenght-radius2,beam_w+anchor_width-radius2,0
k,14, anchor_lenght+radius1-cossin*radius1,beam_w+radius1-cossin*radius1,0
l,1,2,,,,,,
l,2,3,,,,,,
l,3,4,,,,,,
l,4,5,,,,,,
larc,5,14,12,radius1
larc,14,6,12,radius1
l,6,7,,,,,,
larc,7,8,13,-radius2
l,8,9,,,,,,
l,9,10,,,,,,
l,10,11,,,,,,
l,11,1,,,,,,
l,10,7,,,,,,
l,11,6,,,,,,
l,2,5,,,,,,
l,1,14,,,,,,
!Mesh control
lesize,1,,,20
lesize,2,,,15
lesize,3,,,20
lesize,4,,,15
lesize,5,,,20
lesize,6,,,20
lesize,7,,,20
lesize,8,,,12
lesize,9,,,8
lesize,10,,,12
lesize,11,,,20
```

```
lesize,12,,,20
lesize,13,,, 20
lesize,14,,,20
lesize,15,,,20
lesize,16,,,20
!Create 2-D geometry
A,2,3,4,5
A,1,2,5,14
A,1,14,6,11
A,11,6,7,10
A,9,10,7,8
type,3
eshape,3
asel,s,loc,z,0
amesh,all
!Create Mesh
type,2
mat,2
ESIZE,,4
ASEL,S,Loc,Z,0,
vext,all,,,,,so_thick
NUMMRG,ALL,tol,,,,
!!*****************Apply Boundary Conditions***********************!!
NSEL,S,LOC, X, 0       !select nodes at the anchor
D, ALL, UX, 0          !!Constain all movements
D, ALL, UY, 0
D, ALL, UZ, 0
NSEL,S,LOC, Y, 0      !!Symmetry condition lognitudinal axis
dsym,symm,y,,
!!*********************Apply load*********************************!!
NSEL,S,Loc,x,anchor_lenght+beam_length
*GET, Par, NODE, , count   !Get total number of nodes
!at the anchor fixed end
f,all,fx,0.001/par              !Apply load uniformly on nodes
Allsel,all,all
FINISH
!!!!!!!!!!!!!!!!Solution of static analysis problem!!!!!!!!!!!!!!!!
/SOL
ANTYPE,0
/STATUS,SOLU
SOLVE
FINISH
```

B-3 ANSYS finite element model of a three layer dog bone shaped structure with anchor part

```
!!**This program is modelling a dog bone shaped structure**!!
/FILENAME, Equivalent length of a dog bone structure
/UNITS, SI
/prep7
!!***********************Basic Units*******************************!!
!Same as single layer dog bone
!!****************Define material parameters**********************!!
! * pzt
dens_p=7850                                        !Density in kg/m^3
young_p=40e9  !10,..70e9 tested
poisson_so=0.2
! * Silicon Dioxide (so)
dens_so=2201
young_so=170e9
poisson_so=0.2
! * Platinum (pt)
dens_pt=21440
young_pt=170e9
poisson_pt=0.38
!!************************Mesh paramters***************************!!
!Same as single layer dog bone
!!***********Define geometrical  structural parameters*************!!
PI=3.14159265359
beam_length=200*um
anchor_lenght=30*um
beam_w=25*um                                        !beam width
anchor_width=150*um
pzt_th=1*um
so_thick=1*um
pt_thick=1*um
radius1=20*um
radius2=15*um
COSSIN=cos(45.0*PI/180.0)
!!******************material reference number*********************!!
! material 1 = PZT
! Material 2 = Silicon Dioxide
! Material 3 = Platinum
!!**********************Element type used************************!!
```

```
ET, 1, Shell181        !for very thin layers
ET, 2, SOLID5          !For the tested film
ET, 3, PLANE13         !For meshing areas and plane stress condition
!!*********************Material declaration**********************!!
! * Pzt material
MP, DENS, 1, dens_p
MP, EX, 1, young_p                  !MP,prop,mat no.,parameter name
MP, NUXY, 1, poisson_p
! * Silicon Dioxide material
MP, EX, 2, young_so                  !MP,prop,mat no.,parameter name
MP, DENS, 2, dens_so
MP, NUXY, 2, poisson_so
! * Platinum material
MP, EX, 3, young_pt                  !MP,prop,mat no.,parameter name
MP, DENS, 3, dens_pt
MP, NUXY, 3, poisson_pt
!!***************************Geometry****************************!!
k,1, 0, 0, 0
k,2, anchor_lenght+radius1, 0, 0
k,3, anchor_lenght+beam_length, 0, 0
k,4, anchor_lenght+beam_length, beam_w, 0
k,5, anchor_lenght+radius1, beam_w, 0
k,6, anchor_lenght, beam_w+radius1, 0
k,7, anchor_lenght, beam_w+anchor_width-radius2, 0
k,8, anchor_lenght-radius2, beam_w+anchor_width, 0
k,9, 0, beam_w+anchor_width, 0
k,10,0, beam_w+anchor_width-radius2, 0
k,11,0, beam_w+radius1, 0
k,12, anchor_lenght+radius1,beam_w+radius1,0
k,13, anchor_lenght-radius2,beam_w+anchor_width-radius2,0
k,14, anchor_lenght+radius1-cossin*radius1,beam_w+radius1-cossin*radius1,0
l,1,2,,,,,,
l,2,3,,,,,,
l,3,4,,,,,,
l,4,5,,,,,,
larc,5,14,12,radius1
larc,14,6,12,radius1
l,6,7,,,,,,
larc,7,8,13,-radius2
l,8,9,,,,,,
l,9,10,,,,,,
l,10,11,,,,,,
l,11,1,,,,,,
```

```
l,10,7,,,,,,,
l,11,6,,,,,,,
l,2,5,,,,,,,
l,1,14,,,,,,,
!Mesh control
lesize,1,,,20
lesize,2,,,15
lesize,3,,,20
lesize,4,,,15
lesize,5,,,20
lesize,6,,,20
lesize,7,,,20
lesize,8,,,12
lesize,9,,,8
lesize,10,,,12
lesize,11,,,20
lesize,12,,,20
lesize,13,,, 20
lesize,14,,,20
lesize,15,,,20
lesize,16,,,20
!Create 2-D geometry
A,2,3,4,5
A,1,2,5,14
A,1,14,6,11
A,11,6,7,10
A,9,10,7,8
type,3
eshape,3
asel,s,loc,z,0
amesh,all
!Create Mesh
type,2
mat,2
ESIZE,,4
ASEL,S,Loc,Z,0,
vext,all,,,,,so_thick
NUMMRG,ALL,tol,,,,
!!*****************Apply Boundary Conditions***********************!!
NSEL,S,LOC, X, 0       !select nodes at the anchor
D, ALL, UX, 0          !!Constain all movements
D, ALL, UY, 0
D, ALL, UZ, 0
```

```
NSEL,S,LOC, Y, 0      !!Symmetry condition lognitudinal axis
dsym,symm,y,,
!!*********************Apply load***********************************!!
!!****************************Solution******************************!!
!Same as single layer dog bone
```

C-1 PZT properties from Ferroperm Catalogue

Ferroperm Piezoceramics A/S

Material data based on typical values

Symbol	Unit	Pz21	Pz23	Pz24	Pz26	Pz27	Pz28	Pz29	Pz34	Pz46	Pz26, FEM
e1,rs		3.24E+03	1.37E+03	7.39E+02	1.19E+03	1.80E+03	1.22E+03	2.44E+03	2.37E+02	1.27E+02	1.31E+03
e3,rs		3.98E+03	1.50E+03	4.25E+02	1.33E+03	1.80E+03	9.90E+02	2.87E+03	2.08E+02	1.24E+02	1.08E+03
tan d		0.016	0.013	0.002	0.003	0.017	0.004	0.016	0.014	0.003	0.018
TC >	C	218	350	330	330	350	330	235	400	350	150
e31	C/m2	-2.92	-1.93	-1.45	-2.80	-3.09	-3.60	-5.06	-0.35	1.61	-5.48
e33	C/m2	23.4	15.5	9.9	14.7	16.0	12.4	21.2	6.5	17.6	13.6
e15	C/m2	16.19	10.81	7.62	9.86	11.64	10.67	13.40	2.52	1.16	9.55
c11E	N/m2	1.14E+11	1.57E+11	1.62E+11	1.68E+11	1.47E+11	1.52E+11	1.34E+11	1.45E+11	3.13E+11	1.55E+11
c12E	N/m2	7.57E+10	1.09E+11	8.84E+10	1.10E+11	1.05E+11	9.05E+10	8.97E+10	3.28E+10	2.36E+11	9.41E+10
c13E	N/m2	7.24E+10	9.77E+10	8.75E+10	9.99E+10	9.37E+10	8.74E+10	8.57E+10	1.30E+10	1.49E+11	7.99E+10
c33E	N/m2	1.11E+11	1.23E+11	1.34E+11	1.23E+11	1.13E+11	1.18E+11	1.09E+11	1.39E+11	1.03E+11	1.10E+11
c44E	N/m2	2.63E+10	2.57E+10	3.08E+10	3.01E+10	2.30E+10	2.65E+10	1.85E+10	5.81E+10	3.82E+10	2.73E+10